Magnetic field strength estimations for the main phases of solar cycles 13-24 using magnetohydrodynamic Rossby waves in the lower tachocline

by

Tania Morris

(2291968)

Dissertation

Submitted in fulfilment of the requirements for the degree of

Master of Science

in

Applied Mathematics

in the Faculty of Computer Science and Applied Mathematics,

University of the Witwatersrand, Johannesburg, South Africa

Supervisor: Thama Duba, PhD.

September 2024

Declaration

I declare that this dissertation is my own, unaided work.

It is being submitted for the Degree of Master of Science at the University of the Witwatersrand, Johannesburg.

It has not been submitted before for any degree or examination at any other University.

(Signature of candidate)

16th day of September 2024 at Meyerspark, Pretoria.

Abstract

The magnetic field strength (MFS) estimates used by the existing space weather prediction models (SWPMs) are inaccurate. Consequently, it has been indicated that there is a need to find solutions to rectify the wrong assumption that the magnetic field remains constant in strength and location throughout the solar cycle. This study explores a solution to this problem by increasing the granularity and accuracy of the previous MFS estimations by calculating them for the main phases of the solar cycle (solar minimum and maximum) per hemisphere for solar cycles 13-24. A dispersion relation of the fast magnetohydrodynamic (MHD) Rossby wave was derived analytically in spherical coordinates that included a toroidal magnetic field and latitudinal differential rotation, which adequately captures the dynamics of the lower tachocline. Secondly, a change to the methodology of calculating the MFS that utilises the established connection between the observed Rieger-type periodicity (RTP) in solar activity of 150-190 days and the fast MHD Rossby wave in the lower tachocline was proposed. Furthermore, a new magnetic field profile (MFP) of $B_\phi = B_0 \sin(6\Theta)$ was introduced to improve the model results. This MFP has a maximum and minimum value at the same latitudes associated with sunspot appearances during these extreme solar cycle phases. Consequently, the MFS values were calculated at a latitude of 29° (solar min) and 16° (solar max) using the hemispheric RTP data. The average MFS (RTP) for the solar min and solar max in the dominant hemisphere was established to be 8 kG (212 days) and 76 kG (163 days), respectively. For the non-dominant hemisphere, the average MFS was established to be 5 kG (213 days) and 50 kG (183 days) for the solar min and max, respectively. The results of this study show a significant difference in the results based on latitude. The findings have also revealed that the periodicity of increased solar activity associated with a specific MFS is affected not only by the solar cycle strength and hemispheric asymmetry but also by the solar cycle phase (or latitude) considered. Additionally, we strongly argue that this study's MFS results represent reality more closely than previously calculated results. Therefore, we propose that the MFS estimates reported in this study should be considered for the input to various existing space weather prediction models.

Key words: MHD Rossby waves, Lower tachocline, Rieger-type periodicities, Toroidal magnetic field strength, Space weather

Acknowledgements

I give all the glory to God, my Saviour and King, who gave me the honour of studying His breathtaking creation.

Thank you to Dr. Thama Duba for providing your guidance and supervision throughout this process.

I would like to also extend my gratitude to Dr. Irene Kamara, whose expertise was valuable in the editing of this thesis. She enhanced the clarity and readability of my work which greatly improved its overall quality.

To my husband, Robert, and the van Niekerks - the most incredible support system anyone could ask for. Without you, I could not have finished this journey.

Then, to Kate and Richard, thank you. For everything.

Last but not least. I would like to thank my other family, Jaco, Dhimal, Sibusiso and Dharshini, for the unconditional grace and support you have given me. For always understanding, having time to listen, giving advice, and making me laugh when I desperately needed it.

I am truly blessed to have you all in my life, and I look forward to sharing the next chapter of life with you.

"*When the race is complete, still my lips shall repeat: Yet not I, but through Christ in me.*"
CityAlight.

Contents

List of Figures

List of Tables

List of Symbols

Symbol	Description	Symbol	Description
ω	Frequency	Ω_0	Equatorial rotation rate
t	Time	μ_0	Permeability of free space
k	Wavenumber	∇	Gradient operator
ϕ	Phase constant	S	Surface area
v_p	Phase velocity	A	Unit area
$\boldsymbol{\Omega}$	Angular rotation rate	R_e	Reynolds number
f	Coriolis parameter	$\boldsymbol{v}_a$	Absolute velocity
c_s	Sound speed	v_P	Particle velocity
k_B	Boltzmann constant	T	Temperature
p	Pressure	R_m	Magnetic Reynolds number
ρ	Density	η	Magnetic diffusivity
β_p	Plasma beta	h	Fluid layer thickness
L_0	Characteristic scale length	ϵ	Lamb parameter
U_0	Characteristic plasma velocity	λ	Wavelength (Only in Chapter 3)
μ_d	Dynamic viscosity of the fluid	C_0	Surface gravity speed
ν	Kinematic viscosity	v_A	Alfvén speed
$\mathbf{F}$	Force	B_0	Magnetic field strength
m	Mass (Before Chapter 4)	B_ϕ	Toroidal magnetic field strength
$\mathbf{a}$	Acceleration	B_{max}	Maximum magnetic field strength
V_{vol}	Volume	s_2	Latitudinal differential rotation parameter
$\mathbf{g}$	Gravity	Ω_d	Differential rotation rate
m^*	Mass flux	n	Poloidal wavenumber
Θ	Latitude	m	Toroidal wavenumber (After Chapter 4)
θ	Co-latitude	k_x	Zonal wavenumber
$\mathbf{B}$	Magnetic field	k_y	Meridional wavenumber
$\mathbf{E}$	Electric field	g_e	Effective gravity
β	Coriolis beta parameter	α_0	Magnetic field strength parameter
$\mathbf{J}$	Current density	R_r	Rotation radius
σ	Conductivity of material	R_0	Distance from the solar centre to the tachocline
ρ_r	Resistivity	R	Radius of the Earth
ζ_e	Planetary vorticity	R_{nr}	Rossby number
ζ_r	Relative vorticity	ζ_a	Absolute vorticity

List of Acronyms

Acronym	Full description
AMS	American Meteorological Society
AWSoM	Alfvén Wave Solar-Atmosphere Model
CBPs	Coronal Bright Points
CESSI	Centee of Excellence in Space Studies India
CME	Coronal Mass Ejection
COST	European Cooperation in Science and Technology
CVE	Control Volume Element
EE	Eruptive Event
GMFS	Global Magnetic Field Structure
GPS	Global Positioning System
GRO	Greenwich Royal Observatory
HAO	High Altitude Observatory
HD	Hydrodynamic
ISES	International Space Environmental Services
KSO	Kanzelhohe Solar Observatory
LDR	Latitudinal Differential Rotation
LEO	Low Earth Orbiting (satellite)
MFP	Magnetic Field Profile
MFS	Magnetic field strength
MHD	Magnetohydrodynamic
MWTF	Mount Wilson Total Magnetic Flux
NASA	National Aeronautics and Space Administration
NGS	National Geographic Society
NOAA	National Oceanic and Atmospheric Administration
PDE	Partial Differential Equation
ROB	Royal Observatory of Belgium
RTP	Rieger-Type Periodicity
SWMF	Space Weather Modelling Framework
SWPC	Space Weather Prediction Centre
SWPMs	Space Weather Prediction Models
SDO	Solar Dynamics Observatory
STEREO	Solar Terrestrial Relations Observatory
sunRISE	Sun Radio Interferometer Space Experiment
SWEs	Shallow Water Equations

1 Introduction

1.1 Background

The orbit of Earth around the Sun is positioned such that it falls within the "Goldilocks zone", meaning that the distance from the Sun is far enough such that water remains in liquid form (NASA, 2022). However, a downside of being in this orbit is that Earth is also close enough to be affected by severe solar activity that occurs due to the Sun's dynamic and, at times, unstable magnetic field. Scientists have been studying the Sun to understand the solar events that cause changes in space weather, resulting in geomagnetic (or solar) storms (Dikpati and McIntosh, 2020) that lead to disruptions on Earth that mainly impact various technologies. The space weather modelling framework (SWMF) consists of various space weather prediction models (SWPMs) that aim to forecast the conditions of the Sun that result in solar storms (Gombosi et al., 2021). These SWPMs can use observations of solar activity as an indicator of the conditions within the Sun, another factor contributing to the space weather forecast.

However, solar activity is known to be cyclical, varying in the number of occurrences and location of eruptions, and scientists have been studying the role of waves on the Sun in this cycle. Rossby waves are present in the solar environment due to rotation and the fluid-like nature of solar plasma. In this study, researchers focus on magnetohydrodynamic (MHD) Rossby waves, which are affected by the magnetic field, an essential aspect of solar dynamics.

By applying MHD fluid dynamic principles to the tachocline layer of the Sun, researchers can model the plasma's large-scale behaviour, including flow patterns and Rossby wave propagation. The MHD Rossby waves in the lower part of the solar tachocline are heavily researched due to their connection to a specific periodicity of increased solar activity called the Rieger-type periodicity (RTP) of 150-190 days (Zaqarashvili et al., 2010; Gurgenashvili et al., 2016, 2017; Dikpati et al., 2017; Zaqarashvili and Gurgenashvili, 2018; Zaqarashvili, 2018; Korsós et al., 2023). The connection between MHD Rossby waves and the RTP allows researchers to calculate an estimated value for the magnetic field strength (MFS) (Gurgenashvili et al., 2016; Zaqarashvili and Gurgenashvili, 2018). The observational RTP data can be used as the frequency input to the MHD Rossby wave dispersion relation, such that the MFS is the only unknown variable that can be solved.

Similar to the MFS being a parameter in the MHD Rossby wave model, it is also an input to various existing space weather prediction models (SWPMs). However, current estimated MFS values used by the SWPMs are inaccurate (Borovikov et al., 2017; Kay et al., 2017), resulting in less effective space weather forecasts. Therefore, exploring different MHD Rossby wave models, examining input parameter values, and identifying possible methodology enhancements in calculating the MFS can all contribute to more accurate MFS estimates, which can be subsequently used in the SWPMs.

1.2 Problem statement

It is currently possible to predict solar activity events that can result in geomagnetic storms using two different methods: space weather prediction models (SWPMs) (Gombosi et al., 2021) and the propagation of solar MHD Rossby waves (Dikpati, 2020). However, both of these methods are theoretical and depend on models.

One significant issue with space weather forecasting is determining the magnetic field strength (MFS) used by SWPMs. The MFS is a crucial component, and the current values used provide limited information and lack accuracy (Borovikov et al., 2017; Kay et al., 2017), which leads to errors in the model's space weather forecast. This study aims to demonstrate how the MHD Rossby wave model can be used to estimate the MFS value more accurately.

Moreover, if the MHD Rossby wave model is inadequate, the associated propagation property equations derived from the wave's dispersion relation would also be flawed. This would cause inaccurate forecasting of active regions on the Sun's surface. Therefore, ensuring that the MHD Rossby model, the associated inputs, and the methodology used to calculate the MFS are as precise as possible is critical. If these are not accurate, the respective model's MFS estimates or forecast will be unreliable, and revisiting the model and/or the model inputs becomes necessary.

1.3 Research significance, aim and objectives

1.3.1 Research significance

Both problems highlighted in Section 1.2 can be addressed by improving the underlying MHD Rossby wave model and selecting the associated parameter values more aligned with solar observations. When the MHD Rossby wave model includes all the fundamental forces that describe the dynamics of the solar tachocline, it impacts the resulting equations of the wave dispersion relation. This, in turn, affects the equations for the phase and group velocity used to describe the wave propagation. Therefore, the accuracy of the corresponding wave propagation properties can improve by making the MHD Rossby wave model as comprehensive as possible. As a result, the comprehensive MHD Rossby model enhances the ability to forecast active regions on the surface of the Sun more accurately. Improving the precision of active region forecasts will allow timely warnings of Earth-facing active regions before any solar events occur, enabling necessary precautions to be taken in time.

On the other hand, a more comprehensive MHD Rossby wave model can be used to calculate an estimated value for the MFS, an input parameter in various existing space weather prediction models (SWPMs). However, enhancing the accuracy of a more comprehensive MHD Rossby wave model to calculate the MFS can be further improved when the input parameters used are mainly from observational data suitable for the period under consideration. Therefore, calculating the MFS at a more granular level, i.e. at various stages during the solar cycle, will be essential for the existing SWPMs. Such a dynamic methodology that captures these changes in the MFS over time could also be integrated into the SWPM framework. The framework has the potential to resolve the issues regarding the inaccuracies of the approximated MFS values currently being used in the SWPMs and will subsequently improve their forecasting accuracy. Therefore, it is clear that a refined MHD Rossby wave model, a revised methodology for calculating the magnetic field strength, and carefully chosen parameter values would provide various ways of improving the forecasting of space weather events.

1.3.2 Aim of research

This study aims to increase the granularity of the estimated magnetic field strength values and subsequently improve their accuracy so that they can replace the magnetic field strength proxies currently used in the existing space weather prediction models.

1.3.3 Objectives

The aim of this study will be accomplished through the following objectives:

1. To use empirical methods to determine the most appropriate MHD Rossby wave model and ascertain the most optimal parameter values for the MHD Rossby wave model.

2. To perform a sensitivity analysis to determine the effects of changing input parameters on the resulting MFS estimates for the chosen MHD Rossby wave model and evaluate the current methodology used to calculate the magnetic field strength.

3. To employ the newly proposed methodology and model changes proposed in this study to determine the MFS values at a more granular level and refine the current estimated values.

4. To validate the results by comparing them to observational findings.

1.4 Overview of the study

The first part of our work involves a literature review divided into four topics: the Sun, Rossby waves, the governing equations, and the magnetohydrodynamic (MHD) Rossby wave model. Part I provides the theoretical background necessary to understand the fundamental concepts referred to in this study. Since the environment of this study is the Sun, the first literature review topic is on the Sun. Chapter 2 starts by elaborating on the essential solar cycle dynamics and establishes the connection between sunspots and other types of solar activity. Moreover, the Rieger-type periodicity, observed in sunspots and other solar activity, is introduced. Next, the characteristics of the solar tachocline layer are discussed, including a more detailed explanation of the latitudinal differential rotation exhibited by the Sun. Finally, the necessary context relevant to the solar magnetic field is also provided. The second literature review subject is Rossby waves, the waves studied in this work. Therefore, in Chapter 3, we discuss the fundamental properties of waves, the forces and dynamics relevant to Rossby waves due to a rotating system, and the propagation mechanism of Rossby waves. Moreover, we mention the other waves in the Sun, but they will not be considered further. Lastly, we discuss the literature that proved Rossby waves exist on the Sun through their observations.

As the third part of the literature review, we formulate the governing equations that describe MHD Rossby waves in the chosen solar layer after establishing the solar environment and the specific wave under consideration. In Chapter 4, we formulate various sets of governing equations that differ based on the applied approximations and assumptions, including the commonly used shallow water approximation. Then, Part II of the document reviews the primary literature associated with the magnetohydrodynamic (MHD) Rossby wave models. Here, we derive three specific MHD Rossby wave models. We start with Chapter 5, which derives the most fundamental model in Cartesian coordinates, called the base model. Then, we move on to the spherical model, which additionally considers the effective gravity and the layer thickness as part of the model (Chapter 6). Finally, we derive the MHD Rossby wave model that includes latitudinal differential rotation in Chapter 7.

After defining the model landscape, Part III evaluates these models and their parameter values based on existing literature. The analysis performed in Chapter 8 addresses the problems identified in Section 1.2 and others mentioned throughout this study. Consequently, the outcome of Chapter 8 enables us to define an improved methodology that will be used to calculate the estimated solar magnetic field strength values on a more granular level. Thus, in Section 8.5.2, we explain how the existing methodology of calculating the magnetic field strength can be enhanced and how the accuracy of the MHD Rossby wave model could be improved. In Chapter 9, we provide the magnetic field strength results for the two primary solar cycle phases (solar min and max) per hemisphere for solar cycles 13-24. Finally, we conclude this study in Chapter 10 by discussing the results, highlighting important observations, and mentioning the avenues that future studies can pursue.

Part I

Literature Review: Theoretical Background

2 Literature Review I: The Sun

2.1 Introduction

Chapter 1 briefly introduced the concepts of space weather and geomagnetic storms. Understanding the dynamics involved in the solar cycle is important concerning these terms, as it demonstrates the variability of parameters across and throughout the different solar cycles. Therefore, this chapter will delve into the topics that pertain to the Sun in more detail.

The solar dynamics considered in this study are predominantly related to the migration of the Sun's magnetic polarity to the opposite hemisphere over an 11-year solar cycle. This chapter explores the behaviour of sunspots, a specific type of solar activity that visually represents the dynamics involved in this magnetic pole migration. It challenges the assumption of a static magnetic field. We will show that it is imperative to consider the two primary phases of the solar cycle, as they represent the most extreme periods of solar activity, whether it be a minimum or maximum.

Next, a more detailed explanation of space weather is provided, and the outcomes of current space weather prediction models are discussed. Furthermore, this chapter establishes the connection between sunspots and other more extreme solar activity, such as solar flares and coronal mass ejections (CMEs), which have been known to affect space weather significantly. It argues why sunspot data can be used to inform values used in the analysis of this study. Subsequently, the time scales associated with increased solar activity are explained, and the Rieger-type periodicity is introduced. Finally, the fundamental characteristics of the solar magnetic field are explored.

2.2 Solar cycle dynamics

Sunspots are a common form of solar activity that occurs when the magnetic field breaks through the solar surface. They are characterised by regions on the surface of the Sun where the magnetic field is concentrated (see Appendix A.3). The longevity of sunspots, which are visible for multiple days to weeks, allows them to be easily tracked and recorded over time compared to solar flares and CMEs.

The solar cycle, also known as the Schwabe cycle (named after an amateur astronomer, Heinrich Schwabe, who conducted solar observations from 1826 to 1843), is a well-known cyclical pattern of solar activity. By analysing his observations, Schwabe discovered that the number of sunspots that appear on the solar surface varies over 11 years, revealing a specific behavioural pattern. It was later established that the Sun's magnetic field orientation changed over these 11 years (Livingston, 1966), causing increased and decreased observed solar activity (see Appendix A.1 and A.2).

Figure (2.1) provides an easily observable diagram of the solar cycle and sunspot behaviour over time, recording the number of sunspots for every solar cycle. From this diagram, the 13 recorded 11-year solar cycles are observed (solar cycle 13 to the current cycle 25), illustrating the cycle's different phases according to the frequency of solar activity.

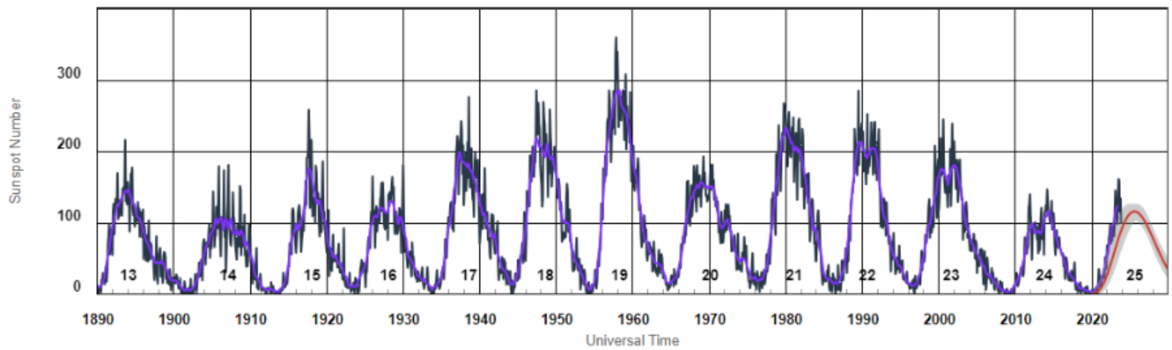

Figure 2.1: The International Space Environmental Services (ISES) Solar Cycle Sunspot Number Progression from the National Oceanic and Atmospheric Administration (NOAA) Space Weather Prediction Centre (SWPC) for solar cycles 13-25.

At the start of a solar cycle, the Sun exhibits little to no solar activity, which explains why this phase is referred to as the **solar minimum**. Over time, the frequency of solar activity increases until the number of sunspots reaches a peak during the **solar maximum**. After this, the solar activity frequency reduces at the end of the cycle to the same level of activity exhibited during a solar minimum. Furthermore, each solar cycle is unique, as shown in Fig.(2.1). Each cycle can be classified according to its strength, which determines the level of solar activity. For example, cycle 19 exhibited more frequent solar activity, making it a stronger cycle than cycle 14, which showed a lower frequency of solar activity. Additionally, we can infer from Fig.(2.1) that the peaks of the cyclical behaviour indicate that the solar events occurring during solar maximum are more frequent and are expected to be more severe, making the Earth more vulnerable during this phase of the solar cycle.

Moreover, the second important sunspot diagram, Fig.(2.2), maps the size and location of sunspots for every solar cycle and is called the butterfly diagram. This unique diagram shows that the latitude of observed sunspots migrates towards the equator throughout the solar cycle.

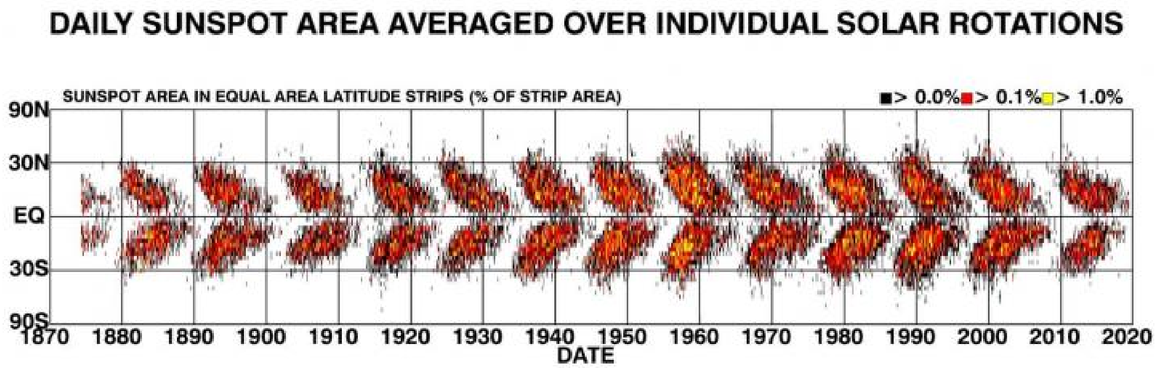

Figure 2.2: The butterfly diagram is the historical record that indicates the latitude and size of every sunspot occurrence for each solar cycle. Image courtesy of NASA.gov.

Now, recalling the solar cycle phases that were identified in Fig.(2.1), and considering the latitudinal information provided by Fig.(2.2), we can determine the corresponding latitudes for each of the solar cycle phases. It can be taken that the start of the solar cycle (solar min) exhibits solar activity mainly at a latitude of 30°. Whereas, during the solar maximum in the middle of the solar cycle, sunspots are primarily located at 16° and 5° near the end of the solar cycle.

Understanding the variance of the solar activity explained here, which is directly linked to the dynamic magnetic field, is essential. The following section will highlight a fundamental problem that involves paying attention to this time-dependent variability.

2.2.1 Problem with considering a static magnetic field location and strength throughout the solar cycle

Considering that magnetic field lines breaking through the solar surface are the source of sunspot formation (Appendix A.3), it can be concluded that the sunspot locations trace out the behaviour of the magnetic field lines close to the surface of the Sun. Therefore, it can be inferred that the magnetic field lines are also migrating towards the equator throughout the solar cycle, with corresponding changes in the strength.

The change in the location and frequency of sunspots can be seen as a consequence of this phenomenon. Thus, the current approach of considering a constant magnetic field strength at a latitude of 45° throughout the solar cycle (Gurgenashvili et al., 2016, 2017; Zaqarashvili and Gurgenashvili, 2018) should be re-evaluated as it directly contradicts this dynamic behaviour of the solar magnetic field described above. Reconsidering this static approach becomes increasingly important when MHD Rossby waves are used in an attempt to explain a cyclical solar phenomenon from observations. This is because the dates of the observational data used should allow us to identify what phase, or phases, of the solar cycle is applicable. Therefore, knowing the specific solar cycle phases under consideration is essential because the parameter values used in the dataset analysis can then be chosen accordingly.

These scenarios demonstrate how observational sunspot data can aid in informing the parameter values to be more appropriate and also show the need to vary parameters not only for each solar cycle but also for each primary phase of the cycle. Nevertheless, the importance of solar activity becomes evident in the next section, as it will explain how it is responsible for changing the space weather conditions.

2.3 Space weather

The European Cooperation in Science and Technology (COST) Action 724 (2009) formally defined **space weather** as "*the physical and phenomenological state of natural space environments. The associated discipline aims, through observation, monitoring, analysis and modelling, at understanding and predicting the state of the Sun, the interplanetary and planetary environments, and the solar and non-solar driven perturbations that affect them, and also at forecasting and nowcasting*[1] *the potential impacts on biological and technological systems.*"

In simplistic terms, space weather is the complex and highly variable conditions of the space

[1] The definition of nowcasting by the Federal Office of Meteorology and Climatology MeteoSwiss is appropriate, which states that it is "*the forecast of weather developments for the next few minutes and up to a maximum of six hours ahead*".

between the Sun and the Earth and changes when certain types of solar activity occur. Thus, before discussing the sporadic solar activity that is strong enough to affect Earth noticeably, we must first consider what the environment between the Sun and the Earth typically looks like without any additional disturbances. The Sun characteristically ejects a constant stream of solar particles, as shown by the arrows in Fig.(2.3a), that extends from the Sun on the left to the Earth, the object on the right, and is referred to as the **solar wind** (NOAA).

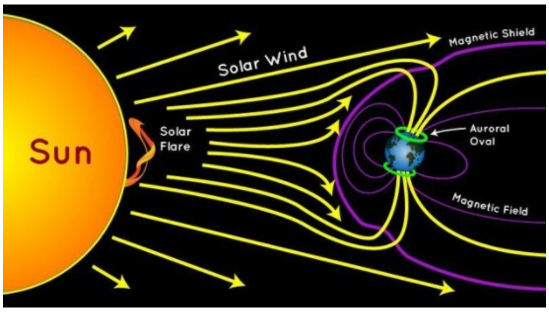

(a) Space weather dynamics.

(b) Aurora Borealis.

Figure 2.3: When solar activity occurs, the event will add additional solar energetic particles (SEPS) to the constant flow of the solar wind particles (yellow arrows), which subsequently interact with the Earth's magnetosphere (purple shield). If these particles penetrate the magnetosphere, they are guided by the magnetic field towards the poles, where collisions with other atmospheric elements result in the display of auroras. Fig.(2.3a) courtesy of NASA/JPL-Caltech. Fig.(2.3b) courtesy of Alexander Kuznetsov/Reuters. The aurora borealis in the sky near Rovaniemi in Lapland, Finland, October 7, 2018.

Solar flares and coronal mass ejections (CMEs) are the two main solar phenomena that alter the space weather environment by releasing solar energetic particles (SEPs) into space (Reames, 1999; 2013). Solar flares are observed as flashes of light on the solar surface. CMEs, on the other hand, are more severe; these are massive bursts of solar wind and magnetic field lines that rise above the Sun's corona and get ejected into space in what appears as an explosion, ejecting a large amount of solar mass into space. When the CME particles are directed towards Earth, they enter the magnetosphere (illustrated by the purple lines in Fig.(2.3a)), a magnetic region around the Earth that deflects them to the polar regions. The change in typical space weather conditions resulting from additional high-energy particles released during a solar flare or CME is called a **geomagnetic (or solar) storm**.

Since the solar storm particles only affect objects in their direct path, determining the location of these eruptions on the surface of the Sun is critical as we are mainly concerned with Earth-facing storms. More specifically we are interested in the solar storms that are magnetically connected to the Earth via heliospheric magnetic field structures of which a Parker spiral (Parker, 1958) is an example. Furthermore, determining whether a solar flare or CME is responsible for a geomagnetic storm is also essential since this can provide information about the expected time of arrival of the solar particles on Earth. For instance, the particles released during a solar flare can reach the Earth as quickly as 15 minutes (Dwivedi, 2003, p.258) compared to the few days the solar mass expelled from a CME would take to reach Earth.

Even though geomagnetic storms do not directly affect people, severe solar storms can significantly damage technology, causing devastating repercussions. Here, we will provide examples of the devastating effects of the most severe solar storms directed at Earth in recorded history to illustrate the worst-case scenario technological impact.

The first solar storm's impact was documented on 1 September 1859, only a few months ahead of solar cycle 10's maximum in 1860. It was a CME that lasted roughly five minutes, according to Richard Carrington, a novice skywatcher who observed the event through his private observatory telescope, after which the storm was named. Another significant solar storm to consider occurred in 1972, causing long-distance phone communications across multiple states in the U.S. to be down because of a solar flare. This event was so severe that the telecommunications company AT&T redesigned its transatlantic cable power system to handle the effects of such an event better (Malik, 2022). Although the cost impact due to the Carrington event and the 1972 solar flare occurred in response to the aftermath of a solar storm, more recent events could have been circumvented if the space weather forecasts had been provided in advance.

During a geomagnetic storm, the atmosphere heats up and expands outwards. As a result, the thermosphere, which ranges about $80 - 1000\,\mathrm{km}$ above the Earth's surface, becomes significantly denser, thereby increasing the drag a moving object will experience in that environment (Malik, 2022). Due to these unexpected environmental changes caused by a geomagnetic storm, the 40 Starlink Low Earth Orbit (LEO) satellites launched by SpaceX on 3 February 2022, with a total estimated cost of R938 million, or $50 million (Bateman, 2022), could not reach their intended orbit as their engines failed to overcome this increased drag force and fell back to Earth (Malik, 2022). Furthermore, a geomagnetic storm can also cause fluctuations in power grids and radio communications (especially short-wave, high-frequency transmissions), which can be as severe as causing complete blackouts. Satellite transmissions, high-latitude electrical networks, and spacecraft in orbit are all affected (Rani, 2022). Other ground-based sensitive electronics, such as ventilators and pacemakers, can also be corrupted by severe geomagnetic storms (HT Tech, 2023). In more extreme cases, solar storms can break down internet services, severely disrupt mobile networks (HT Tech, 2023), and melt power transformers.

Although severe storms occur less frequently, even minor ones can cause significant damage to costly technology. Another important example of a worst-case scenario technological impact is the "superstorm" caused by an extreme CME in July 2012 that missed Earth (Phillips, 2023) in this case. The National Academy of Sciences reported that the estimated economic impact of this storm hitting Earth would have exceeded \$2 trillion, and the damage caused, specifically to multi-ton transformers, would take years to repair (Phillips, 2023).

Finally, the geographical locations most vulnerable to severe impacts from these geomagnetic storms must be addressed. To do so, the spread of the human population across the globe should be considered. For example, the northern hemisphere has a larger human population, much closer to the north pole than the number of people the same distance from the south pole. Therefore, countries in the northern hemisphere are expected to be at a higher risk of experiencing the consequences of a solar storm than countries further away from the south pole[2], such as South Africa, which is much less likely to be impacted by such events. Nonetheless, as a society entirely dependent on electricity and the internet, a severe geomagnetic storm can cause unimaginable havoc. For this reason, it is crucial to accurately predict the time, location, and severity of solar storms so that preventive measures can be taken in advance. However, the current models for space weather forecasting pose particular difficulties, which will be discussed next.

2.3.1 Outcome of current space weather prediction models

The two inaccuracies observed from the existing space weather prediction models (SWPMs) pertain to the *arrival time* and *severity* of the solar storm, respectively. Even though space

[2]Similarly, it should be noted that although aurora borealis is more commonly referred to (see Fig.2.3b), it is merely a perception that auroras occur more often in the northern hemisphere compared to the southern hemisphere. The northern hemisphere has a landmass at much higher latitudes, increasing the human population close to the polar region. This increases the likelihood of humans observing this phenomenon more easily, making the documentation of aurora borealis more frequent than that of the aurora australis.

weather models such as the Centre of Excellence in Space Studies India (CESSI) stated an accurate prediction when their SWPM indicated a high probability of Earth experiencing a solar storm on 14 April 2022 (Gadgets 360, 2022), inaccurately estimating the arrival time or, even worse, not detecting a possible solar storm is common and dangerous. An example of this scenario is the geomagnetic storm that arrived "unexpectedly" in early August 2022.

An example of the effects of inaccuracy in predicting the *severity* or strength of the solar storm is the National Aeronautics and Space Administration's (NASA) prediction models, which showed a chance of a solar flare occurring between 17 and 18 February 2023. The model predicted a high chance of an M-class flare (medium strength) and a minor possibility of an X-class flare (the strongest classification). This was contrary to the experienced flare, classified as a *powerful* X-class flare that erupted from a freshly formed sunspot. In this case, the time prediction of the solar flare was accurate, but not the severity. Therefore, there are still challenges with the prediction accuracy of current SWPMs.

Although any model needs to be as accurate as possible, it is also well-known that the model results are only as good as the input data used. Therefore, we cannot neglect exploring avenues to increase the accuracy of the data used within these models or the amount of available data. In the next section, we will explore how the amount of data could be increased by utilising the connection between sunspots and other, more severe, solar activity.

2.4 Solar activity

As previously mentioned, solar flares and CMEs are the solar phenomena responsible for drastically changing space weather. Although understanding what causes these two types of solar eruptions is beyond the scope of this work, a simple discussion on how these phenomena are connected to the regions of sunspots is required.

First, recognise that the area where sunspots form exhibits a concentrated magnetic field (Appendix A.3), which creates an optimal environment known as **active regions**. It follows that broader solar activity data supports this claim and shows a strong correlation between the average number of sunspots and the number of solar flares over time (Abed et al., 2021), as illustrated in Fig.(2.4).

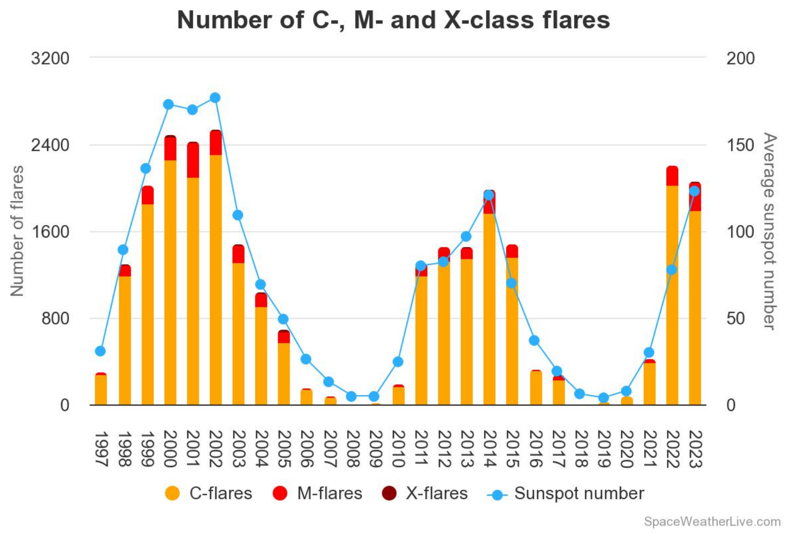

Figure 2.4: Correlation between the total number of solar flares and the average sunspot number per year. Solar flares are classified according to severity as C, M, or X-class. These classifications refer to minor, moderate and severe solar flares. Due to this strong correlation, we can use the more detailed sunspot data to infer information about other solar activity, such as solar flares and CMEs. Courtesy of SpaceWeatherLive.com.

Furthermore, roughly 34% of CMEs are associated with solar flare occurrences (Dwivedi 2003, p.249), which, albeit a weak correlation, still indicates that these phenomena occur in the same regions. Therefore, it is assumed that active regions, marked by sunspots, also present solar flares and CMEs. For this reason, the location and frequency of sunspot data can be used as a good approximation for the behaviour of other solar phenomena. Another benefit from this approximation is that sunspot appearances are more constant and recorded in great detail over many decades, leading to a comprehensive dataset that can be used in an analysis.

Moreover, the three primary periodicities of space weather events are identified as short-term (hours to days), solar seasonal (6-18 months), and decadal or century-time-scale phenomena (Dikpati and McIntosh, 2020). Then, consider that improving the forecast of space weather or active regions requires gathering data on different solar activity time scales over a long enough period to make accurate predictions. It follows that the data should be short enough to be relevant in the short term so that it can be used to prevent the consequences of failing to predict solar storms accurately. Thus, for this study, we will consider solar seasonal periodicity to be the most reasonable solar activity periodicity. More specifically, we will limit the study only to the space weather patterns on the lower end of the solar seasonal periodicity, around 180 days. Consequently, the Rieger-type periodicity (Rieger et al., 1984), discussed in the next section, falls within this duration.

2.4.1 Rieger-type periodicity

The RTP of 154 days was first detected in strong solar flare data for cycle 21 (Rieger et al., 1984), which is considered one of the stronger solar cycles as indicated by the large number of sunspots recorded in Fig.(2.1). After which this relatively short-term periodicity of 152-158 days was again observed in high-energy solar flare data, especially during the stronger solar cycles 19 and 21 (Oliver et al., 1998). Similarly, Carbonell and Ballester (1990) observed that the records of sunspot area, which are directly proportional to the amount of emerging magnetic flux, exhibit a periodicity of around 155 days for the solar cycles 14 to 20. The results of these two studies are essential as they confirm that the RTP is observed in both energetic flare and sunspot data. This observation validates our proposal to utilise the comprehensive and abundant sunspot data to inform and choose parameter values that align with solar observations. Subsequently, the more general duration of 150-160 days was classified as RTP (Carbonell and Ballester, 1992). However, this proved to be the case only for stronger cycles. It was further established that weaker cycles (14, 15 and 24) and stronger cycles (16-23) exhibit periodicities of 185-195 days and 155-165 days, respectively (Gurgenashvili et al., 2016).

In contrast, Chowdhury et al. (2015) claimed that periodicities of 130-180 days are classified as RTPs. However, the validity of this range should be questioned, especially the periodicity on the lower boundary. The reason is that a wave periodicity that is this fast would require a magnetic field of significant strength if it is said to be caused by a fast MHD Rossby wave. Furthermore, a periodicity of up to 190 days is classified as “near” RTP (Chowdhury et al., 2015). This longer periodicity is in line with the upper range presented by Gurgenashvili et al. (2016) for weaker cycles. Consequently, a range of **150-160 days** will be considered as the **initial RTP** and values between **161-195 days** will be classified as **near RTP**. Lastly, the following section will briefly give an overview of the necessary magnetic field terminology and concepts.

2.5 Solar magnetic field

Given the significant role played by the magnetic field in the dynamics of the Sun, it is crucial to include it in the modelling of solar waves. Therefore, it is important to define the relevant terminology and discuss the two different directions of the magnetic field in the

Sun.

2.5.1 Magnetic field terminology

Throughout this study, we will often refer to a **homogeneous** magnetic field. Therefore, we will explain the different variations of a magnetic field in both magnitude and direction.

When the magnetic field lines are equally spaced and parallel to one another such that the strength and the direction of the magnetic field remain *constant* throughout the area, it is referred to as homogeneous. However, it is important to note that this type of magnetic field profile does not have to be purely horizontal (as in the case of a uniform magnetic field); it could exhibit a $\sin\theta$ profile as illustrated in Fig.(2.5).

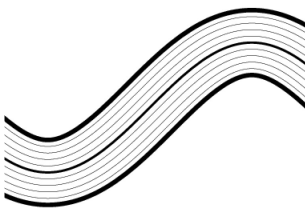

Figure 2.5: Homogeneous magnetic field with a $\sin\theta$ profile. Image courtesy of Krejcirik and Pratelli (2010).

On the contrary, a non-uniform magnetic field *varies* throughout the region. This variation could result from curved or twisted magnetic field lines. In the non-uniform case, magnetic field strength increases or decreases accordingly when magnetic field lines converge or diverge. This type of magnetic field is a natural product of latitudinal differential rotation (Zaqarashvili, 2018), which causes the magnetic field lines around the equatorial region to be more concentrated, or converged (Section 3.5.1). As per the observed behaviour of the magnetic field, it can be inferred that it is non-uniform when the dynamics related to solar differential rotation are taken into account. However, it has been noticed that this suggestion is often ignored for the sake of mathematical simplicity. As a result, even though the latitudinal differential rotation is considered, a uniform magnetic field is assumed (Gurgenashvili et al., 2016).

Furthermore, the terminology of a calm and perturbed magnetic field is also often used. This classification defines whether the magnetic field is impacted by external factors or disturbances present in the environment. Without such external factors, the magnetic field is said to be **unperturbed** or **calm**. On the other hand, we refer to a **perturbed magnetic field** when the surrounding environment disturbs the magnetic field region and subsequently modifies the behaviour thereof. However, it must be mentioned that the perturbations are often considered to be very small.

2.5.2 Characteristics of the solar magnetic field

Next, it is necessary to define the two primary magnetic fields that occur on the Sun, their respective orientations and how they relate to the solar dynamo process, which will also be discussed briefly.

The **solar dynamo** is the process through which the solar magnetic field is generated and sustained (Dwivedi, 2003, p.110). However, this work does not require understanding its full complexity. Nonetheless, being informed about these two different magnetic field orientations will be advantageous in understanding the change in the solar magnetic field over time (Appendix A.1 and A.2).

For clarification, the current model of the solar dynamo action includes a large-scale toroidal, $\boldsymbol{B}_{\text{tor}}$, and a weaker poloidal magnetic field, $\boldsymbol{B}_{\text{pol}}$, illustrated in Fig.(2.6).

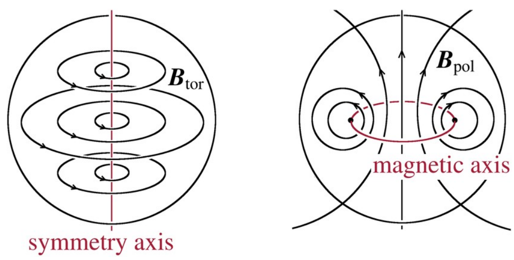

Figure 2.6: The direction of the toroidal ($\boldsymbol{B}_{\text{tor}}$) and poloidal ($\boldsymbol{B}_{\text{pol}}$) magnetic fields as it pertains to the solar structure. Figure courtesy of Herbrik and Kokkotas (2015).

The toroidal magnetic field is considered to be generated at the bottom of the convection zone due to the dynamics of the solar tachocline (Dwivedi, 2003, p.119). Unless indicated otherwise, this toroidal orientation is implied when referring to a magnetic field throughout this study. On the other hand, it is proposed that the poloidal field is regenerated in the convection zone by the cyclonic convection that occurs in that region (Tobias et al., 1998). Although this magnetic field forms part of the solar dynamo, it does not play a direct role in the dynamics of the magneto-Rossby waves under consideration. Therefore, it is not considered part of modelling these specific solar waves.

2.6 Summary

In this chapter, we learned about some of the fundamental components related to the Sun, starting with the 11-year solar cycle. Over the course of these 11 years, the positive and negative poles of the Sun's magnetic field migrate to the opposite hemisphere. Understanding this cyclical magnetic field pattern and how it affects solar activity is important because it indicates the variability of parameter values associated with each solar cycle (Appendix A.1 and A.2).

For instance, the variance in the solar cycle patterns observed in the recorded average number of sunspots over time shows the uniqueness of each solar cycle. This cycle variability further led to the classification of strong (cycles 14, 15, 24) or weak solar cycles (cycles 16-23), which stems from the associated periodicity exhibited by solar activity during each cycle. It has been shown that solar activity during stronger cycles exhibits shorter periods and vice versa.

Lastly, the general shape of the diagram that records the average number of sunspots was used to identify the two main phases of a solar cycle. At the beginning and end of the solar cycle, the number of visible sunspots is at a minimum, which is therefore called a solar minimum. In contrast, the number of sunspots reaches its maximum mid-solar cycle, called the solar maximum.

It was noted that important inferences could be made by combining the context of the two main solar cycle phases identified by the average number of sunspots diagram with the information provided by the butterfly diagram. Specifically, the butterfly diagram was used to identify the latitudes where sunspots are most likely to occur during the solar minimum and maximum, respectively. According to the butterfly diagram, sunspots at the beginning of the solar cycle are likely to appear at latitudes of approximately 40°. However, the number of sunspots occurring at this higher latitude is minimal compared to the more significant amount of sunspots that occur at a latitude of 30°. Therefore, this study will consider 30° as the dominant latitude of solar activity at the beginning of the solar cycle. By further comparing the two sunspot diagrams, it is evident that the solar maximum occurs midway through the solar cycle, and the corresponding latitude for solar activity during this period can be estimated as 16°. As the solar cycle reaches its end, the corresponding latitude for solar activity decreases and appears at a latitude around 5°.

In exploring the concept of space weather, we have found that solar flares and coronal mass ejections (CMEs) are the primary causes of changes in conditions between the Sun and the Earth. These solar activity events release charged particles into space, leading to geomagnetic or solar storms. Identifying where these events occur on the Sun is crucial, as we are only concerned with flares and CMEs that erupt on the Earth-facing side of the Sun. Furthermore, the source of a solar storm also provides information about the lead time before its impact is felt on Earth. Solar flares reach Earth faster than CMEs. We have also shown that the current space weather prediction models are inaccurate in forecasting the severity and timing of these solar storms.

It was also explained that sunspots do not directly cause space weather events. Therefore, a valid argument is essential if sunspot data is to be used in this study. To ensure this, we showed that sunspots provide an optimal environment for solar flares and CMEs also to occur, which affect space weather conditions. Furthermore, the quantitative records of sunspots and solar flare occurrences show a good correlation over time, and CMEs are often observed simultaneously as solar flares. Therefore, it has been confirmed that the comprehensive historical records of sunspot data could be used as a proxy for the more severe solar activity that occurs less frequently on much shorter timescales and can impact space weather.

After analysing the two sunspot diagrams, we have discovered that the sunspot locations' equatorial migration during the solar cycle implies that the latitude associated with the magnetic field should also fluctuate throughout the cycle since it is the source of sunspots. Therefore, the location of the magnetic field should not be considered constant throughout the solar cycle. Additionally, the magnetic field strength varies throughout the solar cycle. It provides evidence that it would be erroneous to assume that the magnetic field is constant in both latitude and strength throughout the solar cycle.

Moreover, by considering the various periodicities associated with increased solar activity, we have identified the Rieger-type periodicity (RTP) as the focus of this study. The associated frequency (150-160 days classified as the initial RTP and values between 161-195 days as near RTP) is long enough to forecast values but short enough to be relevant and help us mitigate costly events such as those discussed in Section 2.3 as a consequence of inaccurate space weather forecasts.

Lastly, it has been established that this study will only focus on the Sun's more dominant toroidal magnetic field, and the magnetic field in the poloidal direction can be neglected. Thus, if we consider a uniform magnetic field in the toroidal direction (ϕ-direction in spherical coordinates), small perturbations of the magnetic field can only occur in the poloidal direction (θ-direction in spherical coordinates). Consequently, the "magnetic field strength" throughout our work will refer to the magnetic field strength in the toroidal direction. Furthermore, to make our text more easily digestible, we will abbreviate the phrase "magnetic field strength" with MFS.

Finally, recall that Chapter 1 suggested that solar Rossby waves are linked to the variability of these periodicities of increased solar activity. Thus, we must explore these waves, their properties, and their associated forces in more detail in the next chapter.

3 Literature Review II: Rossby waves

3.1 Introduction

In Chapter 2, we explored the solar environment in detail and introduced the types of solar activity relevant to changes in space weather, such as solar flares, coronal mass ejections (CMEs), and sunspots. We also established that they exhibit a 150-190 day period of increased frequency known as the Rieger-type periodicity (RTP). In Chapter 1, we mentioned that solar Rossby waves have been extensively studied in connection to this specific periodicity (Zaqarashvili et al., 2010; Gurgenashvili et al., 2016, 2017; Dikpati et al., 2017; Zaqarashvili and Gurgenashvili, 2018; Zaqarashvili, 2018; Korsós et al., 2023). Therefore, this chapter will explore various aspects of Rossby waves, starting with the necessary background of Rossby waves, the solar layer under consideration, and the fundamental wave equations that will be derived from the magnetohydrodynamic (MHD) Rossby wave model.

More specifically, we will first examine the characteristics of hydrodynamic (HD) Rossby waves and their significance on Earth, as they were first discovered in this framework. We will then discuss the magnetohydrodynamic (MHD) Rossby waves that occur in magnetised environments such as the plasma of the Sun. Examining the various studies of solar Rossby waves will allow us to identify the solar layer that will be most suitable for this study, which involves the connection between the MHD Rossby waves, the RTP, and space weather.

After identifying the solar tachocline as the layer where the MHD Rossby waves will be studied, the essential solar dynamic that originates in this layer, the latitudinal differential rotation (LDR), is explained. This phenomenon causes the Sun's rotation rate to vary depending on its latitude. However, it is not only the LDR that plays an important role in the MHD Rossby wave modelling but also the difference between the characteristics of the upper and lower tachocline regions, which we will explore. Understanding the different conditions associated with each of the tachocline layers is important, as they will inform the applicable approximations and other considerations that should be considered when modelling Rossby waves in this specific solar layer.

Next, a brief overview of the development of the MHD Rossby wave model over time is provided, which is necessary since ensuring that this model is as comprehensive as possible is a critical component of this study. We will also discuss the inconsistent or inaccurate usage of input parameter values to these models as a significant problem faced by various studies that derive them.

Finally, the connection between solar Rossby waves and the active regions, discussed in Chapter 2, is established, confirming that specifically, MHD Rossby waves should be studied in connection with solar activity. Next, we will provide the fundamental equations describing wave propagation, which consists of the wave's dispersion relation, group, and phase velocity, all of which are essential in studying the relationship between these MHD Rossby waves and solar activity.

This is followed by a review of three studies that provide observational proof of the existence of solar Rossby waves in various solar measures, which, in part, will demonstrate how these propagation properties are used together with solar observations of Rossby waves. Lastly, we will list the other solar waves that occur in the tachocline, but since the current study focuses on Rossby waves, we will not consider these waves going forward.

3.2 Rossby waves

Rossby waves (Rossby, 1939) occur in rotating fluids, such as the Earth's ocean and atmosphere. These waves are classified as planetary waves due to the large scale of the perturbation, which extends around a full longitude circle. They exhibit low frequencies and can be either equatorially trapped or occur at mid-latitudes. Rossby waves are also classified as dispersive planetary waves, which means that Rossby waves with different wavelengths move at different velocities. Observations show that on the Sun, Rossby waves have a retrograde[1] phase velocity. However, these planetary waves can exhibit a prograde or retrograde group velocity. Furthermore, Rossby waves can be classified as barotropic or baroclinic waves depending on their vertical structure. Rossby waves fall into the barotropic class when they exhibit purely horizontal motions. Conversely, these waves are classified as baroclinic when

[1]As seen from the North pole, counterclockwise and clockwise movement is defined as retrograde and prograde, respectively.

they have a vertical variance. They can also occur in various conditions, such as in a hydrodynamic environment like the Earth's and a magnetohydrodynamic environment like the Sun's.

3.3 Hydrodynamic Rossby waves

In 1939, Carl Gustav Rossby wrote a paper on the theory that thin spherical shells should present global longitudinally propagating waves of vorticity when rotation is present. The theory was expanded to an entire spherical shell by Haurwitz in 1940. Therefore, when there is a thin rotating spherical shell with mainly horizontal fluid flow, Rossby waves are a fundamental property of that system. Observations of these waves in rotating fluids such as the Earth's atmosphere (Rossby, 1939), ocean (Rhines, 1977), outer core (Bardsley, 2018), other planetary atmospheres (Gavrilov and Prodanov, 2008) as well as in stars, confirmed Rossby and Haurwitz's theory.

According to the National Oceanic and Atmospheric Administration (NOAA) **oceanic Rossby waves** are large enough to cause changes in the Earth's climate conditions. They are also responsible for high tides, rising sea levels, coastal flooding in some regions of the world, and the effect of El Niño, which is "*the unusual warming of surface waters in the eastern equatorial Pacific Ocean*," according to the National Geographic Society. **Atmospheric Rossby waves**, on the other hand, attempt to keep the atmosphere in balance by assisting with heat transfer from the tropics towards the poles and moving cold air towards the tropics. Jet streams are more easily located due to atmospheric Rossby waves, and they also map out the track of surface low-pressure systems (NOAA). Due to the slow velocities of Rossby waves, they result in relatively long, persistent weather patterns. Although the magnetohydrodynamic Rossby waves share some similarities with their HD counterpart, they have essential differences, which will be discussed next.

3.4 Magnetohydrodynamic Rossby waves

Rossby waves (Rossby, 1939) are large, slow-moving waves that occur in rotating fluids such as the Earth's atmosphere and ocean as explained in Section 3.3. These waves meander over the globe's surface and behave similarly to slow-moving solar activity patterns. This similarity has led researchers to investigate the presence of Rossby waves in the solar environment to identify a potential connection between Rossby waves and solar activity.

Furthermore, considering that the Sun is a rotating sphere of magnetised plasma that can be treated as a fluid, not only will Rossby waves be present in the solar environment due to the rotation, but the fluid mechanics principles will also hold, which can be used to model these solar waves. However, when applying these fundamental fluid principles, the more commonly used hydrodynamic (HD) fluid dynamic equations should be substituted with their magnetohydrodynamic (MHD) counterparts when studying these waves on the Sun. This substitution captures the impact of the solar magnetic field on wave dynamics in the modelling process. Thus, by applying the MHD fluid dynamic principles to the Sun, we can model and gain insight into the large-scale behaviour of the plasma, including flow patterns and wave propagation, which is of specific interest to us.

Therefore, by limiting the focus to the solar MHD Rossby waves[2], it subsequently informs what layers of the Sun can be considered. Thus, the next step is briefly exploring the solar structure and summarising the existing literature on solar Rossby waves in the various layers. Starting from the deepest part of the solar interior and moving outwards, the solar layers are illustrated in Fig.(3.1) and are as follows. The solar interior consists of the core, the radiative zone, the tachocline and the convection zone. The photosphere is the Sun's surface from where the solar atmosphere, the chromosphere and the corona extend.

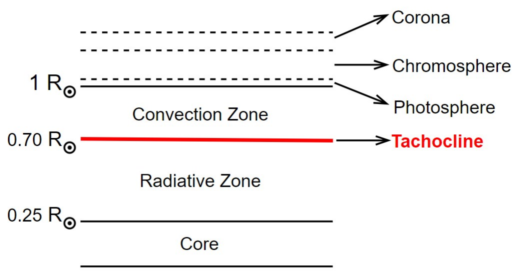

Figure 3.1: The solar interior consists of the core, radiative zone, tachocline, convection zone, and the photosphere (solar surface). The solar atmosphere consists of the chromosphere and corona. (Layer thickness not to scale.)

Rossby waves have been studied in the radiative interior (Blume et al., 2022), tachocline (Zaqarashvili et al., 2007; Zaqarashvili et al., 2009; Zaqarashvili et al., 2010 and many oth-

[2]In literature, Rossby waves are often studied alongside Alfvén, Poincaré, and Kelvin waves (see Section 3.10) as combinations of these waves can occur. Nevertheless, this study will only focus on pure Rossby waves.

ers), convection zone (Busse et al., 2005; Löptien et al., 2018), photosphere (Gilman, 1969; Lou, 2000; Kuhn et al., 2000), and the corona (Gilman, 1969; McIntosh et al. 2017).

However, the solar atmosphere (corona), although showing signs of Rossby waves, will be omitted, as this atmospheric region does not display solar activity, which is an integral part of this study. Similarly, the convection zone will not be considered due to the complexity of the dynamic convective motions that will undoubtedly distort wave propagation in this region. It can also be argued that since the aim is to establish the connection between solar Rossby waves and solar activity, the deeper solar layer of the radiative zone can also be neglected as it is the furthest away from the solar surface, where the solar activity is observed. Thus, the extensively studied MHD Rossby waves within the solar tachocline (Zaqarashvili et al., 2007, 2009, 2010; Gurgenashvili et al., 2016; Zaqarashvili and Gurgenashvili, 2018; Gachechiladze et al., 2019) provides a solid foundation for our work and other further research. Therefore, a deeper exploration of the tachocline layer and its characteristics is required, which will be discussed next.

3.5 Solar tachocline

Spiegel (1992) discovered a thin shear layer between the radiative and convection zones through helioseismology[3]. Spiegel and Zahn (1992) showed that this boundary layer near the base of the convection zone is where the internal rotation goes from solid body rotation to latitudinal differential rotation and named it the tachocline. However, before discussing this transition layer, it is necessary to explain the meaning of latitudinal differential rotation.

3.5.1 Latitudinal differential rotation

The detailed observations of sunspots recorded in the butterfly diagram, Fig.2.2, reveal additional information about the internal rotation of the Sun. By keeping track of the sunspot locations at different latitudes, their gradual shift to the right in the butterfly diagram indicates that the Sun is not exhibiting solid body rotation. On the contrary, it was noted that the solar rotation[4] around the equator was faster, roughly 25 days, than at

[3] This field studies the solar interior using surface wave observations of the Sun (Thompson, 2004).

[4] *The sidereal period is the time required for a celestial body within the solar system to complete one revolution with respect to the fixed stars* (Britannica, 2023).

higher latitudes as it gradually increased to 36 days at the pole (Dwivedi, 2003, p.56). This phenomenon is called **latitudinal differential rotation** (LDR).

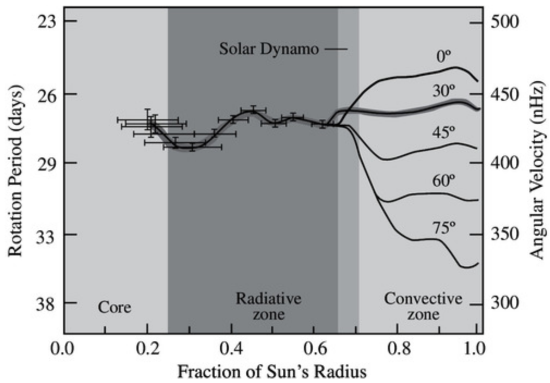

Figure 3.2: Splitting of the angular velocity according to latitude, with the equator at 0°. At the polar regions, the Sun exhibits an angular velocity of $\sim$ 320nHz, which correlates with a rotation period of 36 days. On the other hand, the equatorial region rotates with a period of roughly 25 days and has a corresponding angular velocity of $\sim$ 460nHz. Image courtesy of Alexander G. Kosovichev et al.

Examining Fig.(3.2) shows that the Sun exhibits solid body rotation (constant rotation rate) inside the core and radiative zone as presented by the single angular velocity line for those regions. The light grey region between the radiative and convection zone corresponds to the tachocline, where the rotation rate differs according to latitude. Therefore, differential rotation is important in solar dynamics from the tachocline region and extending outwards.

Furthermore, the LDR may play a role in determining the direction of the primary magnetic field of the Sun. To explain this process, we consider the **Alfvén's frozen-flux theorem**[5]. This theorem states that the conservation of magnetic flux describes the behaviour of magnetic field lines as moving with (or frozen in) the plasma (Priest, 2014, p.92). Due to LDR, the plasma flow will cause the embedded magnetic field lines to be stretched out in the toroidal direction, as indicated by the horizontal blue arrow in Fig.(3.3). As a result, the magnetic field within the solar interior is predominantly in the toroidal direction.

[5]It is important to emphasise that this theorem applies to the solar interior since the necessary criteria are met, as shown in Section 4.3

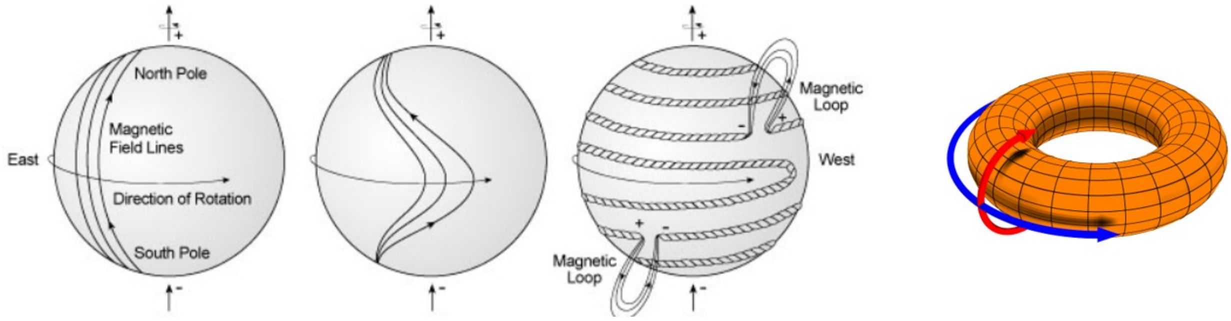

Figure 3.3: Due to latitudinal differential rotation, the Sun rotates faster around the equator than at the poles. Additionally, the magnetic field lines are frozen in the Sun's plasma. Therefore, as the plasma moves, the magnetic field gets dragged along in the toroidal direction (blue arrow). This behaviour results in sunspots moving in the same direction as the differential rotation as the solar cycle progresses. Courtesy of Lang (2001) and Wikimedia.

This toroidal plasma flow also explains the horizontal shift to the right in the sunspot location over time. In contrast, the vertical change, or equatorial drift, in sunspot location can be explained by the meridional circulation that occurs in the Sun (Dwivedi 2003, p.91), see Fig.(3.4).

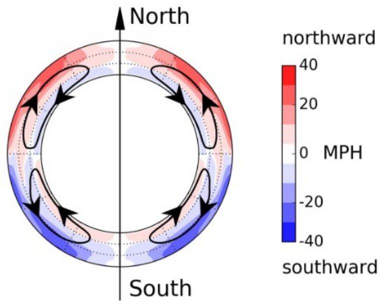

Figure 3.4: The meridional flow in the Sun. This circulation causes the sunspot's slope from higher latitudes to lower latitudes throughout the solar cycle. It also correlates to the poloidal direction indicated by the red arrow in Fig.(3.3). Image courtesy of MPS/Z.-C. Liang.

Together, the downward shift of the meridional flow and the shift to the right due to the LDR cause the characteristic pattern of sunspot migration towards the equator throughout a solar cycle. Nevertheless, the solar tachocline layer indicates where the LDR starts occurring within the Sun, but it is not the only important characteristic. Therefore, in the next section, the structure and additional features of the tachocline will be mentioned.

3.5.2 Tachocline characteristics

Although the tachocline was first studied as one layer (Zaqarashvili et al., 2007), it has been suggested that this layer's upper and lower parts should be considered separately (Gilman, 2000). This argument is due to the significant differences in dynamics between the adjacent layers of the upper and lower tachocline, which consequently influence the neighbouring tachocline region.

The lower two-thirds (Schecter et al., 2001) adjacent to the calmer radiative zone is stably stratified and subadiabatic (Gilman, 2000). Whilst "adiabatic" refers to the general principle of thermodynamic processes where no heat is transferred, the term subadiabatic refers to the rate at which the plasma temperature changes with altitude. It is typically associated with stable atmospheric conditions. Due to a subadiabatic environment, plasma has less tendency to continue rising because it becomes cooler and denser than the surrounding plasma once it starts ascending. Therefore, in such an environment, vertical motions are suppressed. It also means that warmer fluids, which are, by definition, less dense, tend to sink in the lower tachocline (Horstmann et al., 2022). Furthermore, it was shown that the lower tachocline displays a weaker latitudinal differential rotation than the upper tachocline, see Fig.(3.2), also contributing to a more stable environment (Zaqarashvili et al., 2009; Zaqarashvili et al., 2015). However, the magnetic field strength is stronger in the lower part of the tachocline relative to the upper tachocline (Zaqarashvili et al., 2009).

On the other hand, the dynamics of the upper tachocline are primarily due to the characteristics and behaviour of the adjacent convection zone. Firstly, the convection motions overshoot into this region, contributing to a weakly stable stratification (Gilman, 2000). Secondly, the convection zone also causes the upper tachocline to be considered adiabatic or close to superadiabatic, which leads to the fundamental difference between the two tachocline layers. Although the upper tachocline mainly exhibits horizontal motions, it more easily allows vertical motions than the lower tachocline. This characteristic enables warmer plasma from the upper tachocline to enter the convection zone, where it experiences no resistance to buoyancy and rises to the solar surface (Horstmann et al., 2022), as illustrated in Fig.A.7b. Now that we understand the fundamental differences between the two layers of the tachocline, they do have an essential characteristic in common, discussed next.

It is significant to recognise that the tachocline layer can be considered a shallow water body due to its very large horizontal scale compared to its shallow depth. Therefore, we can apply the shallow water approximations to the upper and lower tachocline mathematical models. This approximation also confirms that the fluid motions in this layer can be considered predominantly horizontal but not entirely (Gilman, 1969) because, in the case of purely horizontal motion, the magnetic field will not undergo twisting and stretching, which is needed to simulate the solar cycle. Gilman (2000) further supported the speculation of the tachocline's involvement in solar magnetic field (Spiegel and Zahn, 1992) by suggesting that the tachocline is where the magnetic field generation originates. Hence, including the forces and dynamics associated with a magnetic field in modelling waves in the tachocline is non-negotiable. Therefore, it is necessary to examine the comprehensiveness of the existing Rossby wave models, which are discussed in the next section.

3.6 The solar Rossby wave model progression

In this study, we aim to evaluate the effectiveness of the MHD Rossby wave model by examining how accurately the forces captured in the model reflect the real-world environment. Essentially, the more forces incorporated into the model, the more comprehensively it represents the environment's physical dynamics. Therefore, providing a detailed overview of the development of the solar Rossby wave model is crucial.

The Rossby wave model has progressed from the simplistic HD model in an inertial frame of reference (no acceleration) to the more complex MHD Rossby wave model (Gilman, 2000), which includes the forces that result from the presence of a magnetic field. This following model enhancement (Chapter 5) was to consider the more appropriate rotating frame of reference (Zaqarashvili et al., 2007). This version of the MHD Rossby wave model will be referred to as the "base model" throughout this study since it includes the most fundamental components of rotation and the effect of the magnetic field. The base model has subsequently been improved by considering the effective gravity (Section 6.3) of the specific solar layer instead of normal gravity, capturing the nuances of the layer stratification in the modelling process. Finally, the solar characteristic where the equatorial region of the Sun rotates faster than the poles, called latitudinal differential rotation (LDR), is included in the model derivation of Chapter 7.

It is worth noting that researchers (Zaqarashvili and Gurgenashvili, 2018) still utilise the base MHD Rossby wave model or, even worse, the HD Rossby wave model (Lou, 2000) in their analysis of solar observations without any explanation. This inconsistency in model selection throughout the literature is problematic as it becomes increasingly difficult to compare the results of previous studies when different Rossby wave models are considered. As the earlier versions of the model exclude important solar dynamics, it could lead to unnecessary inaccuracies in the model results. Therefore, evaluating the comprehensiveness of the MHD Rossby wave model that will be used is important. Similarly, there is a need to confirm that the associated model parameter values are consistent across existing literature and align with observations of solar activity.

3.6.1 Inconsistent and inaccurate Rossby wave model parameter values used in literature

Reviewing the literature where Rossby waves are studied in the solar tachocline (Zaqarashvili et al., 2007, 2009, 2010; Gurgenashvili et al., 2016; Zaqarashvili and Gurgenashvili, 2018; Gachechiladze et al., 2019), it became evident that these studies lack consistency in parameter values used as inputs to the MHD Rossby wave model.

This study will highlight the discrepancy between two rotation parameters associated with the MHD Rossby wave model: the equatorial rotation rate Ω_0 and the latitudinal differential rotation parameter, s_2, a coefficient in the equation that describes the differential rotation. The values used throughout the literature for the equatorial rotation rate range from $\Omega_0 = (2.6-2.9)\times 10^{-6}\,\mathrm{s}^{-1}$ (Zaqarashvili et al., 2009; Gurgenashvili et al., 2016) and the LDR parameter, s_2, has values between $s_2 = 0.12 - 0.2$ (Gachechiladze et al., 2019; Gurgenashvili et al., 2016). However, these parameter values are recorded from solar observations and are not expected to vary across the literature. Therefore, studies that use rotational parameters different from the observational data should be identified as problematic for using inaccurate parameter values and contributing to the problem of inconsistency in this field of study.

Moreover, there is also a discrepancy in the latitude ranges associated with the equatorial region and those considered mid to high latitudes. For instance, while Horstmann et al. (2022) identified the non-equatorial region as between $30^\circ - 60^\circ$, the range of $20^\circ - 40^\circ$ was considered for equatorially trapped shallow water waves in the upper tachocline (Zaqarashvili, 2018). Misalignment and inconsistencies in these fundamental definitions across the literature can needlessly complicate the interpretation of model results.

Furthermore, the magnetic field strength values also exhibit an extreme range of values considered for this parameter, ranging from $6-100\,\mathrm{kG}$ (Gachechiladze et al., 2019; Zaqarashvili and Gurgenashvili., 2018). The lack of reasoning behind the chosen values for these specific parameters further exacerbates the difficulty in comparing results from various existing studies. Since these four parameters are explicitly included in the MHD Rossby wave model, their values will undoubtedly affect the results to varying degrees, as explored in the sensitivity analysis performed in Section 8.4. Next, the critical link between solar Rossby waves and active regions on the surface of the Sun is discussed.

3.7 Connection between solar Rossby waves and active regions on the surface of the Sun

It has been established that the tachocline is a suitable layer to study in connection with magnetohydrodynamic (MHD) Rossby waves (Zaqarashvili et al., 2007, 2009, 2010; Gurgenashvili et al., 2016; Zaqarashvili and Gurgenashvili, 2018; Gachechiladze et al., 2019; Dikpati, 2020). Dikpati, a senior scientist at the High Altitude Observatory (HAO) operated by the National Center for Atmospheric Research, further explained that Rossby wave propagation could predict active Sun regions. These **active regions** or “hot spots” on the solar surface indicate areas with a high probability of experiencing solar activity. Dikpati used atmospheric hydrodynamic (HD) Rossby waves on Earth to draw a parallel between these more familiar Rossby waves and the MHD Rossby waves observed in the Sun. On Earth, HD Rossby waves propagating in the northern hemisphere will transport warmer, high-pressure (H in Fig.(3.5)) air towards the polar region. Meanwhile, in lower pressure (L in Fig.(3.5)) areas, cooler air will be moved towards the equatorial region. These jet streams, therefore, act like a waveguide, steering the propagation of the Rossby wave in the Earth’s atmosphere; a similar process occurs with Rossby waves on the Sun (Dikpati, 2020). However, these atmospheric Rossby waves are then used to predict when and where there will be either a cold or heat outbreak and ultimately to predict daily weather on Earth. The right-hand side of Fig.(3.5) illustrates the dynamics of an atmospheric Rossby wave, exemplified by NOAA.

Figure 3.5: Solar Rossby waves (left) move between regions of low (A) and high (B) solar activity likelihood, similar to the Rossby waves on Earth (right) that propagate between high (H) and low-pressure (L) systems. Solar Rossby wave illustration courtesy of Dikpati, 13 March 2020. Earth Rossby wave illustration courtesy of NOAA Climate.gov.

However, the Sun's high-pressure regions cause the tachocline layer of the Sun to experience a swell (illustrated by the areas in Fig.(3.6) circled in black) that allows magnetic field lines initially confined to the tachocline to enter the convection zone. From there, they will rise due to their buoyancy (see Appendix A.3), resulting in active regions on the solar surface where the magnetic field is concentrated, priming the region for solar activity. From this argument, it follows that the high-pressure areas, e.g., region B in Fig.(3.5), indicate the longitude and latitude of an active region, resulting from the swelling in the tachocline. On the contrary, the low-pressure areas, marked by A in Fig. (3.5) or the blue-shaded areas in Fig.(3.6), are calmer regions expected to exhibit little to no solar activity. Therefore, the propagation of solar Rossby waves could predict the location of these active regions and inform how they move over time.

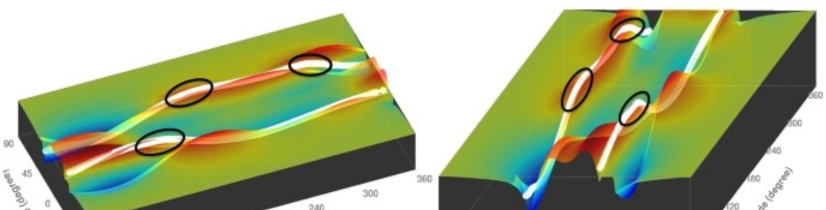

Figure 3.6: Two perspective snapshots of the top-surface (colour-shade) of a tachocline fluid shell, viewed respectively along longitude (left panel) and latitude (right panel), during its MHD evolution; red/orange represents swelling of the fluid and blue/sky-blue the depression. Yellowish-green represents neutral thickness. Portions of the toroidal magnetic bands (two white tubes, one each in the North and South hemispheres) that coincide with swelled fluid are encircled by black ellipses. These portions start entering the convection zone and are more likely to erupt buoyantly at the surface. Figure and description from Dikpati et al. (2018).

The following section will focus on the literature which provides observational evidence of solar Rossby waves.

3.8 Observed solar Rossby waves

In this section, we will briefly discuss three observational studies that revealed physical solar features that were suggested to be direct observations of solar Rossby waves. The research discussed here attempted to establish a connection between specific solar Rossby waves and their observational findings. Moreover, the authors used various techniques and methodologies, contributing to the validity of the findings.

First, the study of Kuhn et al. (2000) revealed observations of 100m high "hills" that displayed uniform spacing of $8.7 \pm 0.6 \times 10^4$ km over the Sun's surface (photosphere). Several potential sources were examined to identify which could be responsible for these observations. It was subsequently concluded that these surface elevations are likely the surface manifestation of Rossby wave oscillations in the convection zone (Kuhn et al., 2000).

Secondly, McIntosh et al. (2017) also observed Rossby-like waves on the Sun. Their study analysed coronal images of two separate spacecraft: the twin Solar Terrestrial Relations Observatory (STEREO) and Solar Dynamics Observatory (SDO). The authors applied their coronal brightpoint detection algorithm to data from 1 June 2010 to 31 May 2013. Whereafter, they determined the average phase velocity for brightpoint clusters in the northern and southern hemispheres. Since the brightpoint clusters displayed wave-train-like behaviour, they also used their method to calculate the group velocities. The estimated values are given in Table 3.1 below.

Hemisphere	**Phase velocity**	**Group velocity**
North	$3.25 \pm 2.25\,\mathrm{ms}^{-1}$	$23.8 \pm 20.8\,\mathrm{ms}^{-1}$
South	$2.65 \pm 1.60\,\mathrm{ms}^{-1}$	$24.4 \pm 15.3\,\mathrm{ms}^{-1}$

Table 3.1: Phase and group velocities of observed coronal bright points exhibiting behaviour associated with Rossby waves (McIntosh et al., 2017).

This dispersive behaviour of differing phase and group velocities, exhibited by the coronal bright points, is a fundamental characteristic of Rossby waves, concluding that these drifting motions are most likely attributed to magnetic Rossby waves. This study was also used in Appendix A.2 to demonstrate how observational data could be chosen more appropriately according to the period of data used to make these observations.

Thirdly, using six years of photospheric intensity images, Löptien et al. (2018) analysed the progression of vorticity features. By doing so, they unambiguously detected vorticity waves in the shallow layer beneath the solar surface. Löptien et al. (2018) considered global-scale vorticity waves at a depth of 21Mm and limited the latitudinal region to a maximum of 20° from the equator. Their analysis used data from several years and detected vorticity waves with retrograde phase- and prograde group velocities. They concluded that these observed vorticity features are likely due to internal solar Rossby waves.

The study by Löptien et al. (2018) can also be used to illustrate the two problems identified in Section 3.6. Their study referred to "classical" Rossby waves throughout its content. It was further mentioned that the region under consideration is mainly controlled by rotation and buoyancy, with no mention of magnetic fields. Based on these facts, it can be concluded that the authors were studying hydrodynamic solar Rossby waves. However, we argue that neglecting to include the effect of the magnetic field on the propagation of these waves is incorrect and that magnetohydrodynamic Rossby waves would be better suited for the solar environment. On the other hand, the latitude of 20° used by Löptien et al. (2018) is highly plausible and appropriate to consider when studying the connection between Rossby waves and solar activity. This contradicts the latitude of 45° commonly used in the study of Rossby waves (Gurgenashvili et al., 2016; 2017) in the tachocline.

Thus, the model selection of Löptien et al. (2018) might be questionable, but the value of the considered latitude is reasonable. Now, recall that one of this study's objectives is to ensure that the MHD Rossby wave model is as comprehensive as possible. Although the observational findings discussed here are not directly utilised in this study, any modifications made to the MHD Rossby wave model, which is used to determine the dispersion relation and, subsequently, the phase and group velocity equations in these observational studies, will be impacted. Hence, the conclusions of this study will affect future investigations. The next section will provide a more detailed explanation of these propagation properties.

3.9 Wave properties

A **wave** is a periodic response to a disturbance that travels in a medium and carries energy without causing a net movement of particles. Therefore, a **medium** refers to the substance through which a wave travels. It can be in the form of a solid, liquid, gas or plasma (as in the case of this study). A **disturbance** is an event which initiates a wave. The fluid particles respond to the disturbance such that an interaction between adjacent particles in the medium causes a temporary displacement. This interaction is what allows the wave to move through the medium. However, for this wave propagation to be sustained, the wave must have a **restoring force**, which differs for each type of wave. For example, the respective restoring forces for atmospheric waves such as acoustic, gravity, surface, and planetary waves are pressure, buoyancy, gravity, and rotation.

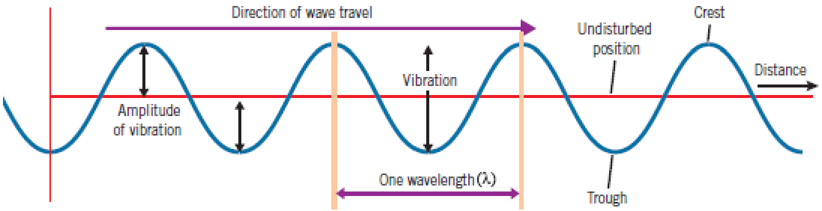

Figure 3.7: Basic properties of a transverse wave.

Let us continue by discussing other fundamental properties of waves. Consider the simple case of a sinusoidal wave as illustrated by Fig.(3.7), travelling in the positive x-direction, with amplitude, A. The particles oscillate parallel to the y-axis. The displacement, y, of the particles at a time t and position x is described by

$$y(x, t) = A \sin(\omega t - kx + \phi). \tag{3.1}$$

Equation (3.1) gives the relationship between the wavenumber, k, and the frequency of the wave, ω (Halliday, 2010, p.416). It is called the dispersion relation[6] and describes how dispersion affects wave properties. **Dispersion** in waves describe the phenomenon where different frequencies, or wavelengths, of a wave travel at different velocities. Therefore, dispersion causes wave components, such as the shape or behaviour, to be spread out as the wave propagates. In eq.(3.1), the phase constant, ϕ, is added to generalise the equation. This parameter's value sets the wave's specific displacement and slope at $t = 0$ and $x = 0$.

[6]See Appendix B.1 for a more detailed explanation of this dispersion relation's wave characteristics and variables.

The speed at which a wave with constant phase, $(\omega t - kx + \phi)$, travels is called the **phase velocity**, v_p, and is derived as follows

$$\frac{d(\omega t - kx + \phi)}{dt} = 0 \implies \omega - k\frac{dx}{dt} = 0 \implies \frac{\omega}{k} = \frac{dx}{dt}.$$

Therefore, the phase velocity for a non-dispersive and dispersive wave is given by

$$\boxed{v_p = \frac{\omega}{k}}. \tag{3.2}$$

In a dispersive wave system, sinusoidal waves travelling at different speeds create a bump (wavepacket) over time. The velocity of this bump is called the **group velocity**, v_g. Assume such a bump is located at $x = 0$ and $t = 0$. To determine the velocity of this feature, we need to identify other values of x and t where the phases are all equal, since then the waves in the system will add constructively and result in another bump. For this reason, the phase needs to be independent of the wavenumber at a specific value for k. Thus, if we set the phase to be independent of k, we can derive the group velocity as

$$\frac{d(\omega t - kx + \phi)}{dk} = 0 \Longrightarrow \frac{d\omega}{dk}t - x = 0 \Longrightarrow \frac{x}{t} = \frac{d\omega}{dk},$$

resulting in the following equation

$$\boxed{v_g = \frac{d\omega}{dk}}. \tag{3.3}$$

To visualise these concepts, we will consider two waves with the following dispersion relations

$$\psi_1(x,t) = A\cos(\omega_1 t - k_1 x), \tag{3.4}$$

$$\psi_2(x,t) = A\cos(\omega_2 t - k_2 x). \tag{3.5}$$

Figure (3.8a) shows the behaviour of the sum of the waves ψ_1 and ψ_2. The wave envelope (energy of the wave, illustrated by the red line) travels at the group speed, and the wave, depicted in blue, travels at the phase velocity. The phase and group velocities can move in either the same or opposite directions, which the sign of the respective velocity will indicate. For **non-dispersive waves**, we have $v_p = v_g$ and frequency not depending on the wavenumber k. Therefore, the red and blue lines will move at the same speed. Furthermore, a non-dispersive wave can travel a long time without changing shape. However, for **dispersive**

waves, we observe $v_g \neq v_p$ when the high-frequency wave (blue line) moves with respect to the wave envelope illustrated in red.

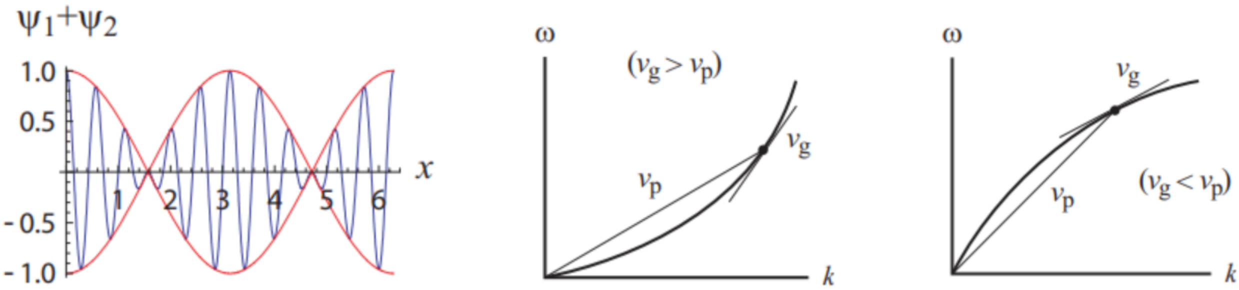

(a) Result of adding two wave functions. **(b)** Case 1. **(c)** Case 2.

Figure 3.8: Illustration of a wave's dispersion relations and how the group and phase velocity relate to it. Fig.(3.8b) shows that waves with larger wavelengths travel slower than those with shorter wavelengths. The opposite is true for Fig.(3.8c). Figures courtesy of Morin (Harvard).

Plotting the dispersion relation lets us gain basic phase and group velocity information. For example, consider two cases where the shape of the dispersion relation could either be concave, Fig.(3.8b), or convex, Fig.(3.8c). In the first case, we have $v_g > v_p$, where the waves with larger wavelengths (small k) travel slower than waves with small wavelengths (large k). In the second case, for the convex function, the contrary is true.

The studies discussed in Section 3.8 have used phase and group velocity equations to investigate the relationship between Rossby waves and certain observed solar features for which these velocity values are known. For instance, McIntosh et al. (2017) identified the observed phase and group velocities of coronal bright points (CBPs). They suggested that the movement pattern of these CBPs indicates the propagation of Rossby waves. Subsequently, Gachchiladze et al. (2019) attempted to link the observational finding of McIntosh et al. (2017) to a specific type of Rossby wave in their study. However, they neglected to consider the effect of latitudinal differential rotation in their MHD Rossby wave model.

It follows that to understand the behaviour of a wave accurately, one needs to know its dispersion relation, which is used in deriving equations that determine the wave propagation properties. Hence, it is crucial to ensure that the governing equations used to derive the dispersion relation are as accurate as possible since the equations for the phase and group velocity will also be affected if the Rossby wave model is not precise. Therefore, observational studies of solar Rossby waves which rely on these group and phase velocity equations will be positively impacted if the solar Rossby wave model is more accurate. Moreover, as mentioned in Section 3.7, the propagation properties of solar Rossby waves are used to predict active regions on the surface of the Sun (Dikpati, 2020). Therefore, this method of predicting space weather will also be impacted if the Rossby wave model is improved. Nonetheless, since Rossby waves are not the only waves on the Sun, the other solar waves are mentioned in the following section for transparency.

3.10 Other solar waves

As different waves occur in the Earth's atmosphere and ocean, the same is true for the Sun. Let us first consider gravity waves, which occur at the boundary where two fluids of different densities meet. As the name suggests, gravity is the restoring force of these waves. Ocean waves are an example of such a wave, as they occur between the boundary of the ocean and air and are, therefore, referred to as a **surface gravity wave**. They exhibit horizontal propagation, with the fluid particles moving in the vertical direction as they travel. Whether these waves are affected by the rotating system, such as the Earth and Sun, depends on various factors such as the wavelength, latitude, and the size of the fluid body in which they occur. For example, large waves with long periods travelling at slow speeds and higher latitudes in the Earth's ocean will be more noticeably impacted by the Coriolis effect (see Appendix B.2.2).

On the Sun, **internal gravity waves** behave slightly differently. Similar to the surface gravity waves on Earth, gravity is also the restoring force for these waves on the Sun. However, these waves occur *within* a stratified fluid where the density varies with depth but is considered stable. This wave also propagates opposite to the surface gravity wave. Internal gravity waves propagate in the vertical direction while the displaced fluid particles move horizontally. **Poincaré waves** (Poincaré, 1910) are the dominant internal gravity waves in the Sun when a shallow fluid layer, such as the tachocline, is considered. **Kelvin waves** (Thompson, 1879) are another gravity wave in rotating fluids. Kelvin waves propagate along boundaries, such as a channel acting as a waveguide or in subsurface regions that exhibit a thermocline. Therefore, they generally occur in the region close to the equator, making them equatorially trapped waves. These low-frequency waves can occur on the surface and within a fluid, and their behaviour is also affected by the Coriolis force. Furthermore, Kelvin waves have a magnetic field counterpart called equatorial magneto-Kelvin waves (Gachechiladze et al., 2019).

Rotating fluids also exhibit **Rossby waves** (Rossby, 1939), classified as planetary waves due to the large scale of the perturbation, which extends around a full longitude circle. The restoring force of these waves is the latitudinal variation of the Coriolis force. Moreover, they exhibit low frequencies and can be either equatorially trapped or occur at mid-latitudes.

Lastly, due to the magnetic field in the Sun, the solar environment also displays other MHD waves called **Alfvén waves** as a result. The particles in these waves move vertically as the wave propagates along the magnetic field line, and their restoring force is the magnetic tension discussed in Appendix A.3. More importantly, the propagation speed of Alfvén waves is a function of the density, ρ, and magnetic field strength, B_0, within the magnetised plasma, given as

$$\boxed{v_A = \frac{B_0}{\sqrt{4\pi\rho}}}. \tag{3.6}$$

This velocity is known as the Alfvén speed, v_A, and is often referred to throughout this study. These waves are essential in MHD turbulence, e.g. in the solar wind, as they are mainly involved in energy transfer. Although many hybrids of these waves occur in the Sun, including in combination with Rossby waves, this study will only focus on the *pure* solar Rossby wave.

3.11 Summary

This chapter discussed the discovery and importance of hydrodynamic (HD) Rossby waves on Earth. However, since this study considers the solar environment, studying these planetary waves in the magnetohydrodynamic (MHD) framework is more appropriate. Similar to the role HD Rossby waves in the atmosphere of the Earth play in determining large-scale weather patterns, it was shown that the propagation of MHD Rossby waves in the solar tachocline can indicate the location of active regions on the surface of the Sun. Establishing this connection is an essential part of this study as we further explore how this relationship can be utilised to improve the accuracy of various methods of predicting space weather.

Next, reviewing the literature on Rossby waves in the Sun led to the conclusion that the focus will be on the Rossby waves that occur in the solar tachocline. Consequently, the tachocline layer was discussed in more detail. It was shown that this is the layer within the Sun where latitudinal differential rotation starts taking place. This means that in this layer, the Sun's rotation rate starts varying according to latitude, decreasing towards the poles and increasing near the equatorial region. This fundamental characteristic of the Sun should play an important role in a realistic model of waves in the Sun.

Furthermore, examining the characteristics of the tachocline showed that the upper and lower regions of the layer exhibit different dynamics and layer stratification that are determined by the dynamics of the adjacent layers. The lower layer is more stable and exhibits a subadiabatic stratification, which limits vertical movement. Conversely, the upper layer is considered an adiabatic environment that is less stable, as the convection motions overshoot into this region. As a result of these fundamental differences in layer characteristics, these two sub-layers of the tachocline should be treated and studied separately (Gilman, 2000; Zaqarashvili et al., 2007, 2009). This suggestion will allow the respective MHD Rossby wave models to include the appropriate forces to represent reality as closely as possible. Lastly, it was noted that because of the thinness of the tachocline layers, fluid motion within them can be treated as primarily horizontal. More specifically, these tachocline layers can both be treated as a shallow water body since their characteristic horizontal length scale (L_0) is much larger than the thickness or depth (H) of the respective layers, such that the condition of a shallow-water body, $L_0/H \ll 1$, is met.

This chapter also discussed three studies (Kuhn et al., 2000; McIntosh et al., 2017; Löptien et al., 2018) that provided evidence of Rossby waves on the Sun through various observational studies. These observational studies often record the group and phase velocities of solar features, which are attributed to the propagation of Rossby waves. Since this study will evaluate the comprehensiveness of the various MHD Rossby wave models, any change to this model will result in a corresponding change in the dispersion relation, which will be used to derive the equations for the phase and group velocity subsequently. Therefore, although this study will not use these observational findings directly, it is important to understand how observational studies such as these will be impacted by this research. Moreover, the argument has been made that it is only necessary for this study to consider MHD Rossby waves. Nevertheless, since these are not the only solar waves, the Poincaré, Kelvin and

Alfvén waves were also briefly discussed for completeness.

Lastly, it was also necessary to summarise the three different MHD Rossby wave models and how they developed over time, each time increasing in accuracy. The first model is referred to as the "base model" (Chapter 5), which in addition to the HD Rossby wave model, considers the impact of a magnetic field. Then, considering the "effective gravity" of the respective tachocline layers provided a way to study the upper and lower tachocline separately, which was the next model enhancement (Chapter 6). Finally, the "latitudinal differential rotation (LDR) model" (Chapter 7) added the dynamics associated with the LDR to the governing equations used to derive the MHD Rossby wave model.

However, the various governing equations are required to derive these respective models. These fundamental mathematical equations describe the behaviour of physical systems, in our case, the MHD Rossby waves in the solar tachocline. These equations are derived from basic laws of physics, such as conservation laws, and, therefore, encapsulate the underlying principles of physics that govern how a given system reacts to external forces. In the next chapter, these governing equations are formulated.

4 Literature Review III: Formulation of governing equations

4.1 Introduction

Recall that the first objective set out by this study is to evaluate the existing magnetohydrodynamic (MHD) Rossby wave models. To achieve this objective successfully, we must investigate the entire modelling process, starting with formulating the governing equations. The system considered in this study consists of two components: firstly, the MHD Rossby waves (Section 3.4) and secondly, the environment where these waves are studied, the tachocline (Section 3.5.2). In the preceding chapter, it has been established that Rossby waves in this solar environment are best described by considering a thin layer of magnetised fluid in a rotating frame of reference (Appendix B.2). The next step in the model derivation process is to identify any physical principles or laws that govern the system's behaviour and to express these laws mathematically. Consequently, this chapter aims to perform this step, which, in our case, results in a set of partial differential equations (PDEs).

These governing equations that form the foundation for modelling Rossby waves start with the **linear momentum equation**, also known as Newton's second law of motion. Since this equation describes the system's dynamics by including the relevant forces and accelerations, we can understand how objects move and react to forces according to the field of classical mechanics[1]. More specifically, in Chapter 3 it was established that the effect of the magnetic field and a rotating frame of reference should ideally be accounted for in these equations.

The second fundamental equation derived is the conservation of mass, also called the **continuity equation**. As the name of this equation suggests, it ensures that the mass or other quantities of interest, for example, magnetic flux, remain conserved. Furthermore, it should be noted that when a hydrodynamic (HD) environment is considered, combining the linear

[1]Classical mechanics is a branch of physics that describes the relationship between the motion of macroscopic objects and the forces that act on them.

momentum and continuity equations would be sufficient. However, when a magnetic field plays an important role in the system dynamics, such as in the solar tachocline, the governing equations should also adequately capture the behaviour of the dynamic magnetic field. To that end, an additional equation is derived, called the **induction equation**, which describes how the magnetic field changes over time.

Therefore, the governing equations include the linear momentum, continuity, and induction equations. We form a closed set of PDEs by additionally considering Gauss's law of magnetism. Although this initial set of equations indicates a well-defined problem, they contain variables such as pressure and density that can be difficult to measure for the internal layers of the Sun. For this reason, approximations and assumptions are often introduced to make the problem manageable. These simplifications could imply that certain forces are neglected, assuming linear behaviour or considering steady-state conditions. Moreover, after deriving the comprehensive governing equations, we will first simplify the equations by considering the behaviour of an ideal plasma (Appendix C), which is taken as inviscid, incompressible and infinitely conducting. Furthermore, it was established earlier in Section 3.5.2 that the shallow water approximation is especially well-suited due to the tachocline layer's thinness. Applying this overarching approximation simplifies the equations, and the methods to solve them become easier.

Finally, it should be noted that Rossby waves are studied in Cartesian (Zaqarashvili et al., 2007), spherical (Zaqarashvili et al., 2007, 2009, 2010; Gurgenashvili et al., 2016, 2017; Zaqarashvili and Gurgenashvili, 2018) and cylindrical coordinates (Hori et al., 2023). However, when we consider perturbations with a much smaller spatial scale than the sphere's radius, the curvature can be neglected, and Cartesian coordinates can be used. On the contrary, when the perturbations are sufficiently large, the curvature plays an important role and should be included using spherical coordinates (Zaqarashvili et al., 2021). Meanwhile, cylindrical coordinates are predominantly used to simplify the mathematics of problems that exhibit axial symmetry, i.e., symmetrical waves around the rotation axis. Since, in our case, Rossby waves are expected to change in the longitudinal direction, this coordinate system will not be considered. We will start deriving the governing equations using the Cartesian coordinates due to the mathematical simplicity, albeit the spherical coordinate system would be most optimal.

4.2 Linear momentum equation

The equation of linear momentum starts by considering Newton's second law of motion, given by

$$\boxed{\mathbf{F} = m\mathbf{a}} \tag{4.1}$$

which states that the net force, $\mathbf{F}$ applied to an object, is equal to the object's mass, m, multiplied by the object's acceleration, $\mathbf{a}$. As mentioned before, this equation must capture all the relevant forces and accelerations that apply to the system we are considering, in this case, the solar tachocline. No assumptions will be made for the initial formulation until the final linear momentum equation has been derived. After which, the applicable approximations and assumptions will be applied, reducing the complexity of the equation. Therefore, we will start by expanding the simpler right-hand side of the momentum equation that describes the acceleration, followed by identifying and describing the forces that should be included.

4.2.1 Acceleration field of a fluid

To derive the acceleration field of a fluid, we start by considering the vector form of a velocity field, $\mathbf{v}$, in Cartesian coordinates, given by

$$\mathbf{v}(r,t) = v_x(x,y,z,t)\mathbf{i} + v_y(x,y,z,t)\mathbf{j} + v_z(x,y,z,t)\mathbf{k}, \tag{4.2}$$

where $\mathbf{i}, \mathbf{j}, \mathbf{k}$ are unit vectors. The acceleration vector field, $\mathbf{a}$, is determined by the rate of change of the velocity of an object over time, such that

$$\mathbf{a} = \frac{d\,\mathbf{v}(x,y,z,t)}{dt} = \frac{\partial \mathbf{v}}{\partial t} + \frac{\partial \mathbf{v}}{\partial x}\frac{\mathrm{d}x}{\mathrm{d}t} + \frac{\partial \mathbf{v}}{\partial y}\frac{\mathrm{d}y}{\mathrm{d}t} + \frac{\partial \mathbf{v}}{\partial z}\frac{\mathrm{d}z}{\mathrm{d}t}. \tag{4.3}$$

By further considering that velocity, v_x in the x-direction, is defined as distance, dx, divided by time, dt, we can write eq.(4.3) as follows

$$\mathbf{a} = \frac{\partial \mathbf{v}}{\partial t} + \left(v_x\frac{\partial \mathbf{v}}{\partial x} + v_y\frac{\partial \mathbf{v}}{\partial y} + v_z\frac{\partial \mathbf{v}}{\partial z}\right), \tag{4.4}$$

and the same can be done for v_y and v_z in the y and z directions, respectively. This acceleration equation is comprised of two different accelerations. The first term on the right-hand side of eq.(4.4) corresponds to the local acceleration, also referred to as the material or Lagrangian acceleration. As the name suggests, it describes how the fluid experiences a change in velocity as it moves over time and is measured by an observer moving with the fluid. On the contrary, the terms in the bracket represent the convective acceleration, also referred to as the Eulerian acceleration. This acceleration measures the acceleration that a fluid would experience moving past a fixed point in space. Therefore, the formulation describes the change in velocity relating to spatial coordinates. The sum of the convective and local acceleration as presented in eq.(4.4) gives the total Eulerian acceleration as is observed from a fixed frame of reference.

Then, considering that the 3-dimensional gradient operator is defined as,

$$\nabla = \frac{\partial}{\partial x}\mathbf{i} + \frac{\partial}{\partial y}\mathbf{j} + \frac{\partial}{\partial z}\mathbf{k}, \tag{4.5}$$

the last three terms of eq.(4.4) can be summarised as

$$v_x\frac{\partial}{\partial x} + v_y\frac{\partial}{\partial y} + v_z\frac{\partial}{\partial z} = \mathbf{v}\cdot\nabla. \tag{4.6}$$

Note that in eq.(4.6) the directed unit vectors ($\mathbf{i}$, $\mathbf{j}$, $\mathbf{k}$) are omitted. This is due to applying the dot product rule between these vectors, which are summarised below

$$\mathbf{i}\cdot\mathbf{i} = \mathbf{j}\cdot\mathbf{j} = \mathbf{k}\cdot\mathbf{k} = 1, \tag{4.7}$$

$$\mathbf{i}\cdot\mathbf{j} = \mathbf{i}\cdot\mathbf{k} = \mathbf{j}\cdot\mathbf{k} = 0. \tag{4.8}$$

Moreover, by making use of the total derivative notation, also known as the substantial or material derivative, written as

$$\frac{D}{Dt} = \frac{\partial}{\partial t} + \mathbf{v}\cdot\nabla, \tag{4.9}$$

the total acceleration vector eq.(4.4) can be written as

$$\mathbf{a} = \left(\frac{\partial}{\partial t} + (\mathbf{v}\cdot\nabla)\right)\mathbf{v}. \tag{4.10}$$

The mass variable, m, is the other variable on the right-hand side of the momentum equation that should be addressed. The mass of a fluid is defined as the fluid density, ρ, multiplied by the volume of the fluid, $V_{vol} = dx\,dy\,dz$. Therefore, it can be written as

$$\boxed{m = \rho \cdot V_{vol} = \rho \cdot dx\,dy\,dz}\,, \tag{4.11}$$

such that the right-hand side of the momentum equation becomes

$$m\mathbf{a} = \left(\frac{\partial \mathbf{v}}{\partial t} + (\mathbf{v} \cdot \nabla)\mathbf{v}\right) \rho \cdot dx\,dy\,dz. \tag{4.12}$$

Since the right-hand side has now been addressed, we can move to the left side of the momentum equation pertaining to the forces.

4.2.2 Hydrodynamic forces

The left-hand side of Newton's second law of motion, eq.(4.1), describes the specific dynamics of the system at hand by including all the relevant forces. Therefore, correctly formulating this part of the momentum equation is essential as it forms the foundation of the modelling that will follow in Part II. The comprehensive momentum equation can be simplified later when applying approximations and assumptions where applicable.

Subsequently, the possible forces that should be considered for the momentum equation are divided into two groups, namely, body and surface forces. The **body forces** refer to those stemming from external forces, such as gravity and magnetic fields. **Surface forces**, on the other hand, result from stresses on the sides of the region under consideration, for example, the pressure gradient. Newton's second law of motion will describe each of these forces independently. Therefore, let us start by considering the more familiar hydrodynamic (HD) forces, starting with gravity.

Gravitational force

To explain how each force term is derived, we will start by formulating the most simple term corresponding to the gravitational force. By first considering Newton's second law of motion, eq.(4.1), then using eq.(4.11) for mass and setting the acceleration to be gravity, $\mathbf{a} = \boldsymbol{g}$, we get

$$d\mathbf{F}_{\mathbf{g}} = \rho\,\boldsymbol{g}\,dx\,dy\,dz. \tag{4.13}$$

In eq.(4.13) gravity, $\boldsymbol{g} = -g\mathbf{k}$, is a vector with a magnitude of g in the z-direction. Gravity is the only HD *body force*. Conversely, the HD *surface forces* of pressure and viscosity will be discussed next.

Pressure gradient force

To describe any force, one is required to understand the dynamics involved. Therefore, it should be noted that plasma follows the convention of moving from a high to a low-pressure environment, and the HD surface force that drives this behaviour is called the pressure gradient force. More specifically, the direction of this force is from the high-pressure to the low-pressure region as illustrated by the dashed arrow in Fig.(4.1).

Thus, to formulate an equation for the pressure gradient force, start by considering that pressure (p) describes the force (F) per unit area (A) and can therefore be written as

$$p = \frac{F}{A}. \tag{4.14}$$

Now, assume we are only considering the x-direction, and we have a sufficiently small control volume element, referred to as the fluid hereafter, with a surface area, S, and a width of dx. The fluid element experiences a horizontal pressure gradient with the lower pressure region on the left-hand side, as illustrated in Fig.(4.1).

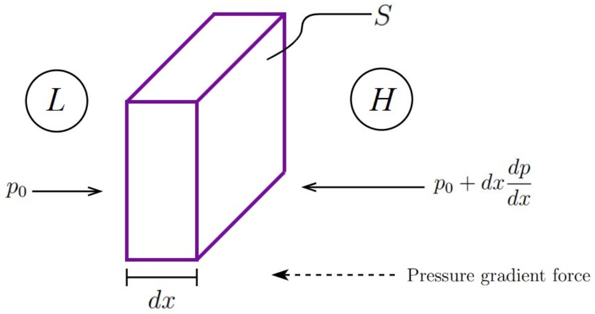

Figure 4.1: Pressure gradient system in the x-direction for a fluid under consideration with a surface area, S, thickness, dx and pressure, p. Where the pressure gradient force points from the high, H, to the low, L, pressure regions.

The pressure on the right-hand side of the fluid is equal to the pressure on the left, plus the pressure change over the fluid thickness (dx). Therefore, to determine the net pressure force on the fluid, we make use of eq.(4.14) in the form of $F = A\,p$ to get

$$\mathbf{F}_{\boldsymbol{p}} = S\left[p_0 - \left(p_0 + dx\frac{dp}{dx}\right)\right] = -S\,dx\,\frac{dp}{dx}, \tag{4.15}$$

where $S\,dx$ is the volume and dp/dx, the pressure change in the x-direction. The negative sign of this acceleration term indicates that the pressure gradient force causes an acceleration in the opposite direction to the increase in pressure. Equation (4.5) can be used to generalise eq.(4.15) such that

$$d\mathbf{F}_{\boldsymbol{p}} = -\nabla \boldsymbol{p}\, dx\, dy\, dz, \tag{4.16}$$

which considers all directions. Finally, the last HD surface body force of viscosity is discussed next.

Viscosity

The viscosity of a fluid is the internal friction experienced when two adjacent fluid layers move past each other. Now, to formulate the associated equation for this force, we start by considering that in fluid mechanics, the viscous stress tensor, τ, is defined as

$$\tau = \nabla \cdot \Big[\mu_d\big(\nabla \mathbf{v} + (\nabla \mathbf{v})^T\big)\Big], \tag{4.17}$$

where $\nabla \mathbf{v}$ is the gradient of the velocity vector field, $(\nabla \mathbf{v})^T$ is the transpose of the gradient velocity vector field, and μ_d is the dynamic viscosity of the fluid. Therefore, eq.(4.17) describes the divergence of the stress tensor. In other words, it is a measure of how the viscous stresses change within the fluid, contributing to the fluid's acceleration.

By expanding eq.(4.17) in the x-direction, we get

$$\begin{aligned}
\tau &= \frac{\partial}{\partial x}\left(2\mu_d \frac{\partial v_x}{\partial x}\right) + \frac{\partial}{\partial y}\left[\mu_d\left(\frac{\partial v_x}{\partial y} + \frac{\partial v_y}{\partial x}\right)\right] + \frac{\partial}{\partial z}\left[\mu_d\left(\frac{\partial v_x}{\partial z} + \frac{\partial v_z}{\partial x}\right)\right] && \text{(4.18a)}\\
&= 2\mu_d \frac{\partial^2 v_x}{\partial x^2} + \mu_d \frac{\partial^2 v_x}{\partial y^2} + \mu_d \frac{\partial^2 v_y}{\partial y \partial x} + \mu_d \frac{\partial^2 v_x}{\partial z^2} + \mu_d \frac{\partial^2 v_z}{\partial z \partial x} && \text{(4.18b)}\\
&= \mu_d \frac{\partial^2 v_x}{\partial x^2} + \mu_d \frac{\partial^2 v_x}{\partial y^2} + \mu_d \frac{\partial^2 v_x}{\partial z^2} + \mu_d \frac{\partial^2 v_x}{\partial x^2} + \mu_d \frac{\partial^2 v_y}{\partial y \partial x} + \mu_d \frac{\partial^2 v_z}{\partial z \partial x} && \text{(4.18c)}\\
&= \mu_d \nabla^2 v_x + \mu_d \frac{\partial}{\partial x}\left(\frac{\partial v_x}{\partial x} + \frac{\partial v_y}{\partial y} + \frac{\partial v_z}{\partial z}\right), && \text{(4.18d)}
\end{aligned}$$

where the Laplacian operator, ∇^2, in Cartesian coordinates is given as

$$\nabla^2 = \frac{\partial^2}{\partial x^2} + \frac{\partial^2}{\partial y^2} + \frac{\partial^2}{\partial z^2}. \tag{4.19}$$

If we then assume an ideal fluid (Appendix C) which is considered to be incompressible, such that $\nabla \cdot \mathbf{v} = 0$ (derived in Section 4.4), the second term of eq.(4.18d) can be set to zero, simplifying the equation as follows

$$\begin{aligned}\tau &= \mu_d \nabla^2 v_x + \mu_d \frac{\partial}{\partial x} \cancelto{0}{(\nabla \cdot \mathbf{v})} \\ &= \mu_d \nabla^2 v_x. \end{aligned} \tag{4.20}$$

By following the same steps for the y and z directions, we get $\mu_d \nabla^2 v_y$ and $\mu_d \nabla^2 v_z$, respectively, which can subsequently be written as

$$\tau = \mu_d \left(\frac{\partial^2 v}{\partial x^2} + \frac{\partial^2 v}{\partial y^2} + \frac{\partial^2 v}{\partial z^2} \right) = \mu_d \nabla^2 \mathbf{v}, \tag{4.21}$$

which describes the spatial variation of the velocity field. Thus, $\nabla^2 \mathbf{v}$ explains how the velocity changes across space. Now, consider that the dynamic viscosity can be written in terms of the kinematic viscosity, ν, and fluid density, ρ, such that

$$\mu_d = \rho \nu, \tag{4.22}$$

can be substituted into eq.(4.21) to get

$$\tau = \rho \nu \nabla^2 \mathbf{v}. \tag{4.23}$$

Therefore, the term that describes the viscosity force in the momentum equation is written as

$$d\mathbf{F}_\nu = \rho \nu \nabla^2 \mathbf{v} \, dx \, dy \, dz, \tag{4.24}$$

describes the diffusion of momentum inside the fluid. In other words, it will account for the spreading or smoothing of velocity gradients within the fluid, which influences fluid behaviour on a small scale. This viscosity term is significant for fluids with a low Reynolds number ($R_e \ll 1$), given by

$$R_e = \frac{U_0^2 / L_0}{\mu_d U_0 / \rho L_0^2} = \frac{\rho U_0 L_0}{\mu_d} = \frac{U_0 L_0}{\nu}, \tag{4.25}$$

where U_0 is the typical fluid flow velocity scale and L_0 is the characteristic length scale. Fluids with higher viscosity experience stronger damping effects on their velocity gradients, which results in slower dissipation of vorticity and also causes slower fluid motion. On the contrary, the diffusion of momentum in low-viscosity fluids is faster, leading to rapid changes in velocity and allowing small-scale flow structures to develop.

Navier-Stokes equation

By combining the gravitational, pressure gradient and viscosity forces along with the fluid acceleration, we get

$$\begin{aligned} \Sigma\mathbf{F} &= m\mathbf{a} \\ d\mathbf{F}_{\mathbf{g}} + d\mathbf{F}_{\boldsymbol{p}} + d\mathbf{F}_{\nu} &= \rho\frac{d\mathbf{v}}{dt}dx\,dy\,dz \\ \big(\rho\,\boldsymbol{g}\,dx\,dy\,dz\big) - \big(\nabla\boldsymbol{p}\,dx\,dy\,dz\big) + \big(\rho\nu\nabla^2\mathbf{v}\,dx\,dy\,dz\big) &= \rho\frac{d\mathbf{v}}{dt}dx\,dy\,dz \end{aligned} \tag{4.26}$$

Dividing eq.(4.26) by volume, $dx\,dy\,dz$, and applying the total time derivative, eq.(4.9), on the right-hand side, we can write the equation for linear momentum as

$$\rho\left(\frac{\partial}{\partial t} + \mathbf{v}\cdot\nabla\right)\mathbf{v} = \rho\boldsymbol{g} - \nabla\boldsymbol{p} + \rho\nu\nabla^2\mathbf{v}. \tag{4.27}$$

This form of the momentum equation is more commonly called the Navier-Stokes equation. Although this fundamental HD equation is widely used, it does not consider the forces due to rotation, which is essential for the existence of Rossby waves. Nor does it include electromagnetic forces that will inevitably be present in the Sun due to its magnetic field. For this reason, the Navier-Stokes equation will be expanded to include these missing components, starting with the forces that appear as a result of rotation, which is described next.

4.2.3 Apparent forces due to rotation

Newton's laws describe forces that act in an **inertial frame of reference**, meaning one that does not accelerate. Conversely, a **rotating frame of reference**, such as the Earth, always accelerates, implying that Newtonian laws do not translate to such a system. Therefore, a rotating system will exhibit additional rotational accelerations that should be added to Newton's laws for an inertial frame. We will, for familiarity, use the Earth as an example to investigate these accelerations and to show how these forces are derived.

Assume the Earth rotates towards the east at a constant angular velocity, $\boldsymbol{\Omega}$, along with a particle that is moving relative to the Earth as illustrated by the crossed-circle in Fig.(4.2).

The absolute velocity that the particle exhibits, $\mathbf{v_a}$, is the sum of the particle velocity, $\mathbf{v_P}$, and the velocity of the Earth, $\mathbf{v_e}$, written as

$$\mathbf{v_a} = \mathbf{v_P} + \mathbf{v_e}. \tag{4.28}$$

The magnitude of Earth's linear velocity at the point under consideration is given by $\mathbf{v_e} = \Omega R_r$. Here, R_r is the radius of rotation, which measures the shortest distance between the considered point on the surface and the rotation axis.

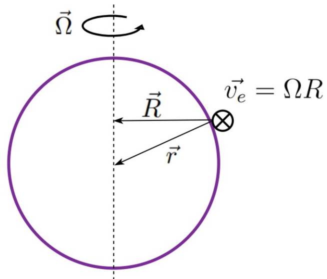

Figure 4.2: The Earth's rotating system with angular velocity, $\vec{\Omega}$, as discussed in Section B.2.1. The vector $\vec{R}$ is the shortest distance from the point under consideration to the rotation axis, and $\vec{r}$ is the position vector from the specific point to the Earth's centre. Note: In the diagram, the arrows indicate the vectors for readability.

This linear velocity, $\mathbf{v_e}$, can be written as a vector since the direction of the velocity is perpendicular to both $\mathbf{\Omega}$ and $\mathbf{R_r}$, which is into the page (indicated by a circle containing an x in Fig.(4.2)). By further considering that the position vector, $\mathbf{r}$, is perpendicular to the axis of rotation, given by $\mathbf{\Omega}$, the cross product can be used to reflect the physics of rotation, and we get the expression for the Earth's velocity as follows

$$\mathbf{v_e} = \Omega R_r = \mathbf{\Omega} \times \mathbf{r}. \tag{4.29}$$

Therefore, eq.(4.28) that relates the absolute velocity to the velocity in a rotating frame of reference can now be written as

$$\mathbf{v_a} = \mathbf{v_P} + (\mathbf{\Omega} \times \mathbf{r}). \tag{4.30}$$

Furthermore, since velocity is equal to the distance over time, we can substitute

$$\mathbf{v_a} = \left.\frac{d\mathbf{r}}{dt}\right|_a \quad \text{and} \quad \mathbf{v_P} = \left.\frac{d\mathbf{r}}{dt}\right|_p, \tag{4.31}$$

in eq.(4.30) such that

$$\left.\frac{d\mathbf{r}}{dt}\right|_a = \left.\frac{d\mathbf{r}}{dt}\right|_p + \mathbf{\Omega} \times \mathbf{r}. \tag{4.32}$$

Although it is beneficial to use a practical example of a particle moving with respect to the Earth to explain the dynamics at first, it remains necessary to generalise the formulation of the equations in the future.

Therefore, since the term on the left-hand side of eq.(4.32) describes the velocity change seen with respect to the inertial frame, the subscript "I" will be used. Whereas, on the right-hand side, the first term represents the change of the relative particle velocity as measured from the rotating frame of reference, for which the subscript "R" is suitable. In this case, the last term gives the velocity change due to the Earth's rotation, which remains unchanged as it applies to any rotating sphere. Therefore, eq.(4.30), eq.(4.31) and eq.(4.32) are written as

$$\mathbf{v_I} = \mathbf{v_R} + (\mathbf{\Omega} \times \mathbf{r}), \tag{4.33a}$$

$$\mathbf{v_I} = \left.\frac{d\mathbf{r}}{dt}\right|_I, \ \mathbf{v_R} = \left.\frac{d\mathbf{r}}{dt}\right|_R, \tag{4.33b}$$

$$\left.\frac{d\mathbf{r}}{dt}\right|_I = \left.\frac{d\mathbf{r}}{dt}\right|_R + \mathbf{\Omega} \times \mathbf{r} = \mathbf{v_R} + \mathbf{\Omega} \times \mathbf{r}. \tag{4.33c}$$

By now, applying the general form of eq.(4.33c) to the rotation velocity, $\mathbf{v_R}$, it gives

$$\left.\frac{d\mathbf{v_R}}{dt}\right|_I = \left.\frac{d\mathbf{v_R}}{dt}\right|_R + \mathbf{\Omega} \times \mathbf{v_R}. \tag{4.34}$$

Next, we substitute $\mathbf{v_R} = \mathbf{v_I} - (\mathbf{\Omega} \times \mathbf{r})$ from eq.(4.33a) into the left-hand side of eq.(4.34), such that

$$\left.\frac{d}{dt}\big[\mathbf{v_I} - (\mathbf{\Omega} \times \mathbf{r})\big]\right|_I = \left.\frac{d\mathbf{v_R}}{dt}\right|_R + \mathbf{\Omega} \times \mathbf{v_R}. \tag{4.35}$$

Then, we rearrange eq.(4.35) so that the left-hand side represents the change velocity with respect to the inertial frame as follows

$$\left.\frac{d\mathbf{v_I}}{dt}\right|_I = \left.\frac{d\mathbf{v_R}}{dt}\right|_R + \mathbf{\Omega} \times \mathbf{v_R} + \frac{d\mathbf{\Omega}}{dt} \times \mathbf{r} + \mathbf{\Omega} \times \left.\frac{d\mathbf{r}}{dt}\right|_I. \tag{4.36}$$

Considering that constant rotation was assumed, such that $d\mathbf{\Omega}/dt = 0$, and substituting eq.(4.33c) into eq.(4.37) it becomes

$$\left.\frac{d\mathbf{v_I}}{dt}\right|_I = \left.\frac{d\mathbf{v_R}}{dt}\right|_R + \mathbf{\Omega} \times \mathbf{v_R} + \mathbf{\Omega} \times \left(\mathbf{v_R} + \mathbf{\Omega} \times \mathbf{r}\right), \tag{4.37}$$

which can be simplified and rearranged to be

$$\left.\frac{d\mathbf{v_R}}{dt}\right|_R = \left.\frac{d\mathbf{v_I}}{dt}\right|_I - 2\mathbf{\Omega} \times \mathbf{v_R} - \mathbf{\Omega} \times (\mathbf{\Omega} \times \mathbf{r}), \tag{4.38}$$

Eq.(4.38) describes the relative velocity rate of change with respect to the rotating frame of reference. The first term on the right-hand side is similar to the term on the left-hand side of eq.(4.38), only here it describes the rate of change of the inertial velocity as viewed from the inertial frame (Vallis, 2019, p.26). Finally, the last two terms represent the apparent forces that appear in rotating systems, called the Coriolis force (Appendix B.2.2) and the centrifugal force, respectively. Although they are generally referred to as the centrifugal and Coriolis *forces*, as seen from the eq.(4.38), they are, in reality, experienced as *accelerations*. Therefore, it would be more accurate to refer to them as pseudo-forces instead.

Therefore, it is clear that these two accelerations or pseudo-forces should be included in the momentum equation when a rotating frame is considered. However, in nature, there is the potential for specific force balances, such as, in this case, the balance between the Coriolis and the pressure gradient forces, called **geostrophic balance**. One can calculate the Rossby number, R_{nr}[2], to test if this balance holds in a specific environment. This characteristic number describes the importance of the rotation in a fluid and is given by

$$R_{nr} = \frac{V_0}{2\Omega L_0},$$

where V_0 and L_0 are the characteristic velocity and length scales, respectively, and Ω is the angular velocity. The Coriolis force dominates in environments where $R_{nr} \ll 1$, while the inertial force, such as the centrifugal force, dominates when $R_{nr} \gg 1$. Since large-scale flows exhibit large L_0 values, it will lead to a small Rossby number and, therefore, are more significantly affected by rotation. As a result, the geostrophic balance approximation is frequently used to describe large-scale movements in oceans and atmospheres. The solar tachocline is

[2]Although the common notation for the Rossby number is R_0, in this document, it instead denotes the distance from the solar centre to the tachocline. Therefore, we introduce the new notation for the Rossby number as R_{nr} to avoid confusion.

no exception and satisfies the first condition, with a value of $R_{nr} \leq 0.1$ (Dikpati et al., 2018), indicating that the fluid motions in that layer are primarily influenced by rotation.

Therefore, it is argued that the centrifugal forces are negligible for slow rotation[3] such the $2.2\,\mathrm{km\,s^{-1}}$ exhibited by the Sun (Dwivedi, 2003, p.59; Boucher, 2023) as it will further reduce the Rossby number. Consequently, only the Coriolis force is added to the Navier-Stokes momentum equation, eq.(4.27), which gives the comprehensive HD momentum equation in a rotating frame of reference, such that it becomes

$$\boxed{\rho\left[\frac{\partial \mathbf{v}}{\partial t} + (\mathbf{v}\cdot\nabla)\mathbf{v} + 2\boldsymbol{\Omega}\times\mathbf{v}\right] = \rho\boldsymbol{g} - \nabla\boldsymbol{p} + \nu\nabla^2\mathbf{v}}\,. \tag{4.39}$$

Now that the effect of rotation has been added to the momentum equation, the final step is to incorporate the resulting force due to the presence of a magnetic field.

4.2.4 Electromagnetic forces

The presence of a strong and changing magnetic field on the Sun leads us to the following field of study that should be considered, namely **electromagnetism**. The theory that describes electromagnetic forces resulted from independent studies of electricity and magnetism. It explains how these two forces are related to each other. Fundamentally, it is based on André-Marie Ampère (1775-1836), proving the hypothesis that all magnetic phenomena result from electric charges in motion as well as the discovery by Michael Faraday (1791-1867), that a moving magnet generates an electric current. James Clerk Maxwell (1831-1879) then completed this successful theory by summarising electromagnetism in the set of the four famous Maxwell's equations. These equations describe the behaviour of magnetic and electric fields and how they relate to each other (Griffiths, 2008, p.232). Hendrik Lorentz (1853-1928) also derived an equation that describes the electromagnetic force exerted on a charged particle moving through a region with a magnetic and electric field, which is often used in combination with Maxwell's equations.

Additionally, the properties of an ideal plasma should be considered (Appendix C). An ideal plasma, similar to an ideal fluid, uses approximations to simplify the fluid behaviour and

[3] In comparison, Altair is another star close to Earth exhibiting a fast rotation rate of $240\,\mathrm{km\,s^{-1}}$ (Monnier et al., 2007)

its subsequent properties. Consequently, an ideal plasma can be assumed to have a constant density (**incompressible**), it neglects viscosity (**inviscid**) and is infinitely conducting (**negligible resistivity**). Let us, therefore, investigate how electromagnetic forces are included in the momentum equation and how the properties of an ideal fluid contribute to the formulation of the force equation.

Lorentz force

As previously mentioned, the linear momentum equation describes the net force of the system. Therefore, the momentum equation should account for the associated electromagnetic forces when considering an environment like the Sun. The specific force that is present forms part of Maxwell's equations and is called the Lorentz force, $\mathbf{F}_L$.

This magnetic force that acts upon a volume current is given by

$$\mathbf{F}_L = \int (\mathbf{J} \times \mathbf{B}) \, dV. \tag{4.40}$$

Here, the current density, $\mathbf{J}$, measures the electric charge flow per unit area, and its direction aligns with that of the positive charge flow. Whereas $\mathbf{B}$ is the magnetic field. Furthermore, the cross-product indicates that the Lorentz force acts in a direction that is perpendicular to both $\mathbf{J}$ and $\mathbf{B}$.

However, due to the lack of resistivity in an ideal plasma, the current density, $\mathbf{J}$, must be eliminated from the Lorentz force equation. This is accomplished by substituting $\mathbf{J}$ from another Maxwell equation for magnetostatics - in this case **Ampère's law**, given by

$$\nabla \times \mathbf{B} = \mu_0 \mathbf{J}$$
$$\mathbf{J} = \frac{1}{\mu_0} \nabla \times \mathbf{B},$$

into eq.(4.40). The resulting Lorentz force is

$$\mathbf{F}_L = \frac{1}{\mu_0} (\nabla \times \mathbf{B}) \times \mathbf{B}. \tag{4.41}$$

This form of the Lorentz force will be added to the momentum equation. The permeability of free space constant, μ_0, can also be expressed as $1/4\pi$, which is often used in equations for simplicity. By including the Lorentz force in eq.(4.39) as follows

$$\boxed{\rho\left[\frac{\partial \mathbf{v}}{\partial t}+(\mathbf{v}\cdot\nabla)\mathbf{v}+2\boldsymbol{\Omega}\times\mathbf{v}\right]=\rho\boldsymbol{g}-\nabla\boldsymbol{p}+\nu\nabla^2\mathbf{v}+\left[\frac{1}{\mu_0}(\nabla\times\mathbf{B})\times\mathbf{B}\right]}, \tag{4.42}$$

it gives the comprehensive MHD momentum equation, which includes all the relevant forces that apply to the solar environment.

However, now that the ideal plasma properties have been introduced, the momentum equation can be simplified further by considering that the plasma is inviscid. This property implies that viscosity can be neglected, therefore dropping the associated term on the right-hand side of the momentum equation such that we get the simplified MHD momentum equation of the form

$$\rho\left[\frac{\partial \mathbf{v}}{\partial t}+(\mathbf{v}\cdot\nabla)\mathbf{v}+2\boldsymbol{\Omega}\times\mathbf{v}\right]=\rho\boldsymbol{g}-\nabla\boldsymbol{p}+\frac{1}{\mu_0}(\nabla\times\mathbf{B})\times\mathbf{B}. \tag{4.43}$$

It is important to note that the magnetic field also affects the pressure inside the Sun, which is discussed next.

Horizontal pressure gradient

A plasma consists of charged particles that are free to move. Therefore, when a magnetic field line is placed inside a plasma, such as in the case of the Sun, the magnetic field line exerts pressure on these particles in a direction that is perpendicular to the magnetic field line. This interaction causes a change in the pressure gradient that is discussed in Section 4.2.2.

In the case of the Sun, the horizontal pressure gradient, $\nabla\boldsymbol{p}$, subsequently expresses the balance between the previously considered plasma pressure, $g\nabla h$, and the newly added magnetic pressure as follows

$$\nabla\boldsymbol{p}=g\nabla h-\nabla\left(\frac{\boldsymbol{B}\cdot\boldsymbol{B}}{2}\right), \tag{4.44}$$

where h is the fluid layer thickness, g is gravity and $\boldsymbol{B}$ is the magnetic field.

To determine which of these two pressures will dominate in a specific region, the plasma-beta ratio, β_p, can be considered. This numerator of the ratio is set as the plasma pressure, β_p, which is the ideal gas law given by $p = nk_BT$, where n is the number density, $k_B = 1.3806 \times 10^{-24}\,\mathrm{m^2kg\,s^{-2}K^{-1}}$, is the Boltzmann constant, and T is the temperature.

$$\beta_p = \frac{p}{B^2/8\pi}. \tag{4.45}$$

The denominator is the magnetic pressure, whereas B is the applied magnetic field (Gurnett and Bhattacharjee, 2017, p.196).

For large plasma beta values, $\beta_p \gg 1$, it is the plasma pressure that dominates, whereas a small ratio value, $\beta_p \ll 1$, indicates that the role of the magnetic pressure is more significant (Priest, 2014, p.90). However, calculating this ratio for the Sun is challenging as the values for the parameters used in the eq.(4.45) are only estimations. Therefore, we will not explicitly focus on calculating this ratio due to this lack of certainty regarding these values. Nonetheless, it is widely accepted that $\beta_p \gg 1$ holds for the solar interior (Toriumi and Wang, 2019), and it is thus safe to assume that plasma pressure will dominate. Subsequently, the last term on the right-hand side of eq.(4.44), representing the magnetic pressure, can be neglected in this study, and the system's pressure under consideration remains unchanged.

Since the momentum equation derived up to this point, eq.(4.43), includes all the necessary forces, the following governing equation can be derived, which describes the behaviour of the magnetic field over time.

4.3 Induction equation

Continuing the process of deriving the governing equation for a system that includes a magnetic field, it naturally follows that Maxwell's equations will be used. These well-known laws specify the curl and divergence of magnetic and electric fields, resulting in a complete and elegant formulation of both electro- and magnetostatics, of which the latter is of interest for this study. This set of equations comprises Gauss's law, the divergence-free condition for magnetic fields, Faraday's law, and Ampère's law.

Since Faraday's law contains a term that describes how the magnetic field changes over time, it is appropriate to use it at the start of the modelling. **Faraday's law** states that a changing magnetic field, $\mathbf{B}$, gives rise to an electric field, $\mathbf{E}$, and is given by

$$\nabla \times \mathbf{E} = -\frac{\partial \mathbf{B}}{\partial t}. \tag{4.46}$$

Considering that we are only interested in the effects of the magnetic field, it follows that the electric field in eq.(4.46) should ideally be removed.

Ohm's law (Griffiths, 2008, p.285) can be used to find an equation for the electric field, which can be used to replace this unwanted variable, $\mathbf{E}$, in Faraday's law. This fundamental electrodynamics law shows that the current density, $\mathbf{J}$, is proportional to $\mathbf{F}$, the force per unit charge, and is dependent on the conductivity of the material, σ, and is expressed as

$$\mathbf{J} = \sigma \mathbf{F}. \tag{4.47}$$

The electromagnetic force, $\mathbf{F}$, in eq.(4.47) is a combination of the electric field acting on a particle at rest, $\mathbf{E}$, as well as an additional force described by $\mathbf{v} \times \mathbf{B}$, that is exerted on a particle as it moves with a velocity, $\mathbf{v}$, through a region with a magnetic field, $\mathbf{B}$.
The total electromagnetic force is, therefore, given as

$$\mathbf{F} = \mathbf{E} + \mathbf{v} \times \mathbf{B}, \tag{4.48}$$

such that eq.(4.47) becomes

$$\mathbf{J} = \sigma(\mathbf{E} + \mathbf{v} \times \mathbf{B}). \tag{4.49}$$

However, eq.(4.49) can be simplified by recalling that an infinitely conducting plasma ($\sigma \to \infty$) that exhibits no resistivity is being considered. For this reason, we can use the equation for resistivity, ρ_r, inside a conductor given as

$$\rho_r = \frac{\mathbf{E}}{\mathbf{J}} = \frac{1}{\sigma}, \tag{4.50}$$

to get the following approximation

$$\mathbf{E} = \frac{\mathbf{J}}{\sigma} \to 0. \tag{4.51}$$

By now, applying eq.(4.51) to eq.(4.49) we get what is called the **ideal Ohm's law**

$$\mathbf{E} = -\mathbf{v} \times \mathbf{B}. \tag{4.52}$$

Then by substituting eq.(4.52), into Faraday's law, eq.(4.46), we get the **induction equation**, given by

$$\boxed{\frac{\partial \mathbf{B}}{\partial t} = \nabla \times (\mathbf{v} \times \mathbf{B})}, \tag{4.53}$$

which describes how the magnetic field changes over time.

Lastly, for completeness, we will briefly discuss the outcome of the induction equation if the **resistive Ohm's law** had been used, which is given by

$$\mathbf{E} + \mathbf{v} \times \mathbf{B} = \eta \mathbf{J}, \tag{4.54}$$

where η represents the magnetic diffusivity. The derivation of the induction equation, in this case, will lead to the following result

$$\frac{\partial \mathbf{B}}{\partial t} = \nabla \times (\mathbf{v} \times \mathbf{B}) + \frac{\eta}{\mu_0} \nabla^2 \mathbf{B}, \tag{4.55}$$

where μ_0 is the permeability constant. In eq.(4.55), the first term on the right represents convection, and the newly added second term describes diffusion. We can determine the dominant term of the two by making use of the dimensionless magnetic Reynolds number, R_m, given below

$$R_m = \frac{L_0 U_0}{\eta}, \tag{4.56}$$

where L_0 and U_0 are the characteristic length and velocity scale, respectively. The magnetic Reynolds number measures the coupling strength between a magnetic field and the flow. For the case of $R_m \ll 1$, it indicates a weak coupling and that the magnetic field will be diffused throughout the plasma (Priest, 2014, p.91), which is generally true for plasma created in laboratories. In contrast, when $R_m \gg 1$, a strong coupling exists between the plasma and the magnetic field, and advection dominates.

However, the values for the Sun's magnetic diffusivity needed for this calculation are difficult to determine. Nonetheless, the estimated range of values for the magnetic diffusivity at the solar surface and stratified solar core is given as $\eta_{surf} = 10^{12} - 10^{14}\,\text{cm}^2 \cdot \text{s}^{-1}$ and $\eta_{core} = 5 \times 10^8\,\text{cm}^2 \cdot \text{s}^{-1}$, respectively (Hotta and Yokoyama, 2010). This shows that the condition for $R_m \gg 1$ is satisfied, as is generally true for astrophysical applications. For this reason, the effect of electrical resistivity inside the plasma is not important, and the diffusion term in eq.(4.55) can be safely neglected.

The strong coupling between the magnetic field and the plasma flow when $R_m \gg 1$ is satisfied is formalised by **Alfvén's frozen flux theorem**, which states that the magnetic field lines and the magnetic flux are conserved under this condition (Priest, 2014, p.92). In other words, it is assumed that the magnetic field is frozen in the plasma, as the name suggests and has significant implications for this study. Since we are deriving equations that allow us to describe and study the flow of plasma, this theorem allows the behavioural understanding of the plasma flow to be extended to that of the magnetic field as they move together. Finally, it can also be noted that under this condition, a magnetic field can be amplified when stretching a magnetic field line. This characteristic becomes important for regions like the convection zone, where the magnetic field lines get stretched over the height of this layer until they reach the solar surface to form sunspots. Lastly, we will derive the conservation of mass equation, concluding the derivations of the governing equations used in this study.

4.4 Continuity equation

Alfvén's frozen flux theorem discussed in Section 4.3 states that the magnetic field lines are conserved, and so is the system's mass under consideration. Therefore, the mass continuity equation will be derived to complete the governing equations, and the divergence-free condition for a magnetic field will be described in this section.

4.4.1 Conservation of mass

When considering fluid flow in a **closed system**, where no energy or matter transfer takes place, the mass of this system should remain constant over time. This is known as the conservation of mass, which is illustrated in Fig.(4.3).

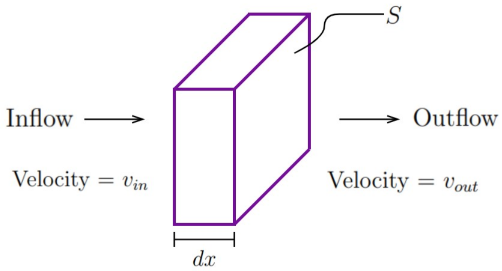

Figure 4.3: Consider a flow in the x-direction through a controlled volume element, with surface area, S, thickness, dx, and in- and outflow velocities, v_{in} and v_{out}, respectively.

Assume a fluid flowing through a controlled volume element (CVE), such as represented by the box in Fig.(4.3). Recalling the equation for mass, eq.(4.11), and the fact that volume (V_{vol}) is surface area (S) times displacement (dx), we can write the mass flow rate as follows

$$\frac{dm}{dt} = \frac{\rho\, dV_{vol}}{dt} = \rho\, S \frac{dx}{dt}. \tag{4.57}$$

Further substituting distance over time as velocity (v) in eq.(4.57), we get

$$\frac{dm}{dt} = \rho\, S\, dv. \tag{4.58}$$

Following this, the rate of change of mass inside the CVE is the difference between the mass that flows in and out. If one considers a flow in only the x-direction, then the corresponding surface area is $S = dy\, dz$. From this, we get the equation for the rate of change in mass in the CVE as

$$\frac{dm_{cve}}{dt} = (\rho\, v_{in}\, dy\, dz) - (\rho\, v_{out}\, dy\, dz). \tag{4.59}$$

Up to this point, a finite volume element was considered to understand the basic concepts. However, realistically, we would rather consider an infinitesimal volume element. This will imply that the mass flux will change along the x-direction and is, therefore, necessary to introduce a gradient of mass flux as

$$\frac{\partial(\rho v_x)}{\partial x}. \tag{4.60}$$

Over a distance of dx the mass flux (m^*) will change as follows

$$dm^*_{between} = \frac{\partial\, (\rho v_x)}{\partial x}\, dx. \tag{4.61}$$

The outflowing mass flux is, therefore, given as

$$m^*_{out} = m^*_{in} + dm^*_{between} \tag{4.62a}$$
$$= m^*_{in} + \frac{\partial\left(\rho v_x\right)}{\partial x}\, dx. \tag{4.62b}$$

Now that we have the flow inside and out of the CVE, the change of mass over time inside the element is as follows

$$\frac{\partial m_{cve}}{\partial t} = \frac{\partial m^*_{in}}{\partial t}\, dy\, dz - \frac{\partial m^*_{out}}{\partial t}\, dy\, dz \tag{4.63a}$$
$$= \frac{\partial m^*_{in}}{\partial t}\, dy\, dz - \left(m^*_{in} + \frac{\partial\left(\rho v_x\right)}{\partial x}\, dx\right)\, dy\, dz \tag{4.63b}$$
$$= -\frac{\partial(\rho v_x)}{\partial x}\, dx\, dy\, dz \tag{4.63c}$$
$$= -\frac{\partial(\rho v_x)}{\partial x}\, dV_{vol} \tag{4.63d}$$

The negative sign here shows that the mass inside the CVE will decrease over time as the incoming flow is less than the outgoing flow for a positive gradient. This implies that the density inside the control volume may change as the mass changes over time. This is formulated as

$$\frac{\partial m_{cve}}{\partial t} = \frac{\partial \rho}{\partial t}\, dV_{vol}. \tag{4.64}$$

Combining eq.(4.63d) and eq.(4.64), we get the equation that is known as the continuity equation in the x-direction as

$$\frac{\partial \rho}{\partial t} = -\frac{\partial(\rho v_x)}{\partial x}\, dV_{vol}. \tag{4.65}$$

This equation states that for a specific point, the mass flux gradient corresponds to the density change at that point over time. This one-dimensional equation can be generalised to include all three dimensions, which the mass continuity equation will be derived to complete the governing equations of the three-dimensional continuity equation follows similar steps to those above, and by dividing with volume, dV_{vol}, we get the following equation,

$$\frac{\partial \rho}{\partial t} = -\left[\frac{\partial(\rho v_x)}{\partial x} + \frac{\partial(\rho v_y)}{\partial y} + \frac{\partial(\rho v_z)}{\partial z}\right] \tag{4.66}$$

which was further simplified by applying the 3D gradient operator, eq.(4.5), and is written as

$$\boxed{\frac{\partial \rho}{\partial t} = -\nabla \cdot (\rho \mathbf{v})}. \tag{4.67}$$

Since an ideal fluid is incompressible, the left-hand side of eq.(4.67) should be set to zero. Furthermore, the density is also constant throughout the fluid and can, therefore, also be removed from the term on the right-hand side of the equation. The simplified equation represents the continuity equation for incompressible fluids, which is given below as

$$\boxed{\nabla \cdot \mathbf{v} = 0}. \tag{4.68}$$

By noting that the dot product is commutative, such that $\nabla \cdot \mathbf{v} = \mathbf{v} \cdot \nabla = 0$, it follows that the momentum equation for an ideal fluid can be simplified. By applying eq.(4.68) to eq.(4.43), the convective acceleration term on the left-hand side of the momentum equation is equal to zero, giving

$$\boxed{\rho \left(\frac{\partial \mathbf{v}}{\partial t} + 2\mathbf{\Omega} \times \mathbf{v} \right) = \rho \boldsymbol{g} - \nabla \boldsymbol{p} + \frac{1}{\mu_0} (\nabla \times \mathbf{B}) \times \mathbf{B}}. \tag{4.69}$$

However, not only mass but also the magnetic flux is conserved in this system, as explained in the next section.

4.4.2 Conservation of magnetic flux

Gauss's law for magnetism is the final equation that makes up the governing equations for the system under consideration in this study. This equation is part of the magnetostatic Maxwell's equations and imposes a divergence-free condition on the magnetic field. To understand the meaning of this equation, we must consider another characteristic of magnetic field lines. Specifically, they are continuous and have no beginning or end. In other words, a magnetic field line can either extend to infinity or form a closed loop (Griffiths, 2008, p.232). Since the latter is mostly considered, it requires a nonzero divergence, which is written as

$$\boxed{\nabla \cdot \mathbf{B} = 0}. \tag{4.70}$$

This equation is used as an initial condition for the other time-dependent governing equations discussed until now (Priest, 2014, p.87).

4.5 Summary of governing equations

To recap the developments thus far in this chapter, the comprehensive governing equations were initially derived using the Cartesian coordinate system in a rotating frame of reference with no assumptions or approximations applied. Furthermore, this first part also included the shift from considering the HD framework to the more appropriate MHD framework. In this preferred framework, the magnetic field forces on the system were accounted for by including the Lorentz force in the momentum equation and deriving the induction equation, which describes how the magnetic field changes over time.

The second part of the equation formulation involved re-evaluating the comprehensive governing equations under the assumption of an ideal fluid (Appendix C). Under this assumption, the fluid is taken to be inviscid, incompressible and infinitely conducting, subsequently leading to the simplified set of governing equations. In the next section, we will show how the simplified governing equations are used as the foundation for deriving the shallow water equations in the MHD framework.

4.6 The shallow water approximation

In nature, when the horizontal extent of a fluid body is greater than its depth, it is defined as a shallow water fluid. Since this definition holds for most water bodies, it led to the formulation of the commonly used shallow water equations (SWEs) (Pedlosky, 1987) derived from the governing equations listed in the preceding section. More specifically, the set of SWEs describes a fluid in a realistic environment with a rigid bottom and a free surface top, which can be deformed. Therefore, unlike other types of fluid dynamics, SWEs account for the variable thickness of the fluid layer due to the free top surface. Consequently, it is necessary to derive an additional equation that describes the variation in layer thickness over time.

Furthermore, since the SWEs are derived from the governing equations, an ideal fluid is considered in the derivation, simplifying the momentum equation since viscosity can be ignored and constant density is assumed. Hence, the only equations the shallow water approximation will impact include viscosity or density, whilst any magnetic field terms or equations remain unaffected. Therefore, for simplicity, we will temporarily omit the Lorentz force in the simplified MHD momentum equation, eq.(4.69), and the induction equation from this part of the derivation. However, this magnetic term and equation will be added back to the set of shallow water equations in their original form at the end of the chapter.

4.6.1 Shallow water momentum equation

To formulate the momentum equation under the shallow water approximation, it is useful to consider eq.(4.69) as the starting point. However, it could be simplified for this section by omitting the last term on the right-hand side of the equation that is associated with the Lorentz force due to the magnetic field. This is because the shallow water approximation would not affect this term and could be added back at the end of this section after the changes to the remaining terms have been made. Therefore, the following simplified momentum equation will be used to apply the shallow water approximation

$$\rho\left(\frac{\partial \mathbf{v}}{\partial t} + 2\boldsymbol{\Omega}\times\mathbf{v}\right) = \rho\boldsymbol{g} - \nabla\boldsymbol{p}. \tag{4.71}$$

The first step in applying the shallow water approximation is to write the momentum equation in component form for each direction. For this step, it is best to consider each term individually.

Coriolis force in component form

Start by considering the components of the two vectors used to describe the Coriolis force, the angular rotation vector, $\boldsymbol{\Omega}$ (Vallis, 2006, p.66)

$$\boldsymbol{\Omega} = (0,\, \Omega\cos\Theta,\, \Omega\sin\Theta), \tag{4.72}$$

where, Θ is latitude, and the velocity vector, $\mathbf{v}$, given by

$$\mathbf{v} = (v_x, v_y, v_z). \tag{4.73}$$

The acceleration due to the Coriolis force can then be determined by evaluating the curl of these vectors as follows

$$2\mathbf{\Omega} \times \mathbf{v} = \begin{vmatrix} \boldsymbol{i} & \boldsymbol{j} & \boldsymbol{k} \\ 0 & 2\Omega\cos\Theta & 2\Omega\sin\Theta \\ v_x & v_y & v_z \end{vmatrix} \tag{4.74}$$

$$= (2\Omega v_z \cos\Theta - 2\Omega v_y \sin\Theta)\,\boldsymbol{i} - (-2\Omega v_x \sin\Theta)\,\boldsymbol{j} + (-2\Omega v_x \cos\Theta)\,\boldsymbol{k}. \tag{4.75}$$

However, eq.(4.75) can be simplified by applying the shallow water approximation, which requires that the vertical components of both the velocity and the Coriolis force are negligible (Horstmann et al., 2022), such that

$$v_z \approx v_x \cos\Theta \approx 0. \tag{4.76}$$

Equation (4.75) subsequently becomes

$$2\mathbf{\Omega} \times \mathbf{v} = (-2\Omega\sin\Theta v_y,\, 2\Omega\sin\Theta v_x,\, 0). \tag{4.77}$$

Furthermore, only the component of the rotation vector perpendicular to the sphere will affect fluid motion, and it is, therefore, the only component of importance. Then, by recalling eq.(B.6), which defined the Coriolis parameter as $f = 2\Omega\sin\Theta$, substituting it into eq.(4.77) resulting in

$$\boxed{2\mathbf{\Omega} \times \mathbf{v} = (-fv_y,\, fv_x,\, 0)}\,. \tag{4.78}$$

From this point, eq.(4.78) can be expanded by applying either the $f-$ or β-plane approximations for the Coriolis parameter.

Coriolis parameter approximation

Since Rossby waves are planetary waves, they are influenced by rotation and the latitudinal variation of f. Therefore, the simplistic ***f*-plane approximation**, which assumes a constant value for the vertical component of the rotation vector for all latitudes, would not capture the essential dynamics involved in Rossby waves. Thus, the β-plane approximation should be considered instead.

The **$\boldsymbol{\beta}$-plane approximation** is derived by assuming a slight variation in latitude, such that $\Theta = \Theta_0 - \Theta_1$, where Θ_0 is the initial latitude, and Θ_1 is the perturbed latitude which can be written as $\Theta_1 = y/R$, from geometry, where R is the radius of the Earth. The Coriolis parameter can then be approximated by using the Taylor expansion to only the first approximation around the reference latitude, Θ_0, as follows

$$f = 2\Omega \sin\Theta_0 + 2\Omega \frac{y}{R} \cos\Theta_0 + \dots . \tag{4.79}$$

Then, the first term can be expressed as

$$f_0 = 2\Omega \sin\Theta_0, \tag{4.80}$$

and the second term can be simplified by defining

$$\boxed{\beta = \frac{2\Omega}{R} \cos\Theta_0}, \tag{4.81}$$

to get the approximation of the Coriolis parameter as

$$f = f_0 + \beta y. \tag{4.82}$$

The linear βy term in eq.(4.82) will account for the latitudinal variation of the Coriolis parameter and subsequently capture the fundamental effect of the Earth's curvature on Rossby wave propagation.

The Coriolis parameter can be simplified further according to the latitude under consideration. For low latitudes, $\Theta_0 = 0°$, eq.(4.82) reduces to

$$f \approx \beta y, \tag{4.83}$$

which describes the equatorial β-plane (Vallis, 2006 p.347). For mid-latitudes, the Coriolis parameter can be approximated as

$$f \approx f_0, \tag{4.84}$$

since in this region $f_0 \gg \beta y$ (Zaqarashvili et al., 2007). Lastly, for the polar regions, the second term in eq.(4.82) is small (Cai et al., 2021) and setting $\Theta_0 = 90°$, then f simplifies to

$$f \approx 2\Omega. \tag{4.85}$$

Nevertheless, the β-plane approximation is applied to the momentum equation by keeping $f = f_0 + \beta y$. By then also expanding the acceleration terms on the left-hand side of the momentum equation and taking into consideration that gravity only acts in the vertical direction, the component form of the momentum equation is written as

$$\rho\left(\frac{\partial v_x}{\partial t} - f v_x\right) = -\frac{\partial p}{\partial x}, \tag{4.86a}$$
$$\rho\left(\frac{\partial v_y}{\partial t} + f v_y\right) = -\frac{\partial p}{\partial y}, \tag{4.86b}$$
$$\rho\left(\frac{\partial v_z}{\partial t}\right) = -\rho g - \frac{\partial p}{\partial z}. \tag{4.86c}$$

Since the acceleration terms of the momentum equation have been addressed, the pressure, density, and gravitational force terms will be explored in the shallow water approximation in the following section.

Pressure, density and gravitational force

Since the **Boussinesq approximation**[4] utilises the smallness of fluid density variations (Vallis, 2006) and is suitable for thin layers (Mihaljan, 1962); it can be used to simplify eq.(4.86a)-(4.86c) further. Specifically, the Boussinesq approximation assumes that constant density, ρ_0, is considered except when referred to in the buoyancy term, ρg. The buoyancy term is included in the vertical momentum equation, and the associated density, ρ, is temperature and pressure-dependent. Therefore, when applying the Boussinesq approximation, the density in all other terms in the momentum equations above can be replaced by the constant density (Gilman, 2000), and we divide it throughout to give

$$\frac{\partial v_x}{\partial t} - f v_x = -\frac{1}{\rho_0}\frac{\partial p}{\partial x}, \tag{4.87a}$$
$$\frac{\partial v_y}{\partial t} + f v_y = -\frac{1}{\rho_0}\frac{\partial p}{\partial y}, \tag{4.87b}$$
$$\frac{\partial v_z}{\partial t} = -\frac{\rho}{\rho_0} g - \frac{\partial p}{\partial z}. \tag{4.87c}$$

[4]The anelastic approximation is similar to the Boussinesq approximation but more suitable for thicker layers with large density variations, which is not considered in this study.

We will set $\rho/\rho_0 = \rho$ in eq.(4.87c) to simplify the mathematical notation, which is valid since the density variation is small.

Since we are deriving the SWEs, the thickness of the fluid layer should play an important role. A fluid layer can be characterised as a shallow fluid when the horizontal scale is much larger than the vertical scale. The result of such an environment is that the horizontal velocities are often more dominant than the vertical velocities. Another consequence of the large horizontal scale compared to the vertical scale is a balance between gravity and pressure, called **hydrostatic balance**, which can be assumed despite small vertical motions (Gilman, 2000). The effect of this assumption becomes evident in the vertical component of the equation of motion.

Under the hydrostatic balance assumption, the vertical acceleration term on the left-hand side of eq.(4.87c) is considered negligible. This means that the gravitational term is balanced by the pressure term for the vertical component of the equation of motion (Gilman, 1969), and therefore, the vertical momentum equation can be written as

$$\frac{\partial p}{\partial z} = -\rho g, \tag{4.88}$$

to a good approximation. However, not only the vertical component of the momentum equations is affected by pressure, but also the horizontal components. Let us examine the relevant dynamics to determine how.

Given eq.(4.88) and the fact that the density is assumed to be constant, we can integrate this equation with respect to z to get a function for pressure as follows

$$p(x, y, z, t) = -\rho\, gz + C(x, y, t), \tag{4.89}$$

where C is the integration constant. Moreover, when considering a fluid with a height of $h(x, y, t)$, the hydrostatic balance also assumes that the pressure at the top of the fluid surface is zero. Thus $p = 0$ at $z = h$, which allows eq.(4.89) to be written as

$$p = -\rho g(z - h). \tag{4.90}$$

The next step is to determine the horizontal pressure gradient for the horizontal momentum equations. By then applying $\nabla = \left(\frac{\partial}{\partial x}, \frac{\partial}{\partial y}\right)$ to eq.(4.90) it follows that

$$\nabla p = -\rho g \nabla z + \rho g \nabla h. \tag{4.91}$$

Dividing with density and dropping the first term as the vertical direction is not being considered, eq.(4.91) simplifies to

$$\frac{\nabla p}{\rho} = g \nabla h. \tag{4.92}$$

Now, substituting eq.(4.92) into eq.(4.87a) and eq.(4.87b) the simplified set of the horizontal momentum equations become

$$\frac{\partial v_x}{\partial t} - f v_x = -g \frac{\partial h}{\partial x}, \tag{4.93a}$$

$$\frac{\partial v_y}{\partial t} + f v_y = -g \frac{\partial h}{\partial y}. \tag{4.93b}$$

Next, by first adding the Lorentz force term, $1/\mu_0(\nabla \times \mathbf{B}) \times \mathbf{B}$, back to the right-hand side of the momentum equation and then by recalling that we must divide this term and the others on the left-hand side of the momentum equation with density, the vector form of the horizontal momentum equation can be written as

$$\boxed{\frac{\partial \mathbf{v}}{\partial t} + 2\mathbf{\Omega} \times \mathbf{v} = \frac{1}{4\pi\rho}(\nabla \times \mathbf{B}) \times \mathbf{B} - \boldsymbol{g} \nabla h}. \tag{4.94}$$

However, in eq.(4.94), the $1/\mu$ is replaced with its equivalent value of $1/4\pi$ for simplicity.

At this point, the existing formulation of the respective momentum equations introduces the height variable into the governing SWEs as indicated by the h in eq.(4.94). Next, we will consider how the continuity equation changes with the change in topography considered in the shallow water environment.

4.6.2 Shallow water continuity equation

The derivation of the shallow water mass continuity equation presented in this section, which includes the fluid height as a variable, is given by Vallis (2019, p.65). To derive how mass is conserved when the top surface of the fluid is allowed to be deformed, it is helpful to examine the behaviour of a fluid column within the fluid body as depicted in Fig.(4.4). Let the height of the fluid column be h, and the cross-sectional area be given by A. Assume the fluid column moves to the right in the horizontal x direction.

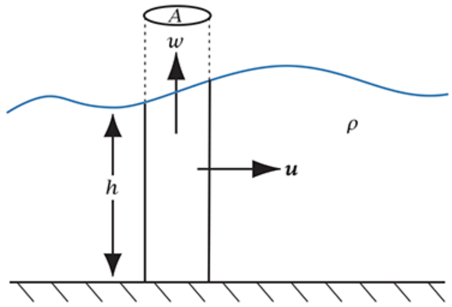

Figure 4.4: The conservation of mass for a fluid column with a surface area A situated in a flat-bottomed shallow-water system. The fluid depth and density are given by h and ρ, respectively. The fluid velocity vector is $\boldsymbol{u}$, and the fluid column height will increase in the w-direction after mass flux increases. Image courtesy of Vallis (2019, p.65).

Recall eq.(4.11), which says that mass is the product of density times volume, then it follows that the mass within the fluid column is given by

$$\int_A \rho_0 h \, dA. \tag{4.95}$$

If, by advection, there is an increase in the average flow rate (net flux) across the boundary of the fluid column, it must only be considered in the fluid column's mass for the balance to be maintained. This increase in mass is accomplished by increasing the height of the fluid column. However, the inflow of mass flux entering through the area of the vertical boundary of the water column, S, is given by

$$F_{massflux} = -\int_s \rho_0 \mathbf{u} \cdot dS. \tag{4.96}$$

Furthermore, the surface area of the column can also be written as $h\boldsymbol{n}\delta l$, which represents the small elements of the area. Here, δl is the line element that bounds the fluid column, and $\boldsymbol{n}$ is the outwards pointing unit vector that is perpendicular to the fluid column boundary, such that

$$F_{massflux} = -\oint \rho_0 h \boldsymbol{u} \cdot \boldsymbol{n} \, dl. \tag{4.97}$$

The dot product of $\boldsymbol{u} \cdot \boldsymbol{n}$ ensures that only the component of velocity that is normal to the fluid column surface contributes to the mass flux. By using the 2D divergence theorem eq.(4.97) can be simplified to

$$F_{massflux} = -\int_A \nabla \cdot (\rho_0 h \mathbf{u})\, dA, \tag{4.98}$$

where the integral is taken over the fluid column's cross-sectional area. As explained earlier, this increase in mass flux, eq.(4.98), must correspond to an increase in the height of the fluid column, which is given as

$$F_{height} = \frac{d}{dt}\int \rho_0\, dV. \tag{4.99}$$

However, taken that $dV = h\, dA$, eq.(4.99) can be written as

$$F_{height} = \frac{d}{dt}\int_A \rho_0\, h\, dA = \int_A \rho_0 \frac{\partial h}{\partial t} dA. \tag{4.100}$$

Finally, because the fluid density, ρ_0, is constant, the balance between eq.(4.98) and eq.(4.100) gives

$$\int_A \left[\frac{\partial h}{\partial t} + \nabla \cdot (h\mathbf{u})\right] dA = 0, \tag{4.101}$$

and considering that the area is arbitrary, the integral should vanish such that

$$\boxed{\frac{\partial h}{\partial t} + \nabla \cdot (h\mathbf{u}) = 0}, \tag{4.102}$$

which is defined as the continuity equation for a shallow-water system.

4.6.3 Conservation of magnetic flux under the shallow water approximation

To determine how the divergence-free condition, $\nabla \cdot \mathbf{B} = 0$, is written for the shallow water approximation, we consider the HD assumption that the top of a fluid surface is a material surface. This implies that the particles comprising the fluid surface are part of the fluid itself. When this assumption is applied to a magnetic field, it describes a system that restricts the behaviour of a magnetic field. It specifically states that when the fluid surface initially contains a magnetic field, it will remain so and will remain parallel to the local free surface (Gilman, 2000). The divergence-free condition, therefore, becomes

$$\nabla \cdot \big[(1+h)\mathbf{B}\big] = 0, \tag{4.103}$$

which can be simplified by recalling, $\nabla \cdot \mathbf{B} = 0$, such that

$$\cancelto{0}{\nabla \cdot \mathbf{B}} + \nabla(\cdot h\mathbf{B}) = 0, \tag{4.104}$$

and we get

$$\boxed{\nabla \cdot (h\mathbf{B}) = 0}. \tag{4.105}$$

Although eq.(4.105) agrees with the ideal MHD framework, it has important consequences worth mentioning. This formulation of magnetic field behaviour excludes the possibility of a magnetic flux transfer across the upper boundary of the fluid layer either by magnetic buoyancy or diffusion (Gilman, 2000). This assumption does not significantly affect our results since we only consider the stable lower layer of the tachocline in this study. However, this assumption can be detrimental when considering the magnetic field within the unstable upper tachocline and when the solar dynamo is considered as a whole. This is because the magnetic field within the upper tachocline is not trapped and does cross the layer boundary as it enters the convection zone due to the buoyancy of magnetic field lines. Therefore, this assumption must be reconsidered for more unstable solar layers or when more realistic solar models are required.

4.7 Summary

In this chapter, we have derived three sets of governing equations. The individual equations describe the plasma motion within the solar tachocline (equation of motion), how the magnetic field changes over time (induction equation), capture the conservation of mass and magnetic flux (continuity equation) and include the divergence-free condition of a magnetic field (Gauss's law).

The first comprehensive set of governing equations was derived from the simplistic hydrodynamic framework. This set of equations was adapted to include the effect of a magnetic field on the system dynamics and considered a rotating frame of reference. More specifically, the momentum equation included gravity, pressure, viscosity forces and the Lorentz force due to the magnetic field present. Below is a summary of this comprehensive set of governing equations.

Comprehensive governing equations

HD momentum equation in a rotating frame of reference

$$\rho\Big[\underbrace{\frac{\partial \mathbf{v}}{\partial t} + (\mathbf{v}\cdot\nabla)\mathbf{v}}_{\text{Fluid acceleration}} + \underbrace{2\boldsymbol{\Omega}\times\mathbf{v}}_{\text{Coriolis force}}\Big] = \overbrace{\rho\boldsymbol{g}}^{\text{Gravity}} \; \overbrace{-\nabla\boldsymbol{p}}^{\text{Pressure}} + \overbrace{\nu\nabla^2\mathbf{v}}^{\text{Viscosity}} \tag{4.39}$$

Comprehensive governing MHD equations in a rotating frame

Momentum $$\rho\left[\frac{\partial \mathbf{v}}{\partial t} + (\mathbf{v}\cdot\nabla)\mathbf{v} + 2\boldsymbol{\Omega}\times\mathbf{v}\right] = \rho\boldsymbol{g} - \nabla\boldsymbol{p} + \nu\nabla^2\mathbf{v} + \underbrace{\frac{1}{\mu_0}(\nabla\times\mathbf{B})\times\mathbf{B}}_{\text{Lorentz force}} \tag{4.43}$$

Induction $$\frac{\partial \mathbf{B}}{\partial t} = \nabla\times(\mathbf{v}\times\mathbf{B}) \tag{4.53}$$

Continuity $$\frac{\partial \rho}{\partial t} - \nabla\cdot(\rho\mathbf{v}) = 0 \tag{4.67}$$

Divergence-free condition $$\nabla\cdot\mathbf{B} = 0 \tag{4.70}$$

Subsequently, the comprehensive governing MHD equations given above were simplified by considering an ideal fluid that is inviscid, incompressible and infinitely conducting, resulting in the equations summarised below. This ideal fluid assumption impacted the momentum equation such that the viscosity term is no longer present, and the continuity equation has also been simplified. The summary of these simplified governing equations is given below.

Simplified governing MHD equations in a rotating frame

Momentum $$\rho\left[\frac{\partial \mathbf{v}}{\partial t} + 2\boldsymbol{\Omega}\times\mathbf{v}\right] = \rho\boldsymbol{g} - \nabla\boldsymbol{p} + \frac{1}{\mu_0}(\nabla\times\mathbf{B})\times\mathbf{B} \tag{4.69}$$

Induction $$\frac{\partial \mathbf{B}}{\partial t} = \nabla\times(\mathbf{v}\times\mathbf{B}) \tag{4.53}$$

Continuity $$\nabla\cdot\mathbf{v} = 0 \tag{4.68}$$

Divergence-free condition $$\nabla\cdot\mathbf{B} = 0 \tag{4.70}$$

Finally, the more overarching shallow water approximation was applied to the simplified MHD governing set of equations. This commonly used approximation is appropriate when the horizontal dimension of a fluid under consideration is much larger than its depth. This approximation also accommodates an environment with a rigid bottom and a free upper surface that can deform. As a result, the layer thickness, h, enters the governing equations as a variable. Furthermore, the shallow water approximation is associated with three other approximations: the β-plane -, Boussinesq - and hydrostatic balance approximation. In summary, we will briefly state why these approximations are particularly important.

After Gilman (2000) derived the MHD shallow water equations, Schecter et al. (2001) used these equations to study the shallow water waves in the solar tachocline. However, because the f-plane approximation was applied, large-scale planetary waves, such as Rossby waves, were prevented from appearing in their solutions. To correct this, Zaqarashvili et al. (2007) used the β-plane approximation, which resulted in solutions associated with Rossby waves, among other solar waves. Consequently, when large-scale waves are important, the β-plane approximation is better suited and will be used when deriving the Rossby wave model using the set of shallow water governing equations.

The tachocline was defined earlier (Section 3.5.2) as a very thin layer (Spiegel and Zahn, 1992). As a result, the horizontal dimension of the fluid is much larger than that of the vertical; therefore, the vertical velocity of the fluid flow can be considered negligible (Gilamn, 2000). Since pressure varies with depth, this shallow fluid structure further assumes that pressure can be considered constant over the horizontal plane, referred to as a system in hydrostatic balance. However, it should be mentioned that the hydrostatic balance approximation inherently assumes that the fluid is static and does not account for dynamic effects, such as acceleration or turbulence. Nevertheless, since the Sun has been shown to exhibit slow rotation (Section 4.2.3), and because the solar tachocline is considered a stable layer compared to, for example, the convection zone, this approximation is acceptable for this specific region of the Sun.

Lastly, the Boussinesq approximation is also particularly well suited for modelling waves with wavelengths much greater than the depth of the water. Therefore, this approximation is commonly applied to shallow-water systems and has two favourable consequences for this study. As a result, the momentum equation is simplified by applying the Boussinesq approximation and assuming hydrostatic balance. Moreover, by applying the Boussinesq approximation, the behaviour of acoustic waves, which are not considered in this work, is not captured in the governing equation solutions (Hood and Hughes, 2011). Thus, the Boussinesq approximation is useful for isolating and analysing Rossby waves in the tachocline.

On the contrary, the induction equation and the Lorentz force of the momentum equation remain unchanged when the shallow water approximation is applied to the simplified governing MHD equations. This can be explained by considering how varying layer thickness would impact the magnetic field strength. Assuming that the magnetic field is orientated such that it is parallel to the surface of the fluid, then the fluid depth will determine the distance between the respective magnetic field lines. Moving magnetic field lines closer to each other will increase the magnetic field strength compared to weakening the field if the field lines are spread out more. Therefore, the magnetic field strength is dependent on the fluid depth. However, since the fluid layer is considered sufficiently thin, the changes in the magnetic field strength due to varying thickness will not cause any noticeable changes in the magnetic field strength. Thus, the magnetic field terms and equations stay the same. Therefore, the shallow water momentum and continuity equations were derived using the approximations summarised above and are given below.

Shallow water MHD equations in a rotating frame

Momentum equation
$$\frac{\partial \mathbf{v}}{\partial t} + 2\boldsymbol{\Omega} \times \mathbf{v} = \frac{1}{4\pi\rho}(\nabla \times \mathbf{B}) \times \mathbf{B} - \boldsymbol{g}\nabla h \tag{4.94}$$

Induction equation
$$\frac{\partial \mathbf{B}}{\partial t} = \nabla \times (\mathbf{v} \times \mathbf{B}) \tag{4.53}$$

Continuity equation
$$\frac{\partial h}{\partial t} + \nabla \cdot (h\mathbf{v}) = 0 \tag{4.102}$$

Divergence-free condition
$$\nabla \cdot (h\mathbf{B}) = 0 \tag{4.105}$$

It should also be noted that the Lorentz force can also be written in the form of

$$\frac{1}{\mu_0}(\nabla \times \mathbf{B}) \times \mathbf{B} = \frac{1}{4\pi}\left[-\frac{1}{2}\nabla |B|^2 + (\mathbf{B} \cdot \nabla)\mathbf{B}\right], \tag{4.106}$$

where $\mu_0 \approx 4\pi$. Then, notice that the first term on the right-hand side of eq.(4.107) represents the gradient of the magnetic field magnitude squared, thus describing the spatial variation of this parameter. However, when a uniform or near-uniform magnetic field is being considered, such as in our case, the variation in the magnetic field magnitude should be minimal and thus will cause the gradient term to be zero or close to zero. Therefore, the $\frac{1}{2}\nabla|B|^2$ term can be ignored in this study, and we have the simplified term as

$$\frac{1}{\mu_0}(\nabla \times \mathbf{B}) \times \mathbf{B} = \frac{1}{4\pi}(\mathbf{B} \cdot \nabla)\mathbf{B}. \tag{4.107}$$

Nonetheless, now that the set of simplified governing equations and their shallow-water counterparts have been derived, we can contextualise them and show how the Rossby wave model has been derived throughout the existing literature using these respective sets of equations. Next, in Part II of this work will use these different sets of governing equations to derive three unique MHD Rossby wave models (Zaqarashvili et al., 2007; 2009, 2010, Gurgenahsvili et al., 2016).

Part II

Magnetohydrodynamic (MHD) Rossby wave models

Literature Review IV: Overview

This study aims to measure the comprehensiveness of the MHD Rossby wave model by how closely it reflects reality. Including more forces associated with the physical dynamics of the environment being studied is expected to enhance the model's comprehensiveness. Therefore, each chapter in Part II will showcase a model enhancement, demonstrating the progression of the MHD Rossby wave model over time.

Chapter 5 will begin with the simplest MHD Rossby wave model derived in Cartesian coordinates (Zaqarashvili et al., 2007). However, since Rossby waves are planetary waves spanning the globe, it has been suggested (Zaqarashvili et al., 2007) that spherical coordinates are more suitable for this problem. Hence, the MHD Rossby wave models in the tachocline will be derived in spherical coordinates. This study subsequently identifies three specific MHD Rossby wave models in spherical coordinates, which will be discussed in detail. The first model, referred to as the "base model" (Zaqarashvili et al., 2007), is the spherical counterpart of the model derived in Chapter 5. This name is chosen because the model does not account for the solar-specific latitudinal differential rotation (LDR) phenomenon but only considers the presence of a magnetic field. Zaqarashvili et al. (2009) enhanced the base model by including reduced gravity and considering the fluid layer thickness in Chapter 6. Finally, in the last model derived in Chapter 7, the effect of the LDR was taken into account (Zaqarashvili et al., 2010; Gurgenashvili et al., 2016).

The chapters for each model will include the relevant assumptions and modelling required to arrive at the equations for the MHD Rossby wave dispersion relation, phase and group velocities. Since we will use the governing equations derived in Chapter 4, all the assumptions made throughout the preceding sections will apply to the rest of the equations unless stated otherwise. Therefore, any unique approximation to one of the models below will be stated explicitly.

Regarding the resulting propagation properties, it is worth noting that two directions are involved: the toroidal and poloidal directions illustrated in Fig.(2.6). When considering a small localised area on the torus, the poloidal direction and its associated wavenumber correspond to movement in the vertical direction. The poloidal wavenumber is noted by

k_y and n in the Cartesian and spherical coordinate systems, respectively. On the contrary, the toroidal wavenumber describes wave propagation in the horizontal direction or direction of rotation, noted by k_x or m. Since the Sun's magnetic field is primarily in the toroidal direction at lower latitudes, it hinders vertical wave propagation due to the magnetic tension force described in Section A.3. Thus, the toroidal direction and its associated wavenumber will be of greater importance in the study of Rossby wave propagation. Additionally, the poloidal direction would be of greater importance in regions where the poloidal magnetic field is more dominant, such as the Sun's polar regions, which are not considered in this study due to the lack of solar activity. Hence, the poloidal direction will not be considered for the propagation properties.

Furthermore, only the dispersion relation is of interest for this research. However, since the equations for phase and group velocity can be derived easily from the dispersion relation, they have been included in the respective equation summaries to present all the propagation properties for completeness. Moreover, it should be noted that these respective velocity equations are used to predict the active regions on the Sun's surface, as Dikpati (2020) stated, making them relevant in the bigger picture. With this brief overview of the progression of the Rossby wave model and an explanation of why we only focus on the toroidal direction of MHD Rossby wave models in the lower tachocline, we can start with the derivation of the first model.

5 Base MHD Rossby wave model

5.1 Introduction

In the preceding chapter, the comprehensive, simplified and shallow water magnetohydrodynamic (MHD) governing equations have been derived, as well as the variation of these equations due to the application of the shallow water approximation. One of the goals of this study is to identify the most realistic MHD Rossby wave model that includes all the essential layer dynamics and forces associated with the solar tachocline, which is then referred to as the comprehensive model. To this end, in this second part of this study, we aim to derive three existing MHD Rossby wave models in the tachocline environment, using the various sets of governing equations derived in Chapter 4. Furthermore, to address the problem statement related to the model's comprehensiveness, the characteristics and parameters of the corresponding wave propagation property equations will be briefly examined.

Moreover, as previously mentioned, the development of any mathematical model is expected to start by considering the simplest case. Therefore, it is necessary to explain the mathematical framework that will be considered to derive the first MHD Rossby wave model, starting with identifying the set of governing equations to be used. The MHD shallow water equations (SWEs) were derived in the more appropriate rotating frame of reference in Section 4.6 (Zaqarashvili et al., 2007). Furthermore, considering that the solar tachocline can be treated as a thin fluid layer with a rigid bottom and a free top surface in a magnetic field (Spiegel and Zahn, 1992), the generalised MHD SWEs (Gilman, 2000) are well-suited to study wave dynamics in this environment. Zaqarashvili et al. (2007) were the first to use this set of governing equations to study the impact of a toroidal magnetic field on the dynamics of solar MHD Rossby waves in the tachocline.

By recalling that this is the first and most simplistic (base) model under consideration, it is necessary to provide context for its limitations. In Section 3.5.2, the fundamental difference in the characteristics of the upper and lower tachocline was introduced, which requires them to be studied separately (Gilman, 2000). However, since the base model (Zaqarashvili et al.,

2007) is expected to make more assumptions and simplifications, it is acceptable to consider the two tachocline layers as one for this initial derivation.

Also, it has previously been argued that the spherical coordinate system is more appropriate for studying large-scale waves (Section 4.1). However, Zaqarashvili et al. (2007) initially used SWEs in Cartesian coordinates because they are mathematically simpler. They further argued that when examining perturbations on a sphere with a much smaller spatial scale than the sphere's radius, the curvature can be neglected, and Cartesian coordinates can be utilised. The orientation of the Cartesian coordinates (x, y, z) considered for the derivation of the base model is illustrated in Fig.(A.5).

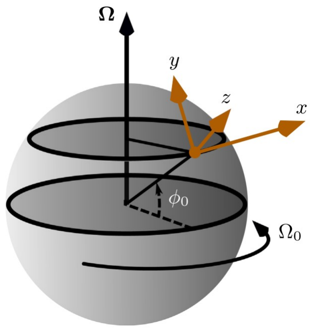

Figure 5.1: Cartesian coordinates orientation, where x is in the direction of rotation, y points to the north and z is directed outwards (Horstmann et al. 2022).

Here, x is in the direction of rotation, also called the zonal or toroidal direction. Conversely, y points to the north, also called the meridional or poloidal direction, and z is orientated directly outwards. The third and last limitation of the base model is that any more complex solar dynamics, such as latitudinal differential rotation (Section 3.5.1), were not considered.

5.2 Derivation of the base model in Cartesian coordinates

Let us consider a shallow water environment consisting of a thin layer of an ideal fluid on a sphere rotating with a given angular velocity, Ω_0. The shallow water fluid system can further be described as having a free upper surface that can deform, contrary to the rigid base. Furthermore, the medium density, ρ, can also be considered constant as the stratification scale height of the fluid is larger than the tachocline's undisturbed layer thickness. With this in mind, and considering the presence of a horizontal uniform magnetic field[1], the MHD Rossby wave model can now be derived using the MHD SWEs.

The momentum eq.(4.94), induction eq.(4.53), and continuity eq.(4.102) associated with the MHD shallow water approximation (Section 4.6) are repeated below

$$
\begin{aligned}
&\text{Momentum equation} && \frac{\partial \mathbf{v}}{\partial t} + 2\boldsymbol{\Omega} \times \mathbf{v} = \frac{1}{4\pi\rho} \left(\mathbf{B} \cdot \nabla\right) \mathbf{B} - g\, \nabla h, \\
&\text{Induction equation} && \frac{\partial \mathbf{B}}{\partial t} = \nabla \times \left(\mathbf{v} \times \mathbf{B}\right), \\
&\text{Continuity equation} && \frac{\partial h}{\partial t} + \nabla \cdot (h\mathbf{v}) = 0,
\end{aligned}
$$

where $\boldsymbol{\Omega}$ is the rotation rate, g the gravitational acceleration. Furthermore, as characterised by the shallow water formulation, the layer thickness, h, is included, and the horizontal velocity and magnetic field are represented by $\mathbf{v}$ and $\mathbf{B}$, respectively. Finally, in this chapter, we will consider the horizontal gradient operator given by

$$
\nabla = \frac{\partial}{\partial x}\hat{\boldsymbol{\imath}} + \frac{\partial}{\partial y}\hat{\boldsymbol{\jmath}}, \tag{5.1}
$$

since only the horizontal behaviour of the waves is of interest.

This MHD shallow water set of non-linear partial differential equations (PDEs) can be approximated by linear terms. This requires us to assume that the magnetic field, velocity and density exhibit a small perturbation from the equilibrium state, which is dependent on time, t, and position, r, such that

$$
\mathbf{B} = \mathbf{B}_0 + \mathbf{B}_1(r,t), \tag{5.2a}
$$

$$
\mathbf{v} = \mathbf{v}_0 + \mathbf{v}_1(r,t) = \mathbf{v}_1(r,t), \tag{5.2b}
$$

$$
\rho = \rho_0 + \rho_1(r,t), \tag{5.2c}
$$

$$
h = H_0 + H_1(r,t), \tag{5.2d}
$$

where the subscripts 1 and 0 correspond to the perturbation and equilibrium states, respectively. In contrast to the perturbation terms, the equilibrium state is considered a constant

[1]When the magnetic field lines are equally spaced and parallel to one another such that the strength of the magnetic field remains *constant* throughout the area.

value. Nevertheless, the simplified eq.(5.2b) requires further explanation. Recall that Zaqarashvili et al. (2007) focused solely on the changes in the solar tachocline waves due to the magnetic field. Therefore, the effect of a significant background flow, $\mathbf{v}_0$, on the wave dynamics should be minimised. To this end, its value is set to zero, $\mathbf{v}_0 = 0$, giving the simplified equation for the linearised velocity to be equal to $\mathbf{v}_1(r, t)$.

Furthermore, Zaqarashvili et al. (2007) defined the unperturbed magnetic field strength as

$$\mathbf{B}_0 = (B_x, 0, 0), \tag{5.3}$$

whereas the horizontal perturbation of the magnetic field strength and the velocity are expressed as

$$\mathbf{B}_1 = (b_x, b_y, 0), \tag{5.4}$$

$$\mathbf{v}_1 = (v_x, v_y, 0). \tag{5.5}$$

Equation (5.2a)-(5.5) will be used to linearise the MHD SWEs, eq.(4.94)-(4.102), which is subsequently written in component form, starting with the induction equation, eq.(4.53).

5.2.1 Linearised induction equation

Substituting the associated variables, $\mathbf{B}$ and $\mathbf{v}$ from eq.(5.2a) and eq.(5.2b), respectively, into the induction equation, eq.(4.53), that is repeated below for convenience,

$$\frac{\partial \mathbf{B}}{\partial t} = \nabla \times (\mathbf{v} \times \mathbf{B}),$$

such that we get

$$\frac{\partial}{\partial t}(\mathbf{B}_0 + \mathbf{B}_1) = \nabla \times [\mathbf{v}_1 \times (\mathbf{B}_0 + \mathbf{B}_1)]. \tag{5.6}$$

Because the unperturbed values are constant, the time derivative of these values will be zero, such that

$$\frac{\partial \mathbf{B}_0}{\partial t} = 0. \tag{5.7}$$

Taking eq.(5.7) into account and multiplying the velocity and magnetic field values inside the brackets, it results in

$$\frac{\partial \mathbf{B}_1}{\partial t} = \nabla \times \left[(\mathbf{v}_1 \times \mathbf{B}_0) + \underbrace{(\mathbf{v}_1 \times \mathbf{B}_1)}_{\text{very small term}} \right]. \tag{5.8}$$

Since the perturbations are defined to be small, any term which multiplies two perturbations can be neglected since it will result in an even smaller value. Therefore, we can neglect the last term on the right-hand side, which gives

$$\boxed{\frac{\partial \mathbf{B}_1}{\partial t} = \nabla \times (\mathbf{v}_1 \times \mathbf{B}_0)}. \tag{5.9}$$

The linearised induction equation, eq.(5.9), can now be written in component form with the help of eq.(5.3) and eq.(5.5). After the substitution, we can first determine the cross-product inside the brackets as

$$\mathbf{v}_1 \times \mathbf{B}_0 = \begin{vmatrix} \hat{\boldsymbol{\imath}} & \hat{\boldsymbol{\jmath}} & \hat{\boldsymbol{k}} \\ v_x & v_y & 0 \\ B_x & 0 & 0 \end{vmatrix} \tag{5.10a}$$

$$= 0\,\hat{\boldsymbol{\imath}} - 0\,\hat{\boldsymbol{\jmath}} + (0 - B_x v_y)\,\hat{\boldsymbol{k}} \tag{5.10b}$$

$$= -B_x v_y\,\hat{\boldsymbol{k}}, \tag{5.10c}$$

which is used to calculate the cross-product with respect to ∇, as follows

$$\nabla \times (\mathbf{v}_1 \times \mathbf{B}_0) = \nabla \times (-B_x v_y\,\hat{\boldsymbol{k}}) \tag{5.11a}$$

$$= \begin{vmatrix} \hat{\boldsymbol{\imath}} & \hat{\boldsymbol{\jmath}} & \hat{\boldsymbol{k}} \\ \frac{\partial}{\partial x} & \frac{\partial}{\partial y} & \frac{\partial}{\partial z} \\ 0 & 0 & -B_x v_y \end{vmatrix} \tag{5.11b}$$

$$= \left(-\frac{\partial}{\partial y} B_x v_y - 0\right)\hat{\boldsymbol{\imath}} - \left(-\frac{\partial}{\partial x} B_x v_y - 0\right)\hat{\boldsymbol{\jmath}} + 0\hat{\boldsymbol{k}} \tag{5.11c}$$

$$= -\frac{\partial}{\partial y} B_x v_y\,\hat{\boldsymbol{\imath}} + \frac{\partial}{\partial x} B_x v_y\,\hat{\boldsymbol{\jmath}} + 0\,\hat{\boldsymbol{k}}. \tag{5.11d}$$

Then, by considering the partial time derivative of eq.(5.4) and eq.(5.11d) for the left and right-hand side of the induction equation, respectively, the component form is written as

$$\frac{\partial b_x}{\partial t} = -B_x \frac{\partial v_y}{\partial y}, \tag{5.12}$$

and

$$\boxed{\frac{\partial b_y}{\partial t} = B_x \frac{\partial v_y}{\partial x}}. \tag{5.13}$$

By further considering the continuity equation for incompressible fluids, eq.(4.68), and expanding it to get

$$\nabla \cdot \mathbf{v} = 0 \Rightarrow \frac{\partial v_x}{\partial x} + \frac{\partial v_y}{\partial y} = 0 \Rightarrow -\frac{\partial v_y}{\partial y} = \frac{\partial v_x}{\partial x}, \tag{5.14}$$

then it follows that the x-component of the induction equation can then be written such that

$$\boxed{\frac{\partial b_x}{\partial t} = B_x \frac{\partial v_x}{\partial x}}, \tag{5.15}$$

indicating that the x-direction is preferred.

5.2.2 Linearised momentum equation

To linearise the momentum equation, we start by considering eq.(4.94), repeated below,

$$\frac{\partial \mathbf{v}}{\partial t} + 2\boldsymbol{\Omega} \times \mathbf{v} = \frac{1}{4\pi\rho} \left(\mathbf{B} \cdot \nabla\right) \mathbf{B} - g\, \nabla h.$$

By recalling that we are considering a constant fluid flow, such that we must set $\mathbf{v}_0 = 0$, it follows that only the perturbed velocity, $\mathbf{v}_1$, is included in the acceleration (first term in eq.(4.94)) and the Coriolis force (second term in eq.(4.94)). As a result the right-hand side of eq.(4.94)) is given by

$$\frac{\partial \mathbf{v}_1}{\partial t} + 2\boldsymbol{\Omega} \times \mathbf{v}_1. \tag{5.16}$$

By further recalling eq.(4.78), given below

$$2\boldsymbol{\Omega} \times \mathbf{v} = \left(-f v_y,\, f v_x,\, 0\right),$$

we can write the component form of eq.(5.16) as follows

$$\frac{\partial \mathbf{v}_1}{\partial t} + 2\boldsymbol{\Omega} \times \mathbf{v}_1 = \frac{\partial}{\partial t}\big(v_x\,\hat{\boldsymbol{\imath}} + v_y\,\hat{\boldsymbol{\jmath}}\big) + (-f v_y\,\hat{\boldsymbol{\imath}} + f v_x\,\hat{\boldsymbol{\jmath}}), \tag{5.17a}$$

$$= \left(\frac{\partial v_x}{\partial t} - f v_y\right)\hat{\boldsymbol{\imath}} + \left(\frac{\partial v_y}{\partial t} + f v_x\right)\hat{\boldsymbol{\jmath}}. \tag{5.17b}$$

Then, eq.(5.3) and eq.(5.4) are substituted into the Lorentz force (first term on the right-hand side of eq.(4.94)) such that

$$(\mathbf{B}\cdot\nabla)\,\mathbf{B} = \big[(\mathbf{B}_0 + \mathbf{B}_1)\cdot\nabla\big]\,(\mathbf{B}_0 + \mathbf{B}_1) \tag{5.18a}$$

$$= \underbrace{(\mathbf{B}_0\cdot\nabla)\mathbf{B}_0}_{\text{constant over space}} + (\mathbf{B}_0\cdot\nabla)\mathbf{B}_1 + \underbrace{(\mathbf{B}_1\cdot\nabla)\mathbf{B}_0}_{\text{constant over space}} + \underbrace{(\mathbf{B}_1\cdot\nabla)\mathbf{B}_1}_{\text{very small term}}, \tag{5.18b}$$

$$= (\mathbf{B}_0\cdot\nabla)\mathbf{B}_1. \tag{5.18c}$$

Here, we must note that $\mathbf{B}_0$ is a constant value directed in the x-direction. Therefore, in this coordinate system, it follows that the first term and third term in eq.(5.18b) can be neglected due to $\partial B_x/\partial x = 0$.

On the other hand, the last term in eq.(5.18b) is the product of two perturbations, which will result in a very small value that can also be ignored. Consequently, we use eq.(5.18c) to write the linearised Lorentz force, given below

$$(\mathbf{B}\cdot\nabla)\,\mathbf{B} = (\mathbf{B}_0\cdot\nabla)\mathbf{B}_1 \tag{5.19a}$$

$$= \left[B_x\,\hat{\boldsymbol{\imath}}\cdot\left(\frac{\partial}{\partial x}\hat{\boldsymbol{\imath}} + \frac{\partial}{\partial y}\hat{\boldsymbol{\jmath}}\right)\right](b_x\,\hat{\boldsymbol{\imath}} + b_y\,\hat{\boldsymbol{\jmath}}), \tag{5.19b}$$

$$= B_x\frac{\partial b_x}{\partial x}\hat{\boldsymbol{\imath}} + B_x\frac{\partial b_y}{\partial x}\hat{\boldsymbol{\jmath}}. \tag{5.19c}$$

Finally, we can write the gravitational force (last term in eq.(4.94)) in component form, such that we get

$$g\nabla h = g\left(\frac{\partial}{\partial x}\hat{\boldsymbol{\imath}} + \frac{\partial}{\partial y}\hat{\boldsymbol{\jmath}}\right)h, \tag{5.20a}$$

$$= g\frac{\partial h}{\partial x}\hat{\boldsymbol{\imath}} + g\frac{\partial h}{\partial y}\hat{\boldsymbol{\jmath}}. \tag{5.20b}$$

In summary, the resulting linearised momentum equation is given by

$$\boxed{\frac{\partial \mathbf{v}_1}{\partial t} + 2\boldsymbol{\Omega} \times \mathbf{v}_1 = \frac{\mathbf{B}_0}{4\pi\rho}\left(\nabla \cdot \mathbf{B}_1\right) - g\,\nabla h}. \tag{5.21}$$

By now, combining the component form of each term derived above, we get the component form of eq.(5.21) as

$$\frac{\partial v_x}{\partial t} - f v_y = \frac{B_x}{4\pi\rho}\frac{\partial b_x}{\partial x} - g\frac{\partial h}{\partial x}, \tag{5.22}$$

$$\frac{\partial v_y}{\partial t} + f v_x = \frac{B_x}{4\pi\rho}\frac{\partial b_y}{\partial x} - g\frac{\partial h}{\partial y}, \tag{5.23}$$

where eq.(5.17b) is on the left-hand side and eq.(5.19c) and eq.(5.20b) are the first and second terms on the right-hand side, respectively.

The associated continuity equation will be considered in the next section to complete the linearisation of the shallow water equations.

5.2.3 Linearised continuity equation

Substituting eq.(5.2b) and eq.(5.2d) into the shallow water continuity equation (or thickness equation), we have

$$\frac{\partial}{\partial t}\left(H_0 + H_1\right) + \nabla \cdot \left[(H_0 + H_1)\mathbf{v}_1\right] = 0, \tag{5.24}$$

which can be simplified by neglecting the product of small terms as well as the first term, given that the time derivative of the unperturbed layer thickness, H_0, is zero. The equation

$$\cancelto{0}{\frac{\partial H_0}{\partial t}} + \frac{\partial H_1}{\partial t} + \nabla \cdot \left[H_0\mathbf{v}_1 + \underbrace{H_1\mathbf{v}_1}_{\text{very small term}}\right] = 0,$$

is then simplified to

$$\boxed{\frac{\partial H_1}{\partial t} + \nabla \cdot \left(H_0\mathbf{v}_1\right) = 0}. \tag{5.25}$$

Now, using the notion where $h = H_1$ indicates the perturbation of the fluid layer thickness (Zaqarashvili et al., 2007) and using the horizontal gradient, eq.(5.1), with eq.(5.5) to evaluate $\nabla \cdot \mathbf{v}_1$, we get the component form of the induction equation as

$$\frac{\partial h}{\partial t} + H_0 \left(\frac{\partial v_x}{\partial x} + \frac{\partial v_y}{\partial y} \right) = 0. \tag{5.26}$$

Then, the linearised MHD shallow water momentum, induction and thickness equations in component form are summarised below.

Linearised MHD shallow water equations in component form

Induction equations

$$\frac{\partial b_x}{\partial t} = B_x \frac{\partial v_x}{\partial x} \tag{5.15}$$

$$\frac{\partial b_y}{\partial t} = B_x \frac{\partial v_y}{\partial x} \tag{5.13}$$

Momentum equations

$$\frac{\partial v_x}{\partial t} - f v_y = \frac{B_x}{4\pi\rho} \frac{\partial b_x}{\partial x} - g \frac{\partial h}{\partial x} \tag{5.22}$$

$$\frac{\partial v_y}{\partial t} + f v_x = \frac{B_x}{4\pi\rho} \frac{\partial b_y}{\partial x} - g \frac{\partial h}{\partial y} \tag{5.23}$$

Continuity equation

$$\frac{\partial h}{\partial t} = -H_0 \left(\frac{\partial v_x}{\partial x} + \frac{\partial v_y}{\partial y} \right) \tag{5.26}$$

5.3 MHD Rossby wave dispersion relation derivation

Let us now derive the MHD Rossby wave dispersion relation as this equation plays an integral role in studying these waves and the solar magnetic field, which is ultimately associated with the severity of space weather events.

The first step is to take the time derivative of the x-component of the momentum equation, eq.(5.22), as follows

$$\frac{\partial^2 v_x}{\partial t^2} - f \frac{\partial v_y}{\partial t} = \frac{B_x}{4\pi\rho} \frac{\partial}{\partial x} \frac{\partial b_x}{\partial t} - g \frac{\partial}{\partial x} \frac{\partial h}{\partial t}. \tag{5.27}$$

Since the Coriolis parameter, f, and gravity, g, are not time-dependent, they are treated as constants and, therefore, not differentiated by time in eq.(5.27).

Now, substitute the time derivative equation for b_x and h using eq.(5.15) and eq.(5.26), respectively into eq.(5.27), such that

$$\frac{\partial^2 v_x}{\partial t^2} - f\frac{\partial v_y}{\partial t} = \frac{B_x^2}{4\pi\rho}\frac{\partial^2 v_x}{\partial x^2} + gH_0\left(\frac{\partial^2 v_x}{\partial x^2} + \frac{\partial^2 v_x}{\partial x \partial y}\right). \tag{5.28}$$

Recall that the Alfvén speed, eq.(3.6) defined in Section 3.10, is a parameter that includes the value of the magnetic field strength, B_0, for which the associated equation is repeated below

$$v_A = \frac{B_0}{\sqrt{4\pi\rho}}$$

and the surface gravity speed is defined as

$$\boxed{C_0 = \sqrt{gH_0}}, \tag{5.29}$$

then we arrive at

$$\frac{\partial^2 v_x}{\partial t^2} - f\frac{\partial v_y}{\partial t} = v_A^2\frac{\partial^2 v_x}{\partial x^2} + C_0^2\left(\frac{\partial^2 v_x}{\partial x^2} + \frac{\partial^2 v_y}{\partial x \partial y}\right). \tag{5.30}$$

Similarly for the y-momentum equation, we take the time derivative of eq.(5.23) followed by the substitution of eq.(5.13) and eq.(5.26) to get

$$\frac{\partial^2 v_y}{\partial t^2} + f\frac{\partial v_x}{\partial t} = v_A^2\frac{\partial^2 v_y}{\partial x^2} + C_0^2\left(\frac{\partial^2 v_x}{\partial x \partial y} + \frac{\partial^2 v_y}{\partial y^2}\right). \tag{5.31}$$

At this point, eq.(5.30) and eq.(5.31) form a system of second-order PDEs and can be simplified by performing a Fourier analysis on the system. A Fourier analysis is commonly used to understand and describe complex wave phenomena as it decomposes complex functions into simpler sinusoidal components, which can be examined more easily. More specifically, the expression for a **plane wave**, $\exp(-i\omega t + ik_x x + ik_y y)$, will be used to describe a wave of constant amplitude and phase spanning over a flat plane, which accurately represents the waves under consideration. In this equation, k_x is the wavenumber for a wavelength of λ_x, such that $k_x = 2\pi/\lambda_x$ and ω represents the wave frequency, similarly for the variables in the y-direction.

Therefore, we perform a Fourier analysis of $\exp(-i\omega t + ik_x x + ik_y y)$ on the system formed by eq.(5.30) and eq.(5.31) and write the resulting equations in matrix notation such that we have

$$A = \begin{bmatrix} -\omega^2 + v_A^2 k_x^2 + C_0^2 k_x^2 & -i\omega f - C_0^2 i k_x \frac{\partial}{\partial y} \\ i\omega f - C_0^2 \frac{\partial}{\partial x} i k_y & -\omega^2 + v_A^2 k_x^2 + C_0^2 k_y^2 \end{bmatrix}.$$

Then, by solving det$A = 0$ and grouping like terms, it yields the following dispersion relation

$$\overbrace{\omega^4 - [2k_x^2 v_A^2 + f_0^2 + C_0^2(k_x^2 + k_y^2)]\omega^2}^{\text{High frequency branch}} + \underbrace{C_0^2 k_x \beta \omega + k_x^2 v_A^2 [k_x^2 v_A^2 + C_0^2(k_x^2 + k_y^2)]}_{\text{Low frequency branch}} = 0, \tag{5.32}$$

that contains both a high and low-frequency solution. In eq.(5.32), the Coriolis parameter, $f = f_0 + \beta y$, is replaced by f_0, see eq.(4.84), because the β-plane approximation for mid-latitudes is applied (Zaqarashvili et al., 2007) such that $f_0 \gg \beta y$. Furthermore, β enters eq.(5.32) as a result of

$$\frac{\partial f}{\partial y} = \beta. \tag{5.33}$$

The high-frequency solution branch stems from the assumption that the ω^4 and ω^2 terms are dominant. Subsequently, the lower-order terms are neglected, resulting in the simplified dispersion relation as follows

$$\omega^2 \left(\omega^2 - \Big[\underbrace{2k_x^2 v_A^2}_{\text{Neglect}(v_A \ll C_0)} + f_0^2 + C_0^2 \left(k_x^2 + k_y^2\right) \Big] \right) = 0. \tag{5.34}$$

Moreover, since the Sun is a slowly rotating star, a small Alfvén speed can be assumed (Zaqarashvili et al., 2007), such that $v_A \ll C_0$, allowing the v_A term to be dropped. The resulting dispersion relation is that of the Poincaré waves

$$\omega^2 = f_0^2 + C_0^2(k_x^2 + k_y^2). \tag{5.35}$$

The dispersion relation of this wave has been included here for completeness, although it will not be discussed as it falls outside the scope of this study.

For the low-frequency branch of eq.(5.32) we consider the terms with ω^2 and ω and dividing by $C_0^2(k_x^2 + k_y^2)$ gives the following dispersion relation

$$\omega^2 + \frac{k_x \beta}{k_x^2 + k_y^2}\omega - k_x^2 v_A^2 = 0. \tag{5.36}$$

The frequency and wavenumber present in eq.(5.36) indicate that the solutions to the dispersion relation depend on the values for the ω and k_x parameters. The first behavioural split occurs when considering long (small k_x values) or short wavelengths (large k_x values). The solution that corresponds to short wavelengths gives the dispersion relation for Alfvén waves as

$$\omega^2 - k_x^2 v_A^2 = 0 \;\Rightarrow\; \omega = \pm k_x v_A^2, \tag{5.37}$$

which are significantly affected by the magnetic field.

On the other hand, the long wavelength solution of eq.(5.36) can be further split into two behavioural branches, only this time they are characterised by the frequency. The high-frequency branch considers the first two terms of eq.(5.36) to give the *fast* MHD Rossby wave dispersion relation, see eq.(5.39a) below. On the contrary, the corresponding low-frequency branch considers the second and last terms of eq.(5.36) and describes the new *slow* MHD Rossby wave given by eq.(5.40a) in the summary.

Cartesian base model MHD Rossby wave propagation properties

Low-frequency branch of the dispersion relation

The dispersion relation for wave frequency, ω and wavenumbers, k_x and k_y is given as

$$\omega^2 + \frac{k_x \beta}{k_x^2 + k_y^2}\omega - k_x^2 v_A^2 = 0, \tag{5.36}$$

where the Alfvén speed is

$$v_A = \frac{B_0}{\sqrt{4\pi\rho}}, \tag{3.6}$$

and the β-plane approximation parameter is

$$\beta = \frac{2\Omega_0}{R_0}\cos\Theta_0\,. \tag{4.81}$$

Cartesian base model MHD Rossby wave propagation properties (continued)

Full solution to the low-frequency branch of the dispersion relation

Using the quadratic formula, we get the full solution of eq.(5.36) as follows

$$\omega = -\frac{k_x\beta}{2(k_x^2+k_y^2)} \pm \frac{1}{2}\sqrt{\left(\frac{k_x\beta}{(k_x^2+k_y^2)}\right)^2 + 4k_x^2 v_A^2}. \tag{5.38}$$

The approximated solutions, as given by Zaqarashvili et al. (2007), are given below.

Fast MHD Rossby wave equations for $v_A \ll C_0$ (high-frequency solution)

$$\text{Dispersion relation} \qquad \omega_+ \approx -\frac{k_x\beta}{k_x^2+k_y^2} \tag{5.39a}$$

$$\text{Phase velocity} \qquad \frac{\omega_+}{k_x} = -\frac{\beta}{k_x^2+k_y^2} \tag{5.39b}$$

$$\text{Group velocity} \qquad \frac{\partial w_+}{\partial k_x} = -\frac{\beta(-k_x^2+k_y^2)}{(k_x^2+k_y^2)} \tag{5.39c}$$

Slow MHD Rossby wave equations for $v_A \ll C_0$ (low-frequency solution)

$$\text{Dispersion relation} \qquad \omega_- \approx \frac{k_x v_A^2(k_x^2+k_y^2)}{\beta} \tag{5.40a}$$

$$\text{Phase velocity} \qquad \frac{\omega_-}{k_x} = \frac{v_A^2(k_x^2+k_y^2)}{\beta} \tag{5.40b}$$

$$\text{Group velocity} \qquad \frac{\partial w_-}{\partial k_x} = \frac{v_A^2(3k_x^2+k_y^2)}{\beta} \tag{5.40c}$$

The notation used to indicate the fast or slow modes uses the standard symbols but with an addition of a "+" and "-" respectively, as a subscript.

5.4 Findings and parameter discussion

The resulting MHD Rossby wave dispersion relation of the base model and its solutions presented a new important finding - the presence of a magnetic field causes the ordinary long wavelength (low-order) Rossby wave to split into a fast (high-frequency) and slow (low-frequency) MHD Rossby mode.

The characteristics of the fast magneto-Rossby wave correspond to those of the HD Rossby wave, which is only partially affected by the magnetic field. Conversely, the magnetic field more strongly affects the slow magneto-Rossby wave, which exhibits very low frequencies compared to other solar waves, such as the comparative HD Rossby waves.

The dispersion relation, phase and group velocity of the fast and slow MHD Rossby wave modes are illustrated below in Fig.(5.2).

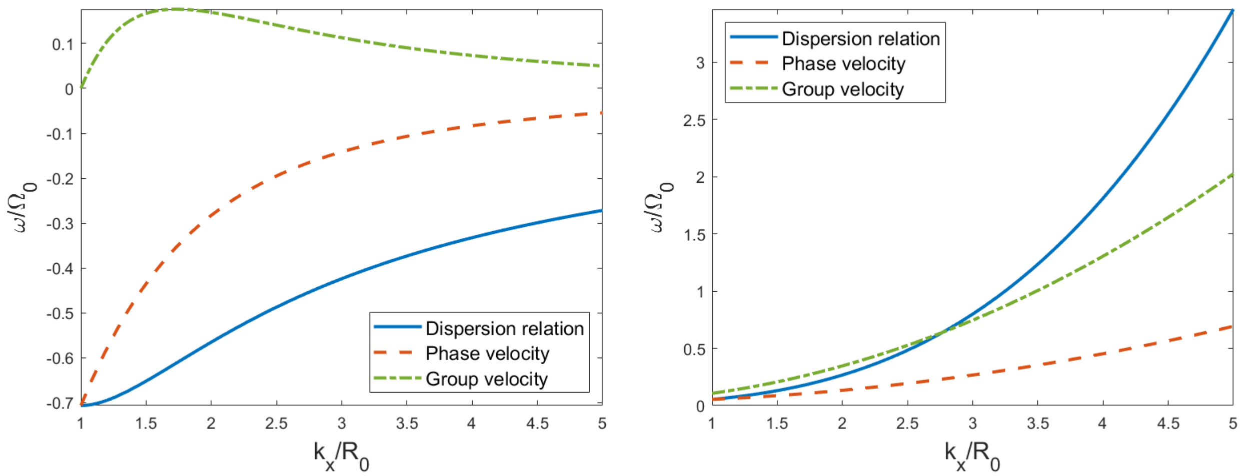

(a) Fast MHD Rossby wave properties.

(b) Slow MHD Rossby wave properties.

Figure 5.2: Base MHD Rossby wave propagation properties for the fast and slow modes. (a) The dispersion relation, phase and group velocity were plotted using eq.(5.39a), eq.(5.39b) and eq.(5.39c) for the fast MHD Rossby mode. (b) The propagation properties are given by eq.(5.40a), eq.(5.40b) and eq.(5.40c) for the slow MHD Rossby mode. Considered: $k_y = 1$, $B_0 = 4 \times 10^4\,\mathrm{G}$, $\Theta = 45°$, $\Omega_0 = 2.6 \times 10^{-6}\,\mathrm{s}^{-1}$, $\rho = 0.2\,\mathrm{g\,cm}^{-3}$ and $R_0 = 5 \times 10^{10}\,\mathrm{cm}$ (Zaqarashvili et al., 2015).

Furthermore, there is a difference in the direction of these two MHD Rossby wave modes as the fast (slow) MHD Rossby wave propagates westward (eastward), shown by the negative (positive) sign in the dispersion relation, also shown in Fig.(5.2a) (Fig.5.2b). Moreover, both the fast and slow MHD Rossby wave exhibit dispersive behaviour as indicated by the different phase and group velocity equations.

Lastly, we must recall that one of the problems identified in Section 1.2 was related to the parameter values used in the respective MHD Rossby wave models. For this reason, we will specifically examine how the parameters for latitude and the magnetic field strength are accounted for in the MHD Rossby wave dispersion relations. Starting with the latitude. Note that latitude enters the dispersion relations by means of the β-parameter, eq.(4.81), as follows

$$\beta = \frac{2\Omega_0}{R_0} \cos\Theta_0 \,,$$

which is included in both the fast and slow MHD Rossby wave equations. Because this parameter is included in the dispersion relations, it indicates that latitude influences the propagation properties of both MHD Rossby waves. More specifically, the fast MHD Rossby wave frequency is directly proportional to latitude. In contrast, the slow MHD Rossby wave dispersion relation shows an indirect proportionality.

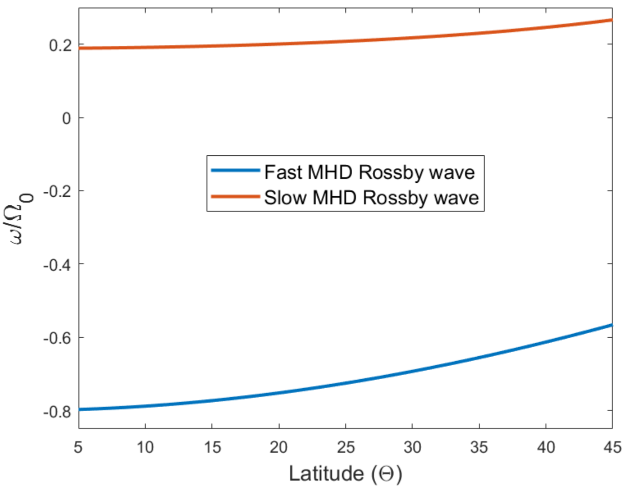

Figure 5.3: The fast and slow MHD Rossby wave dispersion relation dependence on latitude, Θ. The blue (negative) line represents the fast MHD Rossby wave dispersion relation, eq.(5.39a), and the orange (positive), eq.(5.40a) associated with the slow MHD Rossby wave. Furthermore, set $k_x = 2$, $k_y = 1$, $B_0 = 4 \times 10^4\,\mathrm{G}$, $\Omega_0 = 2.6 \times 10^{-6}\,\mathrm{s}^{-1}$, $\rho = 0.2\,\mathrm{g\,cm}^{-3}$ and $R_0 = 5 \times 10^{10}\,\mathrm{cm}$ (Zaqarashvili et al., 2015).

This opposite impact of increasing latitude on the dispersion relations of the respective MHD Rossby waves is illustrated in Fig.(5.3). Here, we see that the slow MHD Rossby wave has a positive dispersion relation for which the frequency increases marginally as the latitude increases. Comparatively, the negative dispersion relation of the fast MHD Rossby wave decreases more significantly for increased latitude values.

On the other hand, the effect of the magnetic field enters the dispersion relations in the form of the Alfvén speed parameter, eq.(3.6) repeated below,

$$v_A = \frac{B_0}{\sqrt{4\pi\rho}} \,.$$

Although, when considering the dispersion relation for the fast MHD Rossby wave, eq.(5.39a), as given by Zaqarashvili et al. (2007), it appears that the magnetic field is not included since the v_A parameter is not included. However, this is merely an approximated equation as $v_A \ll C_0$ was assumed, but when the full equation for the solution is considered as given by eq.(5.38), it shows the presence of the v_A in both MHD Rossby wave dispersion relations. Therefore, it can be concluded that both MHD Rossby wave modes are affected by the presence of a magnetic field.

5.5 Summary

In this chapter, we derived the base MHD Rossby wave model using the MHD shallow water equations in Cartesian coordinates (Section 4.6). This derivation of the base MHD Rossby wave model showed that the low-frequency branch of the dispersion relation, which disregards the higher-order term including ω^4, is associated with the MHD Rossby waves and is given below

$$\omega^2 + \frac{k_x \beta}{k_x^2 + k_y^2}\omega - k_x^2 v_A^2 = 0, \tag{5.36}$$

where the Alfvén speed, eq.(3.6), is

$$v_A = \frac{B_0}{\sqrt{4\pi\rho}},$$

and the β-plane approximation parameter, eq.(4.81), is

$$\beta = \frac{2\Omega_0}{R_0}\cos\Theta_0$$

It should be noted that eq.(5.36) has two solutions due to its quadratic nature. Therefore, the base model derivation shows that adding a magnetic field to the system dynamics causes the ordinary HD Rossby wave to split into a fast and a slow propagating mode. These modes correspond to the two quadratic equation solutions, which are given below. By using the quadratic formula, we can write the dispersion relations as follows, where the + and − are associated with the fast and slow modes, respectively

$$\omega = -\frac{k_x \beta}{2(k_x^2 + k_y^2)} \pm \frac{1}{2}\sqrt{\left(\frac{k_x \beta}{(k_x^2 + k_y^2)}\right)^2 + 4k_x^2 v_A^2}. \tag{5.38}$$

These solutions can be further approximated by the next two equations, which are the simplified dispersion relations of the fast

$$\omega_+ \approx -\frac{k_x \beta}{k_x^2 + k_y^2}, \tag{5.39a}$$

and slow MHD Rossby wave modes

$$\omega_- \approx \frac{k_x v_A^2 (k_x^2 + k_y^2)}{\beta}. \tag{5.40a}$$

Furthermore, we also had to explore the parameters included in this base model to determine how closely it represents reality and identify how it could be improved. Firstly, we noted that as a consequence of using the shallow water approximation, a variable that describes the fluid depth, h, has entered the model, a unique parameter associated with derivations of governing equations using the SWE formulation. Moreover, since a rotating frame of reference was considered, the base model has already improved the initial governing equations presented by Gilman (2000). The β-plane approximation (Section 4.6.1), which is applied to the Coriolis parameter, also more accurately describes reality than the f-plane approximation, which omits the long wavelength Rossby waves as part of the solution (Schecter et al., 2001). However, when setting $\beta = 0$ in the dispersion relations, they transform to those corresponding to the f-plane approximation.

The magnetic field has also been included in the base Rossby wave model, represented by the Alfvén speed, v_A, in the dispersion relations of both the fast and slow MHD Rossby wave. Here, similar to the $\beta = 0$ transformation, it follows that by setting $v_A = 0$, the effect of the magnetic field is removed, and the dispersion relation becomes that of the HD Rossby waves. However, it is crucial that this base model be enhanced as the solar environment and the associated dynamics are better understood. Moving to a spherical coordinate system would be favourable as the curvature of the Sun, currently being neglected in the Cartesian coordinate framework, will inevitably impact the behaviour of large-scale waves such as the Rossby waves under consideration. Secondly, it was suggested by Gilman (2000) and Zaqarashvili et al. (2007) that the unique structure and characteristics of the upper and lower layers of the tachocline should be considered separately (see Section 3.5.2) which would result in a more detailed model of solar waves that occur in these layers respectively. Nevertheless, the base model forms a good foundation for further MHD Rossby wave model development, which will be explored in the next chapter.

6 Effective gravity MHD Rossby wave model

6.1 Introduction

In Chapter 5, we discussed the base MHD Rossby wave model. This first model of these planetary Rossby waves in the context of the solar tachocline was derived by Zaqarashvili et al. (2007), who used the shallow water equations (SWEs) in Cartesian coordinates. However, three fundamental changes should be made to create a more comprehensive model. Firstly, using the governing equations in spherical coordinates, as suggested by Zaqarashvili et al. (2007), is necessary because the curvature of the rotating fluid sphere plays a significant role in large wave perturbations. Secondly, the two layers of the tachocline should be considered separately because of their different characteristics (Gilman, 2000; Zaqarashvili et al., 2007). Finally, the fundamental solar dynamic of latitudinal differential rotation (Section 3.5.1) must be included in the Rossby wave model. In this chapter, we will address the first and second enhancements.

Using spherical coordinates to describe Rossby waves has several benefits. Since Rossby waves occur globally, spherical coordinates allow for a latitude-longitude representation commonly used on the Earth and the Sun. Secondly, spherical coordinates naturally incorporate rotation effects. Lastly, when using the governing equations in spherical coordinates, the conservation of angular momentum is maintained as the rotation occurs around the axis of the rotating sphere. This is essential for this study because the conservation of angular momentum maintains the balance between the Coriolis and pressure gradient force, leading to the existence of Rossby waves (Appendix B.2.3). Therefore, it can be concluded that any Rossby wave model should be derived from the spherical coordinate system.

Specifically, the spherical coordinates (r, θ, ϕ), illustrated in Fig.(6.1), are considered where r is the radial coordinate pointing outwards, θ is the co-latitude (polar angle), and ϕ is the longitude (azimuthal angle). It can also be noted that the ϕ- and θ-direction correspond to the direction of the toroidal and poloidal magnetic field (Section 2.5.2), respectively.

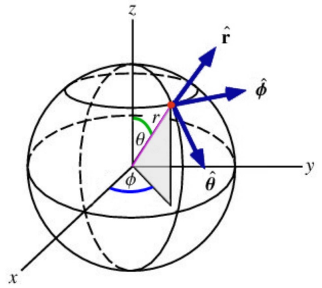

Figure 6.1: Spherical coordinates (*physics orientation*). Here described by (r, θ, ϕ), where r is the outward radial component, θ is co-latitude and ϕ is longitude. Image courtesy of Rosenthal (2015).

Moreover, it is important to mention that the traditional notation for spherical coordinates described here has the potential to cause confusion. Since θ is commonly used as the standard variable for *latitude*, using it to represent co-latitude can be misleading. For this reason, this study will, from this point onwards, change the latitude variable to Θ and use θ for co-latitude instead. Subsequently, the relationship between latitude and co-latitude is given by $\theta = 90° - \Theta$.

In this chapter, the second model enhancement is also discussed, which explains how the distinct characteristics of the upper and lower tachocline layers contribute to different gravitational forces in the respective layers. These characteristics were previously mentioned in Section 3.5.2. As a result, the MHD Rossby wave model is impacted when we consider the effective gravity (Section 6.3) instead of the solar gravity. This leads to separate models for each tachocline layer, and it's necessary to determine whether either one or both models are relevant to this study. We will also elaborate on the specific pattern in solar activity that is the focus of this study in this chapter, namely the Rieger-type periodicity (RTP) (Rieger et al., 1984) (see Section 2.4 for the other durations). The RTP has a duration of 150-180 days and is selected for this study as it is long enough to predict but short enough for Earth to be regularly impacted by solar activity exhibiting this frequency. By comparing the frequencies associated with the MHD Rossby waves in the upper and lower tachocline to those of the RTP, we can determine the most suitable model when we are concerned with relatively short-term changes in space weather.

Therefore, we will start by deriving the base MHD Rossby wave model in spherical coordinates, treating the tachocline as one layer. Then, we will explain effective gravity and show

how it impacts the model. Finally, we will discuss the Rieger-type periodicity further and compare it to the frequencies of the two MHD Rossby wave models in the upper and lower tachocline to determine the applicable model for this study.

6.2 Base MHD Rossby wave model in spherical coordinates considering solar gravity

In addition to deriving the MHD Rossby wave model in Cartesian coordinates, Zaqarashvili et al. (2007) also derived the model using the MHD shallow water equations (SWEs) in spherical coordinates. Since the induction, momentum, and continuity equations have already been linearised in Section 5.2, this chapter uses them and writes them in component form using spherical coordinates.

Therefore, we can write the vectors for the unperturbed, $\mathbf{B}_0$, and perturbed, $\mathbf{B}_1$, magnetic field strength, and the velocity perturbations, $\mathbf{v}_1$, in spherical coordinates. By noting that the x- and y-direction in Cartesian coordinates corresponds to the ϕ- and θ-direction in spherical coordinates, we have

$$\mathbf{B}_0 = (0, 0, B_\phi), \tag{6.1}$$

$$\mathbf{B}_1 = (0, b_\theta, b_\phi), \tag{6.2}$$

$$\mathbf{v}_1 = (0, v_\theta, v_\phi). \tag{6.3}$$

which will be used to determine the component forms of the governing equations.

6.2.1 Linearised induction equation

Starting with the linearised induction equation, eq.(5.9), derived in Section 5.2.1, which is repeated below

$$\frac{\partial \mathbf{B}_1}{\partial t} = \nabla \times (\mathbf{v}_1 \times \mathbf{B}_0),$$

we can substitute $\mathbf{B}_1 = b_\theta\hat{\boldsymbol{\theta}} + b_\phi\hat{\boldsymbol{\phi}}$ from eq.(6.2) in the term on the left-hand side of eq.(5.9) to get

$$\frac{\partial \mathbf{B}_1}{\partial t} = \frac{\partial}{\partial t}(b_\theta\,\hat{\boldsymbol{\theta}} + b_\phi\,\hat{\boldsymbol{\phi}}), \tag{6.4a}$$
$$= \frac{\partial b_\theta}{\partial t}\,\hat{\boldsymbol{\theta}} + \frac{\partial b_\phi}{\partial t}\,\hat{\boldsymbol{\phi}}. \tag{6.4b}$$

Moreover,

$$\mathbf{v}_1 \times \mathbf{B}_0 = \begin{vmatrix} \hat{\boldsymbol{r}} & \hat{\boldsymbol{\theta}} & \hat{\boldsymbol{\phi}} \\ 0 & v_\theta & v_\phi \\ 0 & 0 & B_\phi \end{vmatrix} \tag{6.5a}$$
$$= (v_\theta B_\phi - 0)\,\hat{\boldsymbol{r}} - 0\,\hat{\boldsymbol{\theta}} + 0\,\hat{\boldsymbol{\phi}}, \tag{6.5b}$$
$$= v_\theta B_\phi\,\hat{\boldsymbol{r}}. \tag{6.5c}$$

Then, the curl of the spherical del operator, ∇,

$$\boxed{\nabla = \frac{1}{r^2}\frac{\partial}{\partial r}r^2\hat{\boldsymbol{r}} + \frac{1}{r\sin\theta}\frac{\partial}{\partial\theta}\sin\theta\,\hat{\boldsymbol{\theta}} + \frac{1}{r\sin\theta}\frac{\partial}{\partial\phi}\hat{\boldsymbol{\phi}}}, \tag{6.6}$$

(Priest, 2014, p.489) and eq.(6.5c), is given by

$$\nabla \times (\mathbf{v}_1 \times \mathbf{B}_0) = \begin{vmatrix} \hat{\boldsymbol{r}} & \hat{\boldsymbol{\theta}} & \hat{\boldsymbol{\phi}} \\ \frac{1}{r^2}\frac{\partial}{\partial r}r^2 & \frac{1}{r\sin\theta}\frac{\partial}{\partial\theta}\sin\theta & \frac{1}{r\sin\theta}\frac{\partial}{\partial\phi} \\ v_\theta B_\phi & 0 & 0 \end{vmatrix} \tag{6.7a}$$
$$= 0\,\hat{\boldsymbol{r}} - \left(\frac{1}{r\sin\theta}\frac{\partial}{\partial\phi}v_\theta B_\phi - 0\right)\hat{\boldsymbol{\theta}} + \left(0 - \frac{1}{r\sin\theta}\frac{\partial}{\partial\theta}\sin\theta\big[v_\theta B_\phi\big]\right)\hat{\boldsymbol{\phi}}, \tag{6.7b}$$
$$= -\frac{1}{r\sin\theta}\frac{\partial}{\partial\phi}v_\theta B_\phi\,\hat{\boldsymbol{\theta}} - \frac{1}{r\sin\theta}\frac{\partial}{\partial\theta}\sin\theta\big(v_\theta B_\phi\big)\,\hat{\boldsymbol{\phi}}. \tag{6.7c}$$

The induction equation can then be written in component form by using eq.(6.4b) on the left-hand side and the results of the cross product, eq.(6.7c) on the right-hand side, it results in the following equations

$$\frac{\partial b_\theta}{\partial t} = -\frac{B_\phi}{r\sin\theta}\frac{\partial v_\theta}{\partial\phi}, \tag{6.8}$$
$$\frac{\partial b_\phi}{\partial t} = -\frac{1}{r\sin\theta}\frac{\partial}{\partial\theta}\sin\theta\big(v_\theta B_\phi\big). \tag{6.9}$$

6.2.2 Linearised momentum equation

Now, to linearise the momentum equation in spherical coordinates, we start by considering eq.(5.21), repeated below

$$\frac{\partial \mathbf{v}_1}{\partial t} + 2\boldsymbol{\Omega} \times \mathbf{v}_1 = \frac{\mathbf{B}_0}{4\pi\rho}\,(\nabla \cdot \mathbf{B}_1) - g\,\nabla h,$$

and evaluate each term separately, which will be added together at the end.

The first acceleration term is linearised as follows

$$\begin{aligned} \frac{\partial \mathbf{v}_1}{\partial t} &= \frac{\partial}{\partial t}(v_\theta\,\hat{\boldsymbol{\theta}} + v_\phi\,\hat{\boldsymbol{\phi}}), && (6.10a) \\ &= \frac{\partial v_\theta}{\partial t}\,\hat{\boldsymbol{\theta}} + \frac{\partial v_\phi}{\partial t}\,\hat{\boldsymbol{\phi}}. && (6.10b) \end{aligned}$$

Next, we will linearise the second term on the left-hand side of eq.(5.21), representing the Coriolis force.

Since we are considering the spherical coordinate system, (r, θ, ϕ), illustrated in Fig.(6.1), the angular velocity of the Sun can be written as

$$\boldsymbol{\Omega} = (\Omega \sin\theta, -\Omega\cos\theta, 0), \tag{6.11}$$

where θ is co-latitude. Then, the Coriolis force cross-product is evaluated as

$$\begin{aligned} 2\boldsymbol{\Omega} \times \mathbf{v}_1 &= \begin{vmatrix} \hat{\boldsymbol{r}} & \hat{\boldsymbol{\theta}} & \hat{\boldsymbol{\phi}} \\ 2\Omega\sin\theta & -2\Omega\cos\theta & 0 \\ 0 & v_\theta & v_\phi \end{vmatrix} && (6.12a) \\ &= (-2\Omega\sin\theta v_\phi - 0)\ \hat{\boldsymbol{r}} - (2\Omega\cos\theta v_\phi - 0)\ \hat{\boldsymbol{\theta}} + (2\Omega\cos\theta v_\theta - 0)\ \hat{\boldsymbol{\phi}}, && (6.12b) \\ &= -2\Omega\sin\theta v_\phi\,\hat{\boldsymbol{r}} - 2\Omega\cos\theta v_\phi\,\hat{\boldsymbol{\theta}} + 2\Omega\cos\theta v_\theta\,\hat{\boldsymbol{\phi}}. && (6.12c) \end{aligned}$$

On the other hand, to evaluate the first term on the right-hand side of eq.(5.21), which describes the Lorentz force, we must first recall that in Section 5.2.2 the linearised Lorentz force is given by eq.(5.18c), that is $(\mathbf{B}\cdot\nabla)\,\mathbf{B} = (\mathbf{B}_0\cdot\nabla)\mathbf{B}_1$. Moreover, since the orientation of the magnetic field we are considering is only in the $\boldsymbol{\theta}$- and $\boldsymbol{\phi}$-directions (Section 2.5.2), we can neglect the radial $\boldsymbol{r}$-direction for Lorentz force.

Thus, by substituting eq.(6.1), eq.(6.2) and eq.(6.6) into $\mathbf{B}_0$, $\mathbf{B}_1$ and ∇ of eq.(5.18c), we get

$$\begin{aligned}
(\mathbf{B}_0 \cdot \nabla)\mathbf{B}_1 &= \left[B_\phi \hat{\boldsymbol{\phi}} \cdot \left(\frac{1}{r\sin\theta}\frac{\partial}{\partial\theta}\sin\theta\hat{\boldsymbol{\theta}} + \frac{1}{r\sin\theta}\frac{\partial}{\partial\phi}\hat{\boldsymbol{\phi}}\right)\right]\left(b_\theta\hat{\boldsymbol{\theta}} + b_\phi\hat{\boldsymbol{\phi}}\right), && (6.13a)\\
&= \left[\frac{1}{r\sin\theta}\frac{\partial}{\partial\theta}B_\phi\sin\theta\,\hat{\boldsymbol{\phi}}\hat{\boldsymbol{\theta}} + \frac{1}{r\sin\theta}\frac{\partial}{\partial\phi}B_\phi\,\hat{\boldsymbol{\phi}}\hat{\boldsymbol{\phi}}\right]\left(b_\theta\hat{\boldsymbol{\theta}} + b_\phi\hat{\boldsymbol{\phi}}\right), && (6.13b)\\
&= \left[\frac{1}{r\sin\theta}\left(\frac{\partial B_\phi}{\partial\theta}\sin\theta + B_\phi\cos\theta\right)\hat{\boldsymbol{\phi}}\hat{\boldsymbol{\theta}} + \frac{1}{r\sin\theta}\frac{\partial}{\partial\phi}B_\phi\,\hat{\boldsymbol{\phi}}\hat{\boldsymbol{\phi}}\right]\left(b_\theta\hat{\boldsymbol{\theta}} + b_\phi\hat{\boldsymbol{\phi}}\right), && (6.13c)
\end{aligned}$$

which for simplicity will be further calculated separately for the $\boldsymbol{\theta}$ and $\boldsymbol{\phi}$ directions, starting with the former. Also, consider that here the unit vectors with their associated properties, $\hat{\boldsymbol{\theta}} \cdot \hat{\boldsymbol{\theta}} = \hat{\boldsymbol{\phi}} \cdot \hat{\boldsymbol{\phi}} = 1$ determine the direction of the respective terms, as follows

$$\begin{aligned}
&\left[\frac{1}{r\sin\theta}\left(\frac{\partial B_\phi}{\partial\theta}\sin\theta + B_\phi\cos\theta\right)\hat{\boldsymbol{\phi}}\hat{\boldsymbol{\theta}} + \frac{1}{r\sin\theta}\frac{\partial}{\partial\phi}B_\phi\,\hat{\boldsymbol{\phi}}\hat{\boldsymbol{\phi}}\right] b_\theta\hat{\boldsymbol{\theta}}, && (6.14a)\\
&= \left[\frac{1}{r}\frac{\partial B_\phi}{\partial\theta}\,\hat{\boldsymbol{\phi}}\hat{\boldsymbol{\theta}} + \frac{\cos\theta}{r\sin\theta}B_\phi\,\hat{\boldsymbol{\phi}}\hat{\boldsymbol{\theta}} + \frac{B_\phi}{r\sin\theta}\frac{\partial}{\partial\phi}\,\hat{\boldsymbol{\phi}}\hat{\boldsymbol{\phi}}\right] b_\theta\hat{\boldsymbol{\theta}}, && (6.14b)\\
&= \frac{b_\theta}{r}\frac{\partial B_\phi}{\partial\theta}\,\hat{\boldsymbol{\phi}}\hat{\boldsymbol{\theta}}\hat{\boldsymbol{\theta}} + \frac{\cos\theta}{r\sin\theta}B_\phi b_\theta\,\hat{\boldsymbol{\phi}}\hat{\boldsymbol{\theta}}\hat{\boldsymbol{\theta}} + \frac{B_\phi}{r\sin\theta}\frac{\partial b_\theta}{\partial\phi}\,\hat{\boldsymbol{\phi}}\hat{\boldsymbol{\phi}}\hat{\boldsymbol{\theta}}, && (6.14c)\\
&= \frac{b_\theta}{r}\frac{\partial B_\phi}{\partial\theta}\,\hat{\boldsymbol{\phi}} + \frac{\cos\theta}{r\sin\theta}B_\phi b_\theta\,\hat{\boldsymbol{\phi}} + \frac{B_\phi}{r\sin\theta}\frac{\partial b_\theta}{\partial\phi}\,\hat{\boldsymbol{\theta}}. && (6.14d)
\end{aligned}$$

Then for the ϕ-direction of eq.(6.13c) we get the following subset of equations

$$\begin{aligned}
&\left[\frac{1}{r\sin\theta}\left(\frac{\partial B_\phi}{\partial\theta}\sin\theta + B_\phi\cos\theta\right)\hat{\boldsymbol{\phi}}\hat{\boldsymbol{\theta}} + \frac{1}{r\sin\theta}\frac{\partial}{\partial\phi}B_\phi\,\hat{\boldsymbol{\phi}}\hat{\boldsymbol{\phi}}\right] b_\phi\hat{\boldsymbol{\phi}}, && (6.15a)\\
&= \left[\frac{B_\phi}{r\sin\theta}\left(\frac{\partial}{\partial\theta}\sin\theta + \cos\theta\right)\hat{\boldsymbol{\phi}}\hat{\boldsymbol{\theta}} + \frac{B_\phi}{r\sin\theta}\frac{\partial}{\partial\phi}\,\hat{\boldsymbol{\phi}}\hat{\boldsymbol{\phi}}\right] b_\phi\hat{\boldsymbol{\phi}}, && (6.15b)\\
&= \left[\frac{B_\phi}{r\sin\theta}\left(\cos\theta + \cos\theta\right)\hat{\boldsymbol{\phi}}\hat{\boldsymbol{\theta}} + \frac{B_\phi}{r\sin\theta}\frac{\partial}{\partial\phi}\,\hat{\boldsymbol{\phi}}\hat{\boldsymbol{\phi}}\right] b_\phi\hat{\boldsymbol{\phi}}, && (6.15c)\\
&= \left[2\frac{\cos\theta}{r\sin\theta}B_\phi\,\hat{\boldsymbol{\phi}}\hat{\boldsymbol{\theta}} + \frac{B_\phi}{r\sin\theta}\frac{\partial}{\partial\phi}\,\hat{\boldsymbol{\phi}}\hat{\boldsymbol{\phi}}\right] b_\phi\hat{\boldsymbol{\phi}}, && (6.15d)\\
&= 2\frac{\cos\theta}{r\sin\theta}B_\phi b_\phi\,\hat{\boldsymbol{\phi}}\hat{\boldsymbol{\phi}}\hat{\boldsymbol{\theta}} + \frac{B_\phi}{r\sin\theta}\frac{\partial b_\phi}{\partial\phi}\,\hat{\boldsymbol{\phi}}\hat{\boldsymbol{\phi}}\hat{\boldsymbol{\phi}}, && (6.15e)\\
&= 2\frac{\cos\theta}{r\sin\theta}B_\phi b_\phi\,\hat{\boldsymbol{\theta}} + \frac{B_\phi}{r\sin\theta}\frac{\partial b_\phi}{\partial\phi}\,\hat{\boldsymbol{\phi}}. && (6.15f)
\end{aligned}$$

Then combining eq.(6.14d) and eq.(6.15f), we have the component form of the Lorentz force as follows

$$(\mathbf{B}_0 \cdot \nabla)\,\mathbf{B}_1 = \frac{b_\theta}{r}\frac{\partial B_\phi}{\partial \theta}\,\hat{\boldsymbol{\phi}} + \frac{\cos\theta}{r\sin\theta}B_\phi b_\theta\,\hat{\boldsymbol{\phi}} + \frac{B_\phi}{r\sin\theta}\frac{\partial b_\theta}{\partial \phi}\,\hat{\boldsymbol{\theta}} + 2\frac{\cos\theta}{r\sin\theta}B_\phi b_\phi\,\hat{\boldsymbol{\theta}} + \frac{B_\phi}{r\sin\theta}\frac{\partial b_\phi}{\partial \phi}\,\hat{\boldsymbol{\phi}}, \tag{6.16a}$$

$$= \left(\frac{B_\phi}{r\sin\theta}\frac{\partial b_\theta}{\partial \phi} + 2\frac{\cos\theta}{r\sin\theta}B_\phi b_\phi\right)\hat{\boldsymbol{\theta}} + \left(\frac{b_\theta}{r}\frac{\partial B_\phi}{\partial \theta} + \frac{\cos\theta}{r\sin\theta}B_\phi b_\theta + \frac{B_\phi}{r\sin\theta}\frac{\partial b_\phi}{\partial \phi}\right)\hat{\boldsymbol{\phi}}. \tag{6.16b}$$

Lastly, the gravity term on the right-hand side of eq.(5.21) is linearised by considering that $h = H_0 + H_1$, where H_0 and H_1 is the unperturbed and perturbed layer thickness, respectively. However, we know that the unperturbed layer thickness is considered constant and will, therefore, not be considered here. Also, since gravity does not have a radial component, only the $\boldsymbol{\theta}$- and $\boldsymbol{\phi}$-directions are considered, such that we can write

$$-g\,\nabla h = -g\left(\frac{1}{r\sin\theta}\frac{\partial}{\partial\theta}\sin\theta\,\hat{\boldsymbol{\theta}} + \frac{1}{r\sin\theta}\frac{\partial}{\partial\phi}\,\hat{\boldsymbol{\phi}}\right)H_1, \tag{6.17a}$$

$$= -\frac{g}{r}\frac{\partial H_1}{\partial\theta}\,\hat{\boldsymbol{\theta}} - \frac{g}{r\sin\theta}\frac{\partial H_1}{\partial\phi}\,\hat{\boldsymbol{\phi}}. \tag{6.17b}$$

Now, by combining the acceleration eq.(6.10b), Coriolis force eq.(6.12c), Lorentz force eq.(6.16b) and the gravitational force eq.(6.17b), we get the linearised momentum equation in component form as follows

$$\frac{\partial v_\theta}{\partial t} - 2\Omega_0 v_\phi\cos\theta + \frac{g}{R_0}\frac{\partial h}{\partial\theta} - \frac{B_\phi}{4\pi\rho R_0\sin\theta}\frac{\partial b_\theta}{\partial\phi} + 2\frac{B_\phi}{4\pi\rho R_0}\frac{\cos\theta}{\sin\theta}b_\phi = 0, \tag{6.18}$$

and

$$\frac{\partial v_\phi}{\partial t} + 2\Omega_0 v_\theta\cos\theta + \frac{g}{R_0\sin\theta}\frac{\partial h}{\partial\phi} - \frac{b_\theta}{4\pi\rho R_0}\frac{\partial B_\phi}{\partial\theta} - \frac{B_\phi}{4\pi\rho R_0\sin\theta}\frac{\partial b_\phi}{\partial\phi} - \frac{B_\phi}{4\pi\rho R_0}\frac{\cos\theta}{\sin\theta}b_\theta = 0. \tag{6.19}$$

In these two momentum equations, the following notation changes are made, to conform with the equations given by Zaqarashvili et al. (2016). Firstly, the angular rotation $\boldsymbol{\Omega}$ is replaced with the more specific equatorial rotation rate parameter, Ω_0. The radial distance, r, is replaced by the notation, R_0, indicating that it is the distance from the centre of the Sun to the tachocline. Also, h here represents the perturbation of the fluid layer thickness, previously labelled as H_1.

6.2.3 Linearised continuity equation

Similarly, we use the linearised continuity equation, eq.(5.25), as the starting point, repeated here

$$\frac{\partial H_1}{\partial t} + \nabla \cdot (H_0 \mathbf{v}_1) = 0.$$

Then, following the same approach as what was done for the induction and momentum equations above, we change the notation of H_1 in the first term to h.

Furthermore, since the unperturbed layer thickness, H_0 is a constant, the second term becomes $H_0(\nabla \cdot \mathbf{v}_1)$. Then, because we are not considering velocity changes in the outward radial direction, we use eq.(6.3) and the last two terms of of the del operator, eq.(6.6), to write

$$\frac{\partial h}{\partial t} + H_0 \left(\frac{1}{r \sin\theta} \frac{\partial}{\partial \theta} \sin\theta \hat{\boldsymbol{\theta}} + \frac{1}{r \sin\theta} \frac{\partial}{\partial \phi} \hat{\boldsymbol{\phi}} \right) \cdot (v_\theta \hat{\boldsymbol{\theta}} + v_\phi \hat{\boldsymbol{\phi}}) = 0, \tag{6.20}$$

$$\frac{\partial h}{\partial t} + \frac{H_0}{r \sin\theta} \frac{\partial}{\partial \theta} v_\theta \sin\theta + \frac{H_0}{r \sin\theta} \frac{\partial v_\phi}{\partial \phi} = 0, \tag{6.21}$$

which is the linearised continuity equation in spherical coordinates.

The set of linearised shallow water MHD equations in spherical coordinates are summarised below for ease of reference.

Linearised shallow water equations in spherical coordinate component form

Induction equations

$$\frac{\partial b_\theta}{\partial t} - \frac{B_\phi}{R_0 \sin\theta} \frac{\partial v_\theta}{\partial \phi} = 0 \tag{6.8}$$

$$\frac{\partial b_\phi}{\partial t} + \frac{B_\phi}{R_0 \sin\theta} \frac{\partial}{\partial \theta} (\sin\theta v_\theta) = 0 \tag{6.9}$$

Linearised SWEs in spherical coordinate component form (continued)

Momentum equations

$$\frac{\partial v_\theta}{\partial t} - 2\Omega_0 v_\phi \cos\theta + \frac{g}{R_0}\frac{\partial h}{\partial \theta} - \frac{B_\phi}{4\pi\rho R_0 \sin\theta}\frac{\partial b_\theta}{\partial \phi} + 2\frac{B_\phi}{4\pi\rho R_0}\frac{\cos\theta}{\sin\theta} b_\phi = 0 \tag{6.18}$$

$$\begin{aligned}\frac{\partial v_\phi}{\partial t} + 2\Omega_0 v_\theta \cos\theta + \frac{g}{R_0 \sin\theta}\frac{\partial h}{\partial \phi} - \frac{b_\theta}{4\pi\rho R_0}\frac{\partial B_\phi}{\partial \theta} - \frac{B_\phi}{4\pi\rho R_0 \sin\theta}\frac{\partial b_\phi}{\partial \phi} \\ - \frac{B_\phi}{4\pi\rho R_0}\frac{\cos\theta}{\sin\theta} b_\theta = 0\end{aligned} \tag{6.19}$$

Continuity equation

$$\frac{\partial h}{\partial t} + \frac{H_0}{R_0 \sin\theta}\frac{\partial}{\partial \theta}(v_\theta \sin\theta) + \frac{H_0}{R_0 \sin\theta}\frac{\partial v_\phi}{\partial \phi} = 0 \tag{6.21}$$

6.2.4 MHD Rossby wave dispersion relation derivation

The above shallow water equations are now used to derive the dispersion relation of the MHD Rossby wave. We start by multiplying all the above equations with $\sin\theta$, except for eq.(6.21), which is multiplied by $\sin^2\theta$, we also set

$$\begin{bmatrix} \mathbf{v}_\theta \\ \mathbf{v}_\phi \\ \mathbf{b}_\theta \\ \mathbf{b}_\phi \end{bmatrix} = \sin\theta \begin{bmatrix} v_\theta \\ v_\phi \\ b_\theta \\ b_\phi \end{bmatrix}$$

and consider the magnetic field profile[1] of the form

$$\boxed{B_\phi = B_0 \sin\theta}. \tag{6.22}$$

we arrive at the following set of equations

$$\frac{\partial \mathbf{v}_\theta}{\partial t} - 2\Omega_0 \mathbf{v}_\phi \cos\theta + \frac{g}{R_0}\sin\theta\frac{\partial h}{\partial \theta} - \frac{B_0}{4\pi\rho R_0}\frac{\partial \mathbf{b}_\theta}{\partial \phi} + 2\frac{B_0}{4\pi\rho R_0}\cos\theta \mathbf{b}_\phi = 0, \tag{6.23}$$

$$\frac{\partial \mathbf{v}_\phi}{\partial t} + 2\Omega_0 \mathbf{v}_\theta \cos\theta + \frac{g}{R_0}\frac{\partial h}{\partial \phi} - \frac{B_0}{4\pi\rho R_0}\frac{\partial \mathbf{b}_\phi}{\partial \phi} - \frac{B_0}{4\pi\rho R_0}\cos\theta \mathbf{b}_\theta = 0, \tag{6.24}$$

[1] A mathematical expression that describes the general shape of the magnetic field lines in an environment.

$$\sin^2\theta\frac{\partial h}{\partial t}+\frac{H_0}{R_0}\sin\theta\frac{\partial \mathbf{v}_\theta}{\partial\theta}+\frac{H_0}{R_0}\frac{\partial \mathbf{v}_\phi}{\partial\phi}=0, \tag{6.25}$$

$$\frac{\partial \mathbf{b}_\theta}{\partial t}-\frac{B_0}{R_0}\frac{\partial \mathbf{v}_\theta}{\partial\phi}=0, \tag{6.26}$$

and

$$\frac{\partial \mathbf{b}_\phi}{\partial t}+\frac{B_0}{R_0}\sin\theta\frac{\partial \mathbf{v}_\theta}{\partial\theta}=0. \tag{6.27}$$

Next, we take the time derivative of eq.(6.23) first and substitute eq.(6.26) and eq.(6.27) to get

$$\begin{aligned}\frac{\partial \mathbf{v}_\theta^2}{\partial t^2}-2\Omega_0\cos\theta\frac{\partial \mathbf{v}_\phi}{\partial t}+\frac{g}{R_0}\sin\theta\frac{\partial}{\partial\theta}\frac{\partial h}{\partial t}-\frac{B_0^2}{4\pi\rho R_0^2}\frac{\partial^2\mathbf{v}_\theta}{\partial\phi^2}\\ +2\frac{B_0^2}{4\pi\rho R_0^2}\cos\theta(-\sin\theta\frac{\partial \mathbf{v}_\theta}{\partial\theta})=0.\end{aligned} \tag{6.28}$$

Now, divide eq.(6.28) by $4\Omega_0^2$, substitute the square of Alfvén speed, eq.(3.6), and apply a Fourier analysis of the form $\exp(-i\omega t+im\phi)$ such that

$$\begin{aligned}-\frac{\omega^2}{4\Omega_0^2}\mathbf{v}_\theta-\left(\frac{-i\omega}{2\Omega_0}\right)\cos\theta\mathbf{v}_\phi+\left(\frac{-i\omega}{2\Omega_0}\right)\frac{gh}{2R_0\Omega_0}\sin\theta\frac{\partial}{\partial\theta}+\frac{m^2v_A^2}{4\Omega_0^2R_0^2}\mathbf{v}_\theta\\ +\frac{2v_A^2}{4\Omega_0^2R_0^2}\cos\theta(-\sin\theta\frac{\partial}{\partial\theta})\mathbf{v}_\theta=0.\end{aligned} \tag{6.29}$$

Zaqarashvili et al. (2007) then defined the following parameters to simplify the notation

$$\begin{aligned}\lambda=\frac{\omega}{2\Omega_0},\quad \alpha_0^2=\frac{v_A^2}{4\Omega_0^2R_0^2},\quad \gamma=\frac{gh}{2\Omega_0R_0},\quad \epsilon=\frac{4\Omega_0^2R_0^2}{gH_0},\\ \mu=\cos\theta,\quad\text{and}\quad D=(1-\mu^2)\frac{\partial}{\partial\mu}=-\sin\theta\frac{\partial}{\partial\theta},\end{aligned} \tag{6.30}$$

and substituted eq.(6.30) into eq.(6.29). By further multiplying with i, and setting $i\mathbf{v}_\theta=\tilde{v}_\theta$, we get

$$\boxed{-\lambda^2\tilde{v}_\theta-\mu\lambda\mathbf{v}_\phi-\lambda D\gamma+m^2\alpha_0^2\tilde{v}_\theta+2\alpha_0^2\mu D\tilde{v}_\theta=0}. \tag{6.31}$$

Similarly, from eq.(6.24), we arrive at

$$\boxed{-\lambda^2\mathbf{v}_\phi-\mu\lambda\tilde{v}_\theta+\lambda m\gamma-2m\alpha_0^2\mu\tilde{v}_\theta-\alpha_0^2mD\tilde{v}_\theta=0}. \tag{6.32}$$

Now consider eq.(6.25) and first multiply it with R_0/H_0 to get

$$\sin^2\theta\frac{\partial}{\partial t}\left(\frac{hR_0}{H_0}\right)+\sin\theta\frac{\partial \mathbf{v}_\theta}{\partial\theta}+\frac{\partial \mathbf{v}_\phi}{\partial\phi}=0. \tag{6.33}$$

Then using the Pythagorean identity $\sin^2\theta + \cos^2\theta = 1$ and applying a Fourier analysis of the form $\exp(-i\omega t + im\phi)$ it follows that

$$(1-\cos^2\theta)\left(\frac{hR_0}{H_0}\right)(-i\omega) + \sin\theta\frac{\partial}{\partial\theta}\mathbf{v}_\theta + im\mathbf{v}_\phi = 0, \tag{6.34}$$

where m is the toroidal wavenumber and ω is the wave frequency.

Next, multiply with i throughout, and only the first term with a specific fraction gives

$$\left(\frac{4\,\Omega_0^2\,R_0^2\,g}{4\,\Omega_0^2\,R_0^2\,g}\right)(1-\cos^2\theta)\left(\frac{hR_0\,\omega}{H_0}\right) + \sin\theta\frac{\partial}{\partial\theta}i\mathbf{v}_\theta - m\mathbf{v}_\phi = 0. \tag{6.35}$$

Simplifying eq.(6.35) results in

$$\left(\frac{4\Omega_0^2 R_0^2}{gH_0}\right)\left(\frac{\omega}{2\Omega_0}\right)(1-\cos^2\theta)\left(\frac{gh}{2\Omega_0 R_0}\right) + \sin\theta\frac{\partial}{\partial\theta}i\mathbf{v}_\theta - m\mathbf{v}_\phi = 0. \tag{6.36}$$

Then, by substituting the relevant parameters defined in eq.(6.30) and setting $i\mathbf{v}_\theta = \tilde{v}_\theta$ it can be written as

$$\boxed{\epsilon\lambda(1-\mu^2)\gamma - D\tilde{v}_\theta - m\mathbf{v}_\phi = 0}. \tag{6.37}$$

The next step is to make $\mathbf{v}_\phi$ the subject of eq.(6.32)

$$\mathbf{v}_\phi = -\frac{\mu}{\lambda}\tilde{v}_\theta + \frac{m\gamma}{\lambda} - \frac{2m\alpha_0^2\mu}{\lambda^2}\tilde{v}_\theta - \frac{\alpha_0^2}{\lambda^2}mD\tilde{v}_\theta, \tag{6.38}$$

and substitute it into eq.(6.31) and eq.(6.37) respectively to get

$$-\lambda^2\tilde{v}_\theta + \mu^2\tilde{v}_\theta - (\lambda D + m\mu)\gamma + \mu m\frac{\alpha_0^2}{\lambda}(D+2\mu)\tilde{v}_\theta + m^2\alpha_0^2\tilde{v}_\theta + 2\alpha_0^2\mu D\tilde{v}_\theta = 0, \tag{6.39}$$

and

$$\epsilon\lambda(1-\mu^2)\gamma - D\tilde{v}_\theta + \frac{m}{\lambda}(\mu\tilde{v}_\theta - m\gamma) + \frac{\alpha_0^2}{\lambda^2}m^2(D+2\mu)\tilde{v}_\theta = 0. \tag{6.40}$$

To write eq.(6.39) and eq.(6.40) as one in terms of $\tilde{v}_\theta$, we first get γ from eq.(6.40) and multiply it with λ to simplify the equation. The result is given as

$$-\gamma = \frac{1}{m^2 - \epsilon\lambda^2(1-\mu^2)}\left[\lambda D - m\mu - \frac{\alpha_0^2}{\lambda^2}m^2\lambda(D+2\mu)\right], \tag{6.41}$$

which is then substituted into eq.(6.39) to get

$$
\begin{aligned}
(\lambda D + m\mu)\left\{\frac{1}{m^2 - \epsilon\lambda^2(1-\mu^2)}\left[\lambda D - m\mu - \frac{\alpha_0^2}{\lambda}m^2(D+2\mu)\right]\right\}\tilde{v}_\theta \\
-(\lambda^2-\mu^2)\tilde{v}_\theta + m^2\alpha_0^2\tilde{v}_\theta + 2\alpha_0^2\mu D\tilde{v}_\theta + \mu m\frac{\alpha_0^2}{\lambda}(D+2\mu)\tilde{v}_\theta = 0.
\end{aligned}
\tag{6.42}
$$

However, in this formulation of the MHD Rossby wave model, the Lamb parameter, defined as

$$
\boxed{\epsilon = \frac{4\Omega_0^2 R_0^2}{gH_0}}, \tag{6.43}
$$

in eq.(6.30), where g is gravity, was assumed to be small, such that

$$
\frac{\epsilon}{m^2} \ll 1, \tag{6.44}
$$

where m is the toroidal wavenumber. This approximation holds because of the Sun's slow rotation (Zaqarashvili et al., 2007) and was subsequently omitted from the eq.(6.42), such that we get

$$
\begin{aligned}
\Big[(\lambda D + m\mu)(\lambda D - m\mu) - \frac{\alpha_0^2}{\lambda}m^2(\lambda D + m\mu)(D+2\mu) - m^2(\lambda^2-\mu^2) \\
+m^4\alpha_0^2 + 2\alpha_0^2 m^2\mu D + \mu m^3\frac{\alpha_0^2}{\lambda}(D+2\mu)\Big]\tilde{v}_\theta = 0.
\end{aligned}
\tag{6.45}
$$

However, Zaqarashvili et al. (2007) acknowledged that by applying this approximation, the stratification of the solar tachocline, which is different for the upper and lower layers (Gilman, 2000), was not considered in their model derivation. By incorporating the fluid stratification of the respective tachocline layers into the modelling, the gravity in the Lamb parameter is affected. Therefore, exploring the dynamics and stratification of the two tachocline layers is necessary and will be discussed next.

6.3 Effective gravity in the tachocline

To explain how fluid stratification affects gravity, we first need to consider buoyancy. **Buoyancy** is the upward force experienced by an object submerged within a fluid whose density differs from that of the fluid. When the density of the object is less than the density of the surrounding fluid, the object experiences positive buoyancy and floats. In contrast, when the object's density exceeds the fluid's, the negative buoyancy will cause the object to sink.

Furthermore, to discuss the different types of stratification of fluid layers, we will consider the tachocline and the convection zone as examples demonstrating the different dynamics since they exhibit subadiabatic and superadiabatic stratification, respectively.

Firstly, the fluid temperature decreases with increasing height in a **subadiabatic environment**. Therefore, a fluid parcel at the top of the fluid layer corresponds to a lower temperature, causing an increase in the fluid density. In the case of subadiabatic fluid stratification, the negative buoyancy of the fluid parcel causes it to sink more easily. This results in the fluid effectively experiencing a stronger downward gravitational force, referred to as the **effective gravity**. This variation in gravity is the net force that accounts for any other forces in the same or opposite direction as the gravitational force. From this, we can conclude that larger effective gravity values correspond to heavier fluids (Dikpati et al., 2017).

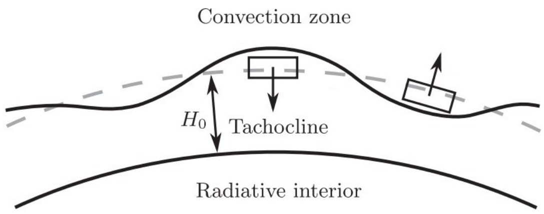

Figure 6.2: The tachocline, with an average depth of H_0, has a rigid bottom and a free upper surface that can deform and partially be pushed further into the convection zone. The small effective gravity due to the superadiabatic convection zone will offer little resistance to upward buoyancy motions for the upper tachocline. The subadiabatic stratification in the lower tachocline increases the effective gravity, leading to negative buoyancy and causing plasma to sink. Adapted image courtesy of Horstmann et al. (2022).

On the other hand, a **superadiabatic environment**, where temperature increases with height, reduces the fluid density at the top of the layer and subsequently strengthens the buoyancy force in that region. Therefore, since fluids with smaller effective gravity values are lighter, the top of such liquid will be more easily deformed.

This is an important observation, as the lower tachocline exhibits higher effective gravity values than the characteristically low values of the upper tachocline (Dikpati et al., 2017). Thus, the dynamics of the lower tachocline are expected to be much more stable than the less stable environment of the upper tachocline. From this observation, one could argue that when considering the upper and lower tachocline layers separately, only the upper tachocline aligns with the environment associated with the shallow water system (a rigid bottom with a free upper surface). Consequently, the shallow water equations are more suitable to the upper tachocline and might be less appropriate when applied to the lower tachocline. However, it will be shown in this study that although the layer depth, H_0, forms part of the equations, it is set to a constant but different value for the upper and lower tachocline, respectively. As a result, it would not be detrimental to use shallow water equations in the context of the lower tachocline despite the lack of a top surface that is easily deformed.

Furthermore, in the solar tachocline literature, the effective gravity discussed here is commonly referred to as “reduced gravity”. However, this terminology must be corrected, as these two terms have very different meanings. Reduced gravity describes an environment that exhibits a gravitational force less than what is experienced on Earth (Persad, 2017). However, in the context of the Sun, it has been suggested that the fluid stratification could either reduce (superadiabatic) or increase (subadiabatic) the normal solar gravity. Therefore, the term “reduced gravity” is inaccurate, whereas “effective gravity” describes this phenomenon better.

Nevertheless, the MHD Rossby wave model was subsequently improved by considering the effective gravity of the respective tachocline layers instead of the standard solar gravity (Zaqarashvili et al., 2009), as Gilman (2000) and Zaqarashvili et al. (2007) suggested.

6.3.1 Impact of considering effective gravity on the base MHD Rossby wave model in spherical coordinates

Since the concept of effective gravity has been explained, we should consider how it affects the MHD Rossby wave model. This is done by exploring the possible values of the Lamb parameter, ϵ given by eq.(6.43), as this parameter includes the gravity variable. However, since this second enhancement of the MHD Rossby wave model replaces the gravity variable, g in eq.(6.43), with the effective gravity value, g_e, the ϵ parameter is now written as

$$\epsilon = \frac{4\Omega_0^2 R_0^2}{g_e H_0}. \tag{6.46}$$

By then considering the non-zero case ($\epsilon \neq 0$) for eq.(6.46), it enables us to adjust the values of the effective gravity and the layer thickness, H_0, such that we get different values for ϵ which is specific to the respective tachocline layers. Table 8.2 below lists the constant values used in this calculation.

Parameter	Symbol	LTC value	UTC value
Distance from center of Sun to the tachocline	R_0	$5 \times 10^{10}\,\mathrm{cm}$	$5 \times 10^{10}\,\mathrm{cm}$
Rotation rate	Ω_0	$2.6 \times 10^{-6}\,\mathrm{s}^{-1}$	$2.6 \times 10^{-6}\,\mathrm{s}^{-1}$
Layer thickness	H_0	$10^9\,\mathrm{cm}$	$5 \times 10^8\,\mathrm{cm}$
Effective gravity	g_e	$(500 - 1.5 \times 10^4)\,\mathrm{cm\,s}^{-2}$	$(0.05 - 5)\,\mathrm{cm\,s}^{-2}$

Table 6.1: Constant parameter values for the lower (LTC) and upper (UTC) tachocline layers used to calculate the ϵ value. The values of R_0, Ω_0, and H_0 are given by Zaqarashvili et al. (2009). Whereas the effective gravity range of values is provided by Schecter et al. (2001).

The respective ranges are $\epsilon = (4.5 \times 10^{-3} - 0.13)\,\mathrm{cm\,s}^{-2}$ (Zaqarashvili et al., 2009) for the lower tachocline and $\epsilon = (27 - 2.7 \times 10^3)\,\mathrm{cm\,s}^{-2}$ (Zaqarashvili et al., 2009) for the upper overshoot layer. In other words, the ϵ value for the lower tachocline satisfied the $\epsilon \ll 1$ case, contrary to the upper tachocline, for which $\epsilon \gg 1$ holds (Zaqarashvili et al., 2009). These two extreme cases for the ϵ value indicate how the effective gravity impacts the MHD Rossby wave model, as the respective approximations must be applied to derive the associated model.

The next step is to determine whether a specific tachocline layer or both should be considered in relation to space weather events. To accomplish this step, we first need to consider the various time scales that show an increase in solar activity to make an informed decision.

6.4 Different periodicities of solar activity

This study aims to further our understanding of the connection between MHD Rossby waves in the tachocline and solar activity, which causes significant changes in space weather. However, an increase in solar activity associated with space weather events is observed over specific periods. In Section 2.4, we have established that we are only interested in the periodicity referred to as a solar season, which ranges from 6-18 months. Limiting the study to only consider space weather patterns on the lower end of the solar seasonal periodicity (roughly 180 days) allows us to be more specific about the MHD Rossby wave model we will be considering.

To briefly review the available models, we must recall the two MHD Rossby wave model developments discussed until now. The first is that the magnetic field splits the HD Rossby wave into fast and slow modes (Zaqarashvili et al., 2007), and the second is that when the effective gravity is considered, the MHD Rossby waves in the upper and lower tachocline are treated separately (Zaqarashvili et al., 2009). In the study of the equatorial MHD shallow water waves in the upper tachocline, Zaqarashvili et al. (2018) determined that the fast MHD Rossby waves in the upper tachocline correspond to periods close to that of the Schwabe cycle (Schwabe, 1844), roughly 11 years, and the slow MHD Rossby wave exhibits a periodicity of 90-100 years. Since both these periodicities extend over many years, they will not be associated with the acute space weather changes we are interested in studying here. Therefore, neither one of the MHD Rossby waves in the upper tachocline will be considered in the remainder of this study.

On the other hand, the fast and slow MHD Rossby wave modes in the lower tachocline correspond to periodicities of less than a year and greater than a year, respectively. The specific periodicity depends on the specific wavenumber and magnetic field strength considered in the MHD Rossby wave model. Nonetheless, based on the same argument for neglecting the MHD Rossby waves in the upper tachocline, the slow MHD Rossby waves in the lower tachocline also exhibit periodicities that are longer than what is considered in this study and will therefore not be considered going forward. This leads us to conclude that this study will only consider the fast MHD Rossby wave mode in the lower tachocline to calculate the magnetic field strength on a more granular level to increase its accuracy.

Since the specific MHD Rossby wave model that will be used in this study has been identified, we can now apply the appropriate effective gravity value for the lower tachocline (where $\epsilon \ll 1$) to get the associated MHD Rossby wave dispersion relation. However, it is worth noting that although we are only interested in the fast MHD Rossby wave mode, the slow mode will always be one of the solutions of the dispersion relation and will thus be included in the derivations of the remaining MHD Rossby wave models for completeness.

6.5 Effective gravity MHD Rossby wave model

Now, we can continue the derivation of the MHD Rossby wave model in the lower tachocline that considers the effective gravity by applying the $\epsilon \ll 1$ approximation (Section 6.3.1) and by further considering a weak magnetic field, such that the α parameter given in eq.(6.30)

$$\alpha_0 = \frac{B_0^2}{4\Omega_0^2 R_0^2 (4\pi\rho)} = \frac{v_A^2}{4\Omega_0^2 R_0^2} \tag{6.47}$$

is approximated as $\alpha_0^2 \ll 1$ (Zaqarashvili et al., 2009). As a result of applying these two approximations, we can neglect the terms in eq.(6.42) containing α_0^2 to get

$$\left[(\lambda D + m\mu)\left\{\frac{1}{m^2 - \epsilon\lambda^2(1-\mu^2)}(\lambda D - m\mu)\right\} - (\lambda^2 - \mu^2)\right] \tilde{v_\theta} = 0, \tag{6.48}$$

where m is the toroidal wavenumber.

Then recall that the wavelength, λ, is defined in eq.(6.30) as

$$\lambda = \frac{\omega}{2\Omega_0}, \tag{6.49}$$

which is subsequently used to define

$$m' = \frac{m}{\lambda} = \frac{2\Omega_0 m}{\omega}. \tag{6.50}$$

It follows that eq.(6.48) can be simplified by considering the identity given by Longuet-Higgins's (1965) eq.(13) repeated below

$$(D + m'\mu)(D - m'\mu) \equiv (1-\mu^2)(\nabla_D^2 - m') + (m^2 - m'^2\mu^2) \tag{6.51}$$

where

$$\nabla_D \equiv \frac{\partial}{\partial\mu}\left[(1-\mu^2)\frac{\partial}{\partial\mu}\right] - \frac{m^2}{1-\mu^2}, \tag{6.52}$$

according to eq.(14) in the study by Longuet-Higgins (1965), such that eq.(6.48) becomes

$$\left[(\nabla_D^2 - m') - \frac{2\epsilon\mu}{m'^2 - \epsilon(1-\mu^2)}(D - m'\mu) + \epsilon(\lambda^2 - \mu^2)\right] \tilde{v_\theta} = 0. \tag{6.53}$$

Moreover, if we consider the non-divergent approximation according to eq.(17) in Longuet-Higgins (1965)

$$\frac{\epsilon}{m'} \to 0 \tag{6.54}$$

which is similar to eq.(6.44), then the first term in eq.(6.53)

$$(\nabla_D^2 - m')\tilde{v_\theta} = 0 \tag{6.55}$$

can be set to zero as given by eq.(18) in Longuet-Higgins (1965). It can be noted that the typical solutions of eq.(6.55) are the Legendre functions of the first kind

$$\tilde{v_\theta} = P_n^m(\cos\theta)e^{(im\phi - i\omega t)} \tag{6.56}$$

only if

$$m' = \frac{2\Omega_0 m}{\omega} = -n(n+1), \tag{6.57}$$

where n is the poloidal wavenumber (from eq.(19) and eq.(20) in Longuet-Higgins, 1965). However, the m', or n^2 values must be large for the non-divergent approximation to be valid. Therefore, if we consider the wider assumption of

$$\frac{\epsilon}{m'} \leq O(1) \tag{6.58}$$

it allows us to compare the order of the terms in eq.(6.53) when n is large and, according to eq.(6.57), $m = O(n^2)$ (Longuet-Higgins, 1965).

It follows that both ∇_D^2 and ϵ are of order n^2. Conversely, we see that $D = O(n)$ and $\lambda = m/m' = O(m/n^2) \leq O(1/n)$. If we subsequently neglect all the terms in eq.(6.53) that are of the order $O(1)$ or less and retaining those of $O(n^2)$, we get the following simplified equation

$$\left[(\nabla_D^2 - m') - \epsilon\mu^2\right]\tilde{v_\theta} = 0, \tag{6.59}$$

which can be written in terms of $\mu = \cos\theta$ given in eq.(6.30), such that it becomes

$$\left[\frac{d}{d\mu}\left\{(1-\mu^2)\frac{d}{d\mu}\right\} - \left(\frac{m^2}{1-\mu^2} + \epsilon\mu^2 + m'\right)\right]\tilde{v_\theta} = 0. \tag{6.60}$$

This form of eq.(6.60) shows that it has been transformed to be the spheroidal wave equation (Abramowitz and Stegun, 1964; Longuet-Higgins, 1965). Therefore, the solutions to eq.(6.60) are the spheroidal wave functions, $S_n^m(\sqrt{\epsilon}, \mu)$, which are finite over $-1 \leq \mu \leq 1$ and go to zero at the poles, $\mu = \pm 1$ (Zaqarashvili et al., 2009).

Then, by using the tables for the computation of $S_n^m(\sqrt{\epsilon}, \mu)$ the approximated solution is given by

$$\tilde{v_\theta} \propto A_0 S_n^m(\epsilon_1, \mu)\sqrt{\frac{m^2 - \epsilon\lambda^2(1-\mu^2)}{\lambda^2 - m^2\alpha_0^2\mu^2}} \tag{6.61}$$

(Stratton et al., 1956; Abramowitz and Stegun, 1964; Zaqarashvili et al., 2009), where A_0 represents the amplitude, and ϵ_1 (Zaqarashvili et al., 2009) is written as follows

$$\epsilon_1 = \sqrt{\epsilon\left(1 + 3\frac{\lambda^2}{m^2} - 2\frac{\lambda}{m}\right) + \frac{\alpha_0^2 m^2}{\lambda^2}\left(7 + \frac{m}{2\lambda}\right)} \tag{6.62}$$

for which the associated dispersion relation (Zaqarashvili et al., 2009) is given by

$$\overbrace{\epsilon(m^2+1)\left(\frac{\lambda}{m}\right)^4 - n(n+1)\left(\frac{\lambda}{m}\right)^2}^{\text{High frequency branch}}\hspace{-9em}\underbrace{\phantom{-n(n+1)\left(\frac{\lambda}{m}\right)^2} - \left(\frac{\lambda}{m}\right) + \alpha_0^2}_{\text{Low frequency branch}} = 0, \tag{6.63}$$

Similar to the structure of the dispersion relation in Chapter 5, the dispersion relation contains a high and a low-frequency branch. Here, the first two terms of eq.(6.63) represent the high-frequency branch that is associated with the magnetic Poincaré waves, which will not be discussed. On the other hand, the dispersion relation of the magnetic Rossby waves stems from the low-frequency branch solution, which consists of the last three terms on the left-hand side of eq.(6.63), therefore

$$n(n+1)\left(\frac{\lambda}{m}\right)^2 + \frac{\lambda}{m} - \alpha_0^2 = 0. \tag{6.64}$$

It is worth mentioning that by substituting

$$\lambda = \frac{\omega}{2\Omega_0} \quad \text{and} \quad \alpha_0 = \frac{B_0}{2\Omega_0 R_0\sqrt{4\pi\rho}}, \tag{6.65}$$

into eq.(6.64) it can also be written in the following form

$$n(n+1)\left(\frac{\omega}{2\Omega_0 m}\right)^2 + \frac{\omega}{2\Omega_0 m} - \left(\frac{B_0}{2\Omega_0 R_0\sqrt{4\pi\rho}}\right)^2 = 0. \tag{6.66}$$

By next evaluating the square and multiplying with $4\Omega_0^2 m^2$ we get

$$n(n+1)\omega^2 + 2m\Omega_0\omega - \frac{B_0^2 m^2}{4\pi\rho R_0^2} = 0. \tag{6.67}$$

Nonetheless, the solutions of this dispersion relation according to eq.(6.64) will correspond to the fast and slow Rossby wave modes and can be calculated using the quadratic formula such that

$$\frac{\lambda}{m} = \frac{-1 \pm \sqrt{1 - 4n(n+1)(-\alpha_0^2)}}{2n(n+1)}, \tag{6.68a}$$

$$\frac{\lambda}{m} = \frac{-1 \pm \sqrt{1 + 4\alpha_0^2 n(n+1)}}{2n(n+1)}, \tag{6.68b}$$

$$\lambda = \frac{-m \pm m\sqrt{1 + 4\alpha_0^2 n(n+1)}}{2n(n+1)}. \tag{6.68c}$$

However, substituting $\lambda = \omega/2\Omega_0$ gives

$$\frac{\omega}{2\Omega_0} = \frac{-m \pm m\sqrt{1 + 4\alpha_0^2 n(n+1)}}{2n(n+1)}, \tag{6.69a}$$

$$\omega = \frac{-2m\Omega_0 \pm 2m\Omega_0\sqrt{1 + 4\alpha_0^2 n(n+1)}}{2n(n+1)}. \tag{6.69b}$$

Now set $\sqrt{1 + 4\alpha_0^2 n(n+1)} = (a+b)^x$, where $x = 1/2$, $a = 1$ and $b = 4\alpha_0^2 n(n+1)$. Then, by using binomial expansion in the form of

$$(a+b)^x = a^x + \frac{xa^{x-1}b}{1!} + \frac{x(x-1)a^{x-2}b^2}{2!} + \ldots, \tag{6.70}$$

we can write

$$\left[1 + 4\alpha_0^2 n(n+1)\right]^{\frac{1}{2}} = 1^{\frac{1}{2}} + \frac{1}{2}1^{\frac{1}{2}-1} \cdot 4\alpha_0^2 n(n+1) + \frac{\frac{1}{2}(\frac{1}{2}-1)1^{\frac{1}{2}-2} \cdot 16\alpha_0^4 n^2(n+1)^2}{2!} + \ldots \tag{6.71a}$$

$$= 1 + 2\alpha_0^2 n(n+1) - \frac{4\alpha_0^4 n^2(n+1)^2}{2!} + \ldots. \tag{6.71b}$$

By recalling that $\alpha_0^2 \ll 1$, we can ignore all the higher order terms in α_0 in eq.(6.69b) and simplify the equation to be

$$\omega = \frac{-2m\Omega_0 \pm 2m\Omega_0\left[1 + 2\alpha_0^2 n(n+1)\right]}{2n(n+1)}, \tag{6.72}$$

which gives the dispersion relation of the fast mode

$$\omega_+ \approx 2\Omega_0\alpha_0^2 m, \tag{6.73}$$

and slow MHD Rossby mode

$$\omega_- \approx \frac{-2\Omega_0 m}{n(n+1)} - 2\Omega_0 \alpha_0^2 m. \tag{6.74}$$

These and the other equations for the propagation properties are summarised below.

Lower tachocline MHD Rossby wave propagation properties ($\epsilon \ll 1$)

The dispersion relation of the low-frequency branch

$$n(n+1)\left(\frac{\lambda}{m}\right)^2 + \frac{\lambda}{m} - \alpha_0^2 = 0, \tag{6.64}$$

is given by

$$\omega = \frac{-2m\Omega_0 \pm 2m\Omega_0\sqrt{1+4\alpha_0^2 n(n+1)}}{2n(n+1)}, \tag{6.69b}$$

where the wavelength is given as

$$\lambda = \frac{\omega}{2\Omega_0}, \tag{6.49}$$

and the magnetic field strength parameter as

$$\alpha_0^2 = \frac{B_0^2}{4\Omega_0^2 R_0^2 (4\pi\rho)} = \frac{v_A^2}{4\Omega_0^2 R_0^2}. \tag{6.47}$$

Fast MHD Rossby wave equations (high-frequency solution)

Dispersion relation $$\omega_- \approx 2\Omega_0 \alpha_0^2 m \tag{6.73}$$

Phase and group velocity $$\frac{\omega_-}{m} = \frac{\partial \omega_-}{\partial m} = 2\Omega_0 \alpha_0^2 \tag{6.75}$$

Slow MHD Rossby wave equations (low-frequency solution)

Dispersion relation $$\omega_+ \approx -\frac{2\Omega_0 m}{n(n+1)} - 2\Omega_0 \alpha_0^2 m \tag{6.74}$$

Phase and group velocity $$\frac{\omega_+}{m} = \frac{\partial \omega_+}{\partial m} = -\frac{2\Omega_0}{n(n+1)} - 2\Omega_0 \alpha_0^2 \tag{6.76}$$

6.6 Discussion

Throughout the study, emphasis was placed on both the model's accuracy and the parameter values utilised in conjunction with it. Therefore, we will discuss each of these points separately for the effective gravity model. Also, note that even though we are only interested in the fast MHD Rossby wave, the corresponding slow magneto-Rossby wave mode will also be included in the following discussion for completeness.

6.6.1 Wave behaviour

The study done by Zaqarashvili et al. (2009) shows that the presence of a magnetic field splits the ordinary Rossby wave into fast (blue solid lines) and slow (red dashed lines) MHD Rossby modes, as indicated by the two dispersion relations, eq.(6.73) and eq.(6.74), which is also displayed in Fig.(6.3a). Therefore, this splitting phenomenon is not unique to the Cartesian coordinate Rossby wave model but also holds for the model derived in spherical coordinates. However, the dispersive behaviour of the base model's (Chapter 5) MHD Rossby waves is not observed here, which is indicated by the same phase and group velocity equations for the fast, eq.(6.75), and slow eq.(6.76), MHD Rossby waves of the effective gravity model. Nonetheless, these two wave modes continue to travel in opposite directions, with the fast and slow MHD Rossby wave travelling westwards and eastwards, respectively.

In this effective gravity model, the dispersion relations, eq.(6.73) and eq.(6.74), include the α_0 parameter, indicating that the magnetic field affects both the fast and slow magneto-Rossby waves. It is, therefore, necessary to investigate the change in the propagation properties of these waves due to variations in the magnetic field strength. This is achieved by using eq.(6.64), which includes both the fast and slow MHD Rossby wave dispersion relations and considering a range of $0 < \alpha_0 \leq 0.5$ (Zaqarashvili et al., 2009) to create Fig.(6.3b) below.

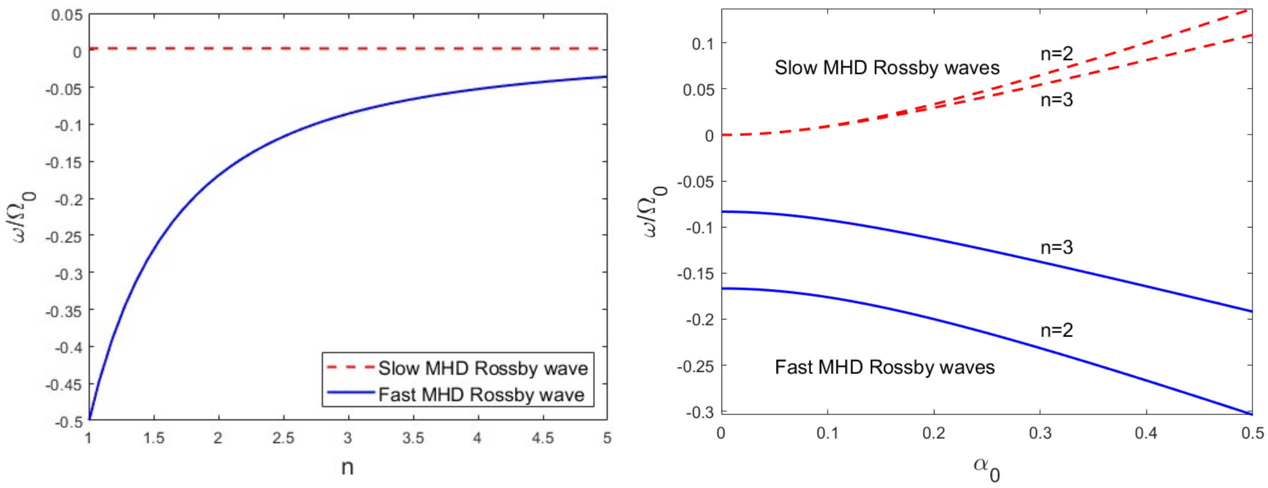

(a) Dispersion relations, varying n, $\alpha_0 = 0.05$.

(b) Dispersion relations, $n = 2, 3$, varying α_0.

Figure 6.3: The two solutions of the low-frequency branch, given by eq.(6.64) and setting $m = 1$, which corresponds to the fast and slow MHD Rossby wave modes when effective gravity was included in the model.

In Fig.(6.3b), the red dashed lines and the solid blue lines show the $m = 1$, $n = 2$ and $m = 1$, $n = 3$ harmonics of the slow and fast magneto-Rossby wave dispersion relations, respectively, where m is the toroidal wavenumber and n the poloidal wavenumber. From Fig.(6.3b), the difference in behaviour between the two MHD Rossby wave branches is clear. The frequency of both MHD Rossby waves increases with increased magnetic field strength. Furthermore, when considering the fast MHD Rossby wave dispersion relations, the difference between the frequency of the $n = 2$ and $n = 3$ harmonic remains close to constant as the magnetic field strength increases. The same can not be said for the slow MHD Rossby waves. For this Rossby wave, the $n = 2$ and $n = 3$ harmonics have the same frequency values until α reaches a value of ~ 0.1 ($B_0 = 4 \times 10^4$G), after which they diverge for stronger magnetic field strengths. We can also see that the $n = 2$ harmonic increases slightly more for the slow MHD Rossby wave. However, the fast magneto-Rossby wave is significantly affected as the magnetic field strength increases.

6.6.2 Parameter values

To ensure that the Rossby wave model applies to solar activity observations from various stages of the solar cycle, which have been shown to migrate towards the equator over time, latitude is, therefore, a non-negotiable parameter that must be included in the Rossby wave model. In the Cartesian model, latitude was included through the β-parameter as a result of applying the β-plane approximation for the Coriolis parameter. However, in the spherical

MHD Rossby wave model, the β-parameter is no longer present, and the latitude is now only included in the magnetic field profile given by eq.(6.22) as $B_\phi = B_0 \sin\theta$.

Moreover, when the $\epsilon \neq 0$ case is considered, it follows that the ϵ parameter is present in the MHD Rossby wave model, allowing the effective gravity and the layer thickness of the tachocline to play a role in the model. However, we observed that the ϵ parameter only affects the high-frequency modes, whilst the low-frequency wave modes remain unchanged. Therefore, this model enhancement, which considers the specific environmental characteristics of the two tachocline layers, has very important consequences, which will be discussed next.

6.7 Summary

The spherical MHD Rossby wave model derived by Zaqarashvili et al. (2007) has been amended by considering the tachocline's stratification (Zaqarashvili et al., 2009). The tachocline's lower, more stable part exhibits a subadiabatic stratification, which causes the effective gravity that is experienced in this layer to be much larger than for the upper part of the tachocline. To include this layer-specific effective gravity and fluid layer thickness in the Rossby wave model, the Lamb parameter,

$$\epsilon = \frac{4\Omega_0^2 R_0^2}{g_e H_0}, \tag{6.46}$$

is used. It has been shown by Zaqarashvili et al. (2009) that the upper and lower layers of the tachocline each have their own Lamb parameter approximation, which satisfies the conditions of $\epsilon \gg 1$ and $\epsilon \ll 1$, respectively. By using these sub-layer-specific Lamb parameter approximations, MHD Rossby waves can be modelled separately for the upper and lower tachocline, resulting in accurate research that captures the specific environmental characteristics of each layer.

However, we are interested in the connection between solar MHD Rossby waves, magnetic field strength, and space weather. Observational data can help narrow the scope of models to be considered for this research. Therefore, Section 6.4 in this chapter identified the solar season time scale as the periodicity of increased solar activity we are interested in studying.

Specifically, we will focus on the lower range of this periodicity, which corresponds to less than 180 days and will include the well-recorded observed Rieger-type periodicity (RTP) of 150-195 days (Section 2.4.1). It has been shown that given a fixed set of input parameters, only the fast MHD Rossby mode in the lower tachocline has a frequency that falls within the observed RTP range. On the other hand, the slow MHD Rossby wave mode in the lower tachocline has periodicities that are generally longer than a year and will not be considered. Similarly, the fast and slow MHD Rossby wave modes in the upper tachocline are associated with periodicities of 11 years and 90-100 years, respectively, and are also omitted from this study. Therefore, we will only consider the fast MHD Rossby waves in the lower tachocline.

Since the approximation of $\epsilon \ll 1$ holds for the MHD Rossby wave model of the lower tachocline, the base model derived in Chapter 5 using the shallow water equations in spherical coordinates (Zaqarashvili et al., 2007) is also applicable to the lower tachocline. Although the Lamb parameter approximation influenced the formulation of the wave model for the lower tachocline, it is not explicitly included in the low-frequency branch of the dispersion relation associated with the MHD Rossby waves. Therefore, the effective gravity and the fluid layer thickness of the lower tachocline have no direct impact on the propagation properties of the MHD Rossby waves, the low-frequency modes. However, applying the shallow water approximation, which introduces these variables to the governing equations, allows valuable approximations to enter the modelling process. Additionally, the results of Zaqarashvili et al. (2009) confirmed that the magnetic field is responsible for splitting the ordinary Rossby wave into the fast and slow Rossby modes, consistent with the observation from the Cartesian MHD Rossby wave model derived by Zaqarashvili et al. (2007). Nonetheless, in this chapter, we have discussed the essential contributions to the MHD Rossby wave modelling by considering the impact of the effective gravity of the two tachocline layers in the modelling process. However, to further enhance the model's accuracy, we need to include the solar characteristic of latitudinal differential rotation (Section 3.5.1).

7 Latitudinal differential rotation MHD Rossby wave model

7.1 Introduction

In this chapter, we will discuss the addition of latitudinal differential rotation (LDR) to the magnetohydrodynamic (MHD) Rossby wave model in the lower tachocline. The LDR is a fundamental characteristic of the Sun's dynamics that was previously neglected in the MHD Rossby wave model (Zaqarashvili et al., 2007, 2009) as it would not significantly affect the resulting MHD Rossby wave dispersion relations[1] (Zaqarashvili, 2018). However, Gurgenashvili et al. (2016) have shown that LDR should be considered as it may influence the spectrum of the resulting Rossby waves. Finally, since it is a fundamental characteristic of the Sun's dynamics, we argue that it should be included in the MHD Rossby wave modelling (Zaqarashvili et al., 2007, 2009) to ensure that it is as comprehensive as possible.

The first step is to identify what governing equations will be used in deriving the MHD Rossby wave model in this chapter, which will now include the effects of LDR. Let us, therefore, start by considering the shallow water governing equations (SWEs) previously used in Chapter 5 and Chapter 6 to derive the base and effective gravity MHD Rossby wave models, respectively. However, we should also recall that the variable associated with the fluid layer thickness is included in the SWEs, and this variable's necessity should be explored here.

To this end, recall that one way the layer thickness enters the governing equations is through the Lamb parameter ϵ given below

$$\epsilon = \frac{4\Omega_0^2 R_0^2}{g_e H_0}. \tag{6.46}$$

In Chapter 6, we showed that the value of this parameter is different for the upper and lower tachocline layers because it uses their respective effective gravity and layer thickness

[1]Another reason for omitting latitudinal differential rotation from the MHD Rossby wave model in the tachocline was due to the possibility that it would lead to instabilities of certain wave modes (Zaqarashvili et al., 2009; Zaqarashvili, 2018), which falls outside the scope of this study.

values. It was subsequently concluded that the approximation of $\epsilon \ll 1$ is applicable to the shallow water governing equations when considering the lower tachocline, which is the layer we are interested in studying, and it also applies to slowly rotating stars, such as the Sun (Zaqarashvili et al., 2007). However, the resulting MHD Rossby wave model that assumed $\epsilon \ll 1$ (Section 6.5) showed that the ϵ parameter is not explicitly included in the dispersion relations for the fast and slow (low frequency) MHD Rossby waves in the lower tachocline. Based on this observation, it can be concluded that the layer thickness and effective gravity do not directly impact the behaviour of the MHD Rossby waves in the lower tachocline.

Moreover, as a result of applying the $\epsilon \ll 1$ approximation, high-frequency waves such as surface gravity waves, or more specifically Poincaré waves, are no longer present in the wave equation, and only Rossby waves remain (Zaqarashvili et al., 2007). Therefore, neglecting the parameters associated with the Lamb parameter has the additional benefit of isolating Rossby wave behaviour in the dispersion relation. From the two arguments provided here, it is important to recall that the simplified governing equations, derived in the first part of Chapter 4, only assume an ideal fluid, and neither the fluid layer thickness nor effective gravity entered these equations. Therefore, these governing equations are also appropriate for the derivation of the MHD Rossby wave model, which will be discussed in this chapter.

The last model enhancement of including LDR was done by two primary studies that will be discussed in this chapter: Zaqarashvili et al. (2010) and Gurgenashvili et al. (2016). Zaqarashvili et al. (2010) were the first to add the effect of LDR to model solar MHD Rossby waves. Their study focused primarily on conducting a stability analysis of MHD Rossby waves. They used the simplified MHD governing equations (without the shallow water approximation as discussed above) and adapted them to include the LDR in a rotating frame for an incompressible fluid. Since then, these simplified governing equations, which include the dynamics of the LDR, have been used to derive the explicit dispersion relation for the magneto-Rossby waves (Gurgenashvili et al., 2016) in the context of the lower tachocline.

Therefore, the mathematical modelling presented in this chapter first follows what is set out by Zaqarashvili et al. (2010). After that, we will continue the derivation of the MHD Rossby wave model that includes LDR, for which the resulting dispersion relation corresponds to that given in Gurgenashvili et al. (2016). However, the first step in adding LDR to the Rossby wave model is to get a mathematical expression that describes this solar characteristic as accurately as possible.

7.1.1 Latitudinal differential rotation

Consequently, to address this gap in the modelling, where LDR is neglected, the following mathematical expression of the differential rotation

$$\Omega_d = \Omega_0(1 - s_2 \cos^2\theta - s_4 \cos^4\theta), \tag{7.1}$$

is used (Howard and Harvey, 1970). Here, Ω_0 is the equatorial solar angular velocity, θ is the co-latitude, and s_2 and s_4 are newly introduced constant differential rotation parameters determined by solar observations. Later, Snodgrass (1982) summarised the solar rotation profiles by fitting them with the following functional form

$$\omega(\phi) = A + B\sin^2\phi + C\sin^4\phi, \tag{7.2}$$

where ϕ is the solar latitude. In eq.(7.2) the coefficient A is considered the absolute rotation rate compared to B and C that describe the differential rotation. The differential rotation formulation given by eq.(7.2) also shows significant agreement with the well-accepted findings of Newton and Nun (1951), who calculated the Sun's rotation based on sunspots. Next, Goode and Dziembowski (1991) derived another formulation of the LDR at the base of the convection zone, given by

$$\frac{\Omega_{cz}}{2\pi} = 462 - 64\cos^2\theta - 73\cos^4\theta. \tag{7.3}$$

However, the variations of the LDR given by eq.(7.2) and eq.(7.3) have not been used by any of the other more recent studies of the solar tachocline and will, therefore, not be considered further in this study.

Nevertheless, a few points should be considered regarding the LDR profile described by eq.(7.1). Firstly, concern was raised that the estimated s_4 parameter values may contain significant errors due to the uncertainty of the differential rotation at high latitudes ($\theta > 45°$) (Gurgenashvili et al., 2016). Secondly, Zaqarashvili et al. (2010) noted that the last term of eq.(7.1) will mainly be significant for higher latitudes. Thirdly, it is observed in studies that included the s_4 term in eq.(7.1) (Zaqarashvili et al., 2010), that the value was set to be $s_2 \approx s_4$. This approximation for the LDR parameters also contributes to the argument that the confidence in the value of the s_4 parameter is low. For these reasons, it is suggested by Zaqarashvili et al. (2010) that eq.(7.1) should be simplified as follows

$$\Omega_d = \Omega_0(1 - s_2 \cos^2 \theta) = \Omega_0 + \Omega_1(\theta), \tag{7.4}$$

where

$$\Omega_1(\theta) = -\Omega_0 s_2 \cos^2 \theta. \tag{7.5}$$

However, it is worthwhile to investigate the effect of neglecting this s_4 term on the resulting angular rotation values, see Fig.(7.1).

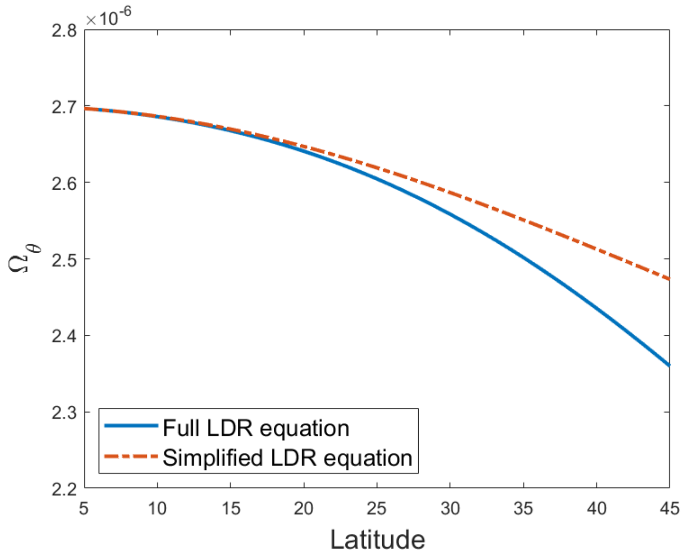

Figure 7.1: The variation of the latitudinal differential rotation Set $s_2 = s_4 = 0.168$ and $\Omega_0 = 2.7{\times}10^{-6}\ s^{-1}$. The blue solid line and the dashed orange line represent the formulation of the latitudinal differential rotation (LDR) as described by eq.(7.1) and eq.(7.4).

In Fig.(7.1), the solid blue and dashed orange lines represent the full and simplified LDR equations, corresponding to eq.(7.1) and eq.(7.4), respectively. These two LDR functions exhibit similar behaviour for lower latitudes. However, they diverge for latitudes $\Theta > 20°$. By further recalling that the waves in the lower tachocline are located in the mid-latitudinal region, which will only extend up to $30°$, the error using the simplified LDR equation is insignificant and can be used without concern.

7.2 LDR MHD Rossby wave model

Therefore, we can write the vectors for the unperturbed, $\mathbf{B}_0$, and perturbed, $\mathbf{B}_1$, magnetic field strength, and the velocity perturbations, $\mathbf{v}_1$, in spherical coordinates. By noting that the x- and y-direction in Cartesian coordinates corresponds to the ϕ- and θ-direction in spherical coordinates, we have from eq.(6.1), eq.(6.2), eq.(6.3)

$$\mathbf{B}_0 = (0, 0, B_\phi), \quad \mathbf{B}_1 = (0, b_\theta, b_\phi), \quad \mathbf{v}_1 = (0, v_\theta, v_\phi),$$

respectively, and eq.(6.6)

$$\nabla = R_0 \frac{\partial}{\partial r}\hat{\boldsymbol{r}} + \frac{1}{R_0 \sin\theta}\frac{\partial}{\partial \theta}\sin\theta\,\hat{\boldsymbol{\theta}} + \frac{1}{R_0 \sin\theta}\frac{\partial}{\partial \phi}\hat{\boldsymbol{\phi}}\,.$$

Furthermore, we write

$$\mathbf{v}_0 = (0, 0, V_\phi). \tag{7.6}$$

7.2.1 Induction equation

The linearisation of the induction equation for the LDR model will differ from the spherical base model since the unperturbed velocity is not equal to zero but instead given by eq.(7.6), therefore, we will linearise the induction equation accordingly. Thus, we start by considering the induction equation given by eq.(4.53), which is repeated below

$$\frac{\partial \mathbf{B}}{\partial t} = \nabla \times (\mathbf{v} \times \mathbf{B}),$$

and expand it as follows

$$\frac{\partial}{\partial t}\big(\mathbf{B}_0 + \mathbf{B}_1\big) = \nabla \times \big[(\mathbf{v}_0 + \mathbf{v}_1) \times (\mathbf{B}_0 + \mathbf{B}_1)\big], \tag{7.7a}$$

$$\frac{\partial \mathbf{B}_0}{\partial t} + \frac{\partial \mathbf{B}_1}{\partial t} = \nabla \times \big[(\mathbf{v}_0 \times \mathbf{B}_0) + (\mathbf{v}_0 \times \mathbf{B}_1) + (\mathbf{v}_1 \times \mathbf{B}_0) + (\mathbf{v}_1 \times \mathbf{B}_1)\big]. \tag{7.7b}$$

Then considering that there is no time variation of the unperturbed magnetic field strength, B_0, the first term on the left-hand side is zero. Also, the cross product between two vectors in the same direction is zero, causing the first term on the right-hand side, $\nabla \times (\mathbf{v}_0 \times \mathbf{B}_0)$, to be zero. Lastly, it was previously argued that the product of two perturbation values, $\nabla \times (\mathbf{v}_1 \times \mathbf{B}_1)$, will be very small comparatively and as a result, may be dropped, simplifying eq.(7.7b) to be

$$\frac{\partial \mathbf{B}_1}{\partial t} = \nabla \times (\mathbf{v}_0 \times \mathbf{B}_1) + \nabla \times (\mathbf{v}_1 \times \mathbf{B}_0). \tag{7.8}$$

Let us now expand each term separately, starting with the left-hand side of eq.(7.8)

$$\frac{\partial \mathbf{B}_1}{\partial t} = \frac{\partial}{\partial t}\big(b_\theta\,\hat{\boldsymbol{\theta}} + b_\phi\,\hat{\boldsymbol{\phi}}\big), \tag{7.9a}$$

$$= \frac{\partial b_\theta}{\partial t}\,\hat{\boldsymbol{\theta}} + \frac{\partial b_\phi}{\partial t}\,\hat{\boldsymbol{\phi}}. \tag{7.9b}$$

By now recalling that the toroidal magnetic field (in the ϕ-direction) does not vary along the field line, we can conclude that only the variation in the θ-direction will be considered, giving

$$\frac{\partial \mathbf{B}_1}{\partial t} = \frac{\partial b_\theta}{\partial t}\,\hat{\boldsymbol{\theta}}. \tag{7.10}$$

The first term on the right-hand side of eq.(7.8) is calculated as follows

$$\mathbf{v}_0 \times \mathbf{B}_1 = \begin{vmatrix} \hat{\boldsymbol{r}} & \hat{\boldsymbol{\theta}} & \hat{\boldsymbol{\phi}} \\ 0 & 0 & V_\phi \\ 0 & b_\theta & b_\phi \end{vmatrix} \tag{7.11}$$

$$= (0 - b_\theta V_\phi)\;\hat{\boldsymbol{r}} - (0-0)\;\hat{\boldsymbol{\theta}} + (0-0)\;\hat{\boldsymbol{\phi}}, \tag{7.12}$$

$$= -b_\theta V_\phi\,\hat{\boldsymbol{r}} \tag{7.13}$$

which gives

$$\nabla \times (\mathbf{v}_0 \times \mathbf{B}_1) = \begin{vmatrix} \hat{\boldsymbol{r}} & \hat{\boldsymbol{\theta}} & \hat{\boldsymbol{\phi}} \\ 0 & \frac{1}{R_0 \sin\theta}\frac{\partial}{\partial\theta}\sin\theta & \frac{1}{R_0\sin\theta}\frac{\partial}{\partial\phi} \\ -b_\theta V_\phi & 0 & 0 \end{vmatrix} \tag{7.14}$$

$$= 0\,\hat{\boldsymbol{r}} - \left(0 - \left[-b_\theta V_\phi \frac{1}{R_0 \sin\theta}\frac{\partial}{\partial\phi}\right]\right)\,\hat{\boldsymbol{\theta}} + \left(0 - \left[-b_\theta V_\phi \frac{1}{R_0\sin\theta}\frac{\partial}{\partial\theta}\sin\theta\right]\right)\,\hat{\boldsymbol{\phi}}, \tag{7.15}$$

$$= -\frac{V_\phi}{R_0\sin\theta}\frac{\partial b_\theta}{\partial\phi}\hat{\boldsymbol{\theta}} + \frac{b_\theta}{R_0\sin\theta}\frac{\partial V_\phi}{\partial\theta}\sin\theta\,\hat{\boldsymbol{\phi}}. \tag{7.16}$$

The second term of eq.(7.8) is calculated following the same steps as those for the first term given above, therefore, not all the steps will be repeated below. Nonetheless, we first consider

$$\mathbf{v}_1 \times \mathbf{B}_0 = \begin{vmatrix} \hat{\boldsymbol{r}} & \hat{\boldsymbol{\theta}} & \hat{\boldsymbol{\phi}} \\ 0 & v_\theta & v_\phi \\ 0 & 0 & B_\phi \end{vmatrix} \tag{7.17}$$

$$= v_\theta B_\phi \, \hat{\boldsymbol{r}}, \tag{7.18}$$

which is then used to calculate

$$\nabla \times (\mathbf{v}_1 \times \mathbf{B}_0) = \begin{vmatrix} \hat{\boldsymbol{r}} & \hat{\boldsymbol{\theta}} & \hat{\boldsymbol{\phi}} \\ 0 & \frac{1}{R_0 \sin\theta}\frac{\partial}{\partial\theta}\sin\theta & \frac{1}{R_0\sin\theta}\frac{\partial}{\partial\phi} \\ v_\theta B_\phi & 0 & 0 \end{vmatrix} \tag{7.19}$$

$$= \frac{1}{R_0 \sin\theta}\frac{\partial}{\partial\phi}(v_\theta B_\phi)\hat{\boldsymbol{\theta}} - \frac{1}{R_0\sin\theta}\frac{\partial}{\partial\theta}\sin\theta(v_\theta B_\phi)\,\hat{\boldsymbol{\phi}}. \tag{7.20}$$

Taking into account the argument that only variations in the θ-direction are considered for the magnetic field, we can write the linearised induction equation as

$$\frac{\partial b_\theta}{\partial t} = -\frac{V_\phi}{R_0\sin\theta}\frac{\partial b_\theta}{\partial\phi} + \frac{B_\phi}{R_0\sin\theta}\frac{\partial v_\theta}{\partial\phi}. \tag{7.21}$$

7.2.2 Momentum equation

For the momentum equation of the LDR model, we again have one difference compared to the spherical base model: the $(\mathbf{v}\cdot\nabla)\mathbf{v}$ term is not equal to zero. Also, since the gravitational force acts radially inwards, it does not have a component in the $\boldsymbol{\theta}$ or $\boldsymbol{\phi}$-direction, and hence we can ignore it while writing the momentum equation. Similarly, the pressure term, ∇p, which also acts mainly in the radial direction, can also be omitted. Therefore, the momentum equation considered here has the following form

$$\rho\left[\frac{\partial\mathbf{v}}{\partial t} + (\mathbf{v}\cdot\nabla)\mathbf{v} + 2\boldsymbol{\Omega}\times\mathbf{v}\right] = \frac{1}{\mu_0}(\nabla\times\mathbf{B})\times\mathbf{B}\,. \tag{7.22}$$

Based on the same linearisation process followed in Section 5.2.2, we can write the linearised momentum equation as

$$\rho\left[\frac{\partial \mathbf{v}_1}{\partial t} + (\mathbf{v}_0\cdot\nabla)\mathbf{v}_1 + 2\boldsymbol{\Omega}\times\mathbf{v}_1\right] = \frac{1}{4\pi\rho}(\mathbf{B}_0\cdot\nabla)\mathbf{B}_1\,. \tag{7.23}$$

For simplicity, we will again evaluate each term individually, starting with the term for the Coriolis force. Since we are considering the spherical coordinate system, (r, θ, ϕ), illustrated in Fig.(6.1), the angular velocity of the Sun can be written as

$$\boldsymbol{\Omega} = (\Omega\cos\theta, -\Omega\sin\theta, 0), \tag{7.24}$$

where θ is co-latitude. Then the cross-product on the left-hand side of eq.(5.21) is evaluated as

$$2\boldsymbol{\Omega}\times\mathbf{v}_1 = \begin{vmatrix} \hat{\boldsymbol{r}} & \hat{\boldsymbol{\theta}} & \hat{\boldsymbol{\phi}} \\ 2\Omega\cos\theta & -2\Omega\sin\theta & 0 \\ 0 & v_\theta & v_\phi \end{vmatrix} \tag{7.25}$$

$$= (-2\Omega\sin\theta v_\phi - 0)\ \hat{\boldsymbol{r}} - (2\Omega\cos\theta v_\phi - 0)\ \hat{\boldsymbol{\theta}} + (2\Omega\cos\theta v_\theta - 0)\ \hat{\boldsymbol{\phi}}. \tag{7.26}$$

Thus, the Coriolis force is written as

$$2\boldsymbol{\Omega}\times\mathbf{v}_1 = -2\Omega\sin\theta v_\phi\,\hat{\boldsymbol{r}} - 2\Omega\cos\theta v_\phi\,\hat{\boldsymbol{\theta}} + 2\Omega\cos\theta v_\theta\,\hat{\boldsymbol{\phi}}. \tag{7.27}$$

Next, we must note the similarity between the terms for $(\mathbf{v}_0\cdot\nabla)\mathbf{v}_1$ and $(\mathbf{B}_0\cdot\nabla)\mathbf{B}_1$. Since the perturbed and unperturbed magnetic field and velocity have the same components, the calculation of these terms will be identical, except for the parameter, which will either be $\mathbf{B}$ or $\mathbf{v}$. Thus, we will only write out the steps for the magnetic field, which will be copied for the velocity term.

Then, we consider the linearised Lorentz form of eq.(6.16b), repeated below for convenience but instead written in terms of velocity, such that we get

$$(\mathbf{v}_0\cdot\nabla)\,\mathbf{v}_1 = \left(\frac{V_\phi}{R_0\sin\theta}\frac{\partial v_\theta}{\partial\phi} - 2\frac{\cos\theta}{R_0\sin\theta}V_\phi v_\phi\right)\hat{\boldsymbol{\theta}} + \left(\frac{v_\theta}{r}\frac{\partial V_\phi}{\partial\theta} + \frac{\cos\theta}{R_0\sin\theta}V_\phi v_\theta + \frac{V_\phi}{R_0\sin\theta}\frac{\partial v_\phi}{\partial\phi}\right)\hat{\boldsymbol{\phi}}. \tag{7.28}$$

The equation above can then also be written in the following form for the Lorentz force,

$$(\mathbf{B}_0 \cdot \nabla)\,\mathbf{B}_1 = \left(\frac{B_\phi}{R_0\sin\theta}\frac{\partial b_\theta}{\partial\phi} - 2\frac{\cos\theta}{R_0\sin\theta}B_\phi b_\phi\right)\hat{\boldsymbol{\theta}} + \left(\frac{b_\phi}{R_0\sin\theta}\frac{\partial}{\partial\theta}(B_\phi\sin\theta) + \frac{B_\phi}{R_0\sin\theta}\frac{\partial b_\phi}{\partial\phi}\right)\hat{\boldsymbol{\phi}}. \tag{7.29}$$

Now, considering that we have the first term on the left-hand side of the momentum equations as

$$\frac{\partial\mathbf{v}}{\partial t} = \frac{\partial v_\theta}{\partial t}\hat{\boldsymbol{\theta}} + \frac{\partial v_\phi}{\partial t}\hat{\boldsymbol{\phi}}, \tag{7.30}$$

we can add eq.(7.27) and eq.(7.28) to get the right-hand side of eq.(7.22) in the linearised component form. Whilst the Lorentz force eq.(7.29) is the term an on the right-hand side, such that we get the component form of the linearised momentum equation as follows

$$\frac{\partial v_\theta}{\partial t} + \frac{V_\phi}{R_0\sin\theta}\frac{\partial v_\theta}{\partial\phi} - 2\Omega_0\cos\theta v_\phi - 2\frac{\cos\theta}{R_0\sin\theta}V_\phi v_\phi = \frac{\Xi}{4\pi\rho R_0\sin\theta}\frac{\partial b_\theta}{\partial\phi} - 2\frac{\Xi}{4\pi\rho R_0}\frac{\cos\theta}{\sin\theta}b_\phi, \tag{7.31}$$

and

$$\frac{\partial v_\phi}{\partial t} + \frac{V_\phi}{R_0\sin\theta}\frac{\partial v_\phi}{\partial\phi} + \frac{v_\theta}{R_0}\frac{\partial V_\phi}{\partial\theta} + 2\Omega_0\cos\theta v_\theta + \frac{\cos\theta}{R_0\sin\theta}v_\theta V_\phi = \frac{\Xi}{4\pi\rho R_0\sin\theta}\frac{\partial b_\phi}{\partial\phi} + \frac{b_\theta}{4\pi\rho R_0\sin\theta}\frac{\partial}{\partial\theta}(\Xi\sin\theta), \tag{7.32}$$

where the notation of Zaqarashvili et al. (2010) was introduced by replacing the azimuthal unperturbed magnetic field notation of B_ϕ with Ξ, where $\Xi = B_\phi$.

7.2.3 Continuity equations

To determine the linearised continuity equations, we must recall two points. The first is that the linearised continuity equation for an incompressible fluid has been derived in Chapter 4 and is given by eq.(4.68), repeated below

$$\boldsymbol{\nabla} \cdot \mathbf{v}_1 = 0. \tag{4.68}$$

The second point we need to consider is the similarity between the velocity and magnetic field, and therefore, we can write the conservation of the magnetic flux, eq.(4.70), as

$$\boldsymbol{\nabla} \cdot \mathbf{B}_1 = 0. \tag{7.33}$$

Therefore, the component form of these continuity equations is then described by

$$\nabla \cdot \mathbf{v}_1 = 0, \tag{4.68}$$

$$\left(\frac{1}{R_0 \sin\theta}\frac{\partial}{\partial\theta}\sin\theta\,\hat{\boldsymbol{\theta}} + \frac{1}{R_0 \sin\theta}\frac{\partial}{\partial\phi}\hat{\boldsymbol{\phi}}\right) \cdot (v_\theta\hat{\boldsymbol{\theta}} + v_\phi\hat{\boldsymbol{\phi}}) = 0, \tag{7.34a}$$

$$\frac{1}{R_0 \sin\theta}\frac{\partial}{\partial\theta}(\sin\theta v_\theta) + \frac{1}{R_0 \sin\theta}\frac{\partial v_\phi}{\partial\phi} = 0, \tag{7.34b}$$

$$\frac{\partial}{\partial\theta}(\sin\theta v_\theta) + \frac{\partial v_\phi}{\partial\phi} = 0, \tag{7.34c}$$

and similarly, the conservation of the magnetic flux becomes

$$\nabla \cdot \mathbf{B}_1 = 0, \tag{7.33}$$

$$\left(\frac{1}{R_0 \sin\theta}\frac{\partial}{\partial\theta}\sin\theta\,\hat{\boldsymbol{\theta}} + \frac{1}{R_0 \sin\theta}\frac{\partial}{\partial\phi}\hat{\boldsymbol{\phi}}\right) \cdot (b_\theta\hat{\boldsymbol{\theta}} + b_\phi\hat{\boldsymbol{\phi}}) = 0, \tag{7.35a}$$

$$\frac{1}{R_0 \sin\theta}\frac{\partial}{\partial\theta}(\sin\theta b_\theta) + \frac{1}{R_0 \sin\theta}\frac{\partial b_\phi}{\partial\phi} = 0, \tag{7.35b}$$

$$\frac{\partial}{\partial\theta}(\sin\theta b_\theta) + \frac{\partial b_\phi}{\partial\phi} = 0. \tag{7.35c}$$

7.2.4 MHD Rossby wave dispersion relation derivation

The simplest way to include the LDR in the governing equations is to consider the reference frame rotating with the equator. The LDR can subsequently be regarded as the unperturbed shearing motion for this frame of reference (Zaqarashvili et al., 2010). It follows from the previous sections that the linearised 2D MHD governing equations in a rotating frame of reference consist of the induction equation given by

$$\frac{\partial b_\theta}{\partial t} + \frac{V_\phi}{R_0 \sin\theta}\frac{\partial b_\theta}{\partial\phi} = \frac{\Xi}{R_0 \sin\theta}\frac{\partial v_\theta}{\partial\phi}, \tag{7.21}$$

the momentum equation for the co-latitude ($\boldsymbol{\theta}$)

$$\frac{\partial v_\theta}{\partial t} + \frac{V_\phi}{R_0 \sin\theta}\frac{\partial v_\theta}{\partial\phi} - 2\Omega_0\cos\theta v_\phi - 2\frac{\cos\theta}{R_0 \sin\theta}V_\phi v_\phi = \frac{\Xi}{4\pi\rho R_0 \sin\theta}\frac{\partial b_\theta}{\partial\phi} - 2\frac{\Xi}{4\pi\rho R_0}\frac{\cos\theta}{\sin\theta}b_\phi, \tag{7.31}$$

and azimuthal or toroidal ($\boldsymbol{\phi}$) directions

$$\frac{\partial v_\phi}{\partial t} + \frac{V_\phi}{R_0 \sin\theta}\frac{\partial v_\phi}{\partial\phi} + \frac{v_\theta}{R_0}\frac{\partial V_\phi}{\partial\theta} + 2\Omega_0\cos\theta v_\theta + \frac{\cos\theta}{R_0 \sin\theta}v_\theta V_\phi = \frac{\Xi}{4\pi\rho R_0 \sin\theta}\frac{\partial b_\phi}{\partial\phi} + \frac{b_\theta}{4\pi\rho R_0 \sin\theta}\frac{\partial}{\partial\theta}(\Xi\sin\theta), \tag{7.32}$$

respectively. Along with the continuity equation

$$\frac{\partial}{\partial \theta}(\sin \theta v_\theta) + \frac{\partial v_\phi}{\partial \phi} = 0, \tag{7.34c}$$

and the conservation of magnetic flux

$$\frac{\partial}{\partial \theta}(\sin \theta b_\theta) + \frac{\partial b_\phi}{\partial \phi} = 0. \tag{7.35c}$$

These linearised 2D MHD governing equations are written in the (θ, ϕ)-plane in spherical coordinates with an angular velocity of the equator, Ω_0. Here, the magnetic and velocity perturbations are given by b_θ, b_ϕ and v_θ, v_ϕ, respectively. Moreover, V_ϕ and

$$\Xi = B_\phi \sin \theta, \tag{7.36}$$

are the azimuthal components of this rotating frame's unperturbed velocity and magnetic field. Also, the standard notation for the medium density, ρ, and the distance from the solar centre to the tachocline, R_0, is used.

In this formulation, the LDR, represented by V_ϕ, with respect to the equator, is given by Zaqarashvili et al. (2010) as

$$V_\phi = R_0 \sin \theta \Omega_1(\theta). \tag{7.37}$$

Then by subsituting eq.(7.37) into eq.(7.31)-eq.(7.35c) we get the 2D linearised system of equations in spherical coordinates for a rotating frame. They represent the horizontal momentum equations for the latitudinal

$$\frac{\partial v_\theta}{\partial t} + \Omega_1(\theta)\frac{\partial v_\theta}{\partial \phi} - 2\Omega_d \cos \theta v_\phi = \frac{B_\phi}{4\pi\rho R_0}\frac{\partial b_\theta}{\partial \phi} - 2\frac{B_\phi \cos \theta}{4\pi\rho R_0} b_\phi, \tag{7.38}$$

where $\Omega_d = \Omega_0 + \Omega_1$ from eq.(7.4), and longitudinal direction

$$\begin{aligned} \frac{\partial v_\phi}{\partial t} + \Omega_1(\theta)\frac{\partial v_\phi}{\partial \phi} + 2\Omega_0 \cos \theta v_\theta + \Omega_1(\theta) \cos \theta v_\theta + v_\theta \frac{\partial}{\partial \theta}\big[\sin \theta \Omega_1(\theta)\big] = \\ \frac{B_\phi}{4\pi\rho R_0}\frac{\partial b_\phi}{\partial \phi} + \frac{b_\theta}{4\pi\rho R_0 \sin \theta}\frac{\partial}{\partial \theta}\big[B_\phi \sin^2 \theta\big]. \end{aligned} \tag{7.39}$$

Along with the associated induction equation

$$\frac{\partial b_\theta}{\partial t} + \Omega_1(\theta)\frac{\partial b_\theta}{\partial \phi} = \frac{B_\phi}{R_0}\frac{\partial v_\theta}{\partial \phi}, \tag{7.40}$$

and the latitudinal variation of the magnetic and velocity perturbations

$$\frac{\partial}{\partial \theta}\big(\sin\theta b_\theta\big) + \frac{\partial b_\phi}{\partial \phi} = 0, \tag{7.41}$$

$$\frac{\partial}{\partial \theta}\big(\sin\theta v_\theta\big) + \frac{\partial v_\phi}{\partial \phi} = 0. \tag{7.42}$$

However, here the newly considered differential rotation, $\Omega_1(\theta)$, is given by eq.(7.5), repeated below

$$\Omega_1(\theta) = -\Omega_0 s_2 \cos^2\theta.$$

Then, we start by defining and then substituting the following stream functions

$$v_\theta = \frac{1}{\sin\theta}\frac{\partial \Psi}{\partial \phi},\ v_\phi = -\frac{\partial \Psi}{\partial \theta},\ b_\theta = \frac{1}{\sin\theta}\frac{\partial \Phi}{\partial \phi},\ b_\phi = -\frac{\partial \Phi}{\partial \theta}, \tag{7.43}$$

into eq.(7.38)-(7.42), under the assumption that $\Phi = \Phi(\theta, \phi)$ and $\Psi = \Psi(\theta, \phi)$. After which, a Fourier analysis of the form $\exp\big[im(\phi - ct)\big]$ is applied to the resulting equations. For simplicity, we will use the induction equation, eq.(7.40), to show the application of these steps, similar to the process for the remaining equations. Therefore, we can rewrite eq.(7.40) as

$$\frac{\partial b_\theta}{\partial t} + \Omega_1(\theta)\frac{\partial b_\theta}{\partial \phi} = \frac{B_\phi}{R_0}\frac{\partial v_\theta}{\partial \phi}, \tag{7.44}$$

and substitute b_θ and v_θ to obtain

$$\frac{\partial}{\partial t}\left(\frac{1}{\sin\theta}\frac{\partial \Phi}{\partial \phi}\right) + \Omega_1\frac{\partial}{\partial \phi}\left(\frac{1}{\sin\theta}\frac{\partial \Phi}{\partial \phi}\right) = \frac{B_\phi}{R_0}\frac{\partial}{\partial \phi}\left(\frac{1}{\sin\theta}\frac{\partial \Psi}{\partial \phi}\right). \tag{7.45}$$

Applying the Fourier form, we arrive at

$$(-imc)\left[\frac{1}{\sin\theta}(im)\Phi\right] + \Omega_1(im)\left[\frac{1}{\sin\theta}(im)\Phi\right] = \frac{B_\phi}{R_0}(im)\left[\frac{1}{\sin\theta}(im)\Psi\right], \tag{7.46}$$

which can be simplified to

$$\frac{m^2 c}{\sin\theta}\Phi - \frac{m^2\Omega_1}{\sin\theta}\Phi = -\frac{B_\phi}{R_0}\frac{m^2}{\sin\theta}\Psi. \tag{7.47}$$

By now multiplying eq.(7.47) with $\frac{\sin\theta}{m^2}$, it reduces to

$$(c-\Omega_1)\Phi = -\frac{B_\phi}{R_0}\Psi. \tag{7.48}$$

Similarly, the Fourier-transformed momentum equations are combined to give the following

$$\begin{aligned}(c-\Omega_1)\left[\frac{\partial}{\partial\theta}\sin\theta\frac{\partial}{\partial\theta}-\frac{m^2}{\sin\theta}\right]\Psi-2\Omega_0\sin\theta\Psi+\frac{d}{d\theta}\left[\frac{1}{\sin\theta}\frac{d}{d\theta}\big(\Omega_1\sin^2\theta\big)\right]\Psi\\ =-\frac{B_\phi}{4\pi\rho R_0}\left[\frac{\partial}{\partial\theta}\sin\theta\frac{\partial}{\partial\theta}-\frac{m^2}{\sin\theta}\right]\Phi+\frac{1}{4\pi\rho R_0}\frac{d}{d\theta}\left[\frac{1}{\sin\theta}\frac{d}{d\theta}\big(B_\phi\sin^2\theta\big)\right]\Phi,\end{aligned} \tag{7.49}$$

as a result. Lastly, the latitudinal variation of the magnetic and velocity perturbations, eq.(7.41) and eq.(7.42), become zero when applying these steps and will, therefore, be ignored going forward.

Next we transform the variables of $\mu=\cos\theta$ in eq.(7.48) and eq.(7.49) and normalise Φ and Ψ by B_0 and $\Omega_0 R_0$, respectively. Here B_0 is the magnetic field profile described by $B_\phi(\theta)\sin\theta$ at a latitude of $\Theta=0$. Then, continuing with the example of the induction equation, we normalise eq.(7.48) accordingly, such that

$$\frac{(c-\Omega_1)}{\Omega_0 R_0}\Phi = \frac{B_\phi}{R_0 B_0}\Psi, \tag{7.50}$$

$$\left(\frac{c}{\Omega_0}-\frac{\Omega_1}{\Omega_0}\right)\Phi = \frac{B_\phi}{B_0}\Psi. \tag{7.51}$$

Furthermore, we define

$$\Omega_d(\mu)=\frac{\Omega_1(\mu)}{\Omega_0},\quad \omega=\frac{c}{\Omega_0},\quad B(\mu)=\frac{B_\phi(\mu)}{B_0} \tag{7.52}$$

similar to Zaqarashvili et al. (2010), which is used to write eq.(7.51) as

$$\boxed{(\Omega_d-\omega)\Phi = B\Psi}. \tag{7.53}$$

Then eq.(7.49) can be simplified by defining the Legendre operator as

$$L=\frac{\partial}{\partial\theta}\sin\theta\frac{\partial}{\partial\theta}-\frac{m^2}{\sin\theta}. \tag{7.54}$$

Considering that $\mu = \cos\theta$, we can write the partial derivative of θ as follows

$$\frac{\partial}{\partial\theta} = \frac{\partial\mu}{\partial\theta}\frac{\partial}{\partial\mu} = (-\sin\theta)\frac{\partial}{\partial\mu}, \tag{7.55}$$

which can be substituted into eq.(7.54) to give

$$L = \left[-\sin\theta\frac{\partial}{\partial\mu}\right]\sin\theta\left[-\sin\theta\frac{\partial}{\partial\mu}\right] - \frac{m^2}{\sin\theta}. \tag{7.56}$$

Next, we multiply eq.(7.56) with $1/\sin\theta$ and use the trigonometric identity: $\sin^2\theta = 1 - \cos^2\theta = 1 - \mu^2$, to get the final expression for the Legendre operator as

$$L = \frac{\partial}{\partial\mu}(1-\mu^2)\frac{\partial}{\partial\mu} - \frac{m^2}{1-\mu^2}. \tag{7.57}$$

Now, by setting

$$\alpha_0^2 = \frac{B_0^2}{4\pi\rho\Omega_0^2 R_0^2}, \tag{7.58}$$

then we can write eq.(7.49) as follows

$$\boxed{(\Omega_d - \omega)L\Psi + \left(2 - \frac{d^2}{d\mu^2}\big[\Omega_d(1-\mu^2)\big]\right)\Psi - \alpha_0^2 BL\Phi + \alpha_0^2\frac{d^2}{d\mu^2}\big[B(1-\mu^2)\big]\Phi = 0}. \tag{7.59}$$

By now, substituting the magnetic field profile of

$$B(\mu) = \frac{B_\phi(\mu)}{B_0} = \frac{B_0\cos\theta}{B_0} = \cos\theta = \mu, \tag{7.60}$$

into eq.(7.53) into eq.(7.59) to get

$$(\Omega_d - \omega)\Phi = \mu\Psi \tag{7.61}$$

and

$$(\Omega_d - \omega)L\Psi + \left(2 - \frac{d^2}{d\mu^2}\big[\Omega_d(1-\mu^2)\big]\right)\Psi - \alpha_0^2\mu L\Phi + \alpha_0^2\frac{\partial^2}{\partial\mu^2}\big[\mu(1-\mu^2)\big]\Phi = 0. \tag{7.62}$$

Evaluating the PDE in the last term of eq.(7.62) leads to

$$\frac{d^2}{d\mu^2}\left[\mu(1-\mu^2)\right] = \frac{d^2}{d\mu^2}\left(\mu-\mu^3\right), \tag{7.63a}$$

$$= \frac{d}{d\mu}\left(1-3\mu^2\right), \tag{7.63b}$$

$$= -6\mu, \tag{7.63c}$$

and substituded into eq.(7.62) we obtain

$$(\Omega_d-\omega)L\Psi + \left(2-\frac{d^2}{d\mu^2}\left[\Omega_d(1-\mu^2)\right]\right)\Psi - \alpha_0^2\mu L\Phi - 6\alpha_0^2\mu\Phi = 0. \tag{7.64}$$

From eq.(7.61), we obtain

$$\Phi = \frac{\mu\Psi}{\Omega_d-\omega}, \tag{7.65}$$

and substituting it into eq.(7.64), we get

$$(\Omega_d-\omega)L\Psi + \left(2-\frac{d^2}{d\mu^2}\left[\Omega_d(1-\mu^2)\right]\right)\Psi - \alpha_0^2\mu L\left(\frac{\mu\Psi}{\Omega_d-\omega}\right) - 6\alpha_0^2\mu\left(\frac{\mu\Psi}{\Omega_d-\omega}\right) = 0. \tag{7.66}$$

Since eq.(7.66) is no longer dependent on both latitude and longitude, it means that the solution can be written as a series of associated Legendre polynomials for each wavenumber, m (Zaqarashvili et al., 2010), given by

$$\Psi = \sum_{n=m}^{\infty} \psi_n^m\, P_n^m(\mu). \tag{7.67}$$

Furthermore, the associated Legendre function, written as

$$\left[\frac{d}{d\mu}(1-\mu^2)\frac{d}{d\mu} - \frac{m^2}{1-\mu^2} + n(n+1)\right] P_n^m(\mu) = 0, \tag{7.68}$$

can be simplified by substituting eq.(7.57) and $\mu = \cos\theta$ into eq.(7.68), such that it becomes

$$[L + n(n+1)]P_n^m(\cos\theta) = 0, \tag{7.69}$$

leading to

$$L = -n(n+1). \tag{7.70}$$

Then, by substituting eq.(7.67) and eq.(7.70) into eq.(7.66) and simplifying, it gives

$$\begin{aligned}-(\Omega_d - \omega)n(n+1) + \left(2 - \frac{d^2}{d\mu^2}\left[\Omega_d(1-\mu^2)\right]\right) + n(n+1)\alpha_0^2\mu\left(\frac{\mu}{\Omega_d - \omega}\right) \\ -6\alpha_0^2\mu\left(\frac{\mu}{\Omega_d - \omega}\right) = 0.\end{aligned} \tag{7.71}$$

Next, the latitudinal differential rotation $\Omega_d = -s_2\mu^2$ is substituted and the partial derivative term evaluated resulting in

$$\begin{aligned}-(-s_2\mu^2 - \omega)n(n+1) + 2 - \left[-2s_2 + 12s_2\mu^2\right] + n(n+1)\alpha_0^2\mu\left(\frac{\mu}{-s_2\mu^2 - \omega}\right) \\ -6\alpha_0^2\mu\left(\frac{\mu}{-s_2\mu^2 - \omega}\right) = 0,\end{aligned} \tag{7.72}$$

which is, in turn, simplified at first by multiplying with the fraction denominator, giving

$$\begin{aligned}-(-s_2\mu^2 - \omega)(-s_2\mu^2 - \omega)n(n+1) + 2(-s_2\mu^2 - \omega) - \left[-2s_2 + 12s_2\mu^2\right](-s_2\mu^2 - \omega) \\ +n(n+1)\alpha_0^2\mu^2 - 6\alpha_0^2\mu^2 = 0.\end{aligned} \tag{7.73}$$

Then simplifying eq.(7.73) further we get

$$\begin{aligned}[-\omega^2 - 2s_2\mu^2\omega - s_2^2\mu^4]n(n+1) - 2s_2\mu^2 - 2\omega - 2s_2^2\mu^2 - 2s_2\omega + 12s_2^2\mu^4 + 12s_2\mu^2\omega \\ +\mu^2\alpha_0^2 n(n+1) - 6\mu^2\alpha_0^2 = 0.\end{aligned} \tag{7.74}$$

At this point, the approximations of slow rotation (Section 4.2.3), $s_2 \ll 1$, and the consideration of low latitudes, $\mu \ll 1$, (Gurgenashvili et al., 2016) are applied. Moreover, given $\alpha_0^2(n(n+1)\mu^2 - 6\mu^2) \approx \alpha_0^2$, since $\alpha_0^2 \gg \mu^2$, eq.(7.74) becomes

$$n(n+1)\omega^2 + 2(1+s_2)\omega - \alpha_0^2 = 0. \tag{7.75}$$

However, if the notation of Gurgenashvili et al. (2016) were used, ω in eq.(7.75) would be replaced by $\hat{\omega}$, such that it is written as

$$n(n+1)\hat{\omega}^2 + 2(1+s_2)\hat{\omega} - \alpha_0^2 = 0. \tag{7.76}$$

Then, considering that Gurgenashvili et al. (2016) defined

$$\hat{\omega} = \frac{\omega}{m\Omega_0} \quad \text{and} \quad \alpha_0^2 = \frac{B_0^2}{4\pi\rho\Omega_0^2 R_0^2} = \frac{v_A^2}{\Omega_0^2 R_0^2}, \tag{7.77}$$

it follows that eq.(7.76) can be written as

$$n(n+1)\frac{\omega^2}{m^2\Omega_0^2} + 2(1+s_2)\frac{\omega}{m\Omega_0} - \frac{v_A^2}{\Omega_0^2 R_0^2}. \tag{7.78}$$

Multiplying eq.(7.78) throughout by $m^2\Omega_0^2$, we obtain

$$n(n+1)\omega^2 + 2m\Omega_0(1+s_2)\omega - \frac{m^2 v_A^2}{R_0^2} = 0. \tag{7.79}$$

The dispersion relation, eq.(7.79), has the fast and slow Rossby modes as solutions, which are presented in the summary provided below, where m now represents the toroidal wavenumber and n remains the poloidal wavenumber. Their respective group and phase velocities are also given.

LDR MHD Rossby wave propagation properties

Dispersion relation

$$n(n+1)\omega^2 + 2m\Omega_0(1+s_2)\omega - \alpha_0^2 = 0, \tag{7.76}$$

where

$$\alpha_0^2 = \frac{B_0^2}{4\pi\rho\Omega_0^2 R_0^2} = \frac{v_A^2}{\Omega_0^2 R_0^2}. \tag{7.77}$$

Fast and slow MHD Rossby wave equations

Dispersion relation

$$\omega_\pm = -\frac{m\Omega_0(1+s_2) \pm \sqrt{(1+s_2)^2 + \alpha_0^2\, n(n+1)}}{n(n+1)} \tag{7.80}$$

Phase and group velocity

$$\frac{\omega_\pm}{m} = \frac{\partial\omega_\pm}{\partial m} = -\frac{\Omega_0(1+s_2) \pm \sqrt{\Omega_0(1+s_2)^2 + \alpha_0^2\, n(n+1)}}{n(n+1)} \tag{7.81}$$

7.3 Discussion

The LDR MHD Rossby wave model for the lower tachocline described in this chapter includes the fundamental characteristic of solar dynamics: the phenomenon where the equator spins faster than the poles, called latitudinal differential rotation. This was suggested to be the last enhancement to the MHD Rossby wave model so that it more accurately represents reality (Zaqarashvili et al., 2007). However, the resulting dispersion relation, eq.(7.76), requires further discussion.

Let us compare eq.(7.76) given below

$$n(n+1)\omega^2 + 2m\Omega_0\boldsymbol{(1+s_2)}\omega - \frac{B_0^2 m^2}{4\pi\rho R_0^2} = 0, \tag{7.76}$$

to the dispersion relation of the effective gravity MHD Rossby wave model, given by eq.(6.67)

$$n(n+1)\omega^2 + 2m\Omega_0\omega - \frac{B_0^2 m^2}{4\pi\rho R_0^2} = 0, \tag{7.82}$$

which is written here in a form that is more easily comparable to eq.(7.76). Then, by comparing these two dispersion relations, it is clear that they are similar apart from the term in the LDR model that additionally includes $(1+s_2)$. It follows that when the LDR parameter, s_2, is set to zero in eq.(7.76), it transforms to the dispersion relation, eq.(7.82), derived by Zaqarashvili et al. (2009). The similarity between these two dispersion relations is a significant finding because they are derived using different sets of governing equations. Recall that in Chapter 6, the shallow water governing equations (SWEs) were used to derive the effective gravity MHD Rossby wave model compared to the simplified governing equations considered in this chapter.

However, it should be noted that although the SWEs apply to a thin layer such as the tachocline, the ability to vary the layer thickness (and effective gravity), which is seen as an advantage of using the SWEs, did not have an impact on the resulting MHD Rossby wave dispersion relations as explained in Section 7.1. Then, considering that the pure 2D governing equations were used to derive eq.(7.76), which neglects the vertical direction altogether, and noting that the SWE dispersion relation, eq.(7.82) ignored layer thickness as well, it explains why these dispersion relations are so closely related to each another. Conversely, based on the characteristics of this overshoot layer, the SWEs are more appropriate when studying the upper tachocline. This is because the upper layer has a rigid bottom adjacent to the lower stable part of the tachocline, and it has a free upper surface, which is deformed as the convection motions overshoot into this region. Therefore, the environment described by the SWEs is more aligned with the conditions of the upper tachocline layer.

Since the similarity between eq.(7.76) and eq.(7.82) has been addressed, plotting these dispersion relations together (see Fig.7.2) will illustrate the effect of the LDR on the behaviour of the MHD Rossby waves.

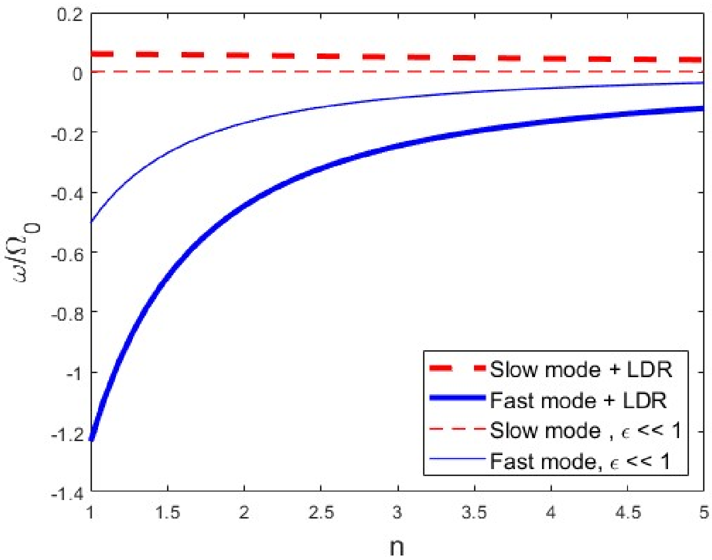

Figure 7.2: The dispersion for the slow (red) and fast (blue) MHD Rossby waves is plotted for two cases. The first case, represented by the thick lines, is the dispersion relations of the model that includes the latitudinal differential rotation (LDR), with the LDR parameter, $s_2 = 0.17$. The second case is for the model considered effective gravity (Zaqarashvili et al., 2009), where $\alpha_0 = 0.05$.

The thin solid blue (fast MHD Rossby wave) and dashed red (slow MHD Rossby wave) lines are plotted with the exact parameter values as in Chapter 6, such that the magnetic field strength is set to be $\alpha_0 = 0.05$. The thicker but same line types represent the fast and slow MHD Rossby waves according to the dispersion relations, eq.(7.80), resulting from the LDR model derived in this chapter. The similarity between the two models is evident considering Fig.(7.2), as the shape of the fast and slow MHD Rossby wave dispersion relations remain largely unaffected. On the other hand, Fig.(7.2) also clearly shows how the LDR affects the MHD Rossby wave behaviour in the lower tachocline. It shows that including the LDR dynamic in the MHD, Rossby wave model leads to higher wave frequencies for both MHD Rossby waves than when LDR is neglected. However, the fast MHD Rossby wave is much more affected by including this characteristic solar dynamic. Therefore, including LDR in this study is all the more important.

7.4 Summary

The MHD Rossby wave model derived in this chapter considered the presence of a toroidal magnetic field. Furthermore, we added the dynamics of the LDR to the momentum equations. The specific governing equations used in this chapter assumed an ideal fluid. However, the shallow water approximation was not applied, in contrast to what was done in Chapter 6. This marks an important difference between the derivation of the equations of these two models, as the effect of changing layer thickness and effective gravity was not considered in the LDR model. We will repeat the associated equations below to explore the impact of this difference in assumptions.

The effective gravity MHD Rossby wave model that was derived in Chapter 6, resulted in the following low-frequency dispersion relation

$$n(n+1)\omega^2 + 2m\Omega_0\omega - \frac{B_0^2 m^2}{4\pi\rho R_0^2} = 0, \tag{6.67}$$

and the same equation for the LDR model is given by

$$n(n+1)\omega^2 + 2m\Omega_0\boldsymbol{(1+s_2)}\omega - \frac{B_0^2 m^2}{4\pi\rho R_0^2} = 0. \tag{7.76}$$

By comparing these equations, we can see that they are the same except for the $(1 + s_2)$ included in the second term of eq.(7.76). This bracket includes the observed LDR parameter s_2. Therefore, by setting $s_2 = 0$ in eq.(7.76), the dispersion relation transforms into eq.(6.67) which corresponds to the one for the effective gravity model. As a result of the similarity between these dispersion relations, we can conclude that although effective gravity and the fluid layer thickness may impact other waves, such as those in the upper tachocline (Zaqarashvili et al., 2009), it can be noted that the propagation properties of the MHD Rossby waves in the lower tachocline are unaffected by these parameters. Consequently, we have shown that applying the shallow water approximation does not impact the resulting MHD Rossby wave dispersion relations in the lower tachocline. However, it does simplify the modelling of these MHD Rossby waves as a result of the assumptions that can be made when applying the shallow water approximation.

Nonetheless, we have established that by including the effect of the magnetic field and considering the dynamics of the LDR in the MHD Rossby wave model, it theoretically results in the most realistic model. This is because the LDR model is essential in capturing fundamental solar dynamics, and omitting it could lead to erroneous results.

Literature Review IV: Summary

Three fundamental models of the MHD Rossby waves in the lower tachocline have been studied. Let us summarise the important contributions of each of these models. The low-frequency branch of the dispersion relation derived from the base model in Cartesian coordinates, using the MHD shallow water equations in Chapter 5, made an important discovery (Zaqarashvili et al., 2007). This discovery was that ordinary Rossby waves in the presence of a magnetic field split into two modes, identified as the fast and slow MHD Rossby waves.

The derivation of the MHD Rossby wave base model in spherical coordinates confirmed that this splitting phenomenon is not unique to the model derived using Cartesian coordinates. The HD Rossby wave split was also observed in the resulting equations when using the more appropriate spherical formulation (Zaqarashvili et al., 2007). Subsequently, it was established that due to the difference in the stratification of the upper and lower layers of the tachocline, they each exhibit a different effective gravity. The Lamb parameter, given by

$$\epsilon = \frac{4\Omega_0^2 R_0^2}{g_e H_0},$$

captures these different effective gravity, g_e values. Furthermore, it was shown that for the upper and lower tachocline, their respective Lamb parameter satisfies $\epsilon \gg 1$ and $\epsilon \ll 1$. Applying these Lamb parameter approximations in deriving the dispersion relation allows researchers to study these two regions separately, resulting in more accurate models that capture their different layer characteristics. This theoretical enhancement was implemented in the spherical shallow water base model in Chapter 6 (Zaqarashvili et al., 2009).

Whereas, in Chapter 7, we discussed the last model enhancement of MHD Rossby waves, which included the effect of latitudinal differential rotation (LDR) using the 2-dimensional (2D) governing equations of Chapter 4. This model accurately describes the MHD Rossby waves in the lower tachocline (Zaqarashvili et al., 2010; Gurgenashvili et al., 2016). We found that the resulting LDR model closely resembles the effective gravity model in Chapter 6 (Zaqarashvili et al., 2009), except for a term that now includes the variable, s_2, related to the LDR. However, when the s_2 rotation variable is set to zero, there is no difference between the dispersion relations resulting from these respective MHD Rossby wave models. This suggests that the lower tachocline's effective gravity and layer thickness, associated with the effective gravity model, do not directly affect the behaviour or propagation equations of the MHD Rossby waves. Nevertheless, using the shallow water governing equations is a better option for the MHD Rossby wave model derivation as it allows for more approximations that simplify the modelling process than the 2D governing equations. Thus, we suggest that these governing equations should be used for any future derivations of the MHD Rossby waves in a shallow water environment.

Furthermore, we can conclude the following regarding the comprehensiveness of the respective MHD Rossby wave models. The LDR dynamic causes the solar plasma around the equatorial region to rotate faster than at higher latitudes and starts in the tachocline. Since we showed that the magnetic field can be treated as frozen in the plasma (Section 3.5.1), this phenomenon also affects the magnetic field's behaviour, which in turn impacts the MHD Rossby waves. The LDR model derivation in Chapter 7 has included this phenomenon in formulating the governing equations. Since the LDR model considers both the presence of a magnetic field and the effect of LDR, it is considered to be the most comprehensive MHD Rossby wave model for the solar tachocline from a theoretical standpoint. However, this hypothesis needs empirical validation through observational data and testing of various calculations to establish its accuracy. Finally, we must examine the existing literature to understand how these models are practically implemented to determine the estimated solar magnetic field strength.

Lastly, various periodicities of increased solar activity have been explored in Section 6.4. The Rieger-type periodicity (RTP) of 150-190 days was, subsequently identified as the optimal frequency to consider for space weather forecasting. This is because it is long enough to predict using various space weather prediction models and short enough to be relevant for us on Earth, who will experience adverse effects from geomagnetic storms that occur within this duration. In Part III of this study, we will combine the dispersion relation of the fast MHD Rossby wave in the upper tachocline derived in the LDR model with the RTP data to perform the analysis necessary to refine the methodology used to calculate estimated values for the solar magnetic field strength.

Part III

Analysis and results

8 Model, input parameter and methodology validation

8.1 Introduction

This chapter seeks to validate the models and input parameter values used in the three magnetohydrodynamic (MHD) Rossby wave models outlined in Chapters 5-7. The argument presented throughout Part II confirmed, from a theoretical standpoint, that the latitudinal differential rotation (LDR) model is the most comprehensive as it includes the most significant dynamics that will impact the propagation of MHD Rossby waves in the lower layer of the solar tachocline, namely a magnetic field and the LDR. Therefore, the LDR model will be our primary focus throughout the analysis as it will likely be the most appropriate model for this study. Consequently, the associated dispersion relation of the low-frequency branch, eq.(7.76), is repeated below for ease of reference

$$n(n+1)\omega^2 + 2m\Omega_0(1+s_2)\omega - \frac{B_0^2 m^2}{4\pi\rho R_0^2} = 0.$$

In eq.(7.76) n and m are the poloidal and toroidal wavenumbers, respectively; ω is the wave frequency, s_2 the LDR parameter, B_0 the magnetic field strength, ρ the density of the tachocline, and R_0 is the radial distance from the centre of the Sun to the tachocline.

Recall that since we are interested in the periodicity of solar activity that occurs over several months, it has subsequently been established in Section 6.4 that only the fast MHD Rossby wave in the lower tachocline has comparable periods. More specifically, it has been shown (Gurgenashvili et al., 2016. 2017; Zaqarashvili and Gurgenashvili, 2018; Gachechiladze et al., 2019) that the $m = 1$, $n = 4$ harmonic of the fast MHD Rossby wave exhibits periodicities in the range of the expected 150-180 days (Sections 2.4.1 and 6.4) associated with the Rieger-type periodicity (RTP) (Rieger et al., 1984). The dispersion relation of this specific LDR magneto-Rossby wave model corresponds to the positive solution of eq.(7.80) and is given below

$$\omega_+ = \frac{-m\Omega_0(1+s_2) + \sqrt{(1+s_2)^2 + \alpha_0^2\ n(n+1)}}{n(n+1)}, \tag{8.1}$$

where α_0^2 is given by eq.(8.2) as follows

$$\alpha_0^2 = \frac{B_0^2}{4\pi\rho\Omega_0^2 R_0^2} = \frac{v_A^2}{\Omega_0^2 R_0^2},$$

and v_A is the Alfvén speed, eq.(3.6), is expressed as

$$v_A = \frac{B_0}{\sqrt{4\pi\rho}}.$$

It is essential to note that while the LDR model has been identified as the most comprehensive MHD Rossby wave model, adding more forces to the governing equations or including more system dynamics in a model does not necessarily correlate with improved forecasting accuracy. For this reason, a more quantitative approach must be taken to verify the assumption that the LDR model is the most accurate. Similarly, it is also important to conduct thorough evaluations to address the problems of incorrect parameter values used for the MHD Rossby wave model (Section 3.6.1) as well as the assumption of a static magnetic field throughout the solar cycle (Section 2.2.1). Therefore, we critically evaluate the MHD Rossby wave models (derived in Part II), model input parameter values, and lastly, the methodology employed in calculating the magnetic field strength (MFS), a pivotal factor in improving existing space weather prediction models (SWPMs) forecasting capabilities. The accuracy and reliability of these models and their input parameters are fundamental to the validity of the conclusions drawn from our research.

Firstly, we will examine the sources and rationale behind the chosen input parameter values associated with the MHD Rossby wave dispersion relation used in the existing literature[1]. We will assess their appropriateness in the context of this study. Then, we will provide an overview of the selected MHD Rossby wave models. We will discuss their relevance to our research objectives and compare various model results to confirm our hypothesis that the LDR model is the most plausible for the Rossby waves in the lower tachocline. After that, we will perform a sensitivity analysis to explore how varying input parameters impact

[1]The "existing literature" referred to in this chapter mainly pertains to the studies of Zaqarashvili et al. (2007, 2009) and Gurgenashvili et al. (2016, 2017). They will be explicitly mentioned if any other research is of concern.

the model results. Lastly, we will examine the methodology currently used to calculate the MFS and evaluate its strengths and limitations. Based on the MFS methodology evaluation findings, we propose a new methodology that will improve the accuracy of the estimated MFS values. Finally, we will offer concluding remarks on the overall performance of the models, input parameter values, and methodology and their implications for interpreting our research findings.

8.2 Input parameter value validation

Three sets of input parameters will be used in this study. The first set is the observational data, which includes the latitudinal differential rotation (LDR) parameter, s_2, the equatorial rotation rate, Ω_0, and the Rieger-type periodicity (RTP) that is associated with solar activity. The second set are constant values that describe the properties of the Sun, namely, the density and the distance from the Sun's centre to the tachocline. Finally, we have added the third dataset for transparency, which tables the pure magnetic field strength values calculated here. Each parameter set will be given and discussed below.

8.2.1 Observational rotation parameter values

Table 8.1 lists each solar cycle's different observational parameter values. The s_2 and Ω_0 values were recorded by Javaraiah et al. (2005). Zaqarashvili et al. (2018) provide more detailed Greenwich Royal Observatory (GRO) data for the RTP in the northern and southern hemispheres. Moreover, it is necessary to convert the RTP values, which were initially recorded in days, to the corresponding frequency in Hertz. This is because, in the International System of Units, Hertz is the unit of frequency, and it is expected in this notation if it is to be used in the dispersion relation for the MHD Rossby wave. Therefore, we have added the corresponding frequency of the RTP in nano-Hertz (nHz) in the last two columns of Table 8.1 for transparency since this information was missing from the literature:

Rotation parameters and RTP (GRO data)						
Cycle	s_2	Ω_0 ($\times 10^{-6} s^{-1}$)	N (days)	S (days)	N (nHz)	S (nHz)
13	0.168	2.9242	168	187	432.87	388.89
14	0.15	2.9270	165	194	440.74	374.85
15	0.18	2.9310	171	185	425.27	393.09
16	0.17	2.9290	160	195	454.51	372.93
17	0.20	2.9330	153	193	475.30	376.80
18	0.18	2.9200	160	175	454.51	415.55
19	0.19	2.9250	158	177	460.26	410.86
20	0.16	2.9270	165	190	440.74	382.75
21	0.14	2.9250	183	158	397.39	460.26
22	0.14	2.9090	180	160	404.01	454.51
23	0.17	2.9200	175	160	415.55	454.51
24	0.168	2.9200	190	180	382.75	404.01

Table 8.1: Rotation parameter values, s_2 and Ω_0 for each solar cycle (Javaraiah et al., 2005) and the associated RTP for each hemisphere per cycle in days (Zaqarashvili et al., 2018) which is transformed here into a frequency in nano-Hertz (nHz). These are the most plausible input parameter values used in the analysis as they originate from observations.

Furthermore, Gurgenashvili et al. (2016) did not provide values for solar cycles 13 and 24, so we use the average of the respective values over all other cycles to get the s_2 and Ω_0 values for cycle 13. Conversely, for cycle 24, the RTP for the northern and southern hemispheres ranges from $190 - 210$ days and $180 - 190$ days, respectively (Gurgenashvili et al., 2021). Since we are interested in shorter periods, only the lower end of the possible values for the respective hemispheres will be considered here. We can further explore the common findings of these values as they are used throughout the literature discussed in this research.

The observed values (Javaraiah et al., 2005) for the rotation parameters (s_2 and Ω_0) vary for each solar cycle and remain unchanged after they are recorded. However, when the RTP and MFS are calculated in the existing literature (Gurgenashvili et al., 2016), these two parameter values are taken as the same constant value for all solar cycles, contradicting the observed cycle variability of these parameters. Even more problematic is that the constant values being considered in the existing literature differ (Section 3.6.1). This inconsistency in the rotation parameter values would no longer be considered acceptable and will be explored further in the sensitivity analysis done in Section 8.4. Also, since this research emphasises the importance of representing reality as closely as possible to increase the accuracy of the model results, it can be concluded that using the varying values for each solar cycle is the preferred dataset for these rotation parameters.

Furthermore, the granularity of the RTP values has changed over time, starting from one value per solar cycle (Gurgenashvili et al. 2016) to the more specific hemispheric values per solar cycle (Gurgenashvili et al. 2017). The RTP is recorded by multiple sources such as the Greenwich Royal Observatory (GRO) (Gurgenashvili et al., 2016; 2017; Zaqarashvili and Gurgenashvili, 2018), Royal Observatory of Belgium (ROB) (Gurgenashvili et al., 2016), Kanzelhohe Solar Observatory (KS0) (Gurgenashvili et al., 2017), and Mount Wilson Total Magnetic Flux (MWTF) data (Gurgenashvili et al., 2017). Nevertheless, this study will only consider the GRO RTP dataset as it is the common dataset used across the literature discussed in this study, making the various results directly comparable.

8.2.2 Constant parameter values

The second set of input parameters that this study uses is the following constant values (Gurgenashvili et al., 2016), given in Table 8.2 below, that describe the properties of the lower tachocline.

Properties of the lower tachocline		
Parameter	Symbol	Value
Medium density	ρ	$0.2\,\mathrm{g\,cm^{-3}}$
Distance from centre of Sun to the tachocline	R_0	$5 \times 10^{10}\,\mathrm{cm}$

Table 8.2: Constant parameter values for the lower tachocline.

The literature does not vary these variables; therefore, they do not require further discussion. On the other hand, estimating the values of the magnetic field is complex and requires the pure magnetic field strength, B_0, as an input, which will be discussed next.

8.2.3 Pure magnetic field strength values

In Part II of this study, the magnetic field profile (MFP) has been introduced in the modelling chapters, and the MFP was explained in Section 2.5.1. For instance, in the base model, the MFP of $\sin\theta$ is applied to the magnetic field strength, B_0, to obtain the expression for the toroidal MFS as $B_\phi = B_0 \sin\theta$ (Zaqarashvili et al., 2007). This equation shows that both B_0 and co-latitude, θ, parameter values are inputs. However, none of the research papers discussed in this study provide specific values of B_0. Therefore, we need to calculate this parameter value to fill this gap. We subsequently assume that the fast MHD Rossby wave solution from the LDR model is the most accurate, and its dispersion relation can be used to calculate the value for the MFS since the MFS is a variable in the equation for the dispersion relation.

Therefore, first make α_0^2 the subject of the dispersion relation, eq.(8.1), and set $m = 1$ (Zaqarashvili et al., 2009; Gurgenashvili et al., 2016, 2017; Zaqarashvili and Gurgenashvili, 2018; Gachechiladze et al., 2019) such that we get

$$\alpha_0^2 = \frac{\left[-n(n+1)\frac{\omega}{\Omega_0} - (1+s_2)\right]^2 - (1+s_2)^2}{n(n+1)}. \tag{8.2}$$

Similarly, by making B_0 the subject of eq.(3.6) we can write the expression for the pure MFS as

$$B_0 = \sqrt{4\pi\rho\Omega_0^2 R_0^2 \alpha_0^2}, \tag{8.3}$$

where eq.(8.2) is substituted for the α_0 parameter.

By using the cycle-specific parameter values in Table 8.1, along with the constant property values in Table 8.2, we can use eq.(8.3) to calculate the respective B_0 values for each hemisphere of solar cycles 13-24 when considering the $m = 1$, $n = 4$ harmonic of the fast MHD Rossby wave. The resulting pure MFS values are given in Table 8.3.

Pure MFS per hemisphere (no MFP applied)												
B_0	13	14	15	16	17	18	19	20	21	22	23	24
North (kG)	**72.4**	**75.9**	**65.1**	**79.9**	**85.8**	**79.2**	**80.6**	**74.9**	56.5	60.6	62.1	44.8
South (kG)	50.6	42.4	48.3	37.6	34.3	60.9	56.9	45.6	**85.6**	**83.8**	**80.3**	**56.5**

Table 8.3: Magnetic field strength, B_0, estimations for the $m = 1$, $n = 4$ harmonic of the fast MHD Rossby wave, considering the dispersion relation, eq.(8.1), along with $\rho = 0.2\,\mathrm{g\,cm^{-3}}$ and $R_0 = 5 \times 10^{10}\,\mathrm{cm}$ and the rotation parameter values (Ω_0 and s_2) as given in Table 8.1. The MFSs in bold indicate the dominant hemisphere for each solar cycle.

The results of this exercise provide a comprehensive set of the pure estimated MFS values, B_0, which ignored the impact of a MFP. This MFS will be subsequently used as the input to the mathematical expression for the MFP in Section 8.3.2. Now that the observational rotation parameter inputs have been discussed, we need to validate whether the LDR model is indeed the most accurate option, which is the next essential step in the analysis.

8.3 MHD Rossby wave model validation

To effectively determine the accuracy of the MHD Rossby wave model, we need to consider two components. The first component is the model development, which examines the formulation of the governing equations, including the coordinate system used, assumptions and approximations applied, and what forces are included to describe the system under consideration, which have been addressed in Chapters 4-7. The second component, which will be discussed here, involves comparing the model results to appropriate observational RTP data in Table 8.1 to determine their degree of similarity.

8.3.1 Comparison of MHD Rossby wave model results

In this section, we aim to prove our hypothesis that incorporating additional system dynamics, such as the latitudinal differential rotation, or augmenting the governing equations with extra forces, like those associated with the magnetic field, does improve the accuracy of the MHD Rossby wave model. This analysis would require comparing the model-predicted values with the corresponding observational data. However, before performing this quantitative analysis, let us first explain the methodology that will be used in this validation exercise.

Let us consider the case of the fast MHD Rossby wave, with the dispersion relation, eq.(8.1), given above, where all parameters are known (using Table 8.1 and Table 8.2) for a specific MHD Rossby wave harmonic ($m = 1$, $n = 4$), except for the frequency, ω, and magnetic field strength, B_0. Then, it follows that eq.(8.1) can be used for two different calculations depending on the available data. The first option would be to plug in a value for the MFS, such that the frequency is the only unknown in the equation and can be solved for. Conversely, if the wave frequency is known, it can be used to determine the corresponding MFS.

To start, let's evaluate the second option, where the MFS is calculated by considering the RTP value in nHz given in Table 8.1 as the frequency waves, ω. Furthermore, we assume the MFS is given by $B_\phi = B_0 \sin\theta \cos\theta$, for which we use the B_0 values in Table 8.3 at a latitude of 45°, as considered by Zaqarashvili et al. (2007, 2009) and Gurgenashvili et al. (2016, 2017). With the scenario described above in mind, the only parameter value that remains to be discussed is the latitudinal differential rotation parameter, s_2. Recall that in Section 7.4, we established that the only difference between the LDR model and the effective gravity model (Chapter 6) is the addition of s_2 in the dispersion relation of the LDR model. Therefore, to determine whether adding the LDR improves the accuracy of the model results, we will calculate the MFS values for the two scenarios where the LDR dynamics are excluded ($s_2 = 0$) and included ($s_2 \neq 0$). The resulting MFS values are given in Table 8.4. The next step in the model validation is to plug the resulting MFS (Table 8.4) into the fast MHD Rossby wave dispersion relation to determine the corresponding periodicity. This periodicity will be converted so that the unit is in days and can be compared to the equivalent observed RTP given in Table 8.5.

MFS per hemisphere of solar cycles 13-24						
	RTP (days)		$s_2 \neq 0$ (kG)		$s_2 = 0$ (kG)	
Cycle	N	S	N	S	N	S
13	**168**	187	**36.2**	25.3	**44.1**	34.8
14	**165**	194	**38.0**	21.2	**45.7**	31.6
15	**171**	185	**32.6**	24.2	**42.5**	35.7
16	**160**	195	**40.0**	18.8	**48.5**	31.2
17	**153**	193	**42.9**	17.1	**52.6**	32.1
18	**160**	175	**39.6**	30.4	**48.5**	40.5
19	**158**	177	**40.3**	28.5	**49.6**	39.5
20	**165**	190	**37.4**	22.8	**45.7**	33.4
21	183	**158**	28.3	**42.8**	36.6	**49.6**
22	180	**160**	30.3	**41.9**	38.0	**48.5**
23	175	**160**	31.1	**40.1**	40.5	**48.5**
24	190	**180**	22.4	**28.3**	33.4	**38.0**

Table 8.4: MFS when $s_2 \neq 0$ and $s_2 = 0$.

RTP per hemisphere of solar cycles 13-24								
	$s_2 \neq 0$ (days)				$s_2 = 0$ (days)			
Cycle	N	$\%^N_{err}$	S	$\%^S_{err}$	N	$\%^N_{err}$	S	$\%^S_{err}$
13	**199**	(18)	207	(11)	**216**	(29)	227	(21)
14	**198**	(20)	210	(8)	**214**	(30)	231	(19)
15	**197**	(15)	203	(10)	**218**	(27)	226	(22)
16	**193**	(21)	207	(6)	**211**	(32)	231	(18)
17	**187**	(22)	203	(5)	**206**	(35)	230	(19)
18	**193**	(21)	199	(14)	**211**	(32)	221	(26)
19	**190**	(20)	199	(12)	**210**	(33)	222	(25)
20	**197**	(19)	207	(9)	**214**	(30)	229	(20)
21	207	(13)	**195**	(23)	225	(23)	**210**	(33)
22	206	(14)	**197**	(23)	223	(24)	**211**	(32)
23	200	(14)	**193**	(21)	221	(26)	**211**	(32)
24	206	(8)	**203**	(13)	229	(21)	**223**	(24)

Table 8.5: RTP results using the MFS in Table 8.4.

Based on the results presented in Table 8.4 and Table 8.5, we can make the following important observations. Firstly, we agree with the finding of Gurgenashvili et al. (2016) that an increase in the MFS corresponds to a decrease in the RTP and vice versa. In simpler terms, stronger solar cycles support shorter period oscillations. Thus, the observed RTP provides information about the MFS of the associated solar cycle. This finding is further supported by the fact that the famous RTP of 155-160 days was discovered using cycle 21 data (Rieger et al., 1984), which was classified as a strong cycle. Therefore, it can be concluded that this specific periodicity of 154 days did not disappear for other solar cycles; instead, it varies and depends on the magnetic field strength (Gurgenashvili et al., 2016). This shorter periodicity is only observed for cycles with a stronger magnetic field, implying that weaker cycles have a longer RTP.

Comparing the resulting MFS of the two cases presented, i.e. $s_2 = 0$ and $s_2 \neq 0$, leads us to the next important finding. When the LDR is not taken into account ($s_2 = 0$), the resulting

MFS values are stronger than when the LDR is included ($s_2 \neq 0$), which agrees with the findings of Zaqarashvili et al. (2010). Lastly, we also confirm the finding of Gurgenashvili et al. (2017), who concluded that each solar cycle has a dominant hemisphere, exhibiting a stronger MFS. The input RTP data (Table 8.1) and results (Tables 8.4 and 8.5) show that the northern and southern hemispheres were dominant for solar cycles 13-20 and 21-24, respectively.

Here, we have also noticed the essential relationship that exists between the LDR parameter, the estimated MFS and the corresponding RTP. When the LDR is included (excluded), it results in a decreased (increased) MFS value, which, in turn, corresponds to an increased (decreased) periodicity. The interplay among these parameters (LDR, MFS and RTP) can validate the MHD Rossby wave model results, as we know the anticipated outcome for specific inputs based on solar observational findings. However, it should be mentioned that Gachechiladze et al. (2019) disagreed and concluded that stronger periodicities correspond to stronger MFS. This contradiction is yet another example of opposing views in this field of study.

Finally, after analysing the percentage error values in Table 8.5, which indicate the difference between the predicted and observed periodicity, it can be concluded that the LDR model ($s_2 \neq 0$) is more accurate in predicting values, as the associated error is considerably lower compared to the $s_2 = 0$ case. Thus, this analysis confirms that the LDR Rossby wave model is the most appropriate model for a study focusing on the connection between the MHD Rossby waves in the lower tachocline and the RTP. Nonetheless, it is worth emphasising that in this exercise, we assumed the magnetic field profile that is used to provide the expression for the MFS was taken as $B_\phi = B_0 \sin\theta\cos\theta$. Since the MFP is another MHD Rossby wave model component, it will be explored in more detail in the next section.

8.3.2 Magnetic field profiles

The magnetic field profile (MFP) is a mathematical expression that describes how the orientation and strength of the magnetic field vary across a defined area. Therefore, the MFP is integral to modelling any solar dynamic, as this profile's expression can take various forms. We will now briefly review the MFPs used in the studies discussed in this work. In Cartesian coordinates, the toroidal MFP was defined purely in the x-direction, $\mathbf{B} = (B_x, 0, 0)$

(Zaqarashvili et al., 2007). However, we have established that the spherical coordinate system is preferable for studying global MHD Rossby waves, which subsequently introduces more than one possible MFP. Since various MFPs in spherical coordinates have been introduced over time, they should each be examined to ensure that this part of the MHD Rossby wave model is also adequate.

In the literature covered thus far, Zaqarashvili et al. (2007) first defined the MFP used for the unperturbed magnetic field in spherical coordinates as

$$B_\phi(\theta) = B_0 \sin\theta, \tag{8.4}$$

where B_0 is the MFS and θ the co-latitude. For this profile, the values of the MFS tend to zero at the poles and reach a maximum at the equator (Zaqarashvili et al., 2007). Subsequently, a different MFP (Gilman and Fox, 1997) of

$$B_\phi(\theta) \approx B_0 \cos\theta \sin\theta, \tag{8.5}$$

was used by Zaqarashvili et al. (2009), who argued that it describes a more realistic toroidal magnetic field latitudinal profile because it has a maximum value at mid-latitudes and changes signs at the equator where it has a minimum value.

We will calculate two sets of MFS values using their respective MFPs to assess the impact of MFPs on resulting MFS estimates. To do this, we will use the same input values in Table 8.1 and use the equations associated with the LDR Rossby wave model. However, we will consider the two MFPs separately and demonstrate their different results at two latitudes: 45° (closer to the polar regions) and 5° (closer to the equatorial region). The resulting MFS values calculated here for these scenarios are given in Table 8.6 and Table 8.7 below.

Northern hemisphere: Toroidal Magnetic Field Strength												
(a) $B_\phi^{N,45°}$ (kG)	13	14	15	16	17	18	19	20	21	22	23	24
$B_0 \sin\theta$	**51.2**	**53.7**	**46.1**	**56.5**	**60.7**	**56.0**	**57.0**	**52.9**	40.0	42.9	43.9	31.7
$B_0 \sin\theta\cos\theta$	**36.2**	**38.0**	**32.6**	**40.0**	**42.9**	**39.6**	**40.3**	**37.4**	28.3	30.3	31.1	22.4

(b) $B_\phi^{N,5°}$ (kG)	13	14	15	16	17	18	19	20	21	22	23	24
$B_0 \sin\theta$	**72.2**	**75.7**	**64.9**	**79.6**	**85.5**	**78.9**	**80.2**	**74.6**	56.3	60.4	61.9	44.6
$B_0 \sin\theta\cos\theta$	**6.3**	**6.6**	**5.7**	**6.9**	**7.5**	**6.9**	**7.0**	**6.5**	4.9	5.3	5.4	3.9

Table 8.6: Estimated toroidal magnetic field strength for the northern hemisphere for varying rotation parameters using the existing magnetic field profiles.

Southern hemisphere: Toroidal Magnetic Field Strength.

(a) $B_\phi^{S,45°}$ (kG)	13	14	15	16	17	18	19	20	21	22	23	24
$B_0 \sin\theta$	35.8	30.0	34.2	26.6	24.2	43.1	40.3	32.2	**60.6**	**59.2**	**56.8**	**40.0**
$B_0 \sin\theta\cos\theta$	25.3	21.2	24.2	18.8	17.1	30.4	28.5	22.8	**42.8**	**41.9**	**40.1**	**28.3**

(b) $B_\phi^{S,5°}$	13	14	15	16	17	18	19	20	21	22	23	24
$B_0 \sin\theta$	50.5	42.3	48.1	37.5	34.2	60.7	56.7	45.4	**85.3**	**83.5**	**80.0**	**56.3**
$B_0 \sin\theta\cos\theta$	4.4	3.7	4.2	3.3	3.0	5.3	4.9	4.0	**7.4**	**7.3**	**7.0**	**4.9**

Table 8.7: Estimated toroidal magnetic field strength for the southern hemisphere for varying rotation parameters using the existing magnetic field profiles.

To discuss the findings presented in Table 8.6 and Table 8.7, we will refer to the $\sin\theta$ and $\sin\theta\cos\theta$ profiles as the "first" and "second" profiles respectively. We find that the first profile values are larger than those estimated using the second profile for the higher latitude of 45° in both the northern and southern hemispheres (by roughly $10-20\,$kG). In addition, we found the discrepancy in the values estimated by these two profiles for the lower latitude of 5°, which is of the order of magnitude which is significant. Furthermore, we reasoned that the MFS values of the second profile for the lower latitude are more expected, as they decrease in value, in contrast to the values of the first profile. The reason for this is that observations of sunspots, recorded in the butterfly diagram, show that when the solar cycle ends, the frequency of solar activity decreases in the equatorial region, resulting in a weaker MFS. This exercise illustrates the significant impact that different MFPs can have on the resulting MFS values.

Nevertheless, Gurgenashvili et al. (2016) further noted that this MFP, eq.(8.5), would have a maximum value at a latitude of specifically 45°, and it goes to zero towards the poles. Subsequently, the new variable for the maximum MFS, B_{max}, is introduced as follows

$$B_\phi(45°) = B_0 \cos(45°)\sin(45°) = \frac{B_0}{2} = B_{max}. \tag{8.6}$$

This MFP is commonly used in studies focusing on magneto-Rossby waves in the lower tachocline (Zaqarashvili et al., 2009; Gurgenashvili et al., 2016, 2017; Zaqarashvili and Gurgenashvili, 2018).

After gaining a better understanding of how changing the MFP affects the estimated MFS values, let us now delve into three problems associated with the existing MFPs. The first problem is the lack of transparency regarding the latitude used in various existing studies. The second problem is that the magnetic field strength is considered static throughout the solar cycle, which is the result of only considering *one* latitude value (Gurgenashvili et al., 2016, 2017; Zaqarashvili and Gurgenashvili, 2018). Furthermore, considering an inappropriate value for the chosen latitude is the third problem (Gurgenashvili et al., 2016, 2017; Zaqarashvili and Gurgenashvili, 2018). Let us now elaborate on each of these issues.

To explain the lack of transparency regarding MFP and latitude in various studies, let us use the following scenario as an example. Authors (Gurgenashvili et al., 2016; 2017) often use the term "magnetic field strength" throughout their study and later use the symbol B_{max} to describe these values in the tables that list their results. However, neglecting to clarify which MFP and latitude are used and then calculating the B_{max} values is misleading as this parameter is associated with the specific combination of the MFP and latitude as described by eq.(8.6). Therefore, it is crucial to clarify the specific MFP and latitude values used in calculating MFS to compare results across studies. Furthermore, the existing literature did not consider a variation of the MFS in the latitudinal direction throughout the solar cycle but only considered the latitude of 45°, where the magnetic field profile $B_\phi = B_0 \sin\theta \cos\theta$ has a maximum value, as described by eq.(8.6). This static magnetic field approach, therefore, forms part of the problem statement discussed in Section 2.2.1 as it goes against observational data, which indicates the migration of the magnetic field towards the equator throughout the solar cycle as indicated by the sunspot behaviour over this period.

Lastly, not only is it problematic to consider a static magnetic field throughout a solar cycle, but the latitude of 45° that is chosen with MFP, eq.(8.5), should also be discussed. Based on observational data, this chosen latitude of 45° is higher than the expected latitude of 30° that is associated with solar activity at the start of the solar cycle[2]. Therefore, it can be

[2]During the beginning of the solar cycle, sunspots are observed at higher latitudes compared to active latitudes observed during the rest of the solar cycle. The latitude range that is associated with the start of the solar cycle is mainly between $30° - 40°$ based on the butterfly diagram. Although the number of

argued that the error caused by considering a fixed latitude is exacerbated by choosing a value that does not align with observations.

The observations described above are especially problematic as our current study proposes that the magnetic field's location and strength change over the solar cycle's duration, implying that the general term of MFS is ambiguous and should be more clearly defined in the future. Moreover, we have proven that the LDR model is the most appropriate for this study and identified the problems related to the MFP. Therefore, we can now perform a sensitivity analysis to determine how various parameter values associated with the LDR, specifically those related to rotation, impact the resulting MFS estimates.

8.4 Model sensitivity analysis: Rotation parameters

This section will focus on a specific component unique to the latitudinal differential rotation (LDR) magneto-Rossby wave model discussed in Chapter 7. This component is the profile used to describe the LDR. As a reminder, LDR refers to the phenomenon where the equatorial region of the Sun rotates faster than the poles and is described by equation (7.4), which we will repeat below

$$\Omega_d = \Omega_0(1 - s_2 \cos^2 \theta),$$

where, Ω_d is the differential rotation rate, Ω_0 is the equatorial solar angular velocity, θ is the co-latitude, and s_2 is a constant differential rotation parameter. We will first determine the impact of different rotation parameters (Ω_0 and s_2) on the resulting angular velocity values of Ω_d. Secondly, we will explore how the different rotation parameters that form part of the LDR profile affect the estimated MFS.

8.4.1 Impact on the latitudinal differential rotation profile

We first need to explore the impact of different values for rotation parameters s_2 and Ω_0 on the LDR function. For example, Gurgenashvili et al. (2016) used the following range of observed s_2 values: $0.14 - 0.2$, with an average value of 0.168. Therefore, we argue that it is acceptable to set $s_2 = 0.17$ (Gurgenashvili et al., 2016) as it is close enough to the average value that the associated error will be negligible. However, Gachechiladze et al. (2019)

sunspots only becomes more noticeable at 30°

considered three s_2 values in their study: $s_2 = 0.12, 0.13$ and 0.2. These values are either not too far below the lower limit ($s_2 = 0.14$) or on the boundary of the upper limit ($s_2 = 0.2$) when compared to the observed values in Table 8.1. This is problematic as the reason for using such a wide range of values in the same study remains unexplained.

On the other hand, for the equatorial rotation rate, Ω_0, there are two commonly used values and an average observed value thereof. The corresponding values are $\Omega_0 = 2.6 \times 10^{-6}\text{s}^{-1}$ (Zaqarashvili et al., 2009; Zaqarashvili and Gurgenashvili, 2018; Gachechiladze et al., 2019), $\Omega_0 = 2.7 \times 10^{-6}\text{s}^{-1}$ (Gurgenashvili et al., 2016) and an average of $\Omega_0 = 2.92 \times 10^{-6}\text{s}^{-1}$ (Gurgenashvili et al., 2016) for the observed values. To illustrate the impact of the differing rotation parameters on the simplified LDR formulation, eq.(7.4), three scenarios will be defined in Table 8.8 below.

Specific cases for Ω_0 and s_2

Case nr	Description	Ω_0 ($\text{s}^{-1} \times 10^{-6}$)	s_2
1	Minimum values	2.60	0.130
2	Commonly used values	2.70	0.170
3	Average of observed values	2.92	0.168

Table 8.8: Three cases for the combination of the rotation parameter values, Ω_0 and s_2, that are commonly used throughout literature.

Figure (8.1) below illustrates the three cases presented in Table 8.8, where the solid blue line is Case 1, the orange dashed line is Case 2 and lastly, the green dotted line is Case 3.

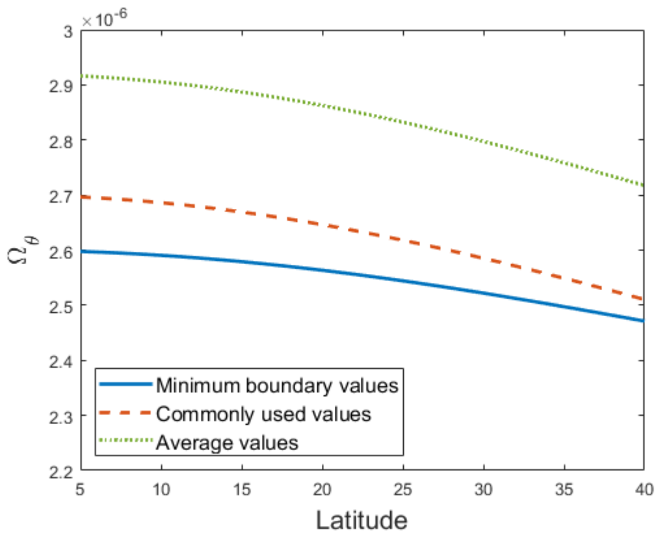

Figure 8.1: The impact of different s_2 and Ω_0 values on the simplified LDR profile according to eq.(7.4). The blue solid line uses the lowest rotation parameter values: $s_2 = 0.13$ and $\Omega_0 = 2.6 \times 10^{-6}\text{s}^{-1}$ (Gachechiladze et al., 2019). The orange dashed line used the most common values, $s_2 = 0.17$ and $\Omega_0 = 2.7 \times 10^{-6}\text{s}^{-1}$. Lastly, the average values of $s_2 = 0.168$ and $\Omega_0 = 2.92 \times 10^{-6}\text{s}^{-1}$ are illustrated by the green dotted line (Gurgenashvili et al., 2016).

The area between the minimum boundary and average functions indicates the wide range of values for these parameters that are considered in the current literature. Moreover, Fig.(8.1) shows that the lower latitudes are slightly more affected by the choice of s_2 and Ω_0 parameter values, which is expected as the effect of LDR is more severe closer to the equatorial region. The next step is to explore how this change in frequency, caused by changing the rotation parameters, affects the resulting MFS when the LDR model is used.

8.4.2 Impact on the model results

Earlier in Section 8.3.1, two cases for the LDR were considered, and the results showed that when LDR is ignored ($s_2 = 0$), the resulting MFS was stronger compared to when LDR was included ($s_2 \neq 0$). A similar exercise will be done here to determine the impact of the rotation parameters on the resulting MFS estimations. However, only the case of $s_2 \neq 0$ will be considered, along with the rotation parameter pairs of Case 1 and 3 (Table 8.8), as these values are on the opposite boundaries of the expected value ranges. Furthermore, to make the resulting MFS values easily comparable to those presented in previous studies, the B_{max}, given by eq.(8.6), will be calculated. Using the constant parameter values for the lower tachocline, given in Table 8.2 along with hemispheric RTP data in Table 8.1, the results for the first (a) and third (b) case are displayed in Table 8.9 below.

Lower range of s_2 and Ω_0 (Case 1)												
(a) B_{max}	13	14	15	16	17	18	19	20	21	22	23	24
North (kG)	**43.5**	**45.1**	**41.9**	**47.9**	**52.1**	**47.9**	**49.1**	**45.1**	36.0	37.4	40.0	32.7
South (kG)	34.1	30.9	35.0	30.4	31.3	40.0	38.9	32.7	**49.0**	**47.9**	**47.9**	**37.4**

Upper range of s_2 and Ω_0 (Case 3)												
(b) B_{max}	13	14	15	16	17	18	19	20	21	22	23	24
North (kG)	**35.3**	**37.1**	**33.5**	**40.2**	**44.8**	**40.2**	**41.5**	**37.1**	26.5	28.3	31.2	22.4
South (kG)	24.2	20.0	25.3	19.3	20.6	31.2	30.0	22.4	**41.5**	**40.2**	**40.2**	**28.3**

Table 8.9: Maximum toroidal MFS, B_{max} (kG), for solar cycles 13-24 for two different rotation parameter scenarios. Consider a MFP of $B_0 \sin\theta \cos\theta$ at a latitude of 45°, with input parameters in Table 8.1 and the calculated B_0 values in Table 8.3. Rotation parameter values for (a) $s_2 = 0.13$ and $\Omega_0 = 2.6 \times 10^{-6}$ and (b) $s_2 = 0.168$ and $\Omega_0 = 2.92 \times 10^{-6}\text{s}^{-1}$. The MFS for the dominant hemisphere in each cycle is highlighted in bold.

From the results of (a) and (b) in Table 8.9, it is observed that the reduced values of Ω_0 and s_2 cause an increase of ± 11 kG and ± 7 kG in the MFS for the non-dominant and dominant hemisphere (bold values), respectively. Furthermore, by comparing these results (Table 8.9), it is observed that when the rotation parameters increase (Case 3), the MFS decreases. The resulting MFS values increase when the rotation parameters decrease (Case 1). Therefore, the initial relationship observed between the LDR value (or, more broadly, the rotation parameters) and the corresponding MFS value (Section 8.3.1) is confirmed.

We further isolate the impact of the individual rotation parameters on the resulting MFS in Fig.(8.2). Here, we plot the baseline MFS (blue line), which considers the average values of the rotation parameters (Case 3 in Table 8.8). Then, we change the s_2 (red dotted line) and Ω_0 (purple dashed lines) to their respective minimum values (Case 1 in Table 8.8).

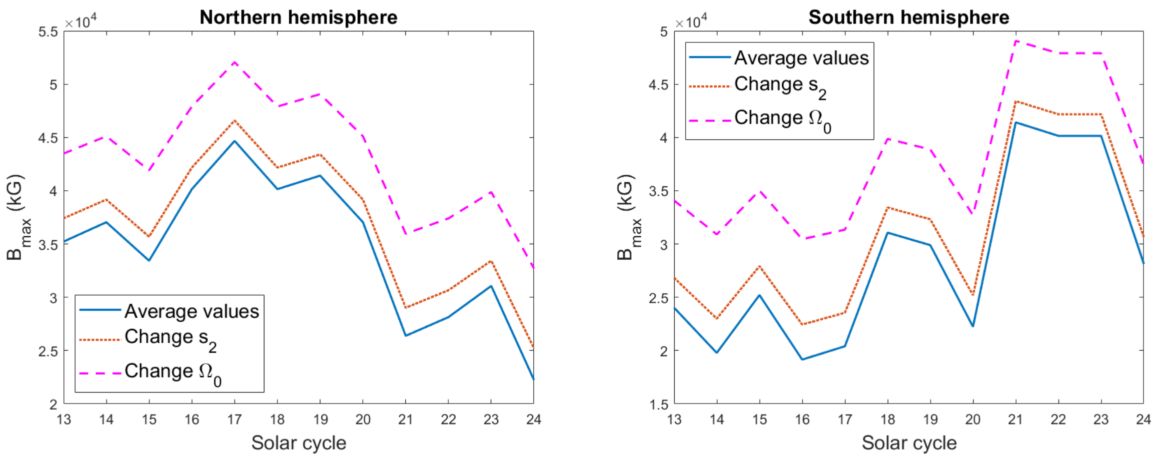

Figure 8.2: The calculated B_{max} values for both hemispheres, considering the upper and lower range of the rotation parameters. Blue line: Magnetic field strength for the average rotation parameters (Case 3). Red dotted line: Change the $s_2 = 0.13$, Ω_0 remained the same as Case 3. Purple dashed line: Change $\Omega_0 = 2.6 \times 10^{-6}\text{s}^{-1}$, keep s_2 the same as Case 3. The southern hemisphere became dominant in cycle 21.

From Fig.(8.2), it can be concluded that a smaller s_2 value (red dotted line) has a lesser effect on the MFS as it increases its value by $\pm 2\,\text{kG}$, compared to the $\pm 7\,\text{kG}$ increase stemming from a reduced Ω_0 value (purple dashed line). This observation shows that the equatorial rotation rate, Ω_0, is the rotation parameter that influences the MFS more significantly and should, therefore, be chosen cautiously. After understanding the effect of changing rotation parameter values, we comprehensively understand the LDR model and its associated input parameters. Therefore, the next step is to examine and critique the existing methodology of calculating the MFS using these two components.

8.5 Methodology validation

This chapter has now validated the LDR model, the associated latitudinal differential rotation and magnetic field profiles, and the relevant input parameter values. Therefore, in this section, we will summarise the existing methodology (Gurgenashvili et al., 2016; 2017) used to calculate the estimated values for the solar MFS and provide the reasoning for the enhancements proposed by our research.

8.5.1 Existing methodology to calculate the MFS

The first case study that we will review used the comprehensive LDR Rossby wave model (Chapter 7) along with RTP for the *solar disk* of solar cycles 14-24 to calculate the estimated B_{max} values (Gurgenashvili et al., 2016) for the $m = 1$, $n = 4$ wave harmonic. This first case study is an example where the appropriate model is used to calculate the estimated MFS values but only considers the high latitude of 45°. Furthermore, the specific wave harmonic was selected because it resulted in a frequency that matches the RTP when considering a proposed MFS ranging between $30 - 50$ kG. However, the RTP data used by Gurgenashvili et al. (2016) is not hemisphere-specific, which can impact the accuracy of the estimated MFS values since it has been shown that for each solar cycle, there is a dominant and non-dominant hemisphere that exhibits different intensities of solar activity (Gurgenashvili et al., 2017).

Studying the MFS hemispheric asymmetry led to the first methodology enhancement introduced by Gurgenashvili et al. (2017). Their study used observational RTP recorded per hemisphere, specifically for solar cycles 19-23, as they have been identified as the cycles that exhibit the most noticeable asymmetry. It was noted that the northern and southern hemispheres were more dominant for the cycles 19-20 and 21-23, respectively. To determine the associated MFS for each hemisphere separately, the authors used the dispersion relation of the fast MHD Rossby wave of the LDR model, eq.(8.1), since it has proven to align well with the observed RTP (Gurgenashvili et al., 2016). According to the results of Gurgenahsvili et al. (2017), when the differential rotation is included ($s_2 \neq 0$), the corresponding MFS estimates are $37 - 43$ kG and $23 - 31$ kG for the stronger and weaker hemispheres, respectively. Furthermore, the difference between the MFSs in the two hemispheres is roughly 10 kG, regardless of the differential rotation parameter value.

Therefore, the current methodology considers the $m = 1$, $n = 4$ harmonic of the fast MHD Rossby wave in the lower tachocline from the LDR model. The rotation parameters are taken as constant per solar cycle as recorded through observations but vary for each solar cycle (Table 8.1). The MFS used in the dispersion relation is calculated as the B_{max}, see eq.(8.6), and is kept constant for each solar cycle. Now that we have analysed each aspect of the current methodology, we can provide recommendations on addressing the issues mentioned throughout this study.

8.5.2 Proposed methodology enhancement

This research proposes two methodological changes that differ from existing literature by reflecting the dynamic behaviour of the magnetic field throughout the solar cycle. The first proposed change addresses the problem of considering the magnetic field strength (MFS) as a constant value throughout the solar cycle. Instead, we suggest a magnetic field moving towards the equator over the solar cycle period, as the sunspot migration observed in the butterfly diagram suggests. Therefore, we propose taking into account a change in the latitude, which is used to estimate the value of the MFS, by considering a latitude range of approximately $30° - 5°$ based on observed latitude ranges of recorded sunspots. This latitudinal variation has not been explored before when calculating the MFS values.

We have also shown that the frequency of magnetic solar activity varies over time, as indicated by the variance in the number of sunspots (Fig.(2.1)). The solar max period is associated with the highest frequency of solar activity. Therefore, we assume the magnetic field strength should be at its maximum during this period. Consequently, we estimate that the relevant latitude associated with this solar cycle phase is 16°. With this in mind, we propose that the existing magnetic field profile (MFP), eq.(8.5), which currently has a maximum value at a latitude of 45°, be replaced by a new MFP that has a maximum value at 16° instead. As only the second proposed enhancement requires a change in the associated equation of the MFP, we provide more details on this aspect in the following section.

8.5.3 Adjusted magnetic field profile

It is necessary to recall the two MFP used in the existing literature to estimate the MFS values discussed in Section 8.3.2, before introducing the proposed MFP. The first MFP is that of eq.(8.5), $\sin \Theta$ (Zaqarashvili and Gurgenahsvili, 2018) seen in Fig.(8.3) as the red dashed line and the second is given by eq.(8.4), $\sin \Theta \cos \Theta$ (Gurgenashvili et al. 2016; 2017) and corresponds to the green dot-dash line in Fig.(8.3).

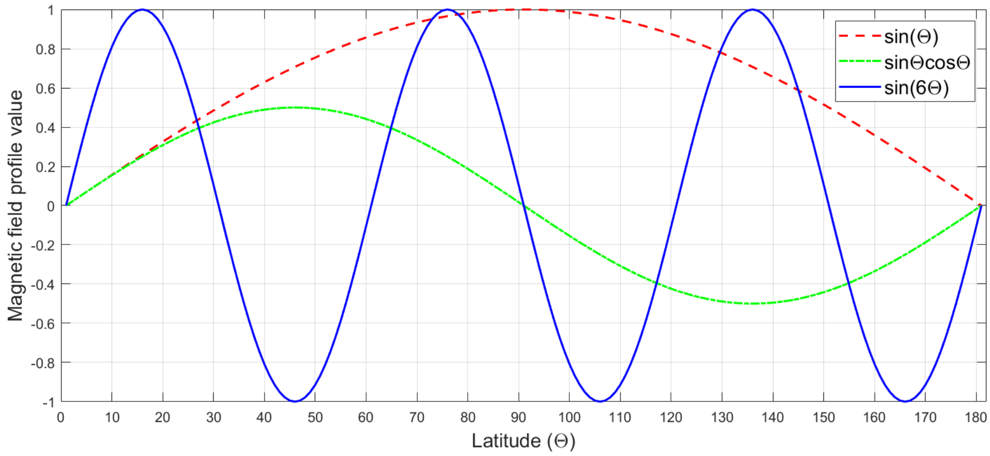

Figure 8.3: The two magnetic field profiles that are currently used in literature, $\sin\Theta$ and $\sin\Theta\cos\Theta$, along with the newly proposed MFP of $\sin(6\Theta)$.

One argument for using the $\sin\Theta\cos\Theta$ MFP mentioned in Section 8.3.2 is that it changes sign at the equator, shown by the green dot-dash line in Fig.(8.3) as it crosses zero. However, since we will be considering different RTP datasets for the respective hemispheres, they will be treated independently. Therefore, the change of signs at the equator is not a required characteristic for the MFP. Instead, aligning the magnetic field profile's minimum values with latitudes corresponding to the solar minimum is essential. These latitudes are close to $30°$ and $5°$ for the start and end of the solar cycle, respectively. Also, a more realistic MFP must have a maximum close to a latitude of $15° - 16°$ as this solar max period falls in the middle of the solar cycle.

Consequently, we propose the following MFP

$$B_\phi = B_0 \sin(6\Theta), \tag{8.7}$$

which is illustrated by the solid blue line in Fig.(8.3), and satisfies all the abovementioned requirements. Here B_ϕ and B_0 are the toroidal and pure MFS, respectively, and Θ is latitude. Implementing our proposed methodology would ensure that the pure magnetic field, B_0, adjusted by the newly introduced MFP, has minimum values at latitudes corresponding to the solar minimum and a maximum at the latitude associated with the solar max phase. Furthermore, since we are using these latitudinal-dependent toroidal magnetic field strength values as an input to the MHD Rossby wave model, we expect that these waves would also exhibit a similar change in strength. However, to confirm that the impact on our model results would be acceptable, we can refer to the findings of Waidele and Zhao's (2023) study, which showed that stronger Rossby waves were observed during solar maximum while weaker Rossby waves were observed during solar minimum. Therefore, the change in strength that our magnetic field will have based on the phase of the solar cycle is also seen in the strength of the solar Rossby waves.

8.6 Summary

This chapter explored the input parameters of the latitudinal differential rotation (LDR) magneto-Rossby wave model. We found that when a parameter varies per solar cycle, such as the rotation parameters Ω_0 and s_2, using the same value for multiple cycles would be incorrect. Instead, we suggest considering the varying values to align the model results with solar observations. We also provided the pure MFS values magnetic field strength (MFS), B_0, used to calculate the toroidal magnetic field strength. These values were not explicitly provided before, so we added them for transparency. Additionally, we added the corresponding frequency in nano-Hertz (nHz) for each RTP given in days. This is crucial because the frequency in nano-Hertz is used in the magnetohydrodynamic (MHD) Rossby wave model to calculate the MFS.

Our evaluation of the model confirmed that the estimated MFS associated with the LDR magneto-Rossby wave model resulted in periodicities closer to the observed RTP than the MHD Rossby wave model, which does not consider the effect of LDR. Therefore, we quantitatively confirmed that the LDR model is the most accurate to use for this research. The model analysis also provided insight into the essential relationship between the LDR, MFS and RTP parameters by confirming that when the LDR is included, the resulting MFS is lower, corresponding to longer periodicities and vice versa. We also noted that for every solar cycle, a dominant hemisphere exhibits a stronger magnetic field strength, and the non-dominant hemisphere exhibits longer periodicities stemming from the patterns in the observational RTP data. This confirms the findings of Gurgenashvili et al. (2017), who showed that the northern hemisphere was dominant for solar cycles 13-20, while for cycles 21-24, it was the southern hemisphere. We also examined how the variables of the LDR profile impact the resulting MFS values. Furthermore, a sensitivity analysis indicated that the equatorial rotation rate, Ω_0, has a greater impact on the MFS value than a change in the s_2 LDR parameter value.

Then, the current methodology used to calculate the estimated MFS values was examined. The existing approach considers a constant magnetic field in position and strength throughout the solar cycle. However, this static approach contradicts the varying behaviour of sunspots, which traces the dynamics of the underlying magnetic field. Since sunspots migrate towards the equator and change in frequency over the solar cycle period, the magnetic field must align with this behaviour as it is the source of these spots. Therefore, we propose that the latitude used to calculate the MFS should correspond to the applicable solar cycle phase associated with the data used as the input to the MHD Rossby wave model and should not exclusively be taken at 45°, such as the case for the current methodology.

Finally, the various magnetic field profiles (MFPs) were analysed since they form part of the MHD Rossby wave model. The commonly used profile, $B_\phi(\theta) \approx B_0 \cos\theta \sin\theta$, has a maximum value at a latitude of 45°. However, we would expect that the maximum magnetic field strength would occur at the latitude where sunspots are observed during the maximum phase of the solar cycle, in other words, at a lower latitude. For this reason, we have proposed a new MFP

$$B_\phi = B_0 \sin(6\Theta), \tag{8.7}$$

where Θ is latitude, which is formulated to have a maximum value at a latitude of 16°, which corresponds to the solar maximum phase in the middle of the solar cycle. Our proposed MFP also has minimum values that align with the latitudes that correspond to the solar minimum at the start (30°) and end (5°) of the solar cycle, making it the profile that is the most representative of the observed sunspot patterns.

This study highlights the significance of incorporating solar observations to improve the theoretical modelling of MHD Rossby waves. This aspect has not been given due attention in the existing literature. Our proposed methodology enhancements focus on aligning the input data with the solar cycle phase to achieve more accurate model results. Without such alignment, attempting to draw inferences between theoretical models and other observed solar features would be futile and could result in misleading conclusions. Furthermore, by utilising the LDR magneto-Rossby wave model, consistently using solar cycle-specific input data and varying the latitude and strength of the MFS, we can address the problem statements discussed in Section 3.6, Section 3.6.1 and Section 2.2.1.

9 Results

9.1 Introduction

In this study, we aimed to estimate the magnetic field strength values of solar cycles 13-24 for the solar cycle's main phases (solar minimum and maximum) per hemisphere. We used appropriate parameter values that stem from observations which have not been used previously and considered the newly formulated MFP (Section 8.5.3). The proposed MFP was designed such that the maximum value of the function corresponds to the solar max latitude of 16°, while the minimum values are at the latitudes associated with solar min (30° and 5°).

This chapter starts by providing an overview of the research methodology employed, based on the primary findings of the analysis in Chapter 8. This is followed by a summary of the input parameters used to calculate the results given in the rest of the chapter. Then, we provide the two sets of estimated toroidal magnetic field strength values per hemisphere for solar cycles 13-24 corresponding to the latitudes of the solar minimum (29°) and the solar maximum (16°), respectively. An additional summary that segments and summarises the results according to the dominant and non-dominant hemispheres is also provided. Lastly, the corresponding periodicity of each estimated MFS is calculated and tabled in the same format as the MFS values.

9.2 Methodology

Ideally, the magnetic field strength (MFS) should be calculated for every latitude in the range of 5°- 30° (latitudes associated with sunspot appearances throughout the solar cycle), such that we have a continuous MFS estimate over time. Still, this work aims only to showcase the effectiveness of our dynamic methodology, which suggests that the magnetic field varies in latitude and strength throughout the solar cycle. Therefore, for simplicity, we will only consider two latitudes that are associated with the main phases of the solar cycle: solar max (16°) and solar min (29°), which will serve as an example of how the MFS values are expected to change throughout the solar cycle. Also, the reason behind choosing the latitude of 29° for the solar minimum phase is because we would like to demonstrate the non-zero MFS values which occur at a latitude close to the one where the MFP has a minimum, i.e. 30°. Moreover, the results of the 29° latitude, associated with the start of the solar cycle, will also apply to the end as it enters a minimum phase again.

To calculate the MFS and later the associated periodicity, we will consider the dispersion relation of the fast MHD Rossby wave mode as derived by the LDR magneto-Rossby wave model (Chapter 7), which is repeated below

$$\omega_+ = -\frac{m\Omega_0(1+s_2) + \sqrt{(1+s_2)^2 + \alpha_0^2\, n(n+1)}}{n(n+1)}, \tag{8.1}$$

where

$$\alpha_0^2 = \frac{B_0^2}{4\pi\rho\Omega_0^2 R_0^2} = \frac{v_A^2}{\Omega_0^2 R_0^2}, \tag{6.47}$$

and v_A is the Alfvén speed is given by

$$v_A = \frac{B_0}{\sqrt{4\pi\rho}}. \tag{3.6}$$

Here, ω_+ is the frequency of the fast MHD Rossby wave, denoted by the "+", m and n are the toroidal and poloidal wavenumbers, respectively. The distance from the Sun's centre to the tachocline is given by R_0, and ρ is the tachocline density. Lastly, B_0 is the pure MFS value, which is not affected by the MFP.

Furthermore, in Section 7.1.1, it was argued that the simplified LDR profile, which only considers the s_2 rotation parameter, can be considered without the risk of introducing significant errors. The expression that describes this profile is as follows

$$\Omega_d = \Omega_0(1 - s_2\cos^2\theta), \tag{7.4}$$

where Ω_d is the differential rotation rate, Ω_0 the equatorial rotation rate, and θ is co-latitude.

Finally, our analysis and, more specifically, the methodology evaluation in Section 8.5 introduced two enhancements, of which proposing a more realistic magnetic field profile (MFP) was one. The more accurate MFP proposed by this study is given by

$$B_\phi = B_0 \sin(6\Theta), \tag{8.7}$$

which has a maximum value at a latitude of 16°, aligning with the latitude where solar activity is mainly observed during solar max, while at the latitudes corresponding to the solar minimum (30° and 5° at the start and end of a solar cycle), its value drops to a minimum.

It follows that the MFS can be calculated for the latitude of 29°, corresponding to the solar minimum phase, by applying the following steps for each set of solar-cycle-specific variables:

1. Calculate the toroidal MFS adjusted according to the magnetic field profile (MFP). In other words, calculate B_ϕ, by substituting the pure MFS, B_0, and latitude value of 29°, into our MFP, eq.(8.7).
2. Calculate the estimated MFS that is associated with the fast MHD Rossby wave in the lower tachocline, by substituting the toroidal MFS from Step 1 and the observed RTP values in nHz (Table 9.1) into eq.(8.1).

This process is repeated for the solar maximum, where the lower latitude of 16° is considered. Calculating the MFS at these two "extreme" latitudes specifically, will show how the MFS changes over the solar cycle and prove that considering it as a constant value in strength and latitude is incorrect. Furthermore, since the expected values for the RTP are known for each hemisphere throughout solar cycles 13-24, calculating the periodicity corresponding to the resulting MFS and comparing them to the observed values could be used to validate our methodology and results further. Therefore, this validation step entails substituting the B_ϕ values into eq.(8.1) so that the frequency can be calculated. After which, the resulting periodicity calculated in nano-Hertz will be converted to days and compared to the observed RTP values. Now that we have established the fundamental equations and the approach to computing the MFS and its corresponding periodicity, we will summarise the necessary input parameter values in the next section.

9.3 Input parameter values

First, we will consider the $m = 1$, $n = 4$ harmonic of the fast MHD Rossby wave as it has been established (Section 8.3.1) that the periodicities associated with this harmonic have values that fall within the range of observed RTP values (Gurgenashvili et al., 2016; 2017). Then, for calculating the MFS values, the RTP frequency (in nano-Hertz) per hemisphere is used along with the pure MFS, B_0, values given in Table 9.1. The observed rotation parameters, s_2 and Ω_0 (Javaraiah et al., 2005), are also provided in Table 9.1 for the respective solar cycles.

Summary of solar-cycle-specific input data						
Cycle	s_2	Ω_0 ($\times 10^{-6} s^{-1}$)	$\mathrm{RTP^N}$ (nHz)	$\mathrm{RTP^S}$ (nHz)	B_0^{N} (kG)	B_0^{S} (kG)
13	0.168	2.9242	432.87	388.89	72.4	50.6
14	0.15	2.9270	440.74	374.85	75.9	42.4
15	0.18	2.9310	425.27	393.09	65.1	48.3
16	0.17	2.9290	454.51	372.93	79.9	37.6
17	0.20	2.9330	475.30	376.80	85.8	34.3
18	0.18	2.9200	454.51	415.55	79.2	60.9
19	0.19	2.9250	460.26	410.86	80.6	56.9
20	0.16	2.9270	440.74	382.75	74.9	45.6
21	0.14	2.9250	397.39	460.26	56.5	85.6
22	0.14	2.9090	404.01	454.51	60.6	83.8
23	0.17	2.9200	415.55	454.51	62.1	80.3
24	0.168	2.9200	382.75	404.01	44.8	56.5

Table 9.1: Rotation parameter values, s_2 and Ω_0 for each solar cycle (Javaraiah et al., 2005) and the associated RTP for each hemisphere per cycle (Zaqarashvili et al., 2018) converted into nano-Hertz (nHz). Pure magnetic field strength values, B_0, from Table 8.3. These are the most plausible input parameter values used in our analysis.

Next, the parameter values that describe the properties of the tachocline remain constant for all calculations and are listed in Table 8.2, which is repeated below.

Properties of the lower tachocline		
Parameter	Symbol	Value
Medium density	ρ	$0.2\,\mathrm{g\,cm^{-3}}$
Distance from center of Sun to the tachocline	R_0	$5 \times 10^{10}\,\mathrm{cm}$

Since we have now provided the equations, input parameter values, and methodology for calculating the MFS, the resulting MFS estimates will be presented in the next section.

9.4 Toroidal magnetic field strength results

After following the steps outlined in Section 9.2 and utilising the inputs provided in Section 9.3, we obtained the resulting MFS values, which are listed in Table 9.2. When analysing these MFS results, it is important to recall that the northern hemisphere was dominant in solar cycles 13-20 and the southern hemisphere in cycles 21-24 (Zaqarashvili and Gurgenashvili, 2018). Therefore, the following results highlight these dominant hemispheric values in bold font to make them easily identifiable in the data.

(a) Northern hemisphere: Toroidal Magnetic Field Strength (kG)

Cycle	13	14	15	16	17	18	19	20	21	22	23	24
$B_\phi(29°)$	**7.6**	**7.9**	**6.8**	**8.4**	**9.0**	**8.3**	**8.4**	**7.8**	5.9	6.3	6.5	4.7
$B_\phi(16°)$	**72.0**	**75.5**	**64.8**	**79.5**	**85.4**	**78.8**	**80.1**	**74.5**	56.2	60.3	61.8	44.5

(b) Southern hemisphere: Toroidal Magnetic Field Strength (kG)

Cycle	13	14	15	16	17	18	19	20	21	22	23	24
$B_\phi(29°)$	5.3	4.4	5.0	3.9	3.6	6.4	6.0	4.8	**9.0**	**8.8**	**8.4**	**5.9**
$B_\phi(16°)$	50.4	42.2	48.0	37.4	34.1	60.6	56.6	45.3	**85.2**	**83.3**	**79.9**	**56.2**

Table 9.2: Results: Estimated toroidal magnetic field strength for the solar minimum (29°) and solar maximum (16°) in the northern and southern hemisphere using the newly introduced magnetic field profile of $B_\phi = B_0 \sin(6\Theta)$.

Below, Fig.(9.1) shows the average number of sunspots per hemisphere (Veronig et al., 2021), which includes the corresponding estimated MFS values marked on the second y-axis. Here, the blue squares (in the middle of the graph) are the MFS values calculated per hemisphere using the methodology presented in Gurgenashvili et al. (2017), which corresponds to the B_{max} values, see eq.(8.6). It is, therefore, considered a static value for each solar cycle but is hemisphere-specific. Conversely, the orange circles (close to the peaks) and purple diamonds (at the bottom of the graph) indicate the MFS values calculated based on our dynamic methodology for the solar max and solar min, respectively, given in Table 9.2 per hemisphere. Figure (9.1) clearly shows the discrepancy between the static (existing) and the dynamic (new) approaches to calculating the MFS.

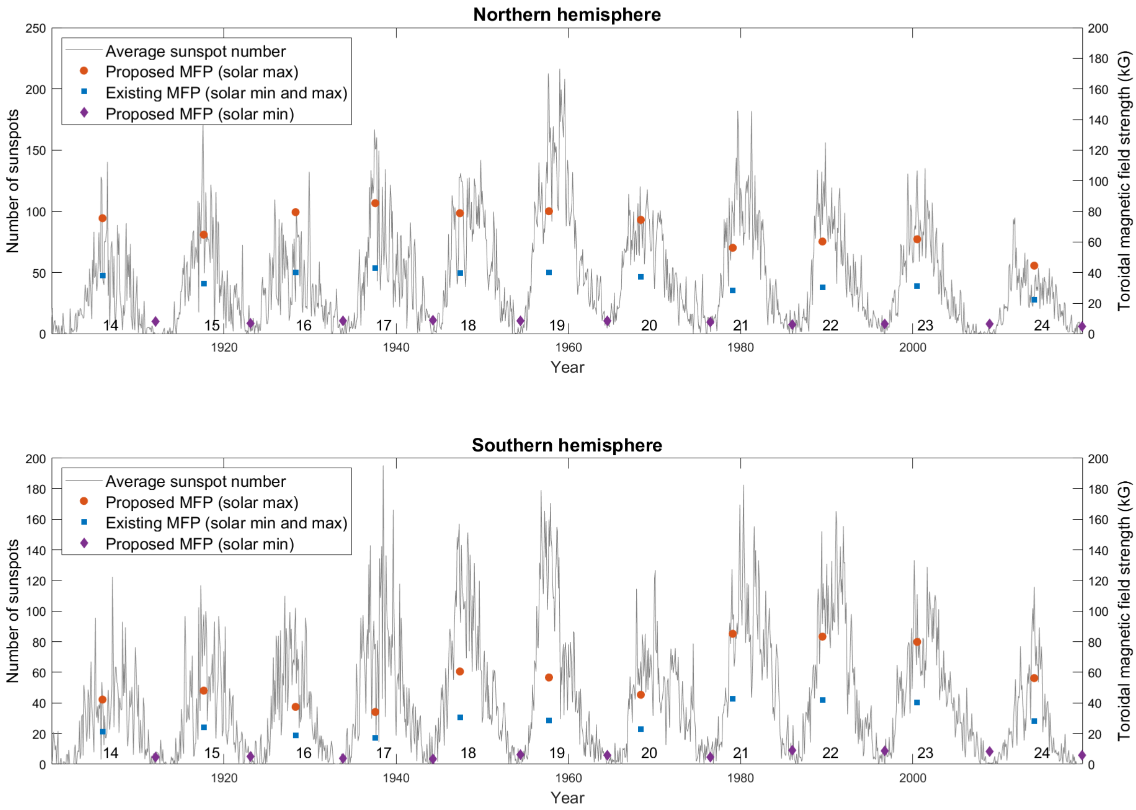

Figure 9.1: Comparison of the results using the dynamic (new) and the static (existing) methodology to calculate the magnetic field strength. Our methodology results are the solar min (purple diamonds) and the solar max (orange circles). The blue squares correspond to the toroidal magnetic field strength determined by Gurgenashvili et al. (2017), which is taken as constant for each hemisphere per solar cycle. Sunspot data courtesy of Veronig et al. (2021).

If we further classify the strength of the solar cycle based on the peak average number of sunspots recorded per solar cycle, then we can define the following three cases:

1. Weak solar cycles have a maximum average number of sunspots between $[100 - 150]$: 13, 14, 16, 24[1].

2. Moderate solar cycles have a maximum average number of sunspots between $[150 - 200)$: 15, 17, 20, 23.

3. Strong solar cycles have a maximum average number of sunspots ≥ 200 : 18, 19, 21, 22.

The average toroidal magnetic field values for the three solar cycle strength classifications are summarised below for the dominant (Table 9.3) and non-dominant (Table 9.4) hemispheres, respectively.

[1]According to Young (2013), cycle 24 is the weakest cycle in the last century.

Dominant hemisphere avg MFS			
	Solar cycle strength		
Cycle phase	Weak	Moderate	Strong
Solar min	7.5 kG	8.0 kG	8.6 kG
Solar max	70.8 kG	76.2 kG	81.9 kG

Table 9.3

Non-dominant hemisphere avg MFS			
	Solar cycle strength		
Cycle phase	Weak	Moderate	Strong
Solar min	4.6 kG	5.0 kG	6.1 kG
Solar max	43.6 kG	47.3 kG	58.4 kG

Table 9.4

In this section, we have provided the primary results of this study, which are the estimated MFS values per hemisphere for the main phases of the solar cycle (solar min and max) for solar cycles 13-24. Now, as a validation step, we can calculate the corresponding periodicities for the respective MFS values to compare them to their observational counterparts.

9.5 Periodicity estimates based on toroidal magnetic field strength results

As discussed in Section 9.2, we can verify the validity of the methodology changes introduced in this study by calculating the periodicity associated with the respective estimated MFS values. More specifically, calculating the respective periodicities will allow us to confirm that the relationship between the MFS and the periodicity (as identified in Section 8.3.1) is observed. In other words, we expect the dominant (non-dominant) hemisphere to have a stronger (weaker) MFS and shorter (longer) periodicity. Also, since we have the observed RTP per solar cycle, we could compare our values to these as an additional verification since we do not expect them to differ significantly. If these two criteria are met, our methodology will not violate other fundamental observations and will provide further empirical evidence of the validity of the proposed methodology enhancements.

When substituting the MFS calculated in the previous section for the respective latitudes of the two hemispheres, the periodicity results are listed in Table 9.2 below.

(a) Northern hemisphere: Periodicity (days)												
Cycle	13	14	15	16	17	18	19	20	21	22	23	24
$B_\phi(29°)$	**215**	**215**	**210**	**211**	**205**	**210**	**208**	**213**	217	219	212	213
$B_\phi(16°)$	**168**	**165**	**171**	**160**	**153**	**160**	**158**	**165**	183	180	175	190

(b) Southern hemisphere: Periodicity (days)												
Cycle	13	14	15	16	17	18	19	20	21	22	23	24
$B_\phi(29°)$	216	216	210	212	206	210	208	214	**217**	**218**	**212**	**213**
$B_\phi(16°)$	187	194	185	195	193	175	177	190	**158**	**160**	**160**	**180**

Table 9.5: Estimated periodicity for the northern and southern hemisphere associated with the toroidal magnetic field strength and varying rotation parameters.

In this chapter, we employed the proposed methodology and magnetic field profile and provided the results of the magnetic field strength estimates for each hemisphere at the two main phases (solar minimum and maximum) of solar cycles 13-24. These are the most granular estimations of the MFS to date. We have also calculated the periodicity associated with each estimated MFS value, which will allow us to evaluate whether the proposed enhancements are advantageous. In the next chapter, we will discuss our findings, compare them to observational values, and make meaningful conclusions.

10 Discussion and Conclusion

10.1 Introduction

This chapter will start by revisiting the connection between the magnetohydrodynamic (MHD) Rossby waves and the Rieger-type periodicity (RTP) in Section 10.2, as this is the cornerstone of this research. Next, the two regions of the tachocline and their associated MHD Rossby waves are discussed in Section 10.3, where we revisit the reasoning for why the fast MHD Rossby wave in the lower tachocline is preferred for this study.

Then, in Section 10.4, we will summarise the various MHD Rossby wave models that were considered. Here, we address the forces and equations that are related to the magnetic field, the shallow water approximation and the Sun's latitudinal differential rotation (LDR). We subsequently propose that the LDR model (Chapter 7) is the most plausible for studying the MHD Rossby waves in the lower tachocline. Next, a discussion of the parameter sensitivity analysis results follows (Section 10.5), where we address how future studies can better align on the choice of input parameter values going forward.

In Section 10.6 we explain how we advanced the field of study through our improved magnetic field profile (MFP) and more dynamic approach to calculating the magnetic field strength (MFS). Moreover, the results of this study are considered to be more granular and, therefore, align better with solar observations. Furthermore, various essential results are discussed in Section 10.7. First, we provide a summary of essential historical findings that will be used to interpret our results more effectively. After this, we discuss general observations that are made based on our findings and the specific MFS values estimated for the solar minimum and maximum per hemisphere for solar cycles 13-24. The comparison of our results to those previously calculated allows us to make the conclusions given in Section 10.8.

Furthermore, we expect our results to improve the accuracy of existing models that form part of the space weather prediction framework (SWPF) since they use the MFS as an input. Thus, in Section 10.9, we discuss the two specific models within the SWPF that could benefit from our resulting MFS estimates. We also note how our enhancements would affect the method used in predicting active regions on the surface of the Sun (Dikpati, 2020). Finally, in Section 10.10, we outline the limitations of this study and suggest how they can be improved in future work to ensure the advancement of knowledge.

10.2 Rieger-type periodicity and MHD Rossby waves

Various observational data of the solar surface show a period of increased solar activity lasting between 150-195 days, referred to as the Rieger-type periodicity. Since this pattern of the RTP is observed in every solar cycle, albeit slightly longer (shorter) periods are exhibited by weaker (stronger) cycles, it was suggested that MHD Rossby waves inside the Sun are likely to be responsible for these periodicities (Lou, 2000; Zaqarashvili et al., 2010; Gurgenashvili et al., 2016, 2017; Dikpati et al., 2017; McIntosh et al., 2017; Zaqarashvili and Gurgenahsvili, 2018). Considering that solar activity and the magnetic field are closely related, it is more appropriate to consider the magnetohydrodynamic (MHD) Rossby wave instead of its hydrodynamic (HD) counterpart (Lou, 2000), when investigating the connection between Rossby waves and the RTP. Furthermore, Horstmann et al. (2022) concluded that due to the resilience of MHD Rossby waves to viscous damping compared to other planetary waves, these waves are more relevant than HD Rossby waves when considering space weather dynamics, thereby confirming that the MHD Rossby waves are better suited for this study.

10.3 MHD Rossby waves in the solar tachocline

Since the MHD Rossby waves in the solar tachocline have been identified as the most plausible source for the observed RTP, various combinations of governing equations and coordinate systems have been used to derive the associated wave dispersion relations (Part II). Afterwards, it was observed that when a magnetic field was added to the system, the normal HD Rossby wave split into a fast and slowly propagating mode (Zaqarashvili et al., 2007). Furthermore, taking into account the respective effective gravity values of the upper and lower regions of the tachocline, it was recommended that these two regions be treated separately (Zaqarashvili et al., 2007, 2009).

Subsequently, Zaqarashvili et al. (2018) determined that the fast MHD Rossby waves in the *upper tachocline* correspond to periods close to that of the Schwabe cycle (~ 11 years) and the slow MHD Rossby wave exhibits a periodicity of 90-100 years. Since these long-term periodicities do not apply to the study of space weather, the upper tachocline was not considered. Similarly, since the slow MHD Rossby wave in the lower tachocline (Zaqarashvili and Gurgenashvili, 2018) exhibits long periodicities (> 1 year), they, too, have been neglected. Consequently, for this study that focuses on the RTP, we only considered the fast MHD Rossby wave dispersion relation in the lower tachocline, which will be discussed in the next section.

10.4 Optimal MHD Rossby wave model identified

Three different MHD Rossby wave models were derived in this study (Part II), each considering additional solar dynamics. From this exercise, we concluded the following. Firstly, because of the strong magnetic field strength in the Sun, the Lorentz force and induction equation that describes a system containing a magnetic field should be included in the MHD Rossby wave modelling.

Secondly, including the effect of latitudinal differential rotation (LDR), where the rotation of the Sun is faster around the equator than at the poles, is essential as it significantly influences the MFS values calculated using the MHD Rossby wave model. Our analysis proved that the periodicity associated with the MFS calculated using the LDR model has the smallest percentage error compared to the observed RTP values, making it the most plausible MHD Rossby wave model for the lower tachocline. As a result of including the dynamics of the LDR, an additional rotation parameter, s_2, is introduced to the governing equations as follows.

The LDR is added to the governing equations by substituting the LDR profile into the equatorial rotation rate parameter, Ω_0. We have also demonstrated (Section 7.1.1) that the simplified LDR profile, as shown in eq.(7.4)

$$\Omega_d = \Omega_0(1 - s_2 \cos^2 \theta), \tag{7.4}$$

is a valid option. This profile only considers the rotation parameter, s_2, which is recorded with greater accuracy than the s_4 parameter included in the full LDR profile, eq.(7.1) via an additional term ($s_4 \cos^4 \theta$).

Thirdly, by applying the shallow water approximation, effective gravity and layer thickness parameters enter the governing equations (Zaqarashvili et al., 2007, 2009). However, the different values for these parameters in the upper and lower parts of the tachocline suggested that they should be studied separately (Zaqarashvili et al., 2007, 2009). It was subsequently noted that neither the effective gravity nor the layer thickness appeared in the dispersion relation of the fast MHD Rossby wave model in the lower tachocline. Furthermore, we found that the MHD Rossby wave dispersion relation obtained using the 2-dimensional governing equations is identical to the one obtained using the shallow water governing equations, except for one term. This term includes a parameter for the LDR (s_2), which was taken into account in the first derivation mentioned. This is an important finding, as it shows both are no differences in the resulting dispersion relations, although the derivations are vastly different. From this, we can conclude that both sets of governing equations (SWEs and 2D) are suitable for studying MHD Rossby waves in the tachocline. However, there are benefits to using the shallow water equations as they allow us to make further assumptions that simplify the modelling process.

10.5 Discussing the parameter sensitivity analysis

It has been shown in this study (Section 8.4) that a change in the two rotation parameter values, Ω_0 and s_2, has a noticeable impact on the resulting MFS and corresponding periodicity. More specifically, we found that when the rotation parameters associated with the LDR increase (decrease), the estimated MFS decreases (increase), which corresponds to longer (shorter) RTP values. However, the study by Gachechiladze et al. (2019) disagrees and argues that stronger periodicities correspond to stronger MFS, another example of opposing views in this field of study. Conversely, our finding is in agreement with the observation of Zaqarashvili et al. (2010) that the behaviour of the unstable MHD Rossby wave harmonics in the solar tachocline is sensitive to the combination of the LDR parameters (s_2 and, in their case, s_4 as well).

Furthermore, the results from the sensitivity analysis show that changing the value of the equatorial rotation rate, Ω_0 significantly impacts the resulting MFS compared to varying the s_2 parameter. Since the value of Ω_0 has a unique value per solar cycle as determined by observations (Table 9.1), setting the value of this parameter as constant for all solar cycles or using a different value compared to what is recorded adds unnecessary inaccuracies in the model results and should be avoided. Therefore, we propose that all future studies consider the observed value of the Sun's rotation rate for the associated solar cycle. Finally, it should also be mentioned that keeping Ω_0 constant throughout the solar cycle is acceptable as it is not expected to change. Instead, the differential rotation rate, Ω_d, changes.

10.6 Methodology for MFS estimations discussion

Lastly, it is worth recalling that the existing methodology to calculate the estimated magnetic field strength (MFS) considers it constant in both latitude and strength throughout the solar cycle. This study challenges this static approach by suggesting that it be varied in strength and latitude according to the occurrences and behaviour of sunspots as recorded throughout the solar cycle (see Fig.(2.1) for the number observed and Fig.(2.2) for the equatorial migration). As a result, two enhancements were proposed to the methodology for calculating MFS, which are discussed next.

10.6.1 The improved magnetic field profile

The starting point is to align the characteristics of the function that describes the magnetic field profile (MFP) with solar observations. This ensures that the profile describes the change in the magnetic field behaviour over the solar cycle as accurately as possible. The MFP currently used, $B_\phi = B_0 \sin\theta \cos\theta$, has a maximum MFS value at a latitude of 45°. Zaqarashvili et al. (2009) further stated that the advantage of this profile is that it changes signs at the equator. Even then, it is argued that the latitude associated with the maximum of this function is too high to be considered for solar activity, as sunspots are mainly observed between latitudes of $30° - 5°$. Furthermore, this research established that the function does not need to change signs at the equator as the input data for RTP are hemisphere-specific, and the calculations are done separately.

Instead, it is essential to align the MFP's minimum values to be at the same latitudes of sunspot occurrences during the solar minimum, which is close to 30° and 5° for the start and end of the solar cycle, respectively. Similarly, a more realistic MFP must have a maximum value close to a latitude of $15° - 16°$, corresponding to the sunspot locations during the solar maximum phase. To this end, we proposed the following MFP

$$B_\phi = B_0 \sin(6\Theta), \tag{8.7}$$

which satisfies all the requirements needed to align with sunspots' behaviour over the solar cycle period.

10.6.2 Considering a dynamic magnetic field throughout the solar cycle

In this study, the researchers have made two enhancements to improve the magnetic field strength (MFS) calculation during the solar cycle. The first enhancement ensures that the MFS aligns with the variance of solar activity throughout the cycle. This means that the MFS starts at a minimum value at a latitude of 5°, gradually increases to reach a peak at a latitude of 16°, and then reduces until it reaches the minimum again at a latitude of 30°.

The second enhancement is to calculate the MFS estimates at different latitudes, corresponding to the extreme cases of the solar cycle, proving its inadequacy in calculating one value and keeping it static for the entire cycle. Its estimated strength would be faulty if the previous MFP were used at a latitude of 45°. Also, this study's results are limited to only two latitudes. Therefore, it is suggested that all latitudes $\leq 30°$ should be considered when solar activity is of interest. This change could be implemented by continuously calculating the MFS instead of considering isolated latitudes, as demonstrated in this study. This better reflects the varying strength of the magnetic field throughout the solar cycle.

The variance in the resulting MFS values at these different latitudes is significant for accurate predictions of space weather. Current space weather prediction models rely on estimated magnetic field strength values as an input, so it is crucial to provide MFS estimates that are more reflective of reality. This means that the MFS estimates should consider the dynamic behaviour observed in the Sun's magnetic field, as demonstrated in this study. This topic is discussed further in Section 10.9. Nonetheless, we will discuss the resulting MFS values of this study in the next section.

10.7 Results discussion

To discuss the findings of this study, it will be beneficial to provide an overview of the data segmentation. First, the solar cycle is classified based on its magnetic field strength (MFS), followed by the solar hemispheres. Finally, the data is segmented according to the latitude used in the calculation of the MFS. Each section guides the discussion of the results.

First, the respective solar cycles are classified according to their strength. To this end, three classes (Section 9.4) are defined based on the maximum average number of sunspots per cycle, summarised as follows:

1. Weak solar cycles: 13, 14, 16, 24,
2. Moderate solar cycles: 15, 17, 20, 23,
3. Strong solar cycles: 18, 19, 21, 22.

Secondly, it has been established that each solar cycle has a dominant and non-dominant hemisphere (Gurgenashvili et al., 2017), where the former exhibits a stronger magnetic field strength (MFS) and, subsequently, a shorter periodicity and vice versa.

Since the equation for the magnetic field profile (MFP) requires the pure MFP, B_0 as input, we first calculated these B_0 values for transparency, as they are not provided in the existing literature discussed in this study (Gurgenashvili et al., 2016, 2017; Zaqarashvili and Gurgenashvili, 2018). Then, considering that the observational RTP data, which exhibit the north-south hemisphere asymmetry, are used to calculate the B_0 values, the same pattern is observed in the calculated B_0 values given in Table 9.1. In other words, our resulting MFS values are expected to exhibit the same pattern where the northern hemisphere is dominant for cycles 13-20 and the southern hemisphere for cycles 21-24.

Furthermore, this study's third data segment is based on the latitudes considered. Therefore, the MFS value is calculated at the latitudes of the two main phases of the solar cycle, called the solar minimum and maximum. Implementing this step enabled the researchers to enhance this field of research by refining the granularity of the magnetic field strength estimates. Moreover, the calculation of the periodicity that is associated with each MFS result is used in a validation exercise to determine if the results contradict any observational findings. Thus, it is important to revisit the RTP (discussed in Section 10.2) with the solar cycle strength classifications in mind to discuss the results in context. Before the extensive research on the RTP began, it was initially noted that the RTP of 154 days (Rieger et al., 1984) was only observed during the solar maximum (Lean, 1990) of specific solar cycles, such as 16-21 (Carbonell and Ballester, 1990, 1992) with no clear reasoning for its absence in cycles 12-15 (Carbonell and Ballester, 1990, 1992). However, note that it was during solar cycle 21 that the RTP of 154 days was observed, which falls within our strong solar cycle classification. Then, by recalling the finding of Gurgenashvili et al. (2017), which proved the anti-correlation between the solar cycle strength and the RTP, meaning stronger cycles would exhibit shorter periodicities, it can be concluded that the RTP was not absent in other weaker cycles. It merely exhibited a longer periodicity than what was initially expected.

Lastly, calculation of the MFS in the context of the dispersion relation requires recalling the two observed frequency ranges associated with the "initial RTP" and "near RTP", defined in Section 2.4.1, as 150-160 days (Rieger et al., 1984) and 161-195 days (Chowdhury et al., 2015), respectively. The MHD Rossby waves are also believed to be responsible for these periodicities. Therefore, if we use the dispersion relation of the fast MHD Rossby wave in the lower tachocline to calculate the MFS, the periodicity of the MFS result is expected to fall within one of these RTP ranges, depending on the hemisphere and latitude.

10.7.1 General findings

As expected, the findings from this study (Table 9.5) reflect the relationship between stronger magnetic fields and shorter periodicities. Conversely, a weaker magnetic field strength corresponds to a longer periodicity. Moreover, observations from comparing the MFS results based on the classification of solar cycle strength showed that transitioning from a weak to moderate to strong solar cycle strength resulted in an average increase of 0.6 kG and 5 kG in the MFS estimates for both solar minimum and maximum, respectively. Conversely, it was established that for each solar cycle, the increase in the estimated MFS as the solar cycle progresses from the solar min to the solar max in the dominant hemisphere is calculated on average as 68 kG. For the non-dominant hemisphere, the average increase from solar min to solar max is 44 kG.

10.7.2 Solar minimum magnetic field strength results and validation

Analysing the data on a more granular level by considering the estimated values for the MFS during the solar minimum ($\theta = 29°$) period displayed the following:

For the dominant hemisphere, the average MFS during the solar minimum is 8 kG, whilst 5 kG is observed for the non-dominant hemisphere. As a result of these low MFS values, the corresponding periodicities are longer ($\geq$ 205 days) and consequently do not fall within the initial or near RTP range. However, results from this study show that at higher latitudes during the solar minimum, there is an average periodicity of 212 days for the northern hemisphere and 213 days for the southern hemisphere. This aligns closely with a significant period of 213 days noted by Chowdhury et al. (2009) in solar magnetic activity. Therefore, the fast MHD Rossby waves, with a magnetic field at 29°, could likely explain this slightly longer observed periodicity. However, this finding needs further verification.

10.7.3 Solar maximum magnetic field strength results and validation

The following observations were made when examining our MFS results calculated at the latitude associated with the solar maximum ($\theta = 16°$).

During the solar maximum phase, the average estimated MFS values for the dominant and non-dominant hemispheres are 76 kG and 50 kG, respectively. Contrary to those for the solar minimum, the periodicities of the estimated MFS value and, subsequently, maximum are aligned with the observed RTP. Therefore, it was established that all the solar maximum phases of the strong cycles exhibit a frequency that falls within the initial RTP range. This is an important observation as it first corroborates the findings of Gurgenashvili et al. (2017). Secondly, it verifies that the results of this study align with historic solar observations (Rieger et al., 1984). Moreover, for the solar cycles with moderate and weaker strengths, the resulting periodicities for the solar maximum phase fall within the near RTP. Based on the results of this study, the researchers propose that in addition to considering the strength of the solar cycle and the asymmetry of the hemispheres, the phase of the solar cycle during which the solar observations are recorded plays a critical role and should not be neglected.

10.8 Conclusion of our findings

The following is a discussion of the differences between the maximum magnetic field strength (MFS) results obtained from the existing and proposed methodologies. The existing methodology makes use of the latitudinal differential rotation (LDR) model and calculates the maximum MFS, represented as B_{max}, per hemisphere using the RTP in Table 9.1. The magnetic field profile given by eq.(8.5) at a latitude of 45° is utilised, and the results are presented in Table 8.4 ($s_2 \neq 0$). It is important to note that the current methodology does not differentiate between the different phases of the solar cycle and, therefore, uses the same estimated MFS values throughout the solar cycle, as shown in Fig.(9.1). Similarly, the researchers in this study use the dispersion relation of the fast MHD Rossby wave in the lower tachocline derived from the LDR model, which includes the important dynamics of latitudinal differential rotation. However, the proposed methodology differs from the existing methodology in the way it uses the improved magnetic field profile (MFP) and calculates the MFS values at two specific latitudes, corresponding to the solar minimum and maximum phases of the solar cycle.

In comparing the maximum MFS values estimated previously with the solar maximum results of analysis for each solar cycle from this study (at a latitude of 16°), the researchers observed that the estimated MFS values, when applying the proposed methodology, for the solar max phase in the northern and southern hemispheres are on average 35 kG and 28 kG stronger than those calculated using the current methodology. To further illustrate the limitations of the static approach, the literature-estimated MFS values are compared with the values calculated for the solar minimum in this study, revealing that they are on average 28 kG and 23 kG weaker for the northern and southern hemispheres, respectively. This large discrepancy in the resulting MFS values highlights the flaw encountered when using the static magnetic field approach in the current methodology.

Therefore, these findings have contributed to the advancement of the field by introducing a more accurate magnetic field profile (MFP) that was informed by sunspot behaviour. Additionally, the proposed methodology, which uses the improved MFP and considers the critical solar cycle phases (solar minimum and maximum), provides a strong argument that the magnetic field strength results obtained in this study are a closer representative of reality than those calculated previously.

10.9 Impact of the results on existing space weather prediction models

It has been established that one of the most significant problems with space weather forecasting is determining the MFS, which is an essential component of the space weather prediction models (Borovikov et al., 2017; Kay et al., 2017). Moreover, the values for the MFS currently used provide limited information and lack accuracy (Borovikov et al., 2017). In light of our work's methodology used to estimate the MFS, two specific models within the space weather modelling framework (SWMF) should be reconsidered.

The first is the Alfvén Wave Solar-Atmosphere Model (AWSoM). In this model, the MFS value is not used directly. Instead, the value of a directional energy flux on the solar surface, which is taken to be proportional to the MFS, is used as a proxy (Gombosi et al., 2021). It would be worth investigating if the MFS estimates calculated in this study could be used as the explicit value of the MFS instead of using a proportionality constant to represent this value. Furthermore, our methodology allows specifying the solar cycle stage using the chosen latitude, which may align well with the expectations for the AWSoM model.

The second model forms part of the Eruptive Event (EE) generator of the space weather modelling framework (SWMF) (Gombosi et al., 2021). The function of this model is to create the initial conditions inside the solar corona, which will result in a coronal mass ejection (CME) (Gombosi et al., 2021). This model, too, uses the MFS as an input. When studying how the global magnetic field structure (GMFS) evolves, Bilenko (2020) noted that it consequently influences CMEs in solar cycles 21-23. Bilenko's results suggested that magneto-Rossby waves in the tachocline cause cyclical changes in the GMFS due to each Rossby wave period preferring a specific GMFS. Therefore, it was proposed that changes in the MHD Rossby wave period would result in the reorganisation of the GMFS and, subsequently, affect the location and occurrence rate of CMEs. Thus, the work by Bilenko (2020) supports the suggestion that the EE generator used to model CME formations would benefit from using the estimated MFS calculated using our suggested methodology derived from the MHD Rossby wave model in the lower tachocline.

Similarly, the method proposed by Dikpati (2020) suggested that the propagation of MHD Rossby waves could be used to predict active regions on the solar surface. By improving the MFP that forms part of the MHD Rossby wave model, the wave dispersion relation, phase and group velocities will all be positively impacted and are expected to align more accurately with observations.

10.10 Future work

In light of the findings presented in this study, it becomes evident that while significant insights have been gained, certain limitations have also surfaced, suggesting avenues for further exploration. This section outlines potential directions for future research, building upon the current study's outcomes while addressing its constraints.

The first limitation of this study was that only one harmonic of the MHD Rossby wave ($m = 1$, $n = 4$) was considered. However, it has been shown that the $m = 1$, $n = 3$ harmonic corresponds to stronger magnetic field strengths (Gurgenashvili et al., 2016; Zaqarashvili and Gurgenashvili, 2018) and, therefore, exhibits shorter periodicities. Consequently, a comprehensive harmonic analysis would provide a more detailed view of the possible range of MFS values.

We have also considered a uniform magnetic field, which could be substituted with the potentially more appropriate non-uniform variation associated with the latitudinal differential rotation (Zaqarashvili, 2018). Furthermore, only calculating the MFS values at the two latitudes associated with the extreme solar cycle phases is another limitation of this study. Although considering the limited cases of MFS at the solar minimum and maximum was sufficient to prove the argument that the MFS should be viewed as changing in both latitude and strength throughout the solar cycle, it still lacks continuity. Realistically, our methodology could be integrated into existing space weather prediction models by calculating these MFS values dynamically over time. This enhancement would require that the MFS constantly vary according to the specific solar cycle phase by adjusting the latitude value of the

MFP.

To explain the last limitation, we need to remember that the magnetic field is considered frozen within the solar plasma, according to Alfvén's magnetic flux theorem (Section 3.5.1). Therefore, the propagation of MHD Rossby waves also describes the behaviour of the magnetic field lines contained within them. Moreover, this field of study needs to understand better how solar MHD Rossby waves, and consequently the magnetic field lines, propagate from the solar interior to the exterior to enhance the realism captured in the associated models. Thus, accurately describing the dynamics of this outward propagation of the magnetic field lines would require studying how they move from the stable lower tachocline into the less stable upper tachocline and then through the convection zone until they reach the solar surface. Although the mechanism or dynamic responsible for the migration of Rossby waves from the lower to the upper tachocline remains unclear, our understanding of the interaction between the upper layer and the convection zone is better understood. It has been shown that the magnetic field lines escape the upper tachocline when the downward convection motions overshoot into this region, pulling additional plasma from the upper tachocline on the way back up. Once the magnetic field lines have entered the convection zone, they are less dense than the surrounding plasma in this solar layer and will consequently rise to the solar surface due to their buoyancy (Appendix A.3).

From this brief description of the magnetic field line movement during this outward migration process, it becomes clear that it would be critical to relax or remove the assumption of $\nabla \cdot \mathbf{B} = 0$ (or $\nabla[H \cdot \mathbf{B}] = 0$), which describes an environment where the magnetic field remains parallel to the fluid layer surface. Applying this approximation allows for studying the behaviour and dynamics of a magnetic field within a region without considering the vertical components or any interactions with surrounding areas. By definition, the outward propagation of the magnetic field lines would violate this horizontal restriction. Thus, a scenario that allows for vertical movement must be accounted for to have a more realistic and comprehensive model of the solar dynamics and how Rossby waves (containing the magnetic field) propagate throughout the Sun. This scenario could be included in the modelling by considering an interchange of instabilities (Grunett and Bhattacharjee, 2017, p.241-246). Such a system involves a perturbation where an interchange of plasma occurs between two magnetic flux tubes adjacent to one another. This theory considers how the magnetic flux will be conserved in the interchange process.

Finally, it is worth noting that the future explorations suggested above are consistent with NASA's objectives, which have expressed the need to improve our understanding of solar dynamics and the causes of solar storms. As a result, their Sun Radio Interferometer Space Experiment (sunRISE) mission is set to launch six small satellites, called CubeSats, in 2024. According to NASA, the aim is for these satellites to "*create detailed 3D maps of where energetic radio emissions occur in the Sun's magnetic atmosphere, which signify the locations of extremely powerful bursts of radiation*". SunRISE will also be the first to create a map of the Sun's magnetic field lines. This research will aid our forecasting capabilities of space weather and further enhance our understanding of the Sun's dynamics.

In conclusion, while this study has proved that a dynamic magnetic field methodology is preferred to improve the accuracy of the estimated magnetic field strength, it is essential to acknowledge the limitations that have influenced our results. Despite these constraints, our findings contribute valuable insights into how the existing space weather models could be improved using the more granular and realistic magnetic field strengths calculated using our dynamic magnetic field methodology. However, future research endeavours should aim to address the identified limitations above and further validate our findings. By doing so, we can deepen our understanding and make meaningful contributions to the knowledge of solar dynamics, MHD Rossby waves, the solar magnetic field and events that cause significant changes in space weather.

Appendices

A Solar dynamics

A.1 Change in the magnetic polarity over the solar cycle

Over time, the polar orientation of the solar magnetic field changes such that polarity observed in the respective hemispheres migrates to the opposite hemisphere over 11 years. This process, known as the Schwabe (Schwabe, 1844) or solar cycle, provides detailed information on solar activity, specifically that of sunspots. Recall that sunspots occur when a magnetic field line breaks through the surface of the Sun. The respective locations where the magnetic field line exits and enters back into the Sun are then regions that exhibit a concentrated magnetic field, which cools down the immediate area on the solar surface, leading to two dark, circular-shaped regions. Since this specific type of solar activity is well recorded, it is often used to illustrate the solar cycle.

Figure A.1 represents the average number of sunspots recorded over time. This diagram easily identifies the solar cycles by the repeating Gaussian distributions that mark individual solar cycles.

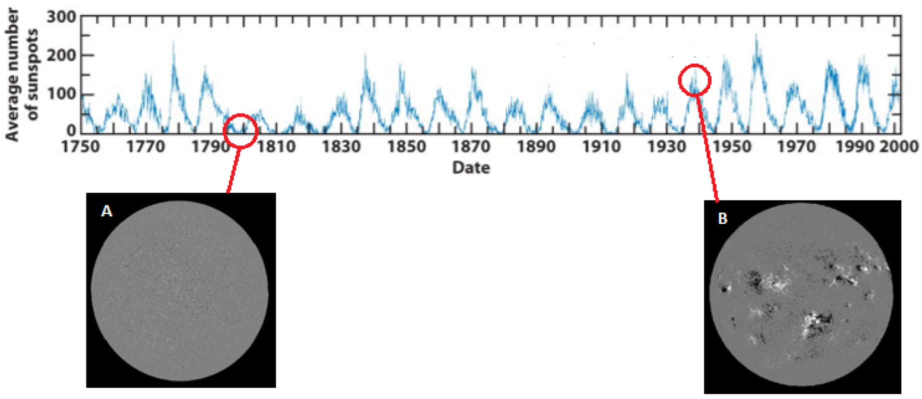

Figure A.1: The top graph shows the variation in the number of sunspots over time. A magnetogram that corresponds to a solar minimum (A) and a solar maximum (B) is added to show the associated magnetic field concentrations and polarity associated with sunspots.

Furthermore, these primary solar cycle phases can also clearly be observed in specific images of the solar disk, such as **magnetograms**, which display the polarity of the solar magnetic field as black and white areas. Based on the historical number of sunspots, the solar minimum phase is expected to exhibit little to no sunspots or other solar activity. This calm phase can be seen by the absence of sunspots in the magnetogram of the solar disk, Fig.(A.1) (A), during a solar minimum. Conversely, during the solar maximum, solar activity peaks, such that the magnetogram, Fig.(A.1) (B), shows various active sunspots during this period.

Solar cycle 24 and its associated sunspot data will be used as an example to provide further insight into the behaviour of sunspots, assuming that the positive pole is initially in the northern hemisphere. The horizontal axis in Fig.(A.2) shows that the cycle starts roughly in 2010, indicating a solar minimum - a period with little to no observable solar activity.

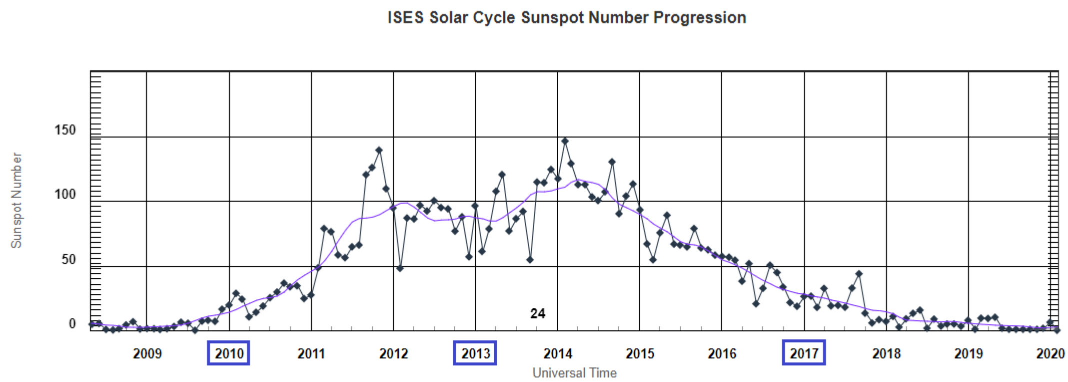

Figure A.2: Monthly sunspot numbers for solar cycle 24. The black dots are the recorded monthly number of sunspots, and the purple line is the smoothed monthly values. It shows an overarching bell-shaped trend for a solar cycle regardless of the short-term volatility in sunspot occurrences. Here, the boxed dates correspond to the cycle's start (min), middle (max), and end (min). Graph and data courtesy of the National Oceanic and Atmospheric Administration (NOAA) Space Weather Prediction Centre.

Furthermore, during this solar cycle phase, the positive and negative polarity of the magnetic field is confined to the respective hemispheres, as illustrated in the first diagram of Fig.(A.3).

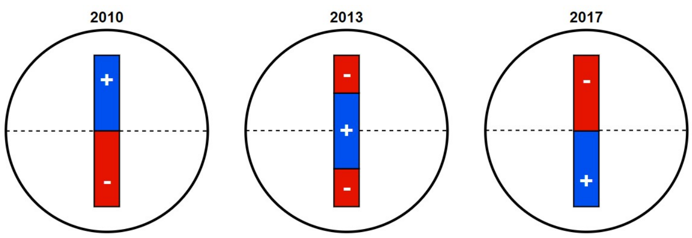

Figure A.3: An example of how the magnetic field's polarity shifts over a solar cycle (e.g. cycle 24). The polarity of the Sun is referred to as positive and negative. The Sun is fully polarised at the start of a solar cycle (2010). Over time, the magnetic field polarity migrates towards the opposite hemisphere (2013). After this, the polarity migration across hemispheres was completed before the start of the next solar cycle.

As the cycle progresses over time, the number of sunspots, see the vertical axis of Fig.(A.2) gradually increases, and referring to a different sunspot diagram becomes useful. The Royal

Greenwich Observatory (RGO) has recorded sunspot observations since solar cycle 12 in 1874 (Hathaway, 2017) in a graph called the "butterfly" diagram. This diagram records the size, location, and number of sunspots, which offers essential insight into the origination and migration of sunspots over a solar cycle.

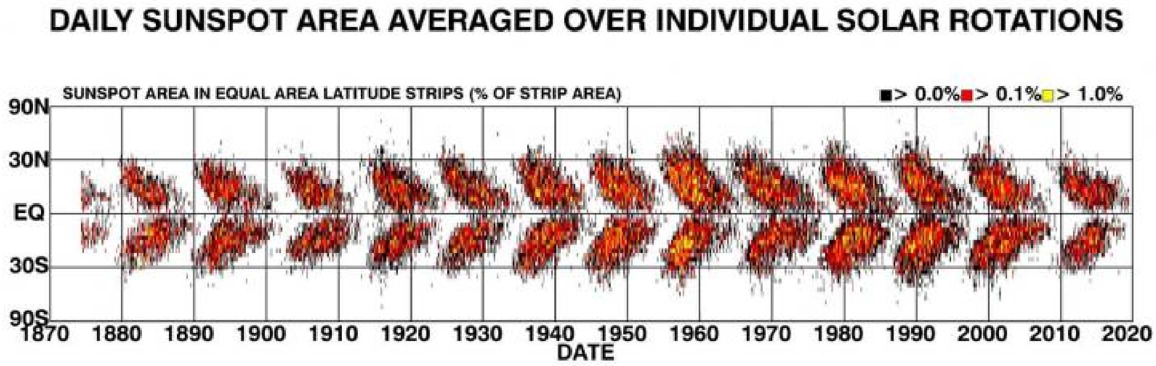

Figure A.4: Top: Butterfly diagram, where the pixel colour represents the sunspot size. Since the solar maximum is reached mid-solar cycle, it can be observed that the sunspots mainly occur in the middle of the equatorial region and latitude of 30°. Image courtesy of NASA.gov.

What is noticeable from the butterfly diagram is that the small number of sunspots at the start of a solar cycle will appear at higher latitudes, roughly between $40° - 50°$. As the solar cycle progresses, the number of sunspots continues to increase (upward trend between 2010-2013 in Fig.(A.2)). The part of the butterfly diagram corresponding to this transition period shows a gradual decline in the latitude of the observable sunspots.

When the solar cycle 24 reaches its midpoint in roughly 2013-2014 (solar maximum), the number of sunspots visible on the solar disk is a maximum. At this point, the magnetic polarity migration is only partially completed, which results in two regions with opposite polarities at mid to low latitudes. This structure is illustrated by the boundaries of the different magnetic poles in the second diagram in Fig.(A.3). This magnetic pole formation, therefore, creates these two latitudinal regions, which are optimal for displaying multiple sunspots at any given time and correspond to what is observed in the butterfly diagram, which shows that sunspots during solar maximum are located predominantly at latitudes at or below 20°.

A gradual decline in solar activity follows the solar maximum until the next solar minimum is reached at the end of the solar cycle. During this period, sunspots appear closer to the equator as the cycle ends. At this point, the solar magnetic field will have completed its polarisation migration, as illustrated in the last diagram of Fig.(A.3). Thus, in our example, the northern hemisphere will now display the negative pole and vice versa for the southern hemisphere.

A.2 Practical example of considering a fixed magnetic field

Suppose there is a specific observed solar feature[1] which has been shown to have different phase and group velocities that travel in opposite directions. Since this dispersion behaviour is associated with the characteristics of Rossby waves, it is natural to consider whether the solar MHD Rossby waves could explain this phenomenon. As presented in Chapter 8, one would require an estimated value of the MFS to calculate the wave frequency and, subsequently, the phase and group velocities. The connection between the MHD Rossby wave and the observed solar feature can be confirmed if the resulting velocities align with those measured from the observations. However, when attempting to explain such observational findings with a theoretical model, the phase of the solar cycle during which the observations were made plays a very important role in choosing appropriate parameter values. Let us explain how by considering the following hypothetical example.

Assume solar data, recorded during the maximum of solar cycle 19, was used to study a specific solar feature that exhibits dispersive behaviour. It follows that when selecting parameter values for the chosen model, the latitude of sunspots, as recorded by the butterfly diagram, indicates that the most plausible latitude for this solar cycle phase is 17.5°. Conversely, suppose the exact phase of the solar cycle has not been explicitly stated, which is the case more often than not, but instead, the dates of the specific dataset are given. In that case, the solar cycle progression graph, Fig.A.5, can infer the appropriate phase.

[1]For example, the wave-like behaviour exhibited by coronal bright points observed by McIntosh et al. (2017), discussed in Section 3.8.

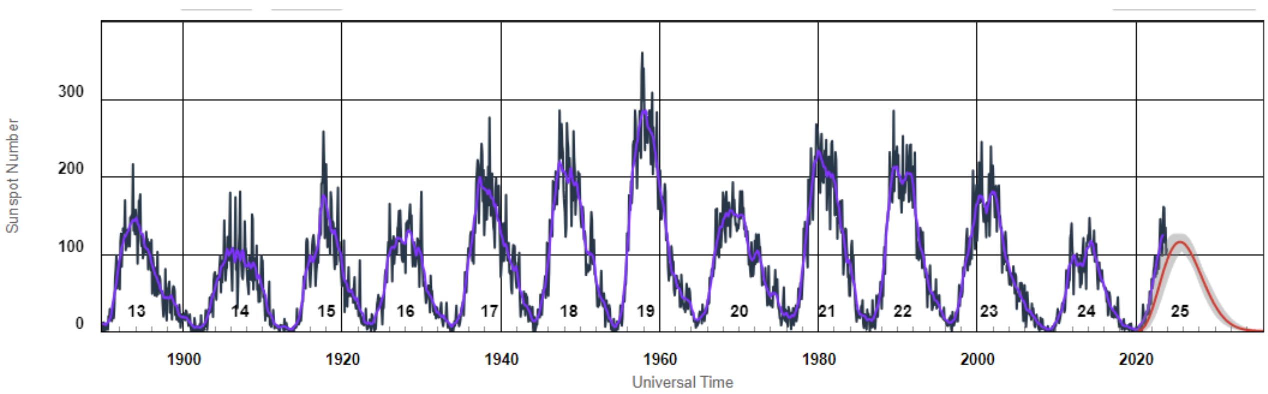

Figure A.5: Solar Cycle Progression from the NOAA for solar cycles 13 up to the current incomplete cycle 25.

For example, if data from December 1974 to May 1977 were used, the chosen latitude should be close to 5° as these dates occur during the solar minimum as cycle 20 ends (see red box in Fig.(A.6) below).

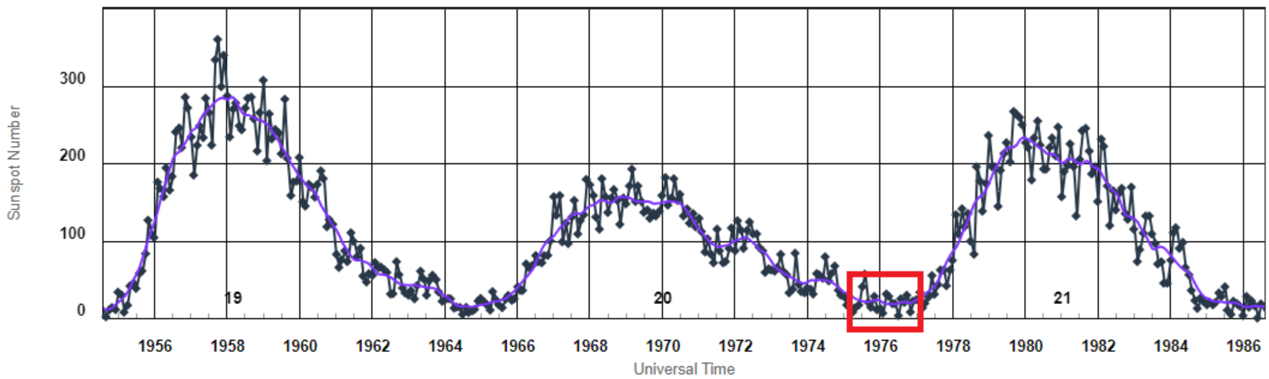

Figure A.6: Solar Cycle Progression from the NOAA for solar cycles 19-21. The red box corresponds to the data from December 1974 to May 1977 used in the example to illustrate that this period falls within the minimum phase of the solar cycle.

Therefore, considering the solar cycle period will allow us to choose appropriate values for input parameters, such as latitude that aligns with observations. Furthermore, since latitude is included in the MFP, it will subsequently affect the estimated MFS used in calculating the wave frequency, phase and group velocities. Considering this methodology would impact the accuracy of active region predictions based on the phase and group velocities of the MHD Rossby waves in the tachocline. Moreover, since this methodology allows the MFS to vary in latitude during the solar cycle, it can also be incorporated into present space weather models. This will enable the MFS to be dynamically calculated, ensuring that the estimated value is always updated to reflect the current phase of the solar cycle.

A.3 Dynamics of sunspot formation

Sunspots occur when a magnetic field line breaks through the surface of the Sun. The respective locations where the magnetic field line exits and enters back into the Sun are then regions that exhibit a concentrated magnetic field, which cools down the immediate area on the solar surface, leading to two dark circular-shaped features seen next to one another on the natural solar disk as seen in Fig.(A.7a). A more comprehensive description of their formation is illustrated in Fig.(A.7b) as initially presented by Parker (1955a) and explained by Priest (2014, p.318), which will guide the discussion that follows.

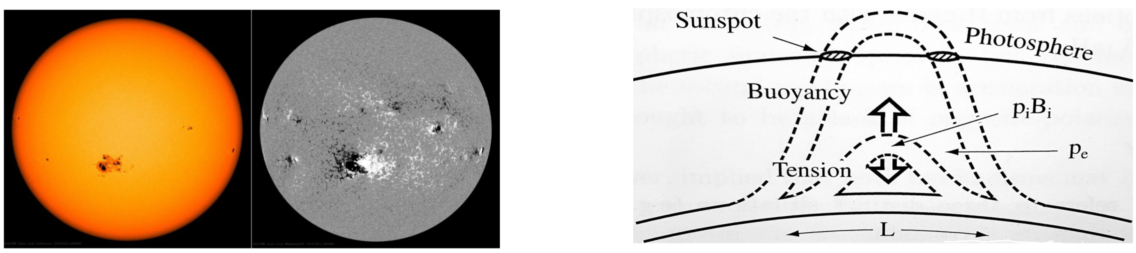

(a) Natural solar disk vs. Magnetogram

(b) Solar dynamics resulting in sunspots.

Figure A.7: Sunspots are a solar phenomenon where the magnetic field lines break through the photosphere, resulting in a pair of spots where the magnetic field exits and enters the solar surface. The illustration (b) of the dynamics that result in sunspots is courtesy of Priest (2014, p.318). The magnetic tension restoring force counteracts a buoyancy force due to pressure differences between the plasma and magnetic field line. When the magnetic field line is sufficiently long, it overcomes the magnetic tension force and rises to the surface, resulting in sunspots.

Consider a plasma with a magnetic field line embedded within it. Adding a magnetic field to an environment has certain consequences as it contributes to additional pressure and forces, described by the Lorentz force equation (Priest, 2014, p.96), as follows

$$\mathbf{j} \times \mathbf{B} = \frac{(\mathbf{B} \cdot \nabla)\mathbf{B}}{\mu_0} - \nabla \left(\frac{B^2}{2\mu_0} \right), \tag{A.1}$$

where $\mathbf{j}$ is the current density and μ_0 the magnetic permeability of free space. In eq.(A.1), the first and second terms on the right-hand side correspond to the **magnetic tension force** and the **magnetic pressure force**, respectively. Let us first determine the effect of the added magnetic pressure on the dynamics.

The magnetic field strength and gas pressure inside (i) the field line are given by B_i and p_i, respectively, and the external (e) pressure by p_e. From there, it follows that the pressure balance in the lateral direction between a magnetic flux tube and the surrounding plasma can be written as

$$p_i + \frac{B_i^2}{2\mu_0} = p_e. \tag{A.2}$$

Furthermore, pressure can be written in terms of density, ρ, by considering the ideal gas law, such that

$$\frac{k_B T \rho_i}{m} + \frac{B_i^2}{2\mu_0} = \frac{k_B T \rho_e}{m}, \tag{A.3}$$

where k_B is the Boltzmann constant, T is temperature, and m is the molecular mass of the gas under consideration, e.g. for purely hydrogen gas, it will be the proton mass. For eq.(A.3) to hold, the internal density, ρ_i, inside the magnetic field line must be less than the external density, ρ_e of the surrounding plasma. This difference in density will cause the plasma within the magnetic field line to experience an upward buoyancy force, resulting in a curved magnetic field line that rises to the solar surface.

However, due to the bending caused by the upward buoyancy force, the magnetic field line will experience a magnetic tension force in the opposite direction to buoyancy, correlating with the first term in eq.(A.1). This restoring force aims to straighten the magnetic field line. However, when the length of a magnetic field line is longer than twice the height of the layer, the buoyancy force in eq.(A.3) will dominate (Priest, 2014, p.318) — causing the magnetic flux tube to rise and break through the solar surface. The behaviour of magnetic field lines within the convection zone further supports the theoretical description of these dynamics. It is suggested that the convection motions and magnetic fields do not mix easily (Dwivedi, 2003, p.109). Consequently, the convection zone is organised vertically into sections where either convection occurs or the magnetic field gets concentrated. The magnetic field is piled up in these columns, and the dynamics described above take place.

B Wave properties

B.1 Wave properties

Characteristic	Symbol	Definition	Formula
Amplitude	A	The maximum displacement from equilibrium. It is measured as the distance between the peak and the trough of the wave. The amplitude represents the energy of the wave. The greater the amplitude the more energy the wave carries.	
Period	T	The time it takes to complete one full oscillation. In other words, the time it takes for one wavelength to pass a certain point.	$T = \frac{1}{f}$
Frequency	f	A wave is the number of oscillations passing a specific point in a certain amount of time, usually measured per second.	$f = \frac{1}{T} = \frac{\omega}{2\pi}$
Wavelength	λ	The distance between consecutive locations in phase. E.g., the length of the wave from one peak to the next.	
Velocity	v	Measured as the distance travelled by a certain point on the wave in a given time interval. The speed of a wave is dependent on three factors: frequency, wavelength, and the properties of the medium the wave is propagating in.	$v = \lambda\left(\frac{1}{T}\right) = \lambda f$
Angular wavenumber	k	It is mathematically expressed as the number of the complete cycle of a wave (2π) over its wavelength measured in radians per meter.	$k = \frac{2\pi}{\lambda}$
Angular frequency	ω	Measured in radian per second.	$\omega = \frac{2\pi}{T}$
Wave phase	$(kx - \omega t)$	Used to describe a location within a single wavelength. Two separate points on two separate waves at the same place are said to be in phase for example the peaks of two consecutive waves are in phase. Travels at phase velocity. Here x is the location (x-coordinate) and t is time.	
Phase constant	ϕ	Added to generalize the equation. The chosen value of ϕ gives the wave a specific displacement and slope at $x = 0$ and $t = 0$	
Group velocity	v_g	Velocity at which the observable wave packet (group of waves) moves with time.	$\frac{d\omega}{dk}$
Phase velocity	v_p	The speed at which the wave's constant phase portion moves.	$\frac{\omega}{k}$

Table B.1: Wave properties. (Halliday, 2010)

B.2 Rotating system dynamics

Since Rossby waves occur in rotating fluids such as the Earth and the Sun, it is important to understand the associated dynamics of such a system as it will provide the necessary context of the forces involved. The dynamics and forces discussed in this section will, therefore, inform the governing equations that are used in the formulation of the Rossby wave model.

Let us start by considering the specific phenomena of vorticity and the Coriolis effect that arise in a rotating frame of reference. We will use Earth's dynamics to explain these concepts for simplicity and familiarity.

B.2.1 Vorticity

The **vorticity**, ζ, of a fluid is a measure of a fluid particle's local spin or rotation. Moreover, four types of vorticity will be considered: planetary, relative, absolute, and potential vorticity.

Any object on Earth will have **planetary vorticity**, as it is associated with the rotation of the Earth. Planetary vorticity has a maximum value at the poles and decreases towards the equator, where it has a value of zero. This vorticity is represented by

$$\zeta_e = 2\mathbf{\Omega}, \tag{B.1}$$

where $\mathbf{\Omega}$ is the angular rotation rate of the rotating system. Since the Earth is considered to be the rotating system in this example, we will use the subscript e in the notation to identify the planetary vorticity.

Relative vorticity, ζ_r, is similar to planetary vorticity but applies to any rotating frame of reference that is of a smaller scale than the planet. This vorticity is the curl of the fluid velocity, $\mathbf{v}$, such that

$$\zeta_r = \nabla \times \mathbf{v}. \tag{B.2}$$

Absolute vorticity, ζ_a, on the other hand, describes how much the fluid is rotating in total; hence, the sum of the relative and the planetary vorticity,

$$\zeta_a = \zeta_r + \zeta_e. \tag{B.3}$$

When considering a hydrodynamic environment that is purely two-dimensional, involving only horizontal motions, the *absolute vorticity is proved to be conserved* (Haurwitz, 1940). This conservation law states that regardless of changes in the planetary and relative vorticities, the value for the absolute vorticity must remain constant.

Lastly, consider the impact of varying fluid depth on the rotation rate, as illustrated in Fig.(B.1). Assume the fluid moves to the right at a velocity $\mathbf{v}$, with an initial fluid depth of h. From there, the fluid experiences a swell, increasing the depth or thickness of the layer and causing the fluid column to be stretched out vertically. This narrowing of the fluid column in the horizontal direction is associated with an increase in the rotation rate, Ω_1.

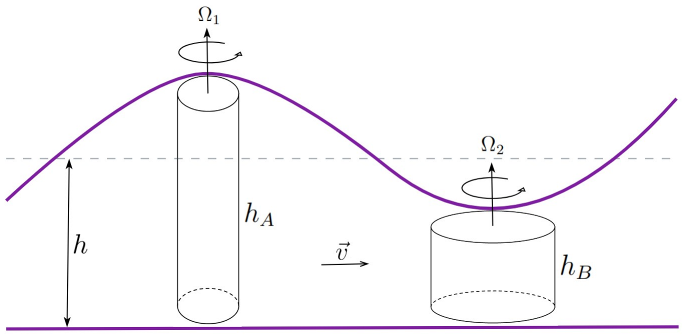

Figure B.1: Shallow water topography with a rigid bottom and a free surface at the top, varying in height, h, as the flow moves to the right from point A to B at a constant velocity $\mathbf{v}$. The fluid column's rotation rate varies with the fluid layer's depth. Therefore, conservation of angular momentum shows that for an increase and decrease in the fluid layer depth, fluid column h_A and h_B rotate such that we have $\Omega_1 > \Omega_2$.

As the fluid column moves to the right, it enters a region where the fluid layer becomes more shallow. Here, the fluid column gets compressed in the vertical and, as a result, expands horizontally, leading to a decrease in the angular velocity, Ω_2. This is a result of the *conservation of angular momentum*[1]. The **potential vorticity**, ζ_p, accounts for this change of fluid depth and is given as

$$\zeta_p = \frac{\zeta_a}{h}, \tag{B.4}$$

where h is the layer thickness. The system illustrated in Fig.(B.1) shows that small vertical motions for the shallow water environment accompany the primary horizontal flow. In this case, absolute vorticity is no longer conserved but rather the potential vorticity. The

[1]This is the same phenomenon as when a figure skater stretches out to spin faster and how their rotation slows down as they crouch back down again.

conservation of potential vorticity is then described as follows

$$\frac{d}{dt}\left(\frac{\zeta_a}{h}\right) = 0. \tag{B.5}$$

The various vorticities described above will aid in understanding the Coriolis effect, another important consequence of a rotating frame of reference.

B.2.2 Coriolis effect

Since we are concerned with the propagation of a wave, it is apparent that Newton's laws of motion should be used to model the system under consideration. However, these laws apply to an **inertial frame of reference**, meaning one that does not accelerate, although a rotating system always accelerates. Consequently, when considering a rotating frame of reference, two apparent acceleration "forces" appear, namely the Coriolis and centrifugal force.

The Coriolis effect can be seen when an object travels a long distance around the Earth. The path of that object is deflected by the Coriolis force, which stems from the rotation of the Earth. The Coriolis force is mathematically described by the vertical component of the planetary vorticity, eq(B.1), such that

$$\boxed{f = 2\Omega \sin\Theta}. \tag{B.6}$$

Eq.(B.6) is called the **Coriolis parameter**, which has the largest values near the poles and tends to zero as it approaches the equator due to the respective latitudes, Θ, of 90° and 0°. It is also proportional to the fluid's rotation rate, $\boldsymbol{\Omega}$. Thus, the strength of the Coriolis force depends on the object's speed in the rotating frame and acts at a 90° angle to the object's direction of motion.

Let us then consider a realistic example of the Coriolis effect involving two spinning objects: the air particles associated with a hurricane as the first object and the Earth as the second.

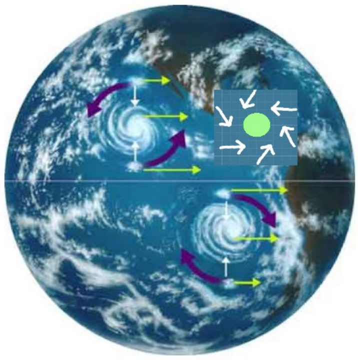

Figure B.2: Storms illustrating the Coriolis effect. The yellow arrows indicate the direction and magnitude of the Earth's rotation, which is slower for higher latitudes (arrow length). The white arrows show the deflection of air particles due to the Coriolis force as they move from the high-pressure area of the storm to the low-pressure area. The purple arrows show the overall rotation caused by the Coriolis effect for the respective hemispheres. Image retrieved from Klina (2016), and adjusted.

In a hurricane, the centre of a storm is a low-pressure area, which is, in contrast, surrounded by a high-pressure area. Air particles naturally move from high-pressure to low-pressure areas based on elemental physics. The direction of the particle movement is illustrated by the white arrows in Fig.(B.2). If the Earth had no rotation, the path of the particle moving from the high to the low-pressure area would be straight. However, this is not what is observed. In reality, the path of the particles moving to the eye of the storm is curved due to the Coriolis force, and the direction of this curvature is hemisphere-dependent. Objects in the northern and southern hemispheres will be deflected to the right and left, respectively. Therefore, if we further assume that the hurricane under consideration is located in the northern hemisphere, all the particles travelling to the middle of the storm are slightly pushed to the right, as indicated by the white arrows in the illustration of the simplified hurricane dynamics on the right-hand side in the northern hemisphere. This particle shift to the right results in a counterclockwise rotation of hurricanes in the northern hemisphere, as indicated by the purple arrows in Fig.(B.2).

The fundamental concepts of a rotating system have now been addressed, which enables us to understand the mechanisms involved in Rossby wave propagation. However, we will first introduce Rossby waves in hydrodynamic environments, as discovered in the Earth's atmosphere and then the ocean.

B.2.3 Rossby wave propagation mechanism

As mentioned, a restoring force must act on a perturbation to produce a wave. For Rossby waves, the interaction between inertia and the latitudinal variation of the Coriolis force leads to the formation of these waves. **Inertia** is the force that attempts to make an object continue in the direction where it has been deflected, and for this study, the object is considered to be a volume of fluid. At the same time, the latitudinal variation of the Coriolis force allows the conservation of vorticity to be utilised. Moreover, the classification of the Rossby wave as barotropic or baroclinic indicates which specific vorticity is conserved. From eq.(B.3), it follows that absolute vorticity considers purely 2D motions. Therefore, it is this vorticity that is conserved for barotropic Rossby waves. For baroclinic Rossby waves that can exhibit vertical motions, no matter how small, such as those occurring in the shallow water environment (Fig.B.1), the potential vorticity, eq.(B.4), is conserved as it includes height as a variable. Still, for simplicity, the conservation of absolute vorticity will be used to explain the propagation mechanism of Rossby waves.

Similar to the scenario above, consider the movement of a fluid particle in the northern hemisphere. The initial location of this fluid particle, illustrated by the dashed line in Fig.(B.3), represents the undisturbed vorticity at a specific latitude. At that latitude, the relative spin of the particle is equal to the planetary spin, $\zeta_r = \zeta_e$.

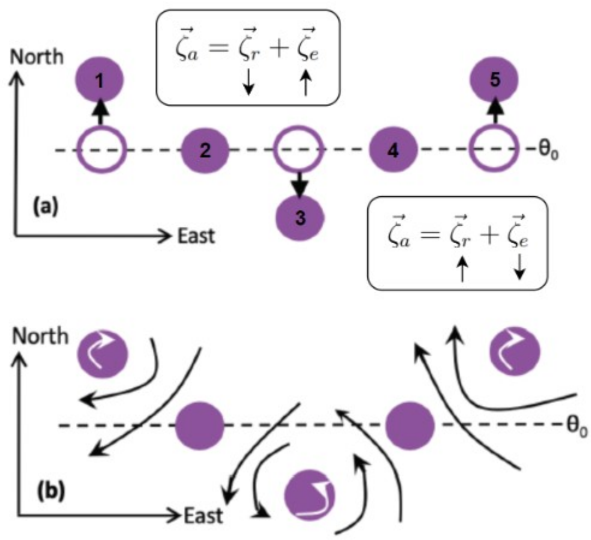

Figure B.3: Dynamics of Rossby wave propagation due to the conservation of absolute vorticity, ζ_a, which is the combined value of the relative spin, ζ_r, and the planetary spin, ζ_e. Image adjusted from Dikpati et al. (2018b).

Now, consider the first particle in Fig.(B.3) moving towards the north. The latitude changes as the particle is displaced, creating a difference between these vorticity values. This increase in latitude, Θ, will subsequently increase the Coriolis parameter, eq.(B.6). Because of inertia, this particle will rotate faster than its new surrounding area. This upward movement is, therefore, associated with an increase in planetary vorticity and, due to the conservation of absolute vorticity, must be accompanied by a decrease in the relative vorticity. This negative relative vorticity perturbation causes a clockwise (anticyclonic) circulation and moves the particle back to position (2). From there, the particle slightly overshoots the unperturbed location to position (3). However, as the particle moves towards the equator, it will experience a decrease in planetary vorticity and an increase in relative vorticity, resulting in a cyclonic (anticlockwise) swirl. Due to the conservation of absolute vorticity, the displaced particles reach their maximum latitudinal displacement and reverse latitudinal direction. Therefore, this repeating pattern of the particle movement results in a westwards propagating wave.

In addition to the fundamental dynamics explaining the direction of these waves, the initial latitude location of these particles that form the wave is also important. Since the Coriolis force is latitude-dependent and has a value of zero at the equator, wave dynamics close to the equatorial region are not significantly affected, leading to faster wave propagation. On the contrary, as the Coriolis force increases with latitude, atmospheric waves at higher latitudes are more severely impacted and propagate much slower comparatively.

C Properties of an ideal plasma

In fluid dynamics, an ideal[1] fluid is often used to simplify calculations due to its specific properties, which will be discussed in this section. Specifically, an ideal fluid is considered incompressible, inviscid and infinitely conducting.

C.1 Incompressible

In natural fluid bodies, the density of a fluid decreases as you move closer to the fluid surface and is, therefore, a function of fluid depth. However, when considering a shallow layer of fluid, where the horizontal extent is much larger than the vertical, the depth will be sufficiently small such that the approximation of constant density is acceptable. In other words, in such an environment, the fluid is considered incompressible, meaning its density is constant.

The resulting error from applying this approximation would be of the same scale as the fluid layer height, which is negligible for specific solar layers, such as the tachocline (Gilman, 2000). To test the validity of making this assumption in our study, we can use two different criteria, which should be met to conclude that it is an appropriate assumption. The first condition requires the sound speed, c_s, to be an order larger than the characteristic plasma speed, U_0, thus $c_s \gg U_0$. The second condition is that the Mach number, given by

$$M = \frac{U_0}{c_s},$$

should satisfy $M < 0.3$ (Kundu et al., 2012).

We can use the following equation (Priest, 2014, p.487) to calculate the estimated value for the sound speed

$$c_s = 152\, T^{\frac{1}{2}}\, \mathrm{m\, s^{-1}}, \tag{C.1}$$

[1]Since plasma is mainly treated as a fluid, we will refer to it as such. However, we will explicitly state where necessary if a characteristic is only relevant to plasma.

where T is the temperature in degrees Kelvin, which at the base of the convection zone of the Sun is estimated at $2\,000\,273\,°\mathrm{K}$ (Hathaway, 2022). This results in a sound speed of $\sim 177\,\mathrm{km\,s^{-1}}$.

On the other hand, determining the estimated value for the typical flow velocity in the tachocline proves more difficult. However, we can consider the convective motions in the adjacent layer to get an approximation for this value. The speed of convection is estimated between $50 - 100\,\mathrm{m\,s^{-1}}$ (Hotta et al., 2014; Hanasoge et al., 2015). Since the convective zone is considered the Sun's most dynamic and moving layer, it is safe to assume that the plasma flow velocity within the tachocline would be less than what is estimated for the convective motions; therefore, even if we take the lower value of the plasma flow in the convection zone ($50\,\mathrm{m\,s^{-1}}$), we get $M \approx 4.27 \times 10^{-4}$, which shows that both conditions are met and treating the solar plasma in the tachocline as incompressible is appropriate.

C.2 Inviscid

To further define the properties of an ideal fluid, we will next consider two specific forces that occur in a fluid flow. The first is the viscous forces.

Viscosity measures the fluid's resistance to flow. Specifically the resistance between particles in a fluid that move parallel to each other but in opposite directions or at different velocities. It is classified as a **shear force** since it arises due to the friction between fluid layers or the fluid and a boundary.

The second is the fluid's **inertial force**, described by Newton's first law of motion: "*a body remains at rest, or in motion at a constant speed in a straight line unless acted upon by a force*". Consequently, viscosity and inertial forces act in opposite directions. The Reynolds number can be used to determine which of these two forces will dominate the flow since it gives the ratio of the inertial to viscous forces.

To determine the units of these respective forces, we make use of the typical fluid flow velocity, U_0, the characteristic length-scale, L_0, along with the density of the fluid, ρ, and the dynamic viscosity of the fluid, μ_d. Then it follows that the units of inertial and viscous forces are given as U_0^2/L_0 and $\mu U_0/\rho L_0^2$, respectively. The Reynolds number is, therefore, written as

$$R_e = \frac{U_0^2/L_0}{\mu U_0/\rho L_0^2} = \frac{\rho U_0 L_0}{\mu} = \frac{U_0 L_0}{\nu},$$

where $\nu = \mu_d/\rho$ is the kinematic viscosity. When the Reynolds number is high, $R_e \gg 1$, viscous effects can be ignored. Conversely, the fluid viscosity should be considered when the Reynolds number is sufficiently low, $R_e \ll 1$.

As before, the values for this equation are not commonly known for the tachocline. However, the density of the photosphere is estimated as $\sim 4.9 \times 10^{-9}\,\mathrm{g\,cm^{-3}}$ and the dynamic viscosity as $\sim 4.1 \times 10^{-4}\,\mathrm{g\,cm^{-1}\,s^{-1}}$ (Cowley, 1990), which results in a Reynolds number of the order $R_e \approx 10^6$. This result shows that $R_e \gg 1$ and, therefore, the assumption of an **inviscid fluid** is appropriate for the photosphere.

As the density increases for lower layers of the Sun, the kinematic viscosity will decrease as a result, which will increase the value of the Reynolds number even further. For example, the estimated value of the Reynolds number for the solar interior is $R_e \approx 10^9$ (Hood and Hughes, 2011). This confirms that we can apply the assumption of an inviscid flow to the solar tachocline.

C.3 Infinitely conducting

The last property of an ideal fluid is that of negligible resistivity, which implies that the fluid is infinitely conducting, and the contribution of the electrical field can, therefore, be neglected. Furthermore, since the electrical currents flowing through such a plasma do not encounter any resistance, no energy will be converted to heat; that is, Ohmic heating does not occur (simplifying the terms describing the Lorentz force in the momentum equation).

C.4 Other ideal plasma properties

An ideal plasma is also assumed to be quasi-neutral, meaning there are approximately an equal number of positive (ions) and negative (electrons) charges, leading to an overall neutral charge density. The individual motions of plasma particles are also ignored, and instead, the plasma is treated as a single fluid that exhibits long wavelengths and low frequencies

(Gilman, 2000). An ideal plasma also exhibits adiabatic behaviour as it is assumed that no heat exchanges occur between the plasma and its surroundings. Lastly, an important contrast to an ideal fluid is that an ideal plasma can be rotational.

Bibliography

[1] Abed, A.K., Qahwaji, R. and Abed, A. (2021) "The automated prediction of solar flares from SDO images using deep learning", *Advances in Space Research*, 67(8), pp. 2544-2557. doi:10.1016/j.asr.2021.01.042.

[2] Abramowitz, M. and Stegun I.A. (1964) *Handbook of Mathematical Functions: With Formulas, Graphs, and Mathematical Tables*, New York: Dover Publications.

[3] Bardsley, O.P. (2018) "Could hydrodynamic Rossby waves explain the westward drift?", *Proceedings of the royal society a Mathematical, Physical and Engineering Sciences*, 474(2213). doi:10.1098/rspa.2018.0119.

[4] Bateman, T. (2022) *SpaceX Starlink satellite's flaming re-entry caught on camera after geomagnetic storm.* EuroNews.next (Accessed: 5 March 2024).

[5] Bilenko, I.A. (2013) "Global magnetic field cycle evolution and prominence eruptions, *Proceedings of the International Astronomical Union*, 8(S300), pp. 168–171. doi:10.1017/S1743921313010922.

[6] Bilenko, I.A. (2020) "Manifestation of Rossby Waves in the Global Magnetic Field of the Sun during Cycles 21-24", *The Astrophysical Journal*, 897(2), L24. doi:10.3847/2041-8213/ab9fa4.

[7] Blume, C., Hindman, B. and Matilsky, L. (2022) "Rossby Waves in the Radiative Interior", *Bulletin of the American Astronomical Society*, 54(7). Bibcode: 2022tess.conf12518B.

[8] Borovikov, D., Sokolov, I.V., Manchester, W.B., Jin, M. and Gombosi, T.I. (2017) "Eruptive event generator based on the Gibson-Low magnetic configuration", *Journal of Geophysical Research: Space Physics*, 122(8), pp. 7979-7984. doi:10.1002/2017JA024304.

[9] Boucher, D. (2023) *The Angular Momentum Of The Sun-Jupiter System.* Exoplanet Science (Accessed: 5 March 2024).

[10] Britannica (2023) *Encyclopedia Britannica*, SiderealPeriod. (Accessed: 16 September 2024).

[11] Busse, F.H., Zhang, K., and Liao, X. (2005) "On slow inertial waves in the solar convection zone", *The Astrophysical Journal*, 631(2), L171-L174. doi:10.1086/497300.

[12] Cai, T., Chan, K.L. and Mayr, H.G. (2021) "Deep, Closely Packed, Long-lived Cyclones on Jupiter's Poles", *The Planetary Science Journal*, 2(2). doi:10.3847/PSJ/abedbd.

[13] Carbonell, M. and Ballester, J.L. (1990) "A short-term periodicity near 155 day in sunspot areas", *Astronomy and Astrophysics*, 238(1-2), pp.377-381. Bibcode: 1990A&A...238..377C.

[14] Carbonell, M. and Ballester, J.L. (1992) "The periodic behaviour of solar activity - The near 155-day periodicity in sunspot areas", *Astronomy and Astrophysics*, 255(1-2), pp.350-362. Bibcode: 1992A&A...255..350C.

[15] Chowdhury, P., Khan, M. and Ray, P.C. (2009) "Intermediate-term periodicities in sunspot areas during solar cycles 22 and 23", *Monthly Notices of the Royal Astronomical Society*, 392(3), pp. 1159-1180. doi:10.1111/j.1365-2966.2008.14117.x.

[16] Chowdhury, P., Choudhary, D.P., Gosain, S. and Moon. .J. (2015) "Short-term periodicities in interplanetary, geomagnetic and solar phenomena during solar cycle 24", *Astrophysics and Space Science*, 356(1), pp. 7-18. doi:10.1007/s10509-014-2188-0.

[17] Cowley, C.R. (1990) "Second Viscosity of the Gas in the Outer Solar Envelope", *Astrophysical Journal*, 348, pp.328. doi:10.1086/168239.

[18] Dikpati, M., Cally, P.S., McIntosh, S.W. and Heifetz, E. (2017) "The Origin of the "Seasons" in Space Weather", *Nature*, 7, 14750. doi:10.1038/s41598-017-14957-x.

[19] Dikpati, M., McIntosh, S.W., Bothun, G., Cally, P.S., Ghosh, S.S., Gilman, P.A. and Umurhan, O.M. (2018) "Role of interaction between magnetic Rossby waves and tachocline differential rotation in producing solar seasons", *The Astrophysical Journal*, 853(2), pp. 19. doi:10.3847/1538-4357/aaa70d.

[20] Dikpati, M. (2020) *Rossby waves on the Sun provide a tool for forecasting space weather.* Interviewed by Dacey, J. Physics World (Accessed: 5 March 2024).

[21] Dikpati, M. and McIntosh, S.W. (2020) “Space weather challenge and forecasting implications of Rossby waves”, *Space Weather*, 18(3). doi:10.1029/2018SW002109.

[22] Dwivedi, B.N. (2003) *Dynamic Sun*, New York: Cambridge University Press.

[23] Gachechiladze, T., Zaqarashvili, T.V., Gurgenashvili, E., Ramishvili, G., Carbonell, M., Olivier, R. and Ballester, J.L. (2019) “Magneto-Rossby Waves in the Solar Tachocline and the Annual Variations in Solar Activity”, *The Astrophysical Journal*, 874(2), pp.13. doi:10.3847/1538-4357/ab0955.

[24] Gadgets 360 Newsdesk (2022) *Geomagnetic Solar Storm to Hit Earth on April 14, May Cause Possible Damage.* Gadgets 360 (Accessed: 5 March 2024).

[25] Gavrilov, M.B. and Prodanov, A.D. (2008) “The characteristics of Rossby waves frequencies on planets of the Solar system”, *Planetary and Space Science*, 56(11), pp. 1480-1484. doi:10.1016/j.pss.2008.05.020.

[26] Gilman, P.A. (1969) “A Rossby-wave dynamo for the Sun, I”, *Solar Physics*, 8(2), pp. 316-330. doi:10.1007/BF00155379.

[27] Gilman, P.A. and Fox, P.A. (1997) “Joint Instability of Latitudinal Differential Rotation and Toroidal Magnetic Fields below the Solar Convection Zone”, *The Astrophysical Journal*, 484(1), 439. doi:10.1086/304330.

[28] Gilman, P.A. (2000) “Magnetohydrodynamics ‘shallow water’ equations for the solar tachocline”, *The Astrophysical Journal*, 544(1), L79-L82. doi:10.1086/317291.

[29] *Goldilocks zone* (2022) National Aeronautics and Space Administration (Accessed: 5 March 2024), Exoplanet Exploration.

[30] Gombosi, T.I., Chen, Y., Glocer, A., Huang, Z., Jia, X., Liemohn, M.W., Manchester, W.B., Pulkkinen, T., Sachdeva, N., Al Shidi, Q., Sokolov, I.V., Szente, J., Tenishev, V., Toth, G., van der Holst, B., Welling, D.T., Zhao, L. and Zou, S. (2021) “What sustained multi-disciplinary research can achieve: The space weather modelling framework”, *Journal of Space Weather and Space Climate*, 11(42). doi:10.1051/swsc/2021020.

[31] Goode, P.R. and Dziembowski, W.A. (1991) "Solar-cycle dependence of the Sun's deep internal rotation shown by helioseismology", *Nature*, 349(6306), pp. 223-225. doi:10.1038/349223a0.

[32] *Gravity wave* (2014) American Meteorological Society (Accessed: 5 March 2024), Glossary of Meteorology.

[33] Griffiths, D.J. (2008) *Introduction to electrodynamics*, 3rd edn. San Francisco: Pearson Benjamin Cummings.

[34] Gurgenashvili, E., Zaqarashvili, T.V., Kukhianidze, V., Oliver, R., Ballester, J.L., Ramishvili, G., Shergelashvili, B., Hanslmeier, A. and Poedts, S. (2016) "Rieger-type periodicity during solar cycles 14-24: Estimation of dynamo magnetic field strength in the solar interior", *The Astrophysical Journal*, 826(1), 55. doi:10.3847/0004-637X/826/1/55.

[35] Gurgenashvili, E., Zaqarashvili, T.V., Kukhianidze, V., Oliver, R., Ballester, J.L., Dikpati, M. and McIntosh, S.W. (2017) "North-South Asymmetry in Rieger-type Periodicity during Solar Cycle 19-23", *The Astrophysical Journal*, 845(2), 137. doi:10.3847/1538-4357/aa830a.

[36] Gurgenashvili, E., Zaqarashvili, T.V., Kukhianidze, V., Reiners, A., Oliver, R., Lanza, A.F. and Reinhold, T. (2021) "Rieger-type periodicity in the total irradiance of the Sun as a star during solar cycles 23–24", *Astronomy and Astrophysics*, 653, A146. doi:10.1051/0004-6361/202141370.

[37] Gurnett, D.A. and Bhattacharjee, A. (2017) *Introduction to Plasma Physics: with space, laboratory and astrophysical applications*, 2nd edn. United Kingdom: Cambridge University Press.

[38] Halliday, D. (2010) *Fundamentals of Physics*, 9th edn. Publisher: John Wiley & Sons.

[39] Hanasoge, S., Gizon, L. and Sreenivasan, K.R. (2015) "Seismic Sounding of Convection in the Sun", *Annual Review of Fluid Mechanics*, 48(1), pp. 191-217. doi:10.1146/annurev-fluid-122414-034534.

[40] Hathaway, D.H. (2017) *The Sunspot Cycle.* NASA.gov (Accessed: 5 March 2024).

[41] Hathaway, D.H. (2022) *The Solar Interior.* NASA.gov (Accessed: 5 March 2024).

[42] HT Tech (2023) *Extreme solar flare eruption sparked blackouts, NASA said; Another solar storm coming?* HT Tech (Accessed: 5 March 2024).

[43] Haurwitz, B. (1940) "Atmospheric disturbances on the rotating Earth", *Eos, Transactions American Geophysical Union*, 21(2), pp. 262-264. doi:10.1029/TR021i002p00262.

[44] Hood, A.W. and Hughes, D.W. (2011) "Solar Magnetic Fields", *Physics of the Earth and Planetary Interiors*, 187(3-4), pp. 78-91. doi:10.1016/j.pepi.2011.04.010.

[45] Hori, K., Nilsson, A. and Tobias, S.M. (2023) "Waves in planetary dynamos", *Reviews of Modern Plasma Physics*, 7(5). doi:10.1007/s41614-022-00104-1.

[46] Horstmann, G.M., Mamatsashvili, G., Giesecke, A., Zaqarashvili, T.V. and Stefani, F. (2022) "Tidally Forced Planetary Waves in the Tachocline of Solar-like Stars", *The Astrophysical Journal*, 944, 48. doi:10.3847/1538-4357/aca278.

[47] Hotta, H. and Yokoyama, T. (2010) "Importance of surface turbulent diffusivity in the solar flux-transport dynamo", *The Astrophysical Journal*, 709(2), pp. 1009-1017. doi:10.1088/0004-637X/709/2/1009.

[48] Hotta, H., Rempel, M. and Yokoyama, T. (2014) "High-resolution calculations of the solar global convection with the reduced speed of sound technique. I. The structure of the convection and the magnetic field without the rotation", *The Astrophysical Journal*, 786(1), 24. doi:10.1088/0004-637X/786/1/24.

[49] Howard, R. and Harvey, J. (1970) "Spectroscopic Determinations of Solar Rotation", *Solar Physics*, 12(1), pp. 23-51. doi:10.1007/BF02276562.

[50] Javaraiah, J., Bertello, L. and Ulrich, R.K. (2005) "Long-Term Variations in Solar Differential Rotation and Sunspot Activity", *Solar Physics*, 232(1-2), pp. 25-40. doi:10.1007/s11207-005-8776-y.

[51] Kay, C., Gopalswamy, N., Reinard, A. and Opher, M. (2017) "Predicting the Magnetic Field of Earth-impacting CMEs", *The Astrophysical Journal*, 835(2), 117. doi:10.3847/1538-4357/835/2/117.

[52] *Kelvin wave* (2012) American Meteorological Society (Accessed: 5 March 2024), Glossary of Meteorology.

[53] Korsós, M.B., Dikpati, M., Erdélyi, R., Liu, J. and Zuccarello, F. (2023) "On the Connection between Rieger-type and Magneto-Rossby Waves driving the Frequency of the Large Solar Eruptions during Solar Cycles 19-25", *The Astrophysical Journal*, 944(2), 180, 10 pp. doi:10.3847/1538-4357/acb64f.

[54] Kuhn, J.R., Armstrong, J.D., Bush, R.I. and Scherrer P. (2000) "Rossby waves on the Sun as revealed by solar 'hills'", *Nature*, 405(6786), pp. 544-546. doi:10.1038/35014530.

[55] Kundu, P.K., Cohen, I.M. and Dowling, D.R. (2012) *Fluid Mechanics*, 5th edn. Boston: Academic Press.

[56] Lean, J.L. (1990) "Evolution of the 155 Day Periodicity in Sunspot Areas during Solar Cycles 12 to 21", *Astrophysical Journal*, 363, pp. 718. Bibcode: 1990ApJ...363..718L

[57] Livington, W.C. (1966) "Magnetic Fields on the Quiet Sun", *Scientific American*, 215(5), pp. 54-63.

[58] Longuet-Higgins, M.S. (1965) "Planetary waves on a rotating sphere. II", *Proceedings of the Royal Society of London. Series A, Mathematical and Physical Sciences*, 284(1396), pp. 40-68. https://www.jstor.org/stable/2415102.

[59] Löptien, B., Gizon, L., Birch, A.C., Schou, J., Proxauf, B., Duvall Jr, T.L., Bogart, R.S. and Christensen, R.C. (2018) "Global-scale equatorial Rossby waves as an essential component of solar internal dynamics", *Nature Astronomy*, 2, pp. 568-573. doi:10.1038/s41550-018-0460-x.

[60] Lou, Y. (2000) "Rossby-type wave-induced periodicities in flare activities and sunspot areas or groups during solar maxima", *The Astrophysical Journal*, 540(2), 1102. doi:10.1086/309387.

[61] Malik, T. (2022) *The worst solar storms in history.* Space.com (Accessed: 5 March 2024).

[62] McIntosh, S.W., Cramer, W.J, Marcano, M.P. and Leamon, R.J. (2017) "The detection of Rossby-like waves on the Sun", *Nature Astronomy*, 1, 0086. doi:10.1038/s41550-017-0086.

[63] Mihaljan, J.M. (1962) "A Rigorous Exposition of the Boussinesq Approximations Applicable to a Thin Layer of Fluid", *Astrophysical Journal*, 136, pp. 1126. doi:10.1086/147463.

[64] Monnier, J.D., Zhao, M., Pedretti, E., Thureau, N., Ireland, M., Muirhead, P., Berger, J.P., Millan-Gabet, R., Van Belle, G., ten Burmmelaar, T., McAlister, H., Ridgway, S., Turner, N., Sturmann, L., Sturmann, J. and Berger, D. (2007) "Imaging the Surface of Altair", *Science*, 317(5836), pp. 342. doi:10.1126/science.1143205.

[65] NASA California Institute of Technology's Jet Propulsion Laboratory (no date) *About the mission.*sunRise mission (Accessed: 5 March 2024).

[66] Newton, H.W. and Nunn, M.L. (1951) "The Sun's rotation derived from sunspots 1934-1944 and additional results" *Monthly Notices of the Royal Astronomical Society*, 111, p.413. doi:10.1093/mnras/111.4.413.

[67] NOAA (2022) *Geomagnetic storm conditions likely 2-3 February, 2022.* Space Weather Predicition Center (Accessed: 5 March 2024).

[68] *Nowcasting* Federal Office of Meteorology and Climatology MeteoSwiss (Accessed: 25 March 2024), Warning and forecasting systems: Nowcasting.

[69] *Oceanic Rossby waves* (2023) National Oceanic and Atmospheric Administration (Accessed: 5 March 2024), NOAA.

[70] Oliver, R., Ballester, J.L. and Baudin, F. (1998) "Emergence of magnetic flux on the Sun as the cause of a 158-day periodicity in sunspot areas", *Nature*, 394(6693), pp. 552-553. doi:10.1038/29012.

[71] Parker, E.N. (1958) "Dynamics of the Interplanetary Gas and Magnetic Fields", *The Astrophysical Journal*, 128, pp.664-676. doi:10.1086/146579.

[72] Pedlosky, J. (1987) *Geophysical Fluid Dynamics*, 2nd edn. New York: Springer-Verlag.

[73] Persad, A.H. (2017) *"Effects of Reduced Gravity", Handbook of Life Support Systems for Spacecraft and Extraterrestrial Habitats*, Springer.

[74] Phillips, T. (2023) *Near Miss: The Solar Superstorm of July 2012.* NASA.gov (Accessed: 5 March 2024).

[75] Poincaré, S. 1910, Théorie des Marées, Leçons de Mécanique Celeste, Vol. 3, (Paris: Gauthiers-Villars)

[76] *Poincaré wave* (2012) American Meteorological Society (Accessed: 5 March 2024), Glossary of Meteorology.

[77] Priest, E. (2014) *Magnetohydrodynamics of the Sun*, 3rd edn. United Kingdom: Cambridge University Press.

[78] Rani, D. (2022) *Fresh Solar Storm Spotted Heading Towards Earth, May Impact GPS Devices: Report.* Gadgets 360 (Accessed: 5 March 2024).

[79] Reames, D.V. (1999) "Particle acceleration at the Sun and in the heliosphere", *Space Science Reviews*, 90, pp. 413-491.

[80] Reames, D.V. (2013) "The two sources of solar energetic particles", *Space Science Reviews*, 175. doi:10.1007/s11214-013-9958-9.

[81] Rhines, P.B. (1977) *The sea: The dynamics of unsteady currents*, New York: Wiley.

[82] Rieger, E., Share, G.H., Forrest, D.J., Kanbach, G., Reppin, C. and Chupp, E.L. (1984) "A 154-day periodicity in the occurrence of hard solar flares?", *Nature*, 312, pp. 623-625. doi:10.1038/312623a0.

[83] Rossby, C.-G. (1939) "Relation between variations in the intensity of the zonal circulation of the atmosphere and the displacements of the semi-permanent centers of action" *Journal of Marine Research*, 2, pp. 38-54. doi:10.1357/002224039806649023.

[84] Schecter, D.A., Boyd, J.F. and Gilman, P.A. (2001) "Shallow-water magnetohydrodynamic waves in the solar tachocline", *The Astrophysical Journal*, 551(2), pp. L185-L188. doi:10.1086/320027.

[85] Schwabe, H. (1844) "Sun observations in the year 1843". *Astronomy News* 21:233.

[86] Snodgrass, H.B. (1982) "Magnetic rotation of the solar photosphere", *The Astrophysical Journal*, 270, pp.288-299. Bibcode: 1983ApJ. . .270 . .2883.

[87] *Solar wind* (no date) National Oceanic and Atmospheric Administration (Accessed: 5 March 2024), NOAA.

[88] Spiegel, E.A. and Zahn, J.P. (1992) “The solar tachocline”, *Astronomy and Astrophysics*, 265, pp. 106-114. Bibcode: 1992A&A...265..106S.

[89] Stratton J.A., Morese, P.M., Chu, L.J., Little, J.D.C. and Corbató, F.J. (1956) *Spheroidal Wave Functions. Including Tables of Separation Constants and Coefficients*, New York: John Wiley & Sons, Inc.

[90] Thomson, W. (1879) “On gravitational oscillations of rotating water”, *Proceedings of the Royal Society of Edinburgh*, 10, pp. 92-100.

[91] Thompson, M.J. (2004) “Helioseismology and the Sun’s interior”, *Astronomy and Geophysics*, 45(4), pp.4.21-4.25. doi:10.1046/j.1468-4004.2003.45404.x.

[92] Tobias, S.M., Brummell, N.H., Clune, T.L. and Toomre, J. (1998) “Magnetic activity and variations in solar luminosity”, *The Astrophysical Journal*, 502, L177-L180.

[93] Toriumi, S. and Wang, H. (2019) “Flare-productive active regions”, *Living Reviews in Solar Physics*, 16, 3. doi:10.1007/s41116-019-0019-7.

[94] Vallis, G.K. (2006) *Atmospheric and Oceanic Fluid Dynamics*, Cambridge: Cambridge University Press.

[95] Vallis, G.K. (2019) *Essentials of Atmospheric and Oceanic Dynamics*. Cambridge: Cambridge University Press.

[96] Veronig, A.M., Jain, S., Podladchikova, T., Pötzi, W. and Clette, F. (2021) “Hemispheric sunspot numbers 1874-2020”, *Astronomy and Astrophysics*, 652(A56). doi:10.1051/0004-6361/202141195.

[97] Waidele, M. and Zhao, J. (2023) “Observed Power and Frequency Variations of Solar Rossby Waves with Solar Cycles”, *The Astrophysical Journal*, 954(1), pp. L26. doi:10.3847/2041-8213/acefd0.

[98] Young, M. (2013) *The weakest solar cycle in 100 years.* Sky & Telescope (Accessed: 5 March 2024).

[99] Zaqarashvili, T.V., Oliver, R., Ballester, J.L. and Shergelashvili, B.M. (2007) “Rossby waves in ‘shallow water’ magnetohydrodynamics”, *Astronomy and Astrophysics*, 470(3), pp. 815-820. doi:10.1051/0004-6361:20077382.

[100] Zaqarashvili, T.V., Oliver, R. and Ballester, J.L. (2009) "Global shallow water magnetohydrodynamic waves in the solar tachocline", *The Astrophysical Journal*, 691(1), pp. L41-L44. doi:10.1088/0004-637X/691/1/L41.

[101] Zaqarashvili, T.V., Carbonell, M., Oliver, R. and Ballester, J.L. (2010) "Magnetic Rossby waves in the solar tachocline and Rieger-type periodicities", *The Astrophysical Journal*, 709(2), pp. 749-758. doi:10.1088/0004-637X/709/2/749.

[102] Zaqarashvili, T.V., Oliver, R., Hanslmeier, A., Carbonell, M., Ballester, J.L., Gachechiladze, T. and Usoskin, I.G. (2015) "Long-term variation in the Sun's activity caused by magnetic Rossby waves in the tachocline", *The Astrophysical Journal*, 805(2), L14. doi:10.1088/2041-8205/805/2/L14.

[103] Zaqarashvili, T.V. and Gurgenashvili, E. (2018) "Magneto-Rossby Waves and Seismology of Solar Interior", *Frontiers in Astronomy and Space Sciences*, 5. doi:10.3389/fspas.2018.00007.

[104] Zaqarashvili, T.V. (2018) "Equatorial magnetohydrodynamics shallow water waves in the solar tachocline", *The Astrophysical Journal*, 856(1), 32. doi:10.3847/1538-4357/aab26f.

[105] Zaqarashvili, T.V., Albekioni, M., Ballester, J.L., Bekki, Y., Biancofiore, L., Birch, A.C., Dikpati, M., Gizon, L., Gurgenashvili, E., Heifetz, E., Lanza, A.F., McIntosh, S.W., Ofman, L., Oliver, R., Proxauf, B., Umurhan, O.M. and Yellin-Bergovoy, R. (2021) "Rossby Waves in Astrophysics", *Space Science Reviews*, 217(1), 15. doi:10.1007/s11214-021-00790-2.

Bibliography: Figures

[1] Alexander G. Kosovichev (convective zone); Sebastien Couvidat, Rafael García and Sylvaine Turck-Chièze (radiative zone). *Latitudinal Differential Rotation*. SunOrbit.net (Accessed: 5 March 2024).

[2] Climate.gov (2022) *What are teleconnection? Connecting Earth's climate patterns via global information superhighways.*. Climate.gov (Accessed: 5 March 2024).

[3] Herbrik, M. and Kokkotas, K. (2015) "Stability Analysis of Magnetised Neutron Stars - A Semi-analytic Approach", *Monthly Notices of the Royal Astronomical Society* 466(2). doi: 10.1093/mnras/stw3098.

[4] Klina, J. (2016) *The Coriolis effect: Physics 211/Web Project*. University of Alaska-Fairbanks: Physics Department (Accessed: 5 March 2024).

[5] Krejcirik, D. and Pratelli, A. (2010) "The Cheeger constant of curved strips", *Monthly Notices of the Royal Astronomical Society* 466(2). doi: 10.1093/mnras/stw3098.

[6] Kuznetsov, A./Reuters (2018) *The aurora borealis in the sky near Rovaniemi in Lapland*. Peakpx (Accessed: 5 March 2024).

[7] NASA/JPL-Caltech (2023) *What is an Aurora?*. NASA: Space Place (Accessed: 5 March 2024).

[8] Lang, K.R. (2001) *The Cambridge Encyclopedia of the Sun*. Cambridge: Cambridge University Press.

[9] Morin D. (2015) *Chapter 6*. Harvard University (Accessed: 5 March 2024).

[10] NASA's Goddard Space Flight Center (2017) *Waves on Sun Give NASA New Insight into Space Weather Forecasting*. NASA.gov (Accessed: 5 March 2024).

[11] NOAA.gov *Solar Cycle Progression*. NOAA Space Weather Prediction Center (Accessed: 5 March 2024).

[12] Rosenthal M. (2015) *Physics 103 - Discussion Notes 3*. Class notes (Accessed: 5 March 2024).

[13] SpaceWeatherLive.com *Number of C, M and X-class solar flares per year*. SpaceWeatherLive.com (Accessed: 5 March 2024).

[14] Wikimedia Commons *Toroidal coord*. Wikimedia Commons, the free media repository (Accessed: 5 March 2024).